

Dissertation
zur Erlangung des akademischen Grades
Dr. rer. nat. im Fach Physik

**Synergies of flavor anomalies with top-quark
physics in the Standard Model Effective Field
Theory and direct searches**

Stefan Bißmann
geboren in Datteln

Dortmund, Januar 2021

Lehrstuhl für Theoretische Physik IV
Fakultät Physik
Technische Universität Dortmund

Gutachter der Dissertation:

Prof. Dr. Gudrun Hiller, Prof. Dr. Kevin Kröniger und Prof. Dr. Michael Spannowsky

Vorsitzender des Promotionsausschusses:

Prof. Dr. Heinz Hövel

Datum der mündlichen Prüfung::

22. Februar 2021

To my partner Sarina and my best friend Clara,

*for all the times you cheered me up when I felt down,
all the times you pushed me on when I thought I could not continue,
and all the times you believed in me when I had doubts.*

Thank you.

Acknowledgement

It has been an amazing and fascinating time to work and live as a PhD student at the department in Dortmund, and a lot of people contributed to this experience. The last three years have deeply affected the way I view the world, and also the way I view myself.

First of all, I want to thank my adviser, Gudrun Hiller, for giving me the opportunity to join the department as a PhD student, and for guiding the development of this work with her wisdom. I am grateful for all the knowledge she shared with me about physics, and for all the things we learned together about theoretical particle physics. Throughout the last years, she encouraged me to work independently on my research projects, while still providing me with all her help and knowledge whenever I ran into challenges or was in the need of guidance. She gave me the opportunity to be part of an international and motivated community; an experience, that deeply changed me and helped me to grow. I am extremely thankful for all her teachings with topics covering physics, teaching, and also the life of a physicist, and in particular for her caring advices that helped my finding my way.

I am also grateful for having the opportunity to work throughout the years together with Kevin Kröniger, and for all the advices and care he spent in our projects, making him a second adviser for my PhD. I owe to him and our discussions a lot of knowledge about statistics and experimental physics, and am very thankful for all the times we spend together in meetings discussing our results. I am still amazed of how much information can be seen in a single distribution, and how seemingly easily he discovered the issues within our computations. I am very grateful that he agreed on being the second appraiser of this thesis.

A large part of this work would not have been possible without Cornelius, who is a fundamental part of most of my projects. Without his continuous support, it would not have been possible to derive most of the results shown in this thesis. I owe to him and all the time we spend in almost daily discussions and working meetings up until late a large part of my knowledge; we often found ourselves sitting in front of a challenge, and only with his continuous support we were able to overcome it. I am grateful for all the time we spend together working and all the statistics schools we visited. Without him the computations would have been less fun and also less successful.

Furthermore, I want to thank Johannes and Daniel for their help and support in our projects, and all the knowledge they provided me with during our meetings and discussions.

The life at the physics department was an incredible experience, and all the conferences and schools I visited created an unforgettable memory. All this would not have been possible without the caring work of Susanne Laurent, and I am very grateful for all the work she spends every day to organize our daily lives at the department.

The last three years were a fun time at the department, and besides giving me a place to work on my projects the department turned out to be like a second home for me. I am very grateful to all the members of T III and T IV who made the last years so special. I particularly want to thank Maggi, Dennis, Rigo, Dominik, Dominik, and Tim for all the help and fun we had, and especially Rigo for all the help he provided me with whenever I needed a helping hand. I am grateful to Maggi and Dennis for their advices in the life as the admin of the department, and particularly Tim for facing this challenge together with me; shared pain truly is less pain. I want to thank Nico and Andrey for the great experience and the discussions that we had every day. Furthermore, I want to thank Marcel and Hector for the amazing time we spend together, starting with our early workouts, the charming early-morning coffee break together with Rigo, and continuing until late with physics discussions, and also for all their support outside of physics. I am also grateful to everybody who reviewed

this manuscript and gave me suggestions for improvement.

I want to thank my great friends outside of the department, Thomas, Tobi, Laurids, Thomas, Henrik, Hannah, and Ben, with who I had a lot of fun throughout the last years. Furthermore, I am grateful to Petra and Guido for all their support and advices they gave me during the last years, and for all the discussions we had. I took nothing of this for granted, and am very grateful for their help in developing myself further.

I am indebted to my parents, Ruth and Günter, as well as my siblings, Anna-Katharina and Sebastian, for all their caring support during every stage of this PhD, and for all the times they cheered me up when I had doubts. I am grateful for all the physics-motivated discussions we had, and for the interest they showed in my work.

The last lines are dedicated to the two persons who have grown closest to my heart throughout the last years. I owe to Clara more than I can write in a few lines, and a significant part of my understanding of theoretical physics as well as the improvement of my English is thanks to her and our discussions. I want to thank her for the fascinating collaboration, and for all her help that went into writing this thesis. She continuously supported me throughout the last years, in physics and beyond, and it is especially the latter that I value the most. I am grateful that I was allowed to find such an amazing friend. I am very thankful for all the moments we shared, all the help she provided me with, and that she always managed to get me back on my feet.

Finally, I want to express my profound gratitude to my partner, Sarina. Words can hardly express how much I owe to her. She deserves tremendous credit for her unequalled support throughout the last years and for believing in me more than I did. I am grateful for all the times she pushed me on and for all the effort she spent on motivating me to develop myself further. She always took the time to listen to my worries and to help me shaking of my doubts. The work that went into this thesis would not have been possible without her and her continuous support.

Kurzfassung

Diese Dissertation beinhaltet eine Studie zur Entdeckung von Physik jenseits des Standard Modells (BSM) geleitet durch die Flavor-Anomalien. Mit dem Ziel, den Top-Quark Bereich der Standard Model Effective Field Theory (SMEFT) mit den Anomalien in $b \rightarrow s$ Übergängen zu verbinden, führen wir zunächst einen globalen Fit an Top-Quark Messungen durch, in dem wir die Gültigkeit des SMEFT-Ansatzes sowie Vorteile und Herausforderungen, die in der Kombination verschiedener Datensätze entstehen, diskutieren. Anschließend führen wir eine erste kombinierte Analyse von Top-Quark und Beauty Daten durch und fitten drei SMEFT Wilson Koeffizienten an $t\bar{t}\gamma$ and $b \rightarrow s\gamma$ Daten. Wir beschreiben die notwendigen Schritte für die Analyse und zeigen, wie Unterschiede in der Sensitivität die Resultate deutlich verbessern. Wir erweitern diese Studie und betrachten semileptonische Operatoren, die im starken Zusammenhang zu den Anomalien in $b \rightarrow s\mu^+\mu^-$ Messungen stehen, in einem Fit an Top-Quark, Zbb , und B -Physik Observablen im Kontext aktueller Messungen sowie mehrerer Zukunftsszenarien für HL-LHC, Belle II, und einem Lepton Collider. Unsere Analyse zeigt eine starke Verbindung von Top-Quark und Beauty Observablen auf, die neue Möglichkeiten für modellunabhängige Fits ermöglichen. Um unsere Analyse abzurunden, untersuchen wir den Fall, dass BSM Physik am LHC produziert werden könnte. Diese neue Physik kann sowohl die Anomalien in den magnetischen Momenten der Leptonen erklären als auch mehrere Probleme des Standard Modells beheben. Wir betrachten dazu zwei asymptotisch sichere Modelle mit vektorartigen Leptonen und Skalaren mit einer nicht-trivialen Flavorstruktur und führen eine detaillierte Analyse für eine Entdeckung am LHC durch. Wir konstruieren Nulltests und stellen fest, dass der Run 2 Datensatz ausreichen könnte, um BSM Physik zu entdecken.

Abstract

This thesis comprises a study on opportunities for physics beyond the Standard Model (BSM) guided by the flavor anomalies. Aiming at linking the top-quark sector of the Standard Model Effective Field Theory (SMEFT) to the anomalies in $b \rightarrow s$ transitions, we perform a global fit to top-quark data detailing on the validity of the SMEFT framework, and highlight benefits and challenges of combining multiple measurements in a combined fit. To combine top-quark and beauty data we perform a first joined fit of three SMEFT Wilson coefficients to $t\bar{t}\gamma$ and $b \rightarrow s\gamma$ data. We work out the steps needed for linking top-quark and B physics within SMEFT, and demonstrate how the complementarity of both sectors enhances constraints significantly. Extending our setup, we analyze semileptonic four-fermion operators, which are of high interest in the context of anomalies seen in $b \rightarrow s\mu^+\mu^-$ data, in a combined fit to top-quark, Zbb , and B -physics observables using present data as well as future scenarios of HL-LHC, Belle II, and a future lepton collider. We observe powerful synergies between top-quark and beauty physics, which open new directions for model-independent searches. To complement our analysis, we investigate the possibility that BSM physics can be well within the reach of the LHC while still accommodating the anomalies within the lepton anomalous magnetic moments and lifting several shortcomings of the Standard Model (SM). The models are an asymptotically safe extension of the SM featuring potentially light vector-like leptons and additional scalars with a non-trivial flavor structure. We perform a detailed study of implications for discovery at the LHC exploiting unique flavor signatures to construct null-tests of the SM, and find that Run 2 data can be sufficient to detect BSM physics, indicating that new physics might be just around the corner.

Publications

This thesis is based on the following publications by the author:

- Stefan Bißmann, Johannes Erdmann, Cornelius Grunwald, Gudrun Hiller, and Kevin Kröninger. "Constraining top-quark couplings combining top-quark and B decay observables", In: *Eur. Phys. J. C* 80.2 (2020), p. 136. DOI: 10.1140/epjc/s10052-020-7680-9. arXiv: 1909.13632 [hep-ph].
- Stefan Bißmann, Johannes Erdmann, Cornelius Grunwald, Gudrun Hiller, and Kevin Kröninger. "Correlating uncertainties in global analyses within SMEFT matters", In: *Phys. Rev. D* 102 (2020), p. 115019. DOI: 10.1103/PhysRevD.102.115019. arXiv: 1912.06090 [hep-ph].
- Stefan Bißmann, Cornelius Grunwald, Gudrun Hiller, and Kevin Kröninger. "Top and Beauty synergies in SMEFT-fits at present and future colliders", In: *JHEP* 06 (2021), p. 010 DOI: 10.1007/JHEP06(2021)010. arXiv: 2012.10456 [hep-ph]
- Stefan Bißmann, Gudrun Hiller, Clara Hormigos-Feliu, and Daniel F. Litim. "Multi-lepton signatures of vector-like leptons with flavor", In: *Eur. Phys. J. C* 81.2 (2021), p. 101 DOI: 10.1140/epjc/s10052-021-08886-3 arXiv: 2011.12964 [hep-ph]

In addition, results have been presented in the following proceedings:

- Stefan Bißmann, Cornelius Grunwald, Gudrun Hiller, and Kevin Kröninger. "Synergies of top and B anomalies in SMEFT", In *55th Recontres de Moriond on Electroweak Interactions and Unified Theories (Moriond EW 2021), March 20-27, 2021*, arXiv: 2105.05257 [hep-ph]

Contents

1	Introduction	1
2	The Standard Model and beyond	5
2.1	The Standard Model of particle physics	5
2.1.1	The principle of gauge invariance	5
2.1.2	The Standard Model as a gauge theory	8
2.1.3	The Yukawa sector	10
2.2	The concept of renormalization and running of couplings	13
2.3	Motivation for physics beyond the Standard Model	18
2.3.1	Landau poles and asymptotic safety	19
2.3.2	Flavor puzzle	20
2.3.3	Hints for New Physics: flavor anomalies	21
3	Effective field theories	25
3.1	Effective theories below the electroweak scale	26
3.2	The Standard Model Effective Field Theory	30
3.2.1	Operator basis	30
3.2.2	Redefinition of parameters and their relations	32
3.2.3	Spontaneous symmetry breaking	32
3.2.4	Linking physics at different scales	34
3.3	The top-quark sector	35
3.4	Higgs Effective Field Theory	36
3.5	EFT <i>fitter</i> : fitting effective theories to data	37
4	Global fit to top-quark data	39
4.1	Effective operators	40
4.2	Fit setup	40
4.3	Fits to data	44
4.3.1	Constraints on Wilson coefficients	45
4.3.2	Comparison to literature	50
4.3.3	Future scenarios	51
4.4	Summary	53
5	Exploring combinations of top and beauty	55
5.1	Effective theories at different scales	55
5.2	Matching at the electroweak scale	56
5.3	Measurements included in the analysis	59
5.4	Computation of observables	60
5.5	Constraints on SMEFT coefficients	61
5.6	Summary	64

6	Synergies of top and beauty	67
6.1	Dimension-six operators	67
6.1.1	Coefficients in the mass basis	68
6.1.2	Matching conditions	70
6.2	Observables	72
6.2.1	Computation of observables	72
6.2.2	Sensitivity to Wilson coefficients	73
6.3	Fits to present data	75
6.3.1	Fits to individual sets	76
6.3.2	Combined fit to present data	80
6.4	Constraints at future colliders	82
6.4.1	Constraints in the near-future scenario	82
6.4.2	Constraints in the far-future scenario	85
6.4.3	Combined fit	86
6.5	Summary	88
7	Asympotic safety confronts collider physics	89
7.1	Asymptotically safe vector-like leptons	90
7.2	Present tests of parameter space	94
7.2.1	Production of final states with at least four light leptons	95
7.2.2	Constraints from transverse momentum distributions	96
7.3	Additional observables with null test potential	98
7.3.1	Definition of observables	99
7.3.2	Distributions at Run 2	100
7.3.3	Distributions at higher luminosities	103
7.3.4	Benchmark scenarios beyond $g - 2$	105
7.4	Summary	107
8	Conclusion	109
A	Parameters and loop functions	111
A.1	Input parameters	111
A.2	Loop functions	112
B	SMEFT Lagrangian at dimension six	115
B.1	Basis of dimension-six operators	115
B.2	Redefinition of SM parameters: the gauge sector	117
B.3	Input scheme dependence	118
B.4	Implications for the low-energy Lagrangian	119
B.5	Solving renormalization group equations	120
C	Weak effective theories	123
C.1	$b \rightarrow s\gamma$ and $b \rightarrow sl^+\ell^-$ transitions	123
C.2	$b \rightarrow s\nu\bar{\nu}$ transitions	123
C.3	$B_s - \bar{B}_s$ mixing	124
D	Search for physics beyond the Standard Model at colliders	125
D.1	Final state radiation and the notion of jets	125
D.2	Parton distribution functions	127

D.3	Related tools	128
E	Toy example for correlation matrices	131
F	Constraints in different correlation scenarios	133
F.1	'No correlation' scenario	133
F.2	'Best guess' scenario	134
F.3	Constraints in future scenarios	136
G	Fiducial cross sections within SMEFT	139
H	Linking top and beauty	141
H.1	Coefficients and operators in the mass basis	141
H.2	Numerical results for matching	142
H.3	Fits to present data	143
H.3.1	Fits to top-quark data	143
H.3.2	Constraints from beauty data	144
H.3.3	Combining top and beauty	144
H.4	Constraints in future scenarios	146
I	Vector-like leptons at hadron colliders	147
I.1	Production of vector-like leptons	147
I.2	Madgraph settings	148
I.3	Distributions of the scalar transverse momentum sum	149
I.4	Novel observables at parton level	150
I.5	More general benchmark scenarios	153
	Bibliography	155
	Glossary	185

1 Introduction

In the past decades, both theoretical and experimental efforts have led to the formulation of the *Standard Model* (SM) of particle physics. This theory allows to describe matter and its interactions at a fundamental level including three of the four fundamental interactions known today. These comprise the *strong*, *weak* and *electromagnetic* interactions, and only gravity remains yet to be included into a fundamental particle theory. A milestone for particle physics was reached in 2012 with the direct detection of a scalar resonance at the *Large Hadron Collider* (LHC) by the ATLAS and CMS experiments [1, 2]. In subsequent analyses this resonance has been found to be compatible with the SM Higgs boson [3–5]. This direct detection completed the SM, and so far further investigations of the properties of the Higgs couplings by ATLAS and CMS are found to be in agreement with the SM predictions [6].

In the future, measurements at the LHC are scheduled to put the SM under further tests by colliding protons at center-of-mass energies of 13 and 14 TeV. This extensive program will necessarily push our knowledge of particle physics into yet unexplored territories. In this regard, two complementary approaches in the hunt for physics *beyond the Standard Model* (BSM) can be applied to enrich our fundamental understanding of nature. First, *direct* searches for resonances allow to discover a particle not included in the SM. Such an event would be truly revolutionary, and would certainly be the starting point for the formulation of a completely new "Standard Model". If, however, no such resonance can be found, *indirect* searches allow to test significantly higher energies by comparing SM predictions to precision measurements. Any significant discrepancy would be a sign of virtual contributions from BSM physics too heavy to be produced with present collider setups. Similarly to a direct detection, any significant deviation from the SM discovered in indirect searches would be an outstanding event, and would serve as a beacon for both model building and further experimental analyses in the hunt for BSM physics.

The situation faced nowadays in particle physics is that various measurements are in good agreement with SM predictions. In addition, no evidence for direct detection of BSM particles is found within present data. However, despite this overall agreement there is a broad range of both hints for BSM physics and known shortcomings of the SM. Starting off with the latter, the SM describes only visible matter. Thus, it lacks any suitable explanation for the existence of both *dark energy* and *dark matter*, which have to be included in the description of the energy content and the acceleration of the expansion of the universe. Nor can the SM sufficiently describe the matter-antimatter asymmetry present in the Universe. Furthermore, the SM suffers from several theoretical shortcomings, such as the breakdown of perturbation theory at high energy scales or the lack of explanation for the patterns observed in both the masses of SM particles and their mixing parameters.

Besides these shortcomings of the SM, there are several indications within data for the presence of BSM physics. While experiments at high-energy colliders have yet to report a direct detection of BSM physics, various hints for deviations from the SM can be found within in the flavor sector. One example, which has raised significant attention in the last years, is found in the B sector. Along with discrepancies in angular distributions of $b \rightarrow s\mu^+\mu^-$ transitions, the so-called B *anomalies* hint at *lepton flavor non-universality*, see *e.g.* [7–12]. This

is in stark contrast to the universal couplings in the SM. While deviations in each observable are (on their own) not significant enough to represent evidence for BSM physics, they seem to draw a consistent pattern over several processes. This makes them an interesting guideline for the construction of models explaining the origin of these anomalies. Another example are discrepancies between data and SM predictions observed in the *anomalous magnetic moments* (AMMs) of both the electron and the muon [13–16]. Similarly to the B anomalies, the AMMs also hint at BSM physics in interactions of charged leptons.

After the successful construction and confirmation of the SM, particle physics has entered an era of searches for BSM physics, which are presently guided by the flavor anomalies. It is to be expected that direct discovery of BSM physics is a prospect of future colliders. The pattern observed in data indicates that the scale of BSM physics can be separated from the scales in the SM. While present data could also be a result of new physics being only very weakly (*i.e.* feebly) interacting or having properties that are not detectable with present search strategies, the possibility that BSM physics could be heavier than energy scales of present experiments is of special interest. The reason is that a decoupling of new physics allows to apply indirect searches in the hunt for BSM physics. However, such indirect searches are in fact highly non-trivial. Any BSM model meant to explain a deviation from the SM found in data must, at the same time, pass constraints from measurements that show agreement with the SM. This raises the question whether there is an efficient method that simultaneously tests multiple observables in one consistent framework and also allows to compare as many models as possible to the results of such an analysis. The answer to this question is found within the concept of *effective field theories* (EFTs), in particular the *Standard Model Effective Field Theory* (SMEFT). This EFT consists of the SM Lagrangian and additional higher-dimensional operators built out of SM fields. Required to be consistent with the SM symmetries, these operators parametrize BSM physics model-independently for energies below the scale of new physics. The only assumptions needed in the construction refer to the particle content and the symmetries at a given scale. In the case of the SMEFT, we assume that only the SM particle content is present below the electroweak scale, and thus the operators are required to be invariant under SM symmetry group, $SU(3)_C \times SU(2)_L \times U(1)_Y$. In this regard, special focus has been placed on the top-quark sector, which has entered a precision era at the LHC. The top quark is too heavy to apply low-energy EFTs, which describe physics below the electroweak scale. Thus, it is the perfect starting point for global SMEFT fits.

However, the true significance of the SMEFT framework has a deeper reasoning than simply performing model-independent fits to data of top-quark physics or other sectors. Instead, it allows to combine observables from various physical processes in a single analysis [17–24]. Furthermore, matching the SMEFT Lagrangian onto low-energy EFTs relates observables measured at different energy scales [21–24]. In particular, this procedure enables us to link the flavor sector, where presently the most promising hints for BSM are found, to top-quark data, which is only very recently considered in model-independent fits. In this spirit, the top-quark sector is truly the ideal starting point for such a combined fit, as $SU(2)_L$ invariance relates top-quark and beauty physics. Combining top and beauty is the first step towards a global fit to various physical processes, leaving no stone unturned in the quest for BSM physics.

In this thesis, which is based on Refs. [23–26], we follow the guidance of the flavor anomalies, and perform a combined analysis of top-quark and beauty data linking anomalies in $b \rightarrow s$ transitions to top-quark observables. To do so, we start by introducing the SM Lagrangian in Chapter 2. We explain how this theory is constructed employing the concept of *gauge symmetries*. We discuss its parameters and field content, which is also used in the

construction of the SMEFT Lagrangian. In Chapter 3, we explain the framework of EFTs, and consider in particular the SMEFT Lagrangian. We discuss specific implications for low-energy observables induced by $SU(2)_L$ invariance. Furthermore, we introduce the concept of global fits within the SMEFT framework, in particular to the top-quark sector, which is studied throughout this thesis. In Chapter 4, we perform a first global fit to data from t -channel single top-quark production and top-quark decay, describing in detail our fitting procedure. In addition, we discuss the validity of the SMEFT expansion as well as benefits and challenges of the combination of different datasets. In Chapter 5, we set the stage for a combined fit to top-quark and beauty data using the example of $t\bar{t}\gamma$ production and $b \rightarrow s\gamma$ transitions. We investigate the feasibility of such a combination, and detail the steps needed to perform a fit to observables measured at different energy scales within the SMEFT framework. In Chapter 6, we build up on this analysis, and perform a global fit to top-quark and beauty data. In particular, we include semileptonic four-fermion operators, which are of special interest regarding the anomalies in $b \rightarrow s$ transitions. We further demonstrate how present data provides the opportunity to probe contact interactions of leptons and top quarks, which are only weakly constrained by LHC data [27]. We discuss the interplay of constraints derived from top-quark and beauty observables in present data and at future colliders. We place special emphasis on top-quark physics at a future lepton collider. In Chapter 7, we use a complementary approach in the search for BSM physics: direct production of BSM particles. BSM physics does not need to be significantly separated in energy from the SM content to accommodate flavor anomalies seen in the lepton AMMs as well as lifting several shortcomings of the SM [28–30]. Thus, flavorful new physics, *i.e.* *vector-like leptons* and additional scalars which are matrices in flavor space, can be just around the corner and well within reach of direct searches at the LHC. We study how such models can be tested at present colliders beyond the framework of global fits. Furthermore, we construct novel observables employing model-specific features. These observables allow for precision tests of the SM and open new directions in the search for direct detection of such flavorful BSM physics at the LHC. We conclude in Chapter 8. Furthermore, various appendices provide information on the parameters, the theoretical framework of EFTs and the different tools used for the description of particle physics at colliders, and give further insights into the topics discussed throughout this thesis.

2 The Standard Model and beyond

In this chapter, we introduce the SM of particle physics in Sec. 2.1. We detail on its construction employing the concept of *gauge symmetries* and the particle content that is described with this theory. The concept of *renormalization* is introduced in Sec. 2.2. In Sec. 2.3, we discuss several shortcomings of the SM, and give examples which motivate the need for BSM physics. Special care is devoted to the *flavor anomalies* in Sec. 2.3.3.

2.1 The Standard Model of particle physics

In the SM, the three fundamental interactions emerge from the principle of symmetries. Each of the three interactions is encoded in a local gauge group. The $SU(3)_C$ group is the underlying gauge group of *quantum chromodynamics* (QCD), which is the gauge theory of strong interactions [31–34]. The *electroweak* (EW) interactions are described by the $SU(2)_L \times U(1)_Y$ symmetry group [35–37].

The matter content of the SM can be divided into two classes: *fermions*, which are spin-1/2 particles, and *bosons*, which are, in the SM, spin-0 and spin-1 particles. Bosons of spin 0 are referred to as *scalars*, while bosons of spin 1 are called *vector bosons*. The fermions can be further divided into *quarks* and *leptons* (and their corresponding antiparticles). Only quarks are charged under the $SU(3)_C$ gauge group and have three different *color* charges.

There are six different *flavors* of quarks: up u , down d , charm c , strange s , beauty, or bottom, b and top t . Two of these quarks together form a so-called *generation* of quarks. The first generation contains u and d , the second c and s , and the third one t and b . Within one generation, the quarks are divided into two classes: those with electric charge $Q = 2/3$ (u, c, t), called *up-type* or *up-sector* quarks, and those with $Q = -1/3$ (d, s, b), referred to as *down-type* or *down-sector* quarks. In the absence of quark masses, these three generations are exact copies of one another.

The other class of fermions are leptons, which are distinguished into charged leptons and neutrinos. Charged leptons have an electric charge of $Q = -1$ while neutrinos are neutral particles. There are three different charged leptons, the electron e^- , the muon μ^- , and the tau τ^- . Similarly, there are three different neutrinos: ν_e, ν_μ and ν_τ . Similarly to the quarks, the leptons are divided in three generations: the first generation contains e^- and ν_e , the second μ^- and ν_μ , and the third τ^- and ν_τ . Only the charged leptons are massive while the neutrinos are massless. Again, neglecting the charged lepton masses these three generations are exact copies of one another. An overview on the different fermions in the SM is given in Tab. 2.1. As in any gauge theory, only interactions that are invariant under gauge transformations are allowed in the SM Lagrangian. In the following, we discuss the concept of gauge symmetries, and apply this framework to construct the SM Lagrangian, which we give in Eq. 2.1.50.

2.1.1 The principle of gauge invariance

The principle of gauge invariance under a symmetry group restricts a Lagrangian to a certain kind of allowed interactions. As an example, we consider a fermion field ψ_i^α that transforms

Particle	$SU(3)_C$	$SU(2)_L$	Y	Q	I_3
$\begin{pmatrix} u \\ d \end{pmatrix}_L, \begin{pmatrix} c \\ s \end{pmatrix}_L, \begin{pmatrix} t \\ b \end{pmatrix}_L$	3	2	1/6	2/3 -1/3	1/2 -1/2
u_R, c_R, t_R	3	1	2/3	2/3	-
d_R, s_R, b_R	3	1	-1/3	-1/3	-
$\begin{pmatrix} \nu_e \\ e \end{pmatrix}_L, \begin{pmatrix} \nu_\mu \\ \mu \end{pmatrix}_L, \begin{pmatrix} \nu_\tau \\ \tau \end{pmatrix}_L$	1	2	-1/2	0 -1	1/2 -1/2
e_R, μ_R, τ_R	1	1	-1	-1	-

Table 2.1: Fermion content of the SM. **3**, **2** and **1** denote triplet, doublet and singlet representations under the different gauge groups, respectively. We work with the convention $Y = Q - I_3$, where I_3 denotes the third component of the isospin.

under an infinitesimal symmetry transformation as¹

$$\psi_i^\alpha \rightarrow \psi_i^\alpha + i\theta^A T_{\alpha\beta}^A \psi_i^\beta, \quad (2.1.1)$$

with a set of independent and constant matrices T^A and real, infinitesimal parameters θ^A , which, in general, depend on time t and space \mathbf{x} , called x in the following. If these symmetry transformations are part of a Lie group, the matrices T^A obey the Lie algebra

$$[T^A, T^B] = if^{ABC} T^C, \quad (2.1.2)$$

where the real constants f^{ABC} are called the *structure constants* of the symmetry group. In the following, we mostly consider the case of $SU(N)$ with $A = 1, \dots, N^2 - 1$. The structure constants define the *adjoint* representation of the Lie group

$$(T_a^A)_{BC} = -if^{BCA}, \quad (2.1.3)$$

which is the representation with the same dimension as the Lie group itself. The free Lagrangian of the fermion field reads

$$\mathcal{L}_0 = \bar{\psi}_i^\alpha (i\cancel{\partial} - m_i) \psi_i^\alpha, \quad (2.1.4)$$

where we use *Einstein's sum convention* and sum over all repeated indices. We use the notation $\cancel{\partial} = \gamma^\mu a_\mu$, where γ^μ are the *Dirac matrices*. The field $\bar{\psi}_i^\alpha$ is defined as $\bar{\psi}_i^\alpha = (\psi_i^\alpha)^\dagger \gamma_0$. As long as the infinitesimal parameter θ^A is constant, \mathcal{L}_0 is invariant under the symmetry transformation in Eq. (2.1.1). This is called *global gauge invariance*. Under a *local gauge transformation* with $\theta^A = \theta^A(x)$ the symmetry transformation in Eq. (2.1.1) does not leave the free Lagrangian invariant anymore. Instead, \mathcal{L}_0 transforms as

$$\mathcal{L}_0 \rightarrow \mathcal{L}_0 + i(\partial_\mu \theta^A(x)) \bar{\psi}_i^\alpha \gamma^\mu T_{\alpha\beta}^A \psi_i^\beta. \quad (2.1.5)$$

According to the *Noether theorem*, the additional term is called the *conserved current* of the symmetry transformation

$$J_\mu^A \equiv \bar{\psi}_i^\alpha \gamma_\mu T_{\alpha\beta}^A \psi_i^\beta, \quad \text{with} \quad \partial^\mu J_\mu^A = 0. \quad (2.1.6)$$

¹Note that in this convention the gauge coupling is absorbed into the generators and structure constants.

To render \mathcal{L}_0 invariant under a local gauge transformation (2.1.1), we need to include a new field G_μ^A , which transforms under local gauge transformations in a way that the additional term $\sim \partial_\mu \theta^A$ in Eq. (2.1.5) is canceled. Since G_μ^A carries an index A , it undergoes a transformation in the adjoint representation of the symmetry group. The infinitesimal transformation of the field G_μ^A reads

$$G_\mu^A \rightarrow G_\mu^A + \partial_\mu \theta^A + i \theta^B (T_a^B)_{AC} G_\mu^C = G_\mu^A - \partial_\mu \theta^A - \theta^B f^{ACB} G_\mu^C, \quad (2.1.7)$$

This field G_μ^A , called the *gauge field* of the symmetry group, allows us to construct a *covariant derivative*:

$$D_\mu \psi_i^\alpha = \partial_\mu \psi_i^\alpha + i G_\mu^A T_{\alpha\beta}^A \psi_i^\beta. \quad (2.1.8)$$

With Eqs. (2.1.1), (2.1.7) and (2.1.2) the covariant derivative transforms under a local gauge transformation as

$$\begin{aligned} D_\mu \psi_i^\alpha &\rightarrow D_\mu \psi_i^\alpha + i (\partial_\mu \theta^A) T_{\alpha\beta}^A \psi_i^\beta - G_\mu^A T_{\alpha\beta}^A (\partial_\mu \theta^B) T_{\beta\gamma}^B \psi_i^\gamma - i \partial_\mu \theta^A T_{\alpha\beta}^A \psi_i^\beta \\ &\quad - i \theta^B f^{ACB} G_\mu^C T_{\alpha\beta}^A \psi_i^\beta \\ &= D_\mu \psi_i^\alpha + i \theta^A T_{\alpha\beta}^A D_\mu \psi_i^\beta, \end{aligned} \quad (2.1.9)$$

so that $D_\mu \psi_i^\alpha$ transforms just as ψ_i^α . This means that the Lagrangian constructed with the covariant derivative

$$\mathcal{L} = \bar{\psi}_i^\alpha (i \not{D} - m_i) \psi_i^\alpha, \quad (2.1.10)$$

is invariant under local symmetry transformations. This Lagrangian includes interactions between ψ_i^α and the gauge field G_μ^A . To construct a physical theory with propagating fields G_μ^A the kinetic terms of the gauge field have to be included. From the gauge transformation in Eq. (2.1.7) we can see that a mass term $\sim G_\mu^A G^{A\mu}$ violates invariance under a symmetry transformation. Hence, the gauge field has to be massless. For the kinetic term, the only gauge- and Lorentz-invariant term that can be constructed at mass dimension ≤ 4 without being a total derivative is

$$F_{\mu\nu}^A F^{A\mu\nu}, \quad \text{with} \quad F_{\mu\nu}^A = \partial_\mu G_\nu^A - \partial_\nu G_\mu^A + f^{ABc} G_\mu^B G_\nu^C. \quad (2.1.11)$$

The tensor $F_{\mu\nu}$ is also referred to as *field strength tensor* and can be connected to the covariant derivative in Eq. (2.1.8) via

$$\mathbf{F}_{\mu\nu} = i [D_\mu, D_\nu] = \partial_\mu \mathbf{G}_\nu - \partial_\nu \mathbf{G}_\mu - i [\mathbf{G}_\mu, \mathbf{G}_\nu] = T^A F_{\mu\nu}^A, \quad (2.1.12)$$

with $\mathbf{G}_\mu = T^A G_\mu^A$. The components $F_{\mu\nu}^A$ transform under the infinitesimal gauge transformation as

$$F_{\mu\nu}^A \rightarrow F_{\mu\nu}^A - f^{ABC} \theta^B F_{\mu\nu}^C, \quad (2.1.13)$$

for both a local and a global gauge transformation. Imposing parity conservation, we can construct the gauge-invariant Lagrangian as

$$\begin{aligned}\mathcal{L} &= -\frac{1}{4}F_{\mu\nu}^A F^{A\mu\nu} + \bar{\psi}_i(i\not{D} - m_i)\psi_i \\ &= -\frac{1}{4}F_{\mu\nu}^A F^{A\mu\nu} + \bar{\psi}_i^\alpha(i\not{D} - m_i)\psi_i^\alpha + i\bar{\psi}_i^\alpha \not{G}^A T_{\alpha\beta}^A \psi_i^\beta,\end{aligned}\tag{2.1.14}$$

where we left the contraction of the α indices of the fermion fields implicit in the first line of Eq. (2.1.14).

For completeness, under a finite gauge transformation the fermion fields transform as

$$\psi_i \rightarrow U \psi_i = \exp(i\theta^A T^A) \psi_i,\tag{2.1.15}$$

where U is a unitary matrix with $\det U = 1$. Again, the summation over the indices α is left implicit in Eq. (2.1.15). With this matrix U , the transformation of the gauge field G_μ^A and the field strength tensor $F_{\mu\nu}^A$ can be written as

$$T^A G_\mu^A \rightarrow U T^A G_\mu^A U^\dagger - i(\partial_\mu U) U^\dagger, \quad T^A F_{\mu\nu}^A \rightarrow U T^A F_{\mu\nu}^A U^\dagger,\tag{2.1.16}$$

and it can be shown that the covariant derivative of ψ_i transforms as ψ_i itself:

$$D_\mu \psi_i \rightarrow U D_\mu \psi_i.\tag{2.1.17}$$

With these properties it can directly be seen that the Lagrangian (2.1.14) is invariant under a finite gauge symmetry transformation.

2.1.2 The Standard Model as a gauge theory

The gauge symmetry group of the SM is $SU(3)_C \times SU(2)_L \times U(1)_Y$. To describe under which representation the fields transform, we need to introduce *right-* and *left-handed* fields $\psi_{R/L} = P_{R/L} \psi = 1/2(1 \pm \gamma^5)\psi$ with $\gamma^5 = i\gamma^0\gamma^1\gamma^2\gamma^3$. These fields transform in the same way under $SU(3)_C$, but differently under $SU(2)_L \times U(1)_Y$. Based on the principles introduced in Sec. 2.1.1 we determine both the transformations under symmetry transformations as well as the phenomenological predictions such as particle content, the form of allowed interactions, and the coupling strength.

QCD is described by the underlying $SU(3)_C$ gauge symmetry. From the different fermions only the quarks transform non-trivially as a triplet under $SU(3)_C$. Thus, each of the six quarks has three possible color charges. The quarks q_f with $f = \{u, d, c, s, t, b\}$ transform in the following way:

$$q_f \rightarrow U q_f = \exp(i\theta^A T^A) q_f,\tag{2.1.18}$$

where, in the *fundamental* representation, the generators are given as $T_A = \lambda^A/2$, with λ^A being the *Gell-Mann* matrices and $A = 1, \dots, 8$ in the fundamental representation of $SU(3)_C$. The corresponding gauge fields G_μ^A are colored vector bosons and are called *gluons*. As they transform in the adjoint representation of $SU(3)_C$, there are in total eight different gluons, which transform according to Eq. (2.1.16) with U given in Eq. (2.1.18):

$$T^A G_\mu^A \rightarrow U T^A G_\mu^A U^\dagger + \frac{i}{g_s} (\partial_\mu U) U^\dagger.\tag{2.1.19}$$

The parameter g_s is called the *strong coupling constant* and parametrizes the strength of the strong interaction. The corresponding field strength tensor $G_{\mu\nu}^A$ is given as

$$G_{\mu\nu}^A = \partial_\mu G_\nu^A - \partial_\nu G_\mu^A + g_s G_\mu^B G_\nu^C f^{ABC}, \quad (2.1.20)$$

where f^{ABC} are the totally antisymmetric and real structure constants of $SU(3)_C$. Quarks and gluons form the particle content of the QCD Lagrangian

$$\begin{aligned} \mathcal{L}_{\text{QCD}} &= -\frac{1}{4} G_{\mu\nu}^A G^{A\mu\nu} + \bar{q}_f \left(i\not{\partial} - g_s \not{G}^A T^A \right) q_f - m_f \bar{q}_f q_f, \\ &= -\frac{1}{4} (\partial_\mu G_\nu^A - \partial_\nu G_\mu^A) (\partial^\nu G^{A\mu} - \partial^\mu G^{A\nu}) + g_s f^{ABC} (\partial_\mu G_\nu^A) (G^{B\mu} G^{C\nu}) \\ &\quad - \frac{g_s^2}{4} f^{ABC} f^{ADE} G_\mu^B G_\nu^C G^{D\mu} G^{E\nu} + \bar{q}_f \left(i\not{\partial} - g_s \not{G}^A T^A \right) q_f - m_f \bar{q}_f q_f. \end{aligned} \quad (2.1.21)$$

Due to the non-abelian structure of $SU(3)_C$ we find not only interaction between quarks and gluons, but also gluon self interactions with both triple and quartic vertices. Without these self interactions QCD would formally be identical to *quantum electrodynamics* (QED).

The EW interactions are realized in the SM with an $SU(2)_L \times U(1)_Y$ symmetry group. In contrast to $SU(3)_C$, all fermions, *i.e.* quarks and leptons, transform under this symmetry group. In the case of $SU(2)_L$, there are two different kinds of representation for left- and right-handed fields: as an *isospin-doublet*, called q_L and l_L for quarks and leptons, respectively, in the fundamental representation and as a *singlet*, called u_R , d_R and e_R for up-type quarks, down-type quarks and charged leptons, respectively, in the trivial representation (see also Tab. 2.1). $SU(2)_L$ -doublets Ψ_L (with $\Psi = q, l$) and singlets ψ_R (with $\psi = u, d, e$) transform in the following way under a finite $SU(2)_L \times U(1)_Y$ gauge transformation:

$$\Psi_L \rightarrow U_L U_Y \Psi_L = \exp(i\theta^I \tau^I) \exp(i\theta Y_L) \Psi_L, \quad (2.1.22)$$

$$\psi_R \rightarrow U_Y \psi_R = \exp(i\theta Y_R) \psi_R, \quad (2.1.23)$$

where Y denotes the (weak) *hypercharge* and τ^I with $I = 1, 2, 3$ are the generators of $SU(2)_L$. In the fundamental representation these matrices are given as $\tau^I = \sigma^I/2$, where σ^I are the *Pauli matrices*. To render the free Lagrangian invariant under local $SU(2)_L \times U(1)_Y$ transformations we introduce the gauge fields W_μ^I with $I = 1, 2, 3$ and B_μ . These transform as

$$W_\mu^I \tau^I \rightarrow U_L W_\mu^I \tau^I U_L^\dagger + \frac{i}{g} (\partial_\mu U_L) U_L^\dagger, \quad B_\mu \rightarrow B_\mu - \frac{1}{g'} \partial_\mu \theta, \quad (2.1.24)$$

where g, g' are the gauge couplings of $SU(2)_L$ and $U(1)_Y$, respectively. The field strength tensors are defined as

$$W_{\mu\nu}^I = \partial_\mu W_\nu^I - \partial_\nu W_\mu^I - g W_\mu^J W_\nu^K \epsilon^{IJK}, \quad B_{\mu\nu} = \partial_\mu B_\nu - \partial_\nu B_\mu, \quad (2.1.25)$$

where ϵ^{IJK} are the totally antisymmetric structure constants of $SU(2)_L$, which are identical to the epsilon tensor with $\epsilon^{123} = +1$. To introduce the covariant derivatives we construct $SU(2)_L$ doublets for quarks and leptons as:

$$q_L = \begin{pmatrix} u_L \\ d_L \end{pmatrix}, \quad l_L = \begin{pmatrix} \nu_L \\ e_L \end{pmatrix}, \quad (2.1.26)$$

and analogously for the second and third generation. With these definitions of the doublets the covariant derivatives are given as

$$D_\mu \Psi_L = (\partial_\mu + ig W_\mu^I \tau^I + ig' Y B_\mu) \Psi_L, \quad D_\mu \psi_R = (\partial_\mu + ig' Y B_\mu) \psi_R. \quad (2.1.27)$$

With the covariant derivatives the Lagrangian that describes the $SU(2)_L \times U(1)_Y$ interactions can be written as:

$$\begin{aligned} \mathcal{L}_{\text{EW}} = & -\frac{1}{4} W_{\mu\nu}^I W^{I\mu\nu} - \frac{1}{4} B_{\mu\nu} B^{\mu\nu} + i\bar{q}_L^i \not{D} q_L^i + i\bar{l}_L^i \not{D} l_L^i + i\bar{u}_R^i \not{D} u_R^i + i\bar{d}_R^i \not{D} d_R^i \\ & + i\bar{e}_R^i \not{D} e_R^i, \end{aligned} \quad (2.1.28)$$

where $i = 1, 2, 3$ denotes the three fermion generations. In contrast to the $SU(3)_C$, local $SU(2)_L \times U(1)_Y$ gauge invariance forbids the inclusion of fermion mass terms.

2.1.3 The Yukawa sector

To include fermion masses as well as vector boson masses the concept of *spontaneous symmetry breaking* (SSB) has to be employed. In the SM, a new complex scalar field φ , which transforms as an $SU(2)_L$ doublet under $SU(2)_L \times U(1)_Y$ with $Y = 1/2$, has to be included in the Lagrangian in Eq. (2.1.28). This model is also referred to as the *Weinberg-Salam model* [35–37].

In general, SSB occurs if the Lagrangian is invariant under a certain symmetry while the vacuum state is not. In the case of the SM, consider the Lagrangian [3–5]

$$\begin{aligned} \mathcal{L}_\varphi = & -\frac{1}{4} W_{\mu\nu}^I W^{I\mu\nu} - \frac{1}{4} B_{\mu\nu} B^{\mu\nu} + (D_\mu \varphi) (D^\mu \varphi) - V(\varphi) \\ = & -\frac{1}{4} W_{\mu\nu}^I W^{I\mu\nu} - \frac{1}{4} B_{\mu\nu} B^{\mu\nu} + (D_\mu \varphi) (D^\mu \varphi) - \mu^2 \varphi^\dagger \varphi - \lambda (\varphi^\dagger \varphi)^2, \end{aligned} \quad (2.1.29)$$

$$D_\mu \varphi = (\partial_\mu + ig' W_\mu^I \tau^I + ig' B_\mu) \varphi. \quad (2.1.30)$$

For parameters $\mu^2 < 0$, $\lambda > 0$ in the potential V we find an infinite number of minima at

$$|\varphi|^2 = \varphi^\dagger \varphi = \frac{-\mu^2}{2\lambda} = v^2, \quad (2.1.31)$$

where v is the *vacuum expectation value* (VEV) of the field φ . In general, the complex $SU(2)_L$ doublet φ describes four real fields φ_i with $i = 1, \dots, 4$. Expanding φ around v we can rewrite it as

$$\varphi(x) = \begin{pmatrix} \varphi_1(x) + i\varphi_2(x) \\ \varphi_3(x) + i\varphi_4(x) \end{pmatrix} = \exp\left(i \frac{\pi^I(x)}{\sqrt{2}v} \tau^I\right) \begin{pmatrix} 0 \\ \frac{v+h(x)}{\sqrt{2}} \end{pmatrix}, \quad (2.1.32)$$

where π^I with $I = 1, 2, 3$ are three massless fields called *Goldstone bosons* [38, 39], and h is referred to as the *Higgs boson*. Inserting this parametrization into Eq. (2.1.29) we see that a mass term for the field h with $m_h^2 = -\mu^2$ is dynamically generated. The field φ transforms as a doublet under local $SU(2)_L \times U(1)_Y$ transformations, similarly to Eq. (2.1.22). Thus, we can choose a specific gauge to set $\pi^I = 0$ fixing the values of three of the four parameters θ^I and θ . This procedure is called *gauge fixing*, and the corresponding gauge is referred to as *unitary gauge*. In this gauge, studying the theory is simpler as no propagating Goldstone

bosons occur.

In unitary gauge, we find that three mass terms for three massive gauge bosons are generated (this is also referred to as: *'the gauge bosons eat the Goldstone bosons'*):

$$(D_\mu\varphi)(D^\mu\varphi) = g^2\frac{v^2}{8} \left[(W_\mu^1)^2 + (W_\mu^2)^2 + \left(\frac{g'}{g}B_\mu - W_\mu^3 \right)^2 \right]. \quad (2.1.33)$$

Defining

$$\begin{aligned} W_\mu^\pm &= \frac{1}{2} (W_\mu^1 \mp iW_\mu^2), \\ Z_\mu &= \cos\theta_w W_\mu^3 - \sin\theta_w B_\mu, \\ A_\mu &= \sin\theta_w W_\mu^3 + \cos\theta_w B_\mu, \end{aligned} \quad (2.1.34)$$

with the *Weinberg angle* θ_w given as

$$\tan\theta_w = \frac{g'}{g}, \quad (2.1.35)$$

we see that Eq. (2.1.33) describes three massive and one massless vector bosons with masses

$$m_W = g\frac{v}{2}, \quad m_Z = g\frac{v}{2\cos\theta_w} = \frac{m_W}{\cos\theta_w}, \quad m_A = 0. \quad (2.1.36)$$

The massless particle described by A_μ is the *photon*, while W_μ^\pm and Z_μ correspond to the massive W and Z bosons, respectively. Furthermore, it follows that the Z boson should be heavier than the W bosons. An alternative way to formulate this connection is (at tree level)

$$\rho = \frac{m_W^2}{m_Z^2 \cos^2\theta_w} = 1, \quad (2.1.37)$$

fixed in the Weinberg-Salam model. Defining the electromagnetic coupling strength as

$$e = g \sin\theta_w = g' \cos\theta_w, \quad (2.1.38)$$

and expanding the $W_{\mu\nu}^I W^{I\mu\nu}$ term we see that the W^\pm bosons have indeed charge ± 1 .

The dynamical generation of fermion masses is realized in a similar way. Including the Higgs field allows to construct additional interaction terms invariant under $SU(2)_L \times U(1)_Y$. Focusing on quark masses, we introduce the quark *Yukawa couplings*

$$\mathcal{L}_{\text{Yuk}} = -Y_{ij}^u \bar{q}_L^i \tilde{\varphi} u_R^j - Y_{ij}^d \bar{q}_L^i \varphi d_R^j + \text{h.c.}, \quad (2.1.39)$$

with $\tilde{\varphi} = i\sigma_2\varphi^*$ and the Yukawa matrices Y^u and Y^d for up-type and down-type quarks, respectively, with generation indices i, j . We observe that each of the terms is invariant under a local $SU(3) \times SU(2) \times U(1)$ transformation. After electroweak symmetry breaking (EWSB) the Yukawa interactions in Eq. (2.1.39) generate mass terms for the quarks:

$$\mathcal{L}_{\text{mass}} = -\frac{v}{\sqrt{2}} \left(Y_{ij}^u \bar{u}_L^i u_R^j + Y_{ij}^d \bar{d}_L^i d_R^j \right) + \text{h.c.}. \quad (2.1.40)$$

In general, the Yukawa matrices are not diagonal. To diagonalize the mass terms we employ

the singular value decomposition of the Yukawa matrices as

$$Y^u = S_L^u M_u S_R^{u\dagger}, \quad Y^d = S_L^d M_d S_R^{d\dagger}, \quad (2.1.41)$$

with two diagonal matrices $M_{u,d}$ and unitary matrices $S_{L,R}^{u,d}$. Absorbing these four rotation matrices into the quark fields defines the *mass basis* as

$$u'_{L/R} = S_{L/R}^{u\dagger} u_{L/R}, \quad d'_{L/R} = S_{L/R}^{d\dagger} d_{L/R}. \quad (2.1.42)$$

This allows us to diagonalize the mass terms in $\mathcal{L}_{\text{mass}}$. The change from the so-called *flavor basis* (u_i, d_i) to the mass basis (u'_i, d'_i) has important consequences for the gauge interactions in Eq. (2.1.28). In the flavor basis, the interactions between the gauge bosons and quarks are written as

$$\begin{aligned} \mathcal{L}_{\text{EW}} \supseteq & (\bar{u}_L \quad \bar{d}_L)^i \left[\left(\frac{g}{2} W^3 \sigma^3 + g' Y_q \not{B} \right) + \frac{g}{2} W^1 \sigma^1 + \frac{g}{2} W^2 \sigma^2 \right] \begin{pmatrix} u_L \\ d_L \end{pmatrix}^i \\ & + \bar{u}_R^i g' Y_u \not{B} u_R^i + \bar{d}_R^i g' Y_d \not{B} d_R^i \\ = & \frac{e}{\sin \theta_w} Z^\mu J_\mu^Z + e A^\mu J_\mu^{\text{EM}} + \frac{g}{\sqrt{2}} (\bar{u}_L^i W_\mu^+ \gamma^\mu d_L^i + \bar{d}_L^i W_\mu^- \gamma^\mu u_L^i) \end{aligned} \quad (2.1.43)$$

with $\sigma^\pm = 1/2(\sigma^1 \mp i\sigma^2)$ and W^\pm , Z and A defined in Eq. (2.1.34). The *neutral currents* J^Z and J^{EM} are defined as

$$J_\mu^Z = \frac{1}{\cos \theta_w} (J_\mu^3 - \sin^2 \theta_w J_\mu^{\text{EM}}), \quad (2.1.44)$$

$$J_\mu^3 = \bar{\psi}_L^i \gamma_\mu T^3 \psi_L^i, \quad (2.1.45)$$

$$J_\mu^{\text{EM}} = Q_i (\bar{\psi}_L^i \gamma_\mu \psi_L^i + \bar{\psi}_R^i \gamma_\mu \psi_R^i), \quad (2.1.46)$$

where $T^3 = \tau^3$ in the fundamental representation, giving 0 when acting on right-handed states, $Q = T^3 + Y$, and $\psi^i = u^i, d^i$. We can see that all interactions between the gauge bosons and the quarks are diagonal in the flavor basis. Rotating to the mass basis leaves the neutral currents (as well as the gluon-quark interactions) invariant as each class of quarks $u'_{L/R}, d'_{L/R}$ has the same quantum numbers regardless of i . The *charged-current* interactions, however, do not remain diagonal in the mass basis [40]:

$$\mathcal{L}_{\text{CC}} = \frac{g}{\sqrt{2}} \left(\bar{u}_L^i W_\mu^+ \gamma^\mu V_{ij} d_L^j + \bar{d}_L^i W_\mu^- \gamma^\mu (V^\dagger)_{ij} u_L^j \right), \quad (2.1.47)$$

where we introduced the unitary matrix $V = (S_L^u)^\dagger S_L^d$ known as the *Cabibbo-Kobayashi-Maskawa* (CKM) matrix [41, 42]. This matrix has in total four degrees of freedom, *i.e.* three angles θ_{12}, θ_{13} , and θ_{23} , and one phase δ . It can be parametrized as [43]:

$$V = \begin{pmatrix} V_{ud} & V_{us} & V_{ub} \\ V_{cd} & V_{cs} & V_{cb} \\ V_{td} & V_{ts} & V_{tb} \end{pmatrix} = \begin{pmatrix} c_{12} c_{13} & s_{12} c_{13} & s_{13} e^{-i\delta} \\ -s_{12} c_{23} - c_{12} s_{23} s_{13} e^{i\delta} & c_{12} c_{23} - s_{12} s_{23} s_{13} e^{i\delta} & s_{23} c_{13} \\ s_{12} s_{23} - c_{12} c_{23} s_{13} e^{i\delta} & -c_{12} s_{23} - s_{12} c_{23} s_{13} e^{i\delta} & c_{23} c_{13} \end{pmatrix}, \quad (2.1.48)$$

with $c_{ij} = \cos \theta_{ij}$ and $s_{ij} = \sin \theta_{ij}$. As long as the phase δ is non-zero CP violation is implied by the CKM matrix.

Similarly to Eq. (2.1.39), Yukawa interactions of charged leptons and left-handed neutrinos can be written as

$$\mathcal{L}_{\text{Yuk},l} = -Y_{ij}^e \bar{l}_L^i \varphi e_R^j + \text{h.c.}, \quad (2.1.49)$$

since right-handed neutrinos are not observed and not included in the SM Lagrangian. It follows that no mass terms for neutrinos are included in the SM, even though it is known today that at least two neutrinos are indeed massive [44–46].

To summarize the discussions about SM gauge symmetries and the particle content of the SM, the SM Lagrangian before SSB reads

$$\begin{aligned} \mathcal{L}_{SM} = & -\frac{1}{4} G_{\mu\nu}^A G^{A\mu\nu} - \frac{1}{4} W_{\mu\nu}^I W^{I\mu\nu} - \frac{1}{4} B_{\mu\nu} B^{\mu\nu} + (D_\mu \varphi)^\dagger (D^\mu \varphi) \\ & - \mu^2 \varphi^\dagger \varphi - \lambda (\varphi^\dagger \varphi)^2 \\ & + i (\bar{l}_L \not{D} l_L + \bar{e}_R \not{D} e_R + \bar{q}_L \not{D} q_L + \bar{u}_R \not{D} u_R + \bar{d}_R \not{D} d_R) \\ & - \left(Y^u \bar{q}_L \tilde{\varphi} u_R + Y^d \bar{q}_L \varphi d_R + Y^e \bar{l}_L \varphi e_R + \text{h.c.} \right), \end{aligned} \quad (2.1.50)$$

where we leave the summation over all contracted color, isospin and generation indices implicit. The covariant derivatives are defined as

$$D_\mu q_L = (\partial_\mu + ig' Y B_\mu + ig \tau^I W_\mu^I + ig_s T^A G_\mu^A) q_L, \quad (2.1.51a)$$

$$D_\mu u_R = (\partial_\mu + ig' Y B_\mu + ig_s T^A G_\mu^A) u_R, \quad (2.1.51b)$$

$$D_\mu d_R = (\partial_\mu + ig' Y B_\mu + ig_s T^A G_\mu^A) d_R, \quad (2.1.51c)$$

$$D_\mu l_L = (\partial_\mu + ig' Y B_\mu + ig \tau^I W_\mu^I) l_L, \quad (2.1.51d)$$

$$D_\mu e_R = (\partial_\mu + ig' Y B_\mu) e_R. \quad (2.1.51e)$$

In Tab. 2.1 we summarize the representations for all fermion fields in the SM. In this work, we use the convention $Y = Q - I_3$.

2.2 The concept of renormalization and running of couplings

In perturbation theory, predictions for observables are computed by expanding them in powers of small coupling constants. Contributions beyond *tree-level* processes are called *loop* contributions. These have to be considered when computing higher-order corrections, depending on the level of accuracy that is needed for the computation. In general, loop diagrams yield divergences from the *ultraviolet* (UV) region of the momentum integrals. In the process referred to as *renormalization* these infinities are removed by absorbing them into the *bare parameters* (*i.e.* coupling constants, masses, fields) in the Lagrangian. By doing so, all parameters of the theory are expressed in terms of renormalized parameters. Examples for these renormalized parameters are couplings and masses measured in experiments.

The process of renormalization has a more physical interpretation beyond the purpose of absorbing infinities: as renormalization connects the bare parameters in the Lagrangian with physical observables, it would also be necessary in theories with convergent integrals. For example, a renormalized field is defined by the condition that its propagator has the same behavior near its pole as the free field, while the renormalized mass refers to the position of this pole. In actual calculations it is, however, simplest to infer that all infinities occurring

at a given expansion order cancel when all parameters are expressed in terms of renormalized quantities.

To renormalize the parameters of the Lagrangian and cancel all infinities occurring in intermediate steps of calculations a *regularization scheme* is employed. This regulator is introduced to make divergences explicit in the calculations. In all physical predictions, the explicit dependence on the regulator must drop out. In this work, we compute diagrams in $4 - \epsilon$ dimension, and divergences occur as poles $\sim 1/\epsilon$ for $\epsilon \rightarrow 0$. This process is referred to as *dimensional regularization*. In addition, all couplings include a factor $\mu^{-\epsilon/2}$ in the relation between renormalized and bare couplings so that renormalized couplings remain dimensionless. The parameter μ itself has dimension of mass and is called the *renormalization scale* or *subtraction point* [47, 48]. In explicit calculations, we apply *minimal subtraction* (MS), *i.e.* absorbing only divergent parts, followed by the rescaling $\mu^2 \rightarrow \mu^2 e^\gamma/4\pi$ with Euler's constant $\gamma = 0.577\dots$. This scheme is called the $\overline{\text{MS}}$ scheme.

Theories, in which all UV divergences can be removed by a finite number of parameter redefinitions, are called *renormalizable theories*. To fix these parameters only a finite number of experimental inputs is needed. The requirement of renormalizability played a crucial role in the formulation of the SM. However, cancellation of UV divergences does not necessarily depend on renormalizability. As long as all of the infinite number of interactions allowed by symmetries are included in the Lagrangian UV divergences are still canceled. In this sense, 'non-renormalizable theories' are just as renormalizable as 'renormalizable theories'. Generalizing this terminology to individual interactions, we distinguish between three kinds of interactions depending on the mass dimension of the couplings: Interactions of dimension $d = 0$ are referred to as *marginal*, those with dimension $d > 0$ as *relevant* and those with dimension $d < 0$ as *irrelevant*. Non-renormalizable interactions are those of mass dimension $d < 0$.

However, fixing all parameters in a non-renormalizable theory would require an infinite number of experimental inputs. This would certainly render non-renormalizable theories completely unpredictable. However, in fact non-renormalizable theories remain predictive [49] as long as we are only interested in physics at low energies. Here, low energies refers to energies smaller than the mass scale Λ appearing in the irrelevant couplings. In the case $E \ll \Lambda$, only a limited number of non-renormalizable interactions are important and can be fixed with a finite number of measurements. In this sense, non-renormalizable theories remain predictive at low energies as long as a finite theoretical precision is sufficient.

One interpretation of this behavior is that theories used to describe physics at a given energy scale are in fact EFTs. These theories can be understood as low-energy approximations to a more fundamental, underlying theory, and necessarily include an infinite number of non-renormalizable interactions. At sufficiently low energies these interactions are strongly suppressed, and the renormalizable parts of the theory retain their special status, even though for reasons different from the original idea of renormalizability.

A simple example for a renormalizable theory is QED. The Lagrangian is given as

$$\mathcal{L}_{\text{QED}} = -\frac{1}{4} F_{\mu\nu}^{(0)} F^{(0)\mu\nu} + i\bar{\psi}^{(0)} \gamma^\mu (\partial_\mu - ie^{(0)} A_\mu^{(0)}) \psi^{(0)} - m_e^{(0)} \bar{\psi}^{(0)} \psi^{(0)}, \quad (2.2.1)$$

where we denote the bare fields, couplings and masses with the superscript (0) and $F_{\mu\nu}^{(0)} = \partial_\mu A_\nu^{(0)} - \partial_\nu A_\mu^{(0)}$. We refer to the parameters as bare masses and fields as they are not the quantities measured by experiments. Instead, couplings and masses measured in experiments are quantities computed taking all higher-order corrections into account. The bare quantities

refer to the fact that *e.g.* vertices are stripped from all loops. To connect the bare parameters in the Lagrangian to physical observables, we define the renormalized fields and parameters as:

$$\psi = \frac{1}{\sqrt{Z_\psi}} \psi^{(0)}, \quad A_\mu = \frac{1}{\sqrt{Z_A}} A_\mu^{(0)}, \quad e = \frac{1}{Z_e} \mu^{-\epsilon/2} e^{(0)}, \quad m_e = \frac{1}{Z_m} m^{(0)}, \quad (2.2.2)$$

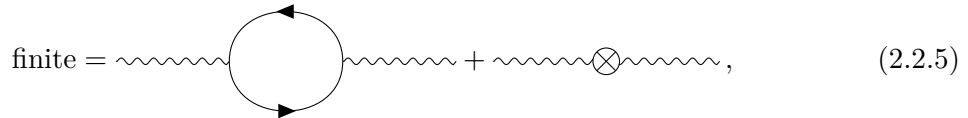
Rewriting \mathcal{L}_{QED} in terms of renormalized fields yields

$$\begin{aligned} \mathcal{L}_{\text{QED}} = & -\frac{1}{4} F_{\mu\nu} F^{\mu\nu} + i\bar{\psi} \gamma^\mu (\partial_\mu - i\mu^{-\epsilon/2} e A_\mu) \psi - m_e \bar{\psi} \psi \\ & -\frac{1}{4} (Z_A - 1) F_{\mu\nu} F^{\mu\nu} + i(Z_\psi - 1) \bar{\psi} \gamma^\mu \partial_\mu \psi \\ & + (\sqrt{Z_A} Z_\psi Z_e - 1) \mu^{-\epsilon/2} e \bar{\psi} \gamma^\mu A_\mu \psi - (Z_\psi Z_m - 1) m_e \bar{\psi} \psi, \end{aligned} \quad (2.2.3)$$

where terms in the second and third line are called *counterterms*. Requiring time-ordered products of renormalized fields (*i.e.* *Green's functions*) to be free of divergences by expressing them in terms of renormalized couplings and masses fixes the renormalization constants Z_i . The exact way how the Z_i are chosen is referred to as *subtraction scheme*. As stated previously, we employ the $\overline{\text{MS}}$ scheme and choose

$$Z_i = 1 + \sum_{m=1}^{\infty} \frac{Z_{i,m}(e)}{\epsilon^m}, \quad (2.2.4)$$

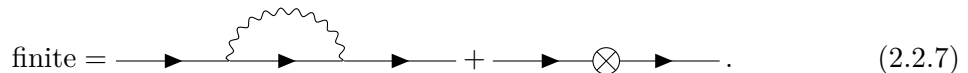
with coefficients $Z_{i,m}$ independent of ϵ , and rescale $\mu^2 \rightarrow \mu^2 e^\gamma / (4\pi)$. The parameters Z_i can, at any given order in the coupling constant, be computed considering loop diagrams together with counterterms requiring that all divergences cancel. As an example, at *next-to leading order* (NLO) in QED the constant Z_A is computed schematically from the condition

$$\text{finite} = \text{diagram with loop} + \text{diagram with counterterm}, \quad (2.2.5)$$


where the left Feynman diagram is the one-loop vacuum polarization correction to the photon propagator, and the right diagram is the counterterm corresponding to $-1/4 (Z_A - 1) F_{\mu\nu} F^{\mu\nu}$. To be finite for $\epsilon \rightarrow 0$ at $\mathcal{O}(e^2)$ the constant is defined as

$$Z_A = 1 - \frac{8}{3} \left(\frac{e^2}{16\pi^2 \epsilon} \right) + \mathcal{O}(e^3). \quad (2.2.6)$$

In a very similar way, Z_ψ and Z_m are fixed by considering higher-order contributions to the electron propagator:

$$\text{finite} = \text{diagram with loop} + \text{diagram with counterterm}. \quad (2.2.7)$$


The first diagram corresponds to vacuum polarization contributions, and the second diagram denotes counterterm contributions from $i(Z_\psi - 1) \bar{\psi} \gamma^\mu \partial_\mu \psi - (Z_\psi Z_m - 1) m_e \bar{\psi} \psi$. The

computation yields

$$Z_\psi = 1 - 2\frac{e^2}{16\pi^2\epsilon} + \mathcal{O}(e^3), \quad Z_m = 1 - 6\frac{e^2}{16\pi^2\epsilon} + \mathcal{O}(e^3). \quad (2.2.8)$$

Considering vertex corrections

$$\text{finite} = \text{---} \rightarrow \text{---} \rightarrow \text{---} \rightarrow \text{---} + \text{---} \rightarrow \text{---} \otimes \text{---} \rightarrow \text{---}, \quad (2.2.9)$$

fixes the remaining renormalization constant, Z_e , to be

$$Z_e = 1 + \frac{4}{3} \left(\frac{e^2}{16\pi^2\epsilon} \right). \quad (2.2.10)$$

Note that up to $\mathcal{O}(e^2)$ we find $Z_e = 1/\sqrt{Z_A}$. With this result, we can now write the bare coupling in Eq. (2.2.2) as

$$e^{(0)} = \mu^{\epsilon/2} e \left(1 + \frac{4}{3} \frac{e^2}{16\pi^2\epsilon} \right). \quad (2.2.11)$$

Since the bare coupling (as all bare parameters) is independent of the renormalization scale μ , we can infer:

$$\frac{de^{(0)}}{d \ln \mu} = 0 = \mu^{\epsilon/2} e Z_e \left(\frac{\epsilon}{2} + \frac{1}{e} \frac{de}{d \ln \mu} + \frac{1}{Z_e} \frac{dZ_e}{d \ln \mu} \right), \quad (2.2.12)$$

$$\Leftrightarrow \frac{1}{e} \frac{de}{d \ln \mu} = -\frac{\epsilon}{2} - \frac{1}{Z_e} \frac{dZ_e}{d \ln \mu}. \quad (2.2.13)$$

This differential equation allows us to define the *beta function* of the renormalized coupling as

$$\beta(e) = \frac{de}{d \ln \mu} = -\frac{\epsilon}{2} e - \frac{e^2}{12\pi^2} + \mathcal{O}(e^3) \stackrel{\epsilon \rightarrow 0}{=} -\frac{e^2}{12\pi^2} + \mathcal{O}(e^3), \quad (2.2.14)$$

and the beta function is finite for $\epsilon \rightarrow 0$. This function describes the scale dependence of the renormalized coupling. A typical choice is $\mu^2 \sim s$, where s is the center of mass energy of the process considered. This value minimizes higher-order terms neglected in the perturbative expansion which scale like $\sim e^{2n} \ln^m(\mu^2/s)$ with $m \leq n$. To solve the *renormalization group equation* (RGE) (2.2.14) we define

$$\alpha_e = \frac{e^2}{4\pi}. \quad (2.2.15)$$

Rewriting the RGE (2.2.14) in terms of α_e yields

$$\beta(\alpha) = \frac{d\alpha}{d \ln \mu} = -2\alpha \left(\frac{\epsilon}{2} + \frac{\alpha}{4\pi} \beta_0 + \frac{\alpha^2}{(4\pi)^2} \beta_1 + \dots \right), \quad (2.2.16)$$

with $\beta_0 = -4/3$ in QED and $d = 4$ dimensions. Solving the RGE we find for the running of

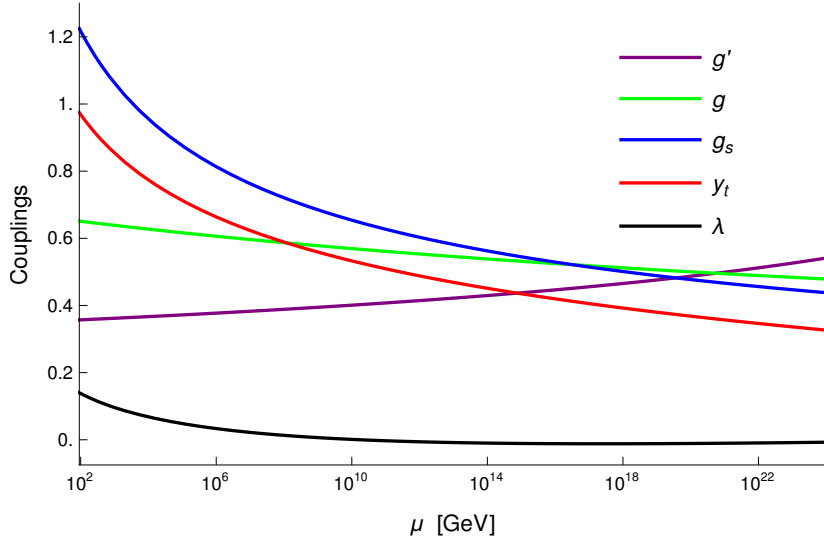


Figure 2.1: Scale dependence of the SM gauge couplings g' , g and g_s , the top-quark Yukawa coupling y_t and the Higgs quartic coupling λ . The parameters are defined in the $\overline{\text{MS}}$ scheme. The running is computed at the three-loop level [50].

the coupling α_e :

$$\alpha_e(\mu) = \frac{2\pi}{\beta_0} \frac{1}{\ln\left(\frac{\mu}{\Lambda_{\text{QED}}}\right)}, \quad (2.2.17)$$

where the scale Λ_{QED} is determined from the measured value of the coupling constant. Taking for example $\alpha_e(m_e) = 1/137$ we obtain $\Lambda_{\text{QED}} \approx 10^{286}$ eV. As α_e is required to be a positive number, we see that for $\beta_0 < 0$ the coupling grows with rising energy. At the scale $\mu = \Lambda_{\text{QED}}$ the solution (2.2.17) diverges, so that Λ_{QED} is referred to as the *Landau pole* of the theory. An equivalent solution of Eq. (2.2.16) is

$$\alpha_e(\mu) = \frac{\alpha_e(\mu_0)}{1 + \frac{\beta_0 \alpha_e(\mu_0)}{2\pi} \ln\left(\frac{\mu}{\mu_0}\right)}, \quad (2.2.18)$$

which is the same as Eq. (2.2.17) in the case $\mu_0 = \Lambda_{\text{QED}}$. Again, one measurement of α_e at a scale μ_0 fixes the running of the coupling.

In the SM, there are multiple couplings that show a scale dependence: the gauge couplings g' , g and g_s , the Yukawa couplings y_i and the couplings in the Higgs potential. This makes the computation of beta functions a non-trivial task, especially at higher orders. In the literature, the SM beta functions for the gauge couplings, the largest Yukawa couplings y_t , y_b , and y_τ of the top quark, bottom quark and tau lepton, respectively, as well as the Higgs couplings have been computed at three-loop level in Ref. [50]. In Fig. 2.1 we give the scale dependence of the three gauge couplings, the top-quark Yukawa coupling and the Higgs quartic coupling computed using the results in Ref. [50]. First of all, we see a unique feature of the Higgs quartic coupling λ : at scales $\mu \sim 10^{10}$ GeV the coupling becomes negative, rendering the vacuum configuration of the Higgs potential metastable given present measurements of the top-quark and Higgs masses [50, 51]. Note that λ is the only coupling which can show this behavior,

since not all terms in the beta function β_λ are proportional to λ itself [50]. In addition, we can identify two distinct behaviors for the gauge couplings. The coupling g' of the $U(1)_Y$ gauge group grows with energy and diverges at the Landau pole, similarly to the QED coupling in Eq. (2.2.17). This pole lies beyond the *Planck scale* $M_{\text{Pl}} \sim 10^{19}$ GeV, where quantum gravity effects are expected to arise. In contrast, the $SU(3)_C$ gauge coupling g_s diverges for $\mu \rightarrow 0$. The exact position of the QCD Landau pole is determined by measurements of the strong coupling constant, and is set to be about $\Lambda_{\text{QCD}} \sim \mathcal{O}(100)$ MeV [13]. The exact value of Λ_{QCD} depends on the number of quarks active at the energy scale μ (active refers to quarks with masses $m_q < \mu$). The divergence at low energies is referred to as *confinement*, and Λ_{QCD} is also called *confinement scale*. Thus, at low energies, $\mathcal{O}(1)$ GeV, QCD with quarks as degrees of freedom is no longer a perturbative theory. Instead, EFTs are used in this energy range, essentially treating the bound states as the new degrees of freedom since non-perturbative effects become important. In this regime, the spectrum of physical states consists of so-called *hadrons*, which are color-singlet states. The two simplest ways a color singlet can be formed out of quarks are *mesons* (quark-antiquark pairs) and *baryons* (three-quark bound states). At high energies $E \rightarrow \infty$ the strong couplings constant shrinks and asymptotically approaches 0. This behavior is referred to as *asymptotic freedom* and can be traced back to the sign of the β_0 coefficient in the QCD equivalent of Eq. (2.2.18). While in QED we find $\beta_0 < 0$, in QCD we have [31–34]

$$\beta_0^{\text{QCD}} = \frac{1}{3}(33 - 2n_f), \quad (2.2.19)$$

where n_f denotes the number of quark flavors. As long as the number of flavors is below $n_f = 17$ we find $\beta_0^{\text{QCD}} > 0$. In the SM, the number of flavors is $n_f = 6$, which yields a positive value for β_0^{QCD} . With this we see from Eq. (2.2.17) that for $\mu \rightarrow \infty$ the value of α_s decreases. The fundamental differences between QED and QCD stem from $SU(3)_C$ being a non-abelian gauge group. Thus, in the Lagrangian we find both triple and quartic gluon self interactions, which affect the renormalization of α_s .

2.3 Motivation for physics beyond the Standard Model

Despite its theoretically elegant and compact formulation and the lack of any direct detection of particles not included in the SM, there is a strong physical motivation for BSM physics. While indeed the SM is in good agreement with various measurements, the particle content governed by this theory describes only about 5% of the energy content of the Universe. Thus, the SM lacks suitable *dark matter* candidates. Another issue is that neutrinos are assumed to be massless in the formulation of the SM. Even though a direct determination of the neutrino masses has yet to be performed, there is an indication for the existence of neutrino masses by the so-called *neutrino oscillations* [44]. Experimentally, neutrino oscillations have been confirmed by the Sudbury Neutrino Observatory [45] and the Super-Kamiokande [46]. In addition, the SM has both theoretical shortcomings such as the presence of a Landau pole in the running of the fundamental coupling constants or the lack of an explanation for EWSB and the patterns observed in the fermion sector. Furthermore, present data hints at deviations from the SM in several observables. In the following, we present sectors representative for both theoretical and phenomenological shortcomings of the SM, and highlight how the inclusion of BSM physics can accommodate these discrepancies.

2.3.1 Landau poles and asymptotic safety

The appearance of a Landau pole is connected to the breakdown of perturbation theory. In the case of QCD, the Landau pole appears at very small energies. As stated above, the physical interpretation is that, at low energies, bound states of quarks become the new degrees of freedom of the theory. In contrast, in QED and also in the $U(1)_Y$ in the SM (see Fig. 2.1) the Landau pole arises at high energies. Thus, perturbation theory breaks down at high energies, which results in incomplete theories as scattering amplitudes cannot be computed at all scales.

As we have seen in Sec. 2.2, QCD does not have a Landau pole at high energies due to the asymptotically free behavior of the coupling. While asymptotic freedom is an important feature of QCD, it is in fact a special case of a more fundamental concept of RGE *fixed points*. Here, the basic idea is to find UV fixed points in the RGE evolution of the couplings so that the theory remains predictive up to highest energy scales [52, 53]. Such fixed points g^* of the beta function $\beta(g)$ are defined by the condition

$$\beta(g^*) = 0. \quad (2.3.1)$$

In the SM, this is for example the case for g_s of $SU(3)_C$. As this fixed point is found at $g^* = 0$, it is called *non-interacting* and the theory is *asymptotically free* [31, 34]. This type of fixed point is also called a *Gaussian fixed point*. However, high-energy fixed points can in principle also be interacting, *i.e.* $g^* \neq 0$. This scenario is referred to as *asymptotic safety* [54, 55], where, in contrast to asymptotic freedom, non-vanishing interactions remain at arbitrarily high energies. Asymptotic safety has applications in the context of *quantum gravity* [56–62]. In the recent years, there has been development to establish asymptotic safety as a new concept for phenomenology-driven model building [28–30, 63, 64]. In this regard, the case of weakly coupled theories is particularly interesting as it allows to apply perturbation theory. For these theories general theorems have been developed [65–70]. To sketch the origin of asymptotic safety in perturbation theory, we consider a general coupling α with the beta function [65]

$$\frac{d\alpha}{d \ln \mu} = \beta(\alpha) = A\alpha - B\alpha^2, \quad (2.3.2)$$

where the coefficients A and B are numbers that stem from loop-level calculations. There are two fixed points, $\alpha^* = 0$ and $\alpha^* = A/B$, where only the latter is interacting and non-trivial. For perturbation theory to be still applicable we impose $A/B \ll 1$. Solving the RGE around the fixed points yields

$$\alpha - \alpha^* = \left(\frac{\mu}{\Lambda}\right)^\theta, \quad (2.3.3)$$

where Λ is a characteristic scale of the theory (similarly to Λ_{QCD}), and the scaling index θ is defined as

$$\theta = \left. \frac{\partial \beta}{\partial \alpha} \right|_{\alpha=\alpha^*}. \quad (2.3.4)$$

For the non-trivial fixed point of Eq. (2.3.2) we find $\theta = -A$. Thus, as long as $A > 0$ we have $\theta < 0$, and deviations from the fixed point become smaller with increasing μ . As such,

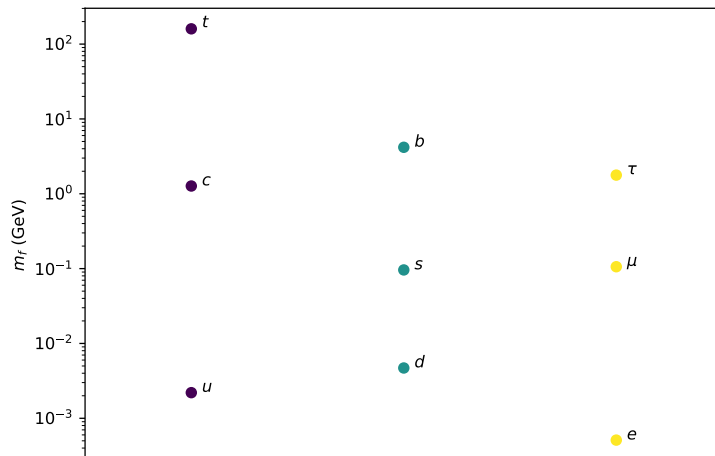


Figure 2.2: Schematic visualization of mass hierarchies in the flavor sector [13]. Quark masses are shown in the $\overline{\text{MS}}$ scheme. Numerical values are given in App. A.1.

the interacting fixed point lies in the UV. If also $B > 0$, we find $\alpha^* > 0$. In contrast, for the trivial fixed point we have $\theta = A$. Thus, for $A > 0$ we have $\theta > 0$ so that the Gaussian fixed point becomes an *infrared* (IR) fixed point.

In gauge-Yukawa theories with $A = 0$ we obtain from the *leading order* (LO) result in Eq. (2.3.2) a degenerated fixed point at $\alpha^* = 0$. This is a UV fixed point for $B > 0$ and the theory is asymptotically free. However, including higher-order corrections a non-trivial fixed point with $0 < \alpha^* \ll 1$ can be found. Denoting such higher-order contributions with a coefficient C we find in the case $A = 0$ for the RGE

$$\beta(\alpha) = -B\alpha^2 + C\alpha^3. \quad (2.3.5)$$

With these additional contributions a non-trivial fixed point is found at $\alpha^* = B/C$. For $B/C \ll 1$, this fixed point is perturbative. If now $B < 0$ and $C < 0$, the fixed point lies in the UV, and the theory becomes asymptotically safe.

2.3.2 Flavor puzzle

The SM Lagrangian in Eq. (2.1.50) has in total 18 free parameters: the three gauge couplings, the two parameters of the scalar potential, 6 quark masses, three lepton masses (neglecting neutrino masses) and three angles as well as one phase in the CKM matrix. As such, most of the free parameters are in the so-called *flavor sector* of the SM, namely the fermion masses and the CKM matrix elements. As shown schematically in Fig. 2.2, the fermion masses show an enormous hierarchy with the heaviest particle, the top quark, being almost 10^6 times heavier than the lightest lepton, the electron. However, there is not only a hierarchy between quarks and leptons but also among the quarks themselves as the mass of the top quark is about five orders of magnitude larger than the mass of the up quark.

Aside from the mass hierarchy, the quark sector shows another pattern in the structure of the CKM matrix in Eq. (2.1.48). Written in terms of the Wolfenstein parameter λ [71], this

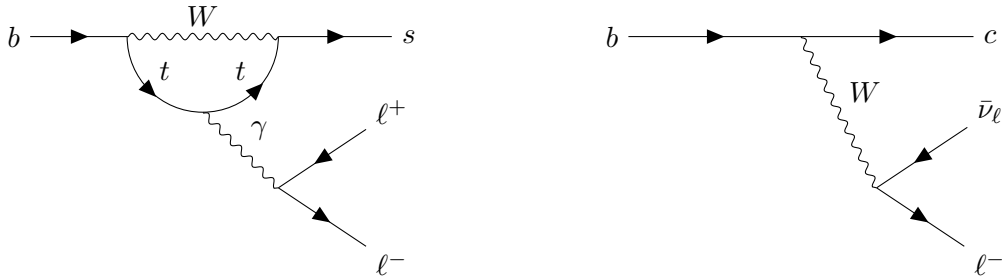


Figure 2.3: Examples for Feynman diagrams at lowest order for flavor changing neutral current $b \rightarrow s\ell^+\ell^-$ (left) and charged current $b \rightarrow c\ell\bar{\nu}_\ell$ (right) transitions in the SM.

matrix shows a hierarchical structure

$$|V| \sim \begin{pmatrix} 1 - \frac{\lambda^2}{2} & \lambda & \lambda^3 \\ \lambda & 1 - \frac{\lambda^2}{2} & \lambda^2 \\ \lambda^3 & \lambda^2 & 1 \end{pmatrix} + \mathcal{O}(\lambda^4), \quad \lambda = \sin \theta_{12} \sim 0.2. \quad (2.3.6)$$

The exact origin of this pattern as well as the mass hierarchy in the quark sector remains unknown.

Flavor symmetries allow to explain the observed fermion masses and the structure of the CKM matrix. As different symmetries and extensions of the SM allow to explain these patterns, the solutions are not unambiguous. These extensions differ by the exact breaking of the flavor symmetries via new couplings and the experimental signatures. One well-known example is the *minimal supersymmetric SM*, where additional masses and mixing of scalar quark and lepton partners (called *squarks* and *sleptons*, respectively) are present.

In an alternative extension, patterns are based on a symmetry consisting of a $U(1)_{\text{FN}}$ *Froggatt-Nielsen* symmetry [72] combined with a discrete non-abelian symmetry A_4 [73], and have been worked out for *leptoquark* extensions of the SM [74–76]. These leptoquarks are particles which can couple to leptons and quarks simultaneously, and have been studied in the context of lepton flavor violation as well as lepton flavor non-universality (see *e.g.* [7, 11, 12, 74, 77–79]).

Instead of imposing a flavor symmetry small Yukawa couplings and CKM mixing angles can be explained by RGE evolution in the IR. As typically Yukawa couplings have only weak logarithmic energy dependence, the RGE flow alone cannot explain the hierarchy even in strongly coupled theories. However, in theories with an almost scale-invariant gauge coupling the running of the Yukawa couplings can be enhanced [80]. By combining the SM gauge group with an additional conformal sector the flavor hierarchy can be generated by strong dynamics of the conformal sector [81, 82]. Alternatively, the RGE running of the Yukawa couplings can be enhanced close to RGE fixed points which also allows to explain the hierarchies in the SM [83].

2.3.3 Hints for New Physics: flavor anomalies

Several measurements of B -decay observables hint at deviations from the SM predictions. These deviations, also referred to as *anomalies*, are found both in *flavor changing neutral current* (FCNC) transitions $b \rightarrow s\ell^+\ell^-$ as well as charged current $b \rightarrow c\ell^-\bar{\nu}_\ell$ transitions. Examples for Feynman diagrams in the SM are shown in Fig. 2.3. In total, the anomalies can

be divided into four groups:

- Suppression of branching ratios of exclusive $b \rightarrow s\mu^+\mu^-$ FCNC transitions [84, 85]. Here, uncertainties are dominated by hadronic form factors [86–88].
- Deviations in the $B \rightarrow K^*\mu^+\mu^-$ angular observables from their SM predictions [89–93]. Hadronic uncertainties are smaller but still dominant [94, 95].
- Deviations from lepton flavor universality (e, μ) in $b \rightarrow s\ell^+\ell^-$ transitions in $B \rightarrow K\ell^+\ell^-$ and $B \rightarrow K^*\ell^+\ell^-$ [96–98]. Theoretical uncertainties are small [99] and sensitivity is still limited by statistical uncertainties.
- Deviations from lepton flavor universality (both e, τ and μ, τ) in $b \rightarrow c\ell^-\bar{\nu}_\ell$ transitions [100–106]. Interestingly, $e - \mu$ universality holds at the percent level [107–109]. The uncertainties are dominated by experimental uncertainties [110–113].

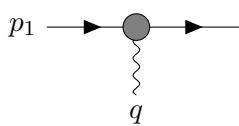
Especially *null tests* are a powerful way to keep theoretical uncertainties under control. The B -decay observables $R_{D^{(*)}}$ and $R_{K^{(*)}}$ test lepton-flavor universality violation in $b \rightarrow c$ and $b \rightarrow s$ transitions, respectively. These observables are defined as

$$R_{D^{(*)}} = \frac{\int dq^2 d\text{BR}(B \rightarrow D^{(*)}\tau\nu_\tau)/dq^2}{\int dq^2 d\text{BR}(B \rightarrow D^{(*)}e\nu_e)/dq^2}, \quad R_{K^{(*)}} = \frac{\int dq^2 d\text{BR}(B \rightarrow K^{(*)}\mu^+\mu^-)/dq^2}{\int dq^2 d\text{BR}(B \rightarrow K^{(*)}e^+e^-)/dq^2}, \quad (2.3.7)$$

and have been measured by the LHCb [96–98, 105, 106, 114, 115], Belle [102, 104, 115–117] and BaBar [100, 101] collaborations and show a tension with the SM predictions [99, 112, 113, 118–120] at the level of about $\sim 2 - 3\sigma$. Note that the latest Belle measurement of $R_{D^{(*)}}$ is in agreement with the SM at the level of 1.2σ .

While deviations in $b \rightarrow s\mu\mu$ transitions can in principle be explained by statistical fluctuations or an underestimation of hadronic uncertainties, they also allow for an interpretation with BSM contributions [121–127]. In simplified models, the anomalies can be explained simultaneously by a single mediator particle (see *e.g.* [7–12]).

The AMM of a particle refers to contributions to the *magnetic moment* of a particle arising at higher loop orders. These AMMs offer an ideal opportunity to test the SM since the electron AMM is among the most precisely measured observables in particle physics. Simultaneously, it is computed to the highest precision available in today's calculations. The magnetic moment of a charged lepton can be via



$$p_1 \longrightarrow \text{---} \bullet \text{---} p_2 = -ie\bar{u}(p_2) \left(F_1 \left(\frac{q^2}{m_\ell^2} \right) \gamma^\mu + \frac{i\sigma^{\mu\nu}}{2m_\ell} q_\nu F_2 \left(\frac{q^2}{m_\ell^2} \right) u(p_1) \right), \quad (2.3.8)$$

where the F_i are so-called *form factors*. The values at tree level are given as

$$F_1 = 1, \quad F_2 = 0. \quad (2.3.9)$$

Computations at one-loop level yield additional contribution to F_1 and F_2 at $\mathcal{O}(\alpha_e)$. Contributions to the form factor F_1 modify the lepton-photon coupling $eA_\mu\bar{\psi}\gamma^\mu\psi$ and renormalize the electric charge. Besides introducing a scale dependence no additional effects arise. In contrast, contributions to F_2 have exactly the structure of a magnetic moment. Given that

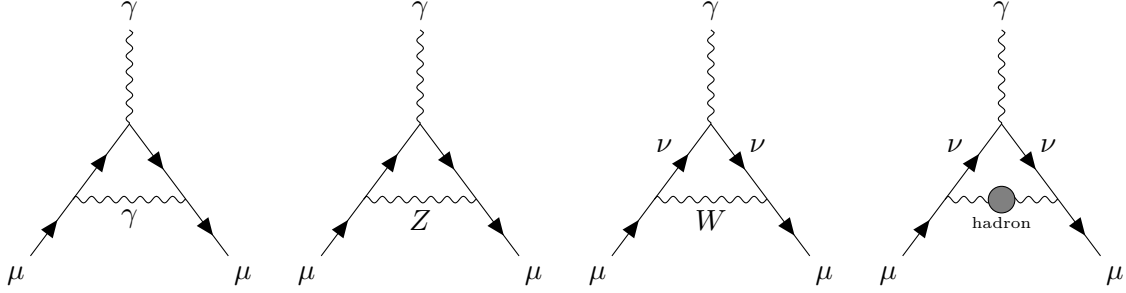


Figure 2.4: Representative Feynman diagrams for higher-order contributions to the muon anomalous magnetic moment a_μ^{SM} in the SM. The first diagram shows QED contributions, the second and third diagram show electroweak contributions at lowest order and the fourth diagram shows lowest-order hadronic contributions.

at tree level we find $F_2 = 0$ one obtains $g = 2$, as predicted by the Dirac equation. Higher order contributions, however, lead to small deviations $\mathcal{O}(\alpha_e)$. Considering the QED one-loop contributions in the first diagram in Fig. 2.4 we find for the form factor at $q^2 = 0$:

$$F_2(0) = \frac{\alpha_e}{2\pi}. \quad (2.3.10)$$

Including these corrections, the magnetic moment reads

$$g = 2 + 2F_2(0) = 2 + \frac{\alpha_e}{\pi}. \quad (2.3.11)$$

Defining the AMM as

$$a_\ell = \frac{g_\ell - 2}{2}, \quad (2.3.12)$$

parametrizes all deviations from $g_\ell = 2$ ($\ell = e, \mu, \tau$).

In the SM, additional EW and hadronic contributions have to be considered. In Fig. 2.4 we give examples for lowest diagrams for EW (second and third diagram) and hadronic (fourth diagram) contribution to the AMM. Especially the latter give rise to sizable theoretical uncertainties.

Measurements of the electron and muon AMMs are found to be in tension with the SM prediction. In the case of the muon, the discrepancy is [13]

$$\Delta a_\mu = a_\mu^{\text{exp}} - a_\mu^{\text{SM}} = 268(63)(43) \cdot 10^{-11}, \quad (2.3.13)$$

where the first and second uncertainty correspond to experimental and theory uncertainties, respectively. Adding both uncertainties in quadrature this value corresponds to a deviation of 3.5σ from the SM. Recent theory predictions [128, 129] find even larger deviations of 4.1σ . At the same time, a computation of the hadronic vacuum polarization from lattice QCD [130] possibly eliminates the anomaly. As this result is in tension with EW data [131, 132] and previous lattice calculations, further investigations are required [133]. Similarly, for the AMM of the electron the difference between experimental and theory value reads

$$\Delta a_e = a_e^{\text{exp}} - a_e^{\text{SM}} = -88(28)(23) \cdot 10^{-14}, \quad (2.3.14)$$

which translates into a deviation of 2.4σ from the SM [14, 15].

Note that the anomalies have an opposite sign comparing electron and muon AMMs. Thus, various models, which introduce additional particles such as light scalars [134–137] or supersymmetric partners [138–140], assume explicit breaking of lepton flavor universality. Conversely, the asymptotically safe extensions in Refs. [28, 30] offer an alternative and simpler explanation of the AMMs. In particular, no further breaking of lepton flavor universality besides the different lepton masses is needed. As discussed in detail in Chapter. 7, the extension of the SM introduce new VLLs and flavorful scalars, which couple to the SM leptons. Both AMMs can be accommodated using a superposition of two effects: one scales linearly with the lepton mass, the other one quadratically. Thus, the different lepton masses in the SM together with the additional particles suffice to explain both AMMs without any explicit flavor universality violation.

3 Effective field theories

Present data at the LHC suggest that the next discovery of a new fundamental particle is a prospect of future colliders with higher energy scales. Given the lack of significant deviations from the SM in direct searches, new physics might be separated in scales from the scales of the SM ($\sim m_W, m_h, m_t$). Facing such a scenario, indirect searches for BSM physics take a leading role. However, knowledge from indirect searches is usually ambiguous in the sense that measurements can be explained by multiple models. As such, a framework is needed to identify deviations from the SM in both a global and model-independent way and to remove as many theoretical ambiguities as possible from the analysis. A tool providing all these properties is an EFT. This framework allows to systematically study large sets of experimental data and offers an efficient approach to test particular models given some degree of separation between the scales of BSM and SM physics. The theorem which ensures the validity of the concept of EFTs is called the *decoupling theorem* [141]. It states that, up to a few exceptions, heavy degrees of freedom decouple at energies significantly below their mass. In this regard, decoupling means that contributions from such heavy particles are suppressed by inverse powers of their mass scale (except for logarithmic contributions).

The basic idea of the EFT framework is to describe physical processes considering only the relevant degrees of freedom. By doing so, heavy states relevant at larger energies do not appear explicitly. An example for such a situation is the decay of the muon, for which the W boson cannot be produced on shell. Instead of the complete SM an EFT is used in which the W boson is integrated out. If the complete theory is known and perturbative, EFTs offer in most cases simplifications for the computation as contributions from decoupled degrees of freedom are contained in the coupling parameters of the low-energy Lagrangian. Additional benefits arise when dealing with large logarithms since EFTs allow to apply renormalization improved perturbation theory, in which such large logarithms are summed to all orders. This significantly enhances the precision of the theory prediction compared to fixed-order calculations. Similarly, EFTs allow to sum IR logarithms of the underlying theory to all orders by converting them into UV logarithms, which can then be summed by integrating the RGEs. Thus, EFTs are to be considered as a theory constructed out of dynamical degrees of freedom relevant for the physical situation that has to be described. The corresponding RGEs serve to sum logarithms of ratios of different scales to all orders.

Not in all cases can the EFT be derived from an underlying theory, *i.e.* when the underlying theory is not known or not perturbative. Exactly in these situations employing EFTs turns from a convenient simplification of calculations into a necessity. EFTs provide an efficient method to parametrize the unknown interactions in terms of *effective operators* and their corresponding *Wilson coefficients*. Within this framework, the underlying theory is encoded within the structure of the operators and the corresponding interactions among the light states. Fitting this parametrization to experimental data allows to systematically study large sets of measurements and to determine the size of the interactions. Different models can be matched onto the EFT, and values for the parameters such as masses and couplings can be derived from values of the Wilson coefficients determined in global analyses. One additional advantage of this method is that a successful explanation of any deviation from the SM is

automatically required to be consistent with the remaining dataset. Even in the case that no significant deviation from the SM is observed in the data, fits in the EFT framework allow to encode the global dataset in a model-independent form. This provides efficient tests of BSM models. Thus, EFTs allow to perform model-independent searches for BSM physics by comparing the SM prediction for these coefficients to the experimental values.

In this chapter, we discuss the concept of EFTs and related topics such as RGEs and the resummation of large logarithms at the example of *Fermi's theory* in Sec. 3.1. We also introduce the *weak effective theory* (WET), which provides a complete basis of operators for physics below the electroweak scale. In Sec. 3.2, we introduce the SMEFT Lagrangian, which has been widely employed in the recent years in the search for BSM physics. In Sec. 3.3, we consider the top-quark sector of SMEFT, introduce the parametrization of matrix elements within the SMEFT framework. We also give a short overview on recent achievements in this field. In Sec. 3.4, we comment on a more general EFT which describes a scalar sector different to both the SM and the SMEFT. Our fitting setup is introduced in detail in Sec. 3.5.

3.1 Effective theories below the electroweak scale

Fermi's theory [142] is an EFT that describes the weak interactions in the SM at energies $E \ll m_W$. In this theory, the massive W and Z bosons are not present and the SM Lagrangian (2.1.50) is not used to describe processes at low energy scales. Instead, an effective Lagrangian

$$\mathcal{L}_{\text{Fermi}} = -\frac{4G_F}{\sqrt{2}} J_\mu^\dagger J^\mu + \mathcal{O}\left(\frac{p^2}{m_W^2}\right), \quad (3.1.1)$$

has to be constructed, where p is a four-momentum characteristic for the process considered and $G_F = \sqrt{2}g^2/(8m_W^2)$ is called the *Fermi constant*. The current J_μ is defined as

$$J_\mu = \sum_{ij} V_{ij} \bar{u}_i \gamma_\mu P_L d_j + \sum_i \bar{\nu}_i \gamma_\mu P_L l_i, \quad (3.1.2)$$

with i, j running over all flavors present at that energy scale. Even though we express Fermi's constant G_F in terms of parameters of the underlying theory, the theory was originally constructed to describe weak interactions at low energies without any information on the EW theory. In the formulation of the Lagrangian (3.1.1) we have, however, neglected contributions from forces other than the weak interactions that can contribute beyond tree level. Consider for example the decay of the muon which is at tree level described by the following part of the Lagrangian in Eq. (3.1.1):

$$\mathcal{L}_{\text{eff}} = -\frac{4G_F}{\sqrt{2}} [\bar{\nu}_\mu \gamma_\alpha P_L l_\mu] [\bar{l}_e \gamma^\alpha P_L \nu_e]. \quad (3.1.3)$$

Beyond tree level, we have to introduce a coefficient C that parametrizes radiative corrections:

$$\mathcal{L}_{\text{eff}} = -\frac{4G_F}{\sqrt{2}} C\left(\frac{m_W}{\mu}, \alpha_e(\mu)\right) (\bar{\nu}_\mu \gamma_\alpha P_L l_\mu) (\bar{l}_e \gamma^\alpha P_L \nu_e). \quad (3.1.4)$$

The exact value of C depends on the scale μ and the value of the electromagnetic coupling α_e . Loop corrections at the scale m_W lead to deviations in the value of C :

$$C(1, \alpha_e(m_W)) = 1 + \mathcal{O}(\alpha_e(m_W)). \quad (3.1.5)$$

The scale dependence is canceled by the dependence of the effective operator so that physical quantities do not depend on μ . In this case, the coefficient C is indeed μ independent (in the limit of vanishing $m_{e,\mu}$), and hence potentially large logarithms of m_W^2/μ^2 do not occur in the expansion¹. However, even when the corrections are non-vanishing the QED coupling is sufficiently small, so that products with large logarithms remain small and perturbation theory can be applied. In turn, for strong interactions this is no longer true and the large logarithms need to be resummed to all orders using RGE evolution. This is discussed in the following.

Consider a general EFT Lagrangian

$$\mathcal{L}_{\text{eff}} = \sum_d \frac{1}{\Lambda^{d-4}} \sum_i C_i^{(d)}(\mu) O_i^{(d)}(\mu), \quad (3.1.6)$$

where Λ is the separation scale between long-distance and short-distance effects, μ is the scale considered for the process, $C_i^{(d)}$ are coefficients containing short-distance effects and $O_i^{(d)}$ denote effective operators. With d we denote the dimension of the operator. For a simpler notation, we drop the (d) superscript in the following. As the scale μ is arbitrary, the theory must not depend on its exact value. Thus, we obtain

$$\frac{d(C_i(\mu)O_i(\mu))}{d \ln \mu} = 0 = \frac{dC_i(\mu)}{d \ln \mu} O_i(\mu) + C_i(\mu) \frac{dO_i(\mu)}{d \ln \mu}. \quad (3.1.7)$$

Similarly to the renormalization of fields in Sec. 2.2, we define bare operators as

$$O_i^{(0)} = Z_{ij} O_j, \quad (3.1.8)$$

where j is summed over. As the bare operator is μ independent, the derivative

$$\frac{dO_i^{(0)}}{d \ln \mu} = 0 = \frac{dZ_{ij}}{d \ln \mu} O_j + Z_{ij} \frac{dO_j}{d \ln \mu} \quad (3.1.9)$$

vanishes. We conclude

$$\frac{dO_i}{d \ln \mu} = -\frac{1}{Z_{ki}} \frac{dZ_{kj}}{d \ln \mu} O_j = -\gamma_{ij} O_j, \quad (3.1.10)$$

where the matrix γ_{ij} is called the *anomalous dimension matrix* (ADM). The μ dependence of the ADM stems solely from the fact that γ_{ij} depends on the coupling constant $\alpha(\mu)$. With the ADM, it follows from Eq. (3.1.7) that

$$\frac{dC_i}{d \ln \mu} = \gamma_{ji} C_j = (\gamma^T)_{ij} C_j, \quad (3.1.11)$$

¹A simple explanation follows from *Fierz identities* that allow to rewrite the operator in Eq. 3.1.4 as $(\bar{\nu}_\mu \gamma_\alpha P_L \nu_e)(\bar{l}_e \gamma^\alpha P_L l_\mu)$. Since neutrinos are not charged under QED, and the charged lepton current is conserved in the limit $m_{e,\mu} = 0$ and does not get renormalized, no renormalization has to be applied to the effective operator.

where we use the fact that the operators O_i are independent. Often, both the ADM and the coefficient can be expanded in powers of the coupling α . For the Wilson coefficients this expansion at the scale Λ reads

$$C_i(\Lambda, \alpha) = \sum_k A_i^{(k)} \left(\frac{\alpha}{4\pi} \right)^k . \quad (3.1.12)$$

The ADM can be expanded as

$$\gamma_{ij}(\alpha) = \sum_k \gamma_{ij}^{(k)} \left(\frac{\alpha}{4\pi} \right)^{k+1} . \quad (3.1.13)$$

At arbitrary scales μ we can write the coefficient as

$$\begin{aligned} C_i(\mu, \alpha) = & B_i^{(00)} \\ & + B_i^{(11)} \left(\frac{\alpha}{4\pi} \right) \ln \left(\frac{\Lambda}{\mu} \right) + B_i^{(10)} \left(\frac{\alpha}{4\pi} \right) \\ & + B_i^{(22)} \left(\frac{\alpha}{4\pi} \right)^2 \ln^2 \left(\frac{\Lambda}{\mu} \right) + B_i^{(21)} \left(\frac{\alpha}{4\pi} \right)^2 \ln \left(\frac{\Lambda}{\mu} \right) + B_i^{(20)} \left(\frac{\alpha}{4\pi} \right)^2 \\ & + \dots \end{aligned} \quad (3.1.14)$$

For $\mu = \Lambda$ all the logarithms vanish and we find $B_i^{(k0)} = A_i^{(k)}$. As the logarithms can potentially become sizable if α is not too small, as is the case in QCD, they need to be resummed. This is taken care of by solving the RGEs in Eq. (3.1.11). Using the first non-vanishing terms in the expansion of γ_{ij} and the beta function of the coupling α defined in Eq. (2.2.16) we find for the case of a single operator

$$C_i(\mu, \alpha) = B_i^{(00)} \left(\frac{\alpha(\Lambda)}{\alpha(\mu)} \right)^{\gamma^{(0)}/(2\beta^{(0)})} . \quad (3.1.15)$$

If there are multiple operators, the ADM are diagonalized before solving the RGEs in the new basis where γ is diagonal before transforming back for the general solution. This solution of the RGEs contains all contributions from the first column in Eq. (3.1.11), *i.e.* all contributions proportional to B_i^{kk} where the logarithm and the coupling appear at the same order are resummed. This approximation is called the *leading logarithm approximation*. In order to go beyond this approximation the second term in the ADM expansion, $\gamma_{ij}^{(1)}$, as well as the coefficient $B_i^{(10)}$ have to be considered. Solving the RGEs at this order resums the second column in addition to the first one, *i.e.* all contributions with coefficients $B_i^{(kk-1)}$. This also requires a matching at the scale Λ at one-loop level.

An example for this procedure is present in Fermi's theory. Consider the weak interaction process $q_1 \bar{q}_3 \rightarrow q_2 \bar{q}_4$ described by the effective Lagrangian

$$\mathcal{L}_{\text{eff}} = -\frac{4G_F}{\sqrt{2}} (C_1 O_1 + C_2 O_2) . \quad (3.1.16)$$

The operators read

$$O_1 = (\bar{q}_2^\alpha \gamma_\mu P_L q_1^\alpha) (\bar{q}_2^\beta \gamma^\mu P_L q_4^\beta) , \quad O_2 = (\bar{q}_2^\beta \gamma_\mu P_L q_1^\alpha) (\bar{q}_2^\alpha \gamma^\mu P_L q_4^\beta) , \quad (3.1.17)$$

where α, β denote color indices that are summed over. We determine the Wilson coefficients by comparing Feynman diagrams in the EFT with the same diagrams in the full theory. At the scale $\mu = m_W$, at which the W boson is integrated out, we find

$$C_1(m_W, \alpha_s(m_W)) = 1 + \mathcal{O}(\alpha_s(m_W)), \quad C_2(m_W, \alpha_s(m_W)) = 0 + \mathcal{O}(\alpha_s(m_W)). \quad (3.1.18)$$

The ADM at lowest order is calculated at one-loop level:

$$\gamma = \frac{\alpha_s}{2\pi} \begin{pmatrix} -1 & 3 \\ 3 & -1 \end{pmatrix}. \quad (3.1.19)$$

As this matrix is not diagonal, mixing between the operators occurs during the RGE evolution. To solve the RGEs we diagonalize the ADM by introducing new coefficients

$$C_{\pm} = C_1 \pm C_2. \quad (3.1.20)$$

In this basis, the ADM is diagonal and we find for the lowest order entries in the expansion (3.1.13)

$$\gamma_+^{(0)} = 4, \quad \gamma_-^{(0)} = -8. \quad (3.1.21)$$

With these entries we can employ the solution in Eq. (3.1.15) and find

$$C_+(\mu) = \frac{1}{2} \left(\frac{\alpha(m_W)}{\alpha(\mu)} \right)^{6/(33-2n_f)}, \quad C_-(\mu) = \frac{1}{2} \left(\frac{\alpha(m_W)}{\alpha(\mu)} \right)^{-12/(33-2n_f)}. \quad (3.1.22)$$

Further information on the general concept of EFTs can be found in Refs. [143–149].

In general, at scales below the mass of the W boson only particles with masses $m_i < m_W$ are considered as physical degrees of freedom. A general low-energy theory describing physics below the EW scale is, as in Fermi's theory, constructed by integrating out the W , Z and Higgs boson, the top quark and any heavy BSM particles. Thus, effective operators in the WET Lagrangian parametrize both SM and potential BSM contributions. The WET has been used excessively in the literature for a variety of low-energy physics, such as B decays or Kaon physics. In fact, FCNCs such as $b \rightarrow s$ transitions impose strong constraints on the flavor sector of BSM physics. Note that in the literature the term *low-energy EFT* (LEFT) is also used for this EFT.

The gauge group of WET is $SU(3)_C \times U(1)_Q$ and only particles lighter than the W boson are included in this theory. Effective operators arise at dimension three, five and higher dimensions and are added to the $SU(3)_C \times U(1)_Q$ invariant Lagrangian

$$\begin{aligned} \mathcal{L} = & -\frac{1}{4} F_{\mu\nu} F^{\mu\nu} - \frac{1}{4} G_{\mu\nu}^A G^{A\mu\nu} + \theta_{\text{QED}} \frac{e^2}{32\pi^2} F_{\mu\nu} \tilde{F}^{\mu\nu} + \theta_{\text{QCD}} \frac{g_s^2}{32\pi^2} G_{\mu\nu}^A \tilde{G}^{A\mu\nu} \\ & + \bar{\psi}_i \not{D} \psi_i + \bar{\psi}_i m_i \psi_i, \end{aligned} \quad (3.1.23)$$

where $\tilde{F}_{\mu\nu} = 1/2 \epsilon_{\mu\nu\alpha\beta} F^{\alpha\beta}$, $\tilde{G}_{\mu\nu}^A = 1/2 \epsilon_{\mu\nu\alpha\beta} G^{A\alpha\beta}$, and $\epsilon_{0123} = +1$. Here, the covariant derivative reads $D_\mu = \partial_\mu + ig_s T^A G_\mu^A + ie Q A_\mu$, and $F_{\mu\nu}$ and $G_{\mu\nu}^A$ are field strength tensors of $U(1)_Q$ and $SU(3)_C$, respectively.

In recent years, a complete basis of the WET Lagrangian up to dimension-six operators has been constructed [150]. The corresponding one-loop ADM of this basis has been computed

in Ref. [151]. In App. B.4, we list the number of operators found in the same reference up to dimension six. For certain processes, such as $b \rightarrow s$ transitions, the QCD running in WET has been computed to significantly higher orders. For example, the matching of the SM onto the WET for $b \rightarrow s\gamma$ transitions is known at three-loop level, while the ADM is computed at four-loop level [152–156].

3.2 The Standard Model Effective Field Theory

The SMEFT is a generalization of the SM. It allows to parametrize possible deviations from the SM and to test for signatures of BSM physics in global fits. To construct the SMEFT Lagrangian two assumptions have to be made:

- Possible extensions of the SM are separated in mass from the SM content *i.e.* the new particles involved are heavier than the measured value of the Higgs VEV $v = 246$ GeV
- The observed Higgs boson belongs to an $SU(2)_L$ doublet so that the EW symmetry is linear realized.

The SMEFT is a toolbox that allows to study low-energy signatures of BSM theories in a consistent, model-independent (besides the assumptions stated earlier) way. At energies below the scale of BSM physics the SMEFT provides a consistent characterization of the low energy limit of BSM physics. Motivated by the large set of precision measurements at the LHC as well as LEP, different groups have performed analyses in the SMEFT framework [20, 157–175].

The SMEFT Lagrangian is constructed by considering the SM Lagrangian as the lowest order term of an expansion in $1/\Lambda$, where Λ is interpreted as the scale at which the BSM particles have been integrated out:

$$\mathcal{L}_{\text{SMEFT}} = \mathcal{L}_{\text{SM}} + \sum_{d=5}^{\infty} \mathcal{L}^{(d)}, \quad \mathcal{L}^{(d)} = \sum_j \frac{1}{\Lambda^{d-4}} C_j^{(d)} O_j^{(d)}. \quad (3.2.1)$$

Here, $O^{(d)}$ denotes higher dimensional operators of dimension $d > 4$ and $C^{(d)}$, are the corresponding Wilson coefficients that parametrize BSM couplings. At each dimension d the higher dimensional operators are suppressed by $d - 4$ powers of the high scale Λ . This means that at energies $E < \Lambda$ BSM contributions are stronger suppressed for higher dimensions. The effective operators are constructed out of SM fields only and are required to be invariant under the gauge symmetries of the SM. The number of independent operators in $\mathcal{L}^{(5)}$ to $\mathcal{L}^{(8)}$ are known [176–183]. In addition, a general algorithm [182–185] allows to construct operator bases at dimensions $d > 8$ defining the SMEFT Lagrangian at all orders in $1/\Lambda$. The SMEFT Lagrangian is a QFT which is renormalizable order by order in $1/\Lambda$ in the sense that at each order all infinities in loop-diagrams cancel when all operators allowed by gauge symmetries are taken into account in the computation. Note that only even-dimensional operators can conserve lepton and baryon number [186, 187].

3.2.1 Operator basis

In the search for BSM physics the leading contributions arise at dimension five. For one generation of fermions, there is only one operator in $\mathcal{L}^{(5)}$ which generates Majorana masses for neutrinos after EWSB [176] and violates lepton-number conservation. Thus, the leading

contributions for phenomenological studies of BSM signatures at the LHC are generated at dimension six. A first categorization of dimension-six operators has been provided in Ref. [178], listing in total 80 operators assuming baryon- and lepton-number conservation. However, it turned out that this set is overcomplete as some of the operators are related after applying the equations of motions. The first non-redundant basis of dimension-six operators has been given in Ref. [179] and is referred to as *Warsaw basis*. For one generation of fermions, this basis contains 59 independent operators conserving lepton and baryon number, which we give in App. B.1. This basis can be divided in eight classes of operators: X^3 , φ^6 , $\varphi^4 D^2$, $X^2 \varphi^2$, $\psi^2 \varphi^3$, $\psi^2 X \varphi$, $\psi^2 \varphi^2 D$ and ψ^4 . In this notation, X denotes the insertion of a field strength tensor, φ the insertion of the Higgs doublet, D a covariant derivative, and ψ a fermion field.

Although there are only 59 independent operators at dimension six that conserve baryon and lepton number, fermion fields in these operators carry additional generation indices. In full flavor generality there are 2499 parameters at dimension six, 1350 CP -even and 1149 CP -odd ones. The ADM at one loop has been computed in Refs. [188–192] building up on results of Refs. [193–214]. For the Warsaw basis, it has been shown that the ADM closes at one loop. The ADM of dimension-six operators can be written as

$$\frac{dC_i}{d \ln \mu} = \gamma_{ij} C_j. \quad (3.2.2)$$

In this notation, γ_{ij} denotes a 8×8 block matrix, where indices refer to the eight operator classes. In the SMEFT, there is a large amount of mixing present in the ADM, which plays an important role when computing observables at the electroweak scale in terms of Wilson coefficients given at the high scale Λ . As a consequence, effects such as CP violation are propagated through the Lagrangian. For example, $X^2 \varphi^2$ operators give CP violating contributions to dipole operators, and thus they are constrained by measurements of electric dipole moments.

The structure of γ_{ij} can best be understood using *Naive Dimensional Analysis* (NDA) [215] and a set of rescaled operators O'_i which are defined as $g^3 X^3$, φ^6 , $\varphi^4 D^2$, $g^2 X^2 \varphi^2$, $y \psi^2 \varphi^3$, $g y \psi^2 X \varphi$, $\psi^2 \varphi^2 D$ and ψ^2 . In this rescaling, each insertion of a field strength tensor X receives an insertion of a gauge coupling g , and each helicity-flipping term $\psi^2 \varphi^3$ and $\psi^2 X \varphi$ is rescaled with an insertion of a Yukawa coupling y . The two bases are related via

$$\mathcal{L}^{(6)} = \frac{1}{\Lambda^2} \sum_i C_i O_i = \frac{1}{\Lambda^2} \sum_i C'_i O'_i. \quad (3.2.3)$$

The RGEs can be rewritten as

$$\frac{dC'_i}{d \ln \mu} = \gamma'_{ij} C'_j, \quad (3.2.4)$$

where the ADMs γ_{ij} and γ'_{ij} are related by the insertion of gauge and Yukawa couplings and their derivatives. For the rescaled operators, the ADM has the following structure for its entries [188]:

$$\gamma'_{ij} \sim \left(\frac{\lambda}{(4\pi)^2} \right)^{n_\lambda} \left(\frac{y^2}{(4\pi)^2} \right)^{n_y} \left(\frac{g^2}{(4\pi)^2} \right)^{n_g}, \quad (3.2.5)$$

so that the perturbative order of the ADM is defined as $N = n_\lambda + n_y + n_g$. The classes of operators can be distinguished by their *NDA weight* w_i : $g^3 X^3$ operators have weight $w_1 = -1$,

φ^6 operators weight $w_2 = 2$, $g^2 X^2 \varphi^2$ and $g y \psi^2 X \varphi$ operators weight $w_{4,6} = 0$, and operators in the remaining classes weight $w_{3,5,7,8} = 1$. Using the NDA weights, N can be computed for each block in γ'_{ij} as [216]

$$N = 1 + \omega_i - \omega_j. \quad (3.2.6)$$

In the ADM blocks with $N < 0$ vanish and blocks on the diagonal always have $N = 1$. However, in the explicit results even blocks with $N \geq 0$ can vanish. The detailed structure of the ADM is given in Ref. [190].

3.2.2 Redefinition of parameters and their relations

Considering the SMEFT as a generalization of the SM, predictions of the SM are altered due to the additional contributions from higher-dimensional operators. This affects the definitions of both fields and parameters in the Lagrangian, which is discussed in detail in Ref. [190]. As an example, we consider in App. B.2 BSM contributions at dimension six to the gauge fields.

In order to define the numerical values of the parameters in the Lagrangian a set of input parameters is needed. Denoting these input parameters and those that are inferred from them as $\check{\theta}_i$ we find additional SMEFT contributions which alter the SM relations among these parameters. In the case of the theoretical predictions of the electroweak parameters, the leading contributions arise at dimension six and depend on the choice of the input parameter scheme. In the literature, two schemes are present: $\{\check{\alpha}_e, \check{m}_Z, \check{G}_F\}$ and $\{\check{m}_W, \check{m}_Z, \check{G}_F\}$. In App. B.3, we give the relations among the parameters of the SMEFT Lagrangian in both input schemes.

Comparing both schemes, the $\{\check{m}_W, \check{m}_Z, \check{G}_F\}$ input scheme has several advantages. First of all, even though the measurement of $\check{\alpha}_e$ at the low scale has a significantly higher precision, this benefit is lost due to large errors introduced in the running, especially in the region of dominant hadronic resonances. Second, the use of \check{m}_W has advantages in the development of one-loop results in the SMEFT framework, as discussed in detail in Refs. [217–220]. As a final point, for phenomenological applications at the LHC the input scales in the $\{\check{m}_W, \check{m}_Z, \check{G}_F\}$ scheme are closer. This results in a reduction of logarithmic enhancements present when using $\check{\alpha}_e$. In addition, the related running of corresponding SMEFT contributions is reduced as well.

3.2.3 Spontaneous symmetry breaking

In the SMEFT Lagrangian, higher-dimensional operators are naturally written in the flavor basis. However, computations of observables which are compared to experimental measurements are performed in the mass basis. As shown in Eq. (2.1.42), mass and flavor bases are related by the rotation matrices $S_{L/R}^{u/d}$. In most cases, these rotations can just be absorbed in the definition of Wilson coefficients which in turn defines the coefficients in the mass basis. Consider as a simple example the operator O_{eu}^{ij} where additional superscripts denote the generation of quark fields. Rotating the quarks from the flavor basis to the mass basis we find

for the operator and the corresponding Wilson coefficient:

$$\begin{aligned}
C_{eu}^{ij} O_{eu}^{ij} &= C_{eu}^{ij} (\bar{e}_R \gamma_\mu e_R) \left(\bar{u}_R^i \gamma^\mu u_R^j \right) \\
&= C_{eu}^{ij} (\bar{e}_R \gamma_\mu e_R) \left(\left(S_R^u \right)_{ki}^\dagger \bar{u}_R^k \gamma^\mu \left(S_R^u \right)_{jl} u_R^l \right) \\
&= C_{eu}^{ij} \left(S_R^u \right)_{ki}^\dagger \left(S_R^u \right)_{jl} (\bar{e}_R \gamma_\mu e_R) \left(\bar{u}_R^k \gamma^\mu u_R^l \right) \\
&= \hat{C}_{eu}^{kl} (\bar{e}_R \gamma_\mu e_R) \left(\bar{u}_R^k \gamma^\mu u_R^l \right) \\
&= \hat{C}_{eu}^{kl} \hat{O}_{eu}^{kl}.
\end{aligned} \tag{3.2.7}$$

Here, we denote by \hat{C}_{eu}^{kl} and \hat{O}_{eu}^{kl} the Wilson coefficients and effective operators, respectively, in the mass basis. In this case, the rotation matrices can simply be absorbed in the definition of the coefficients. In general, as long as the effective operator does not contain an $SU(2)_L$ quark doublet, rotation matrices can be absorbed in the definition of the coefficients, giving rise to Wilson coefficients in the mass basis. However, if at least one quark doublet is present in the operator, flavor rotations have non-trivial effects. As an example, consider the operator O_{eq} and its corresponding Wilson coefficient:

$$\begin{aligned}
C_{eq}^{ij} O_{eq}^{ij} &= C_{eq}^{ij} (\bar{e}_R \gamma_\mu e_R) \left(\bar{q}_L^i \gamma^\mu q_L^j \right) \\
&= C_{eq}^{ij} (\bar{e}_R \gamma_\mu e_R) \left(\bar{u}_L^i \gamma^\mu u_L^j + \bar{d}_L^i \gamma^\mu d_L^j \right) \\
&= C_{eq}^{ij} (\bar{e}_R \gamma_\mu e_R) \left(\left(S_L^u \right)_{ki}^\dagger \bar{u}_L^k \gamma^\mu \left(S_L^u \right)_{jl} u_L^l + \left(S_L^d \right)_{mi}^\dagger \bar{d}_L^m \gamma^\mu \left(S_L^d \right)_{jn} d_L^n \right) \\
&= C_{eq}^{ij} \left(S_L^u \right)_{ki}^\dagger \left(S_L^u \right)_{jl} (\bar{e}_R \gamma_\mu e_R) \left(\bar{u}_L^k \gamma^\mu u_L^l + V_{mk}^\dagger V_{ln} \bar{d}_L^m \gamma^\mu d_L^n \right) \\
&= \hat{C}_{eq}^{kl} (\bar{e}_R \gamma_\mu e_R) \left(\bar{u}_L^k \gamma^\mu u_L^l + V_{mk}^\dagger V_{ln} \bar{d}_L^m \gamma^\mu d_L^n \right) \\
&= \hat{C}_{eq}^{kl} \hat{O}_{eq}^{kl}.
\end{aligned} \tag{3.2.8}$$

In the third to last line we used the relation

$$\left(S_L^d \right)_{ij} = \delta_{ik} \left(S_L^d \right)_{kj} = \left(S_L^u \right)_{il} \left(S_L^u \right)_{lk}^\dagger \left(S_L^d \right)_{kj} = \left(S_L^u \right)_{il} V_{lj}. \tag{3.2.9}$$

As demonstrated in Eq. (3.2.8), even after the absorption of the rotation matrices in the Wilson coefficients residual CKM matrix elements remain. The exact position of the CKM matrix elements depends on the choice which rotation matrices are absorbed in the coefficients: if elements from S_L^u are absorbed, the CKM matrix elements appear in front of left-handed down-type quarks and vice versa. Wilson coefficients in different absorption schemes² are related via CKM matrix elements [221]. As an example, if we choose to absorb the S_L^d matrices in Eq. (3.2.8), the Wilson coefficients \bar{C}_{eq}^{kl} obtained are related to the coefficients \hat{C}_{eq}^{kl} simply by

$$\hat{C}_{eq}^{ij} = V_{ik} V_{jl}^* \bar{C}_{eq}^{kl}. \tag{3.2.10}$$

²Here we refer with 'absorption scheme' to the choice whether elements from S_L^u or S_L^d are absorbed in the coefficients.

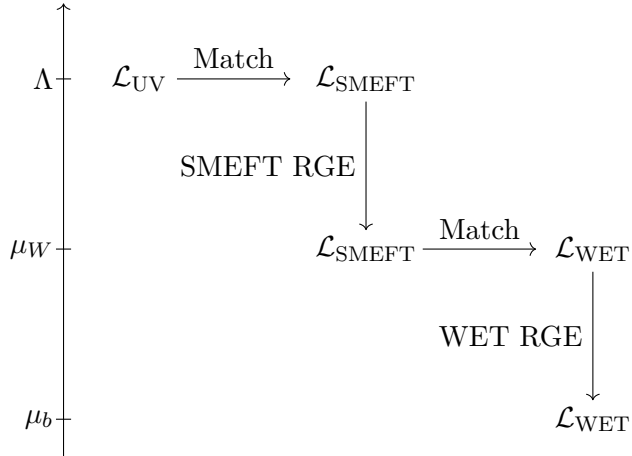


Figure 3.1: Schematic description of the matching and running procedure using both SMEFT and WET. At the high scale Λ Wilson coefficients in the SMEFT are generated. These coefficients are evolved to the EW scale μ_W using the SMEFT RGE and matched onto the WET Lagrangian. In order to compute observables at the low scale μ_b the WET RGEs are employed.

Thus, even if the Wilson coefficients are diagonal in the mass basis FCNCs appear in both definitions: either in the up sector (\bar{C}_i diagonal) or in the down sector (\hat{C}_i diagonal). The explicit expressions for Wilson coefficients in both definitions can be found in Ref. [221]. In this work, we consider the up-mass basis \hat{C}_i where up-quark flavor and mass basis are identical and flavor mixing is entirely in the down sector.

3.2.4 Linking physics at different scales

The one-loop running in WET and SMEFT together with the tree-level matching of the SMEFT basis onto the WET allows to consider SMEFT as the high-energy theory. With this procedure, low-energy observables can be computed in terms of SMEFT Wilson coefficients. By doing so, it is implicitly assumed that BSM physics follows the EWSB mechanism of the SM. Then, a set of SMEFT operators at a given scale can be chosen as a starting point and evolved down to the EW scale μ_W where SMEFT is matched onto WET. The WET RGEs can be employed to run the operators from the scale μ_W to the scale of low-energy experimental observables, $\mu_b \sim m_b$. This procedure is shown schematically in Fig. 3.1. Considering operators that are induced from SMEFT operators up to dimension six, only some contributions arise at tree level. The complete matching is provided in Ref. [150] and the number of operators is summarized in App. B.4.

Considering SMEFT as the underlying theory of WET has interesting implications for flavor physics. Observables and parameters, such as G_F , and their relation to other parameters in the SM, *e.g.* to v , are altered in SMEFT due to dimension-six contributions. In addition, $SU(2)$ invariance of SMEFT relates coefficients of different processes. For example, $b \rightarrow s$ transitions allow to constrain BSM contributions to $t \rightarrow c$ FCNCs [222]. Similarly, linking dilepton and dineutrino couplings in charm physics allows to probe lepton flavor conservation and lepton universality [223]. In addition, this allows to include observables measured at different energy scales in one combined fit to experimental data, see Refs. [21–24] for recent examples.

Dropping the requirement that BSM physics respect the SM EWSB mechanism, the complete basis of WET operators at the scale μ_W can be considered as a starting point and can be evolved to the low scale. The procedure relaxes constraints on WET coefficients imposed by the SMEFT Lagrangian, which are not necessarily satisfied in BSM scenarios. This allows to test the structure of the EWSB.

3.3 The top-quark sector

In the recent years, the SMEFT approach has been employed to study physics both at the LHC as well as lepton colliders [20, 157–175], with the most prominent one being the top-quark sector [18, 163, 224–238]. These searches provide information essential for global SMEFT analyses of LHC data and for BSM signatures in the top-quark sector.

The top quark is special for several reasons: It is the only fermion with a Yukawa coupling of $\mathcal{O}(1)$, and thus plays an important role in BSM scenarios aiming to explain the origin of the EWSB. In addition, due to its short lifetime the top quark decays before it hadronizes. Thus, properties such as the spin information are transferred to the decay products allowing for studies of the properties of a bare quark. At the same time, top-quark physics has entered a precision era as a variety of measurements of production and decay properties of the top quark have been performed at the LHC. Furthermore, significant progress in precise calculations of observables at up to *next-to-next-to leading order* (NNLO) in the SM has been achieved.

In analyses of the top-quark sector of SMEFT leading BSM contributions arise at dimension six. While there are 59 dimension-six operators at one generation and 2499 parameters for all three generations [179], only a significantly smaller subset of operators contributes to top-quark observables. The exact number parameters to be constrained in the analysis depends on the physical process as well as the order in the EFT expansion that is considered. As an example, six Wilson coefficients of operators involving a top quark give contributions at $\mathcal{O}(\Lambda^{-2})$ to $t\bar{t}$ production at the LHC, while five more coefficients contribute at $\mathcal{O}(\Lambda^{-4})$ [237]. Different orders of BSM contributions stem from possible interference terms of dimension-six operators with the SM process. Consider an amplitude \mathcal{M} with contributions \mathcal{M}^{SM} and $\mathcal{M}_i^{\text{BSM}}$ from SM processes and dimension-six operators O_i , respectively. Physical observables depend on the squared matrix element

$$\begin{aligned} |\mathcal{M}|^2 &= \left| \mathcal{M}^{\text{SM}} + \frac{C_i}{\Lambda^2} \mathcal{M}_i^{\text{BSM}} \right|^2 \\ &= \left| \mathcal{M}^{\text{SM}} \right|^2 + 2 \frac{1}{\Lambda^2} \text{Re} \left(C_i \mathcal{M}^{\text{SM}} \left(\mathcal{M}_i^{\text{BSM}} \right)^\dagger \right) + \frac{C_i C_j^*}{\Lambda^4} \mathcal{M}_i^{\text{BSM}} \left(\mathcal{M}_j^{\text{BSM}} \right)^\dagger. \end{aligned} \quad (3.3.1)$$

As can be seen, only BSM-SM interference terms generate a contribution at $\mathcal{O}(\Lambda^{-2})$. For certain operators, these interference terms are suppressed *e.g.* by helicity selection rules [239] or by small SM contributions as in the case of FCNCs. In this case, dimension-six operators do not generate leading contributions at $\mathcal{O}(\Lambda^{-2})$ but instead at $\mathcal{O}(\Lambda^{-4})$. Formally, squared contributions from dimension-six operators contribute at the same order in the EFT expansion as interference terms of the SM with dimension-eight operators neglected in Eq. (3.3.1). Nevertheless, as for some operators the interference term is suppressed, the squared terms is the dominant contributions. An analysis strategy [163] is to repeat the fit twice, both with and without inclusion of quadratic EFT contributions. This procedure can show for which operators the leading contributions do indeed arise in the form of the linear terms. Especially

for four-fermion operators quadratic terms receive an energy enhancement compared to linear terms both at dimension six and eight [22, 163, 237]. In addition, after identifying the independent linear combinations of Wilson coefficients, referred to as *degrees of freedom*, inclusion of the quadratic dimension-six terms removes flat directions that are otherwise present in the linear fit.

Restricting the operator set to those that generate an interference term with the SM at tree level not suppressed by small fermion masses m_i ($i \neq t$) leaves only the real part of the potentially complex valued Wilson coefficients (if the operator is not hermitian) as a free parameter in the analysis. For example, consider a combined fit to $t\bar{t}$, single-top, and $t\bar{t}Z/W/\gamma$ production together with top-quark decay observables. Including only operators that contribute at $\mathcal{O}(\Lambda^{-2})$ leaves eleven degrees of freedom in the fit [231]. Further considering NLO SMEFT contributions as well as operators that do not interfere with the SM process leads to a larger set of 22 operators [237]. The largest set of operators constrained in a global fit to top-quark data consisted of 34 SMEFT operators [234]. In this analysis, constraints on the Wilson coefficients are derived in a fit to data from single top-quark production, top-quark decay, top-quark pair and associated production, $t\bar{t}H$, $t\bar{t}t$, and $t\bar{t}b\bar{b}$ production.

3.4 Higgs Effective Field Theory

In the construction of both the SM and the SMEFT the existence of scalar complex field φ is assumed for two reasons:

- To correctly describe EWSB by introducing three Goldstone boson, *i.e.* the longitudinal components of the EW gauge bosons,
- To introduce a singlet scalar h , which corresponds to the Higgs boson and ensures *exact* unitarity at all energies when computing scattering amplitudes with external Goldstone bosons, see *e.g.* Refs. [240–242]

While the first argument is necessary for a correct description of EWSB, the second assumption can be relaxed by requiring that the theory is unitary only up to a cut-off scale at which the EFT expansion breaks down. An EFT where the second assumption is relaxed is the so-called *Higgs EFT* (HEFT). In this theory, the low-energy degrees of freedom comprise the massive SM fermions, SM gauge bosons, and, instead of the SM Higgs field, a singlet scalar h with free couplings to the SM states. The construction of the HEFT Lagrangian is based on the *Callan-Coleman-Weiss-Zumino* formalism [243, 244] and parametrizes the scalar sector with minimal assumptions. This approach has been used to construct several simple parametrizations, see *e.g.* Refs. [245–248], as well as a complete and self-consistent EFT [245, 249–265]. The HEFT is of particular interest in BSM scenarios in which the Higgs is assumed to be a pseudo-Goldstone boson of a larger spontaneously broken symmetry group. Examples are Technicolor models [266–268] or composite Higgs models [269–274].

The most distinct difference between SMEFT and HEFT lies in the different assumptions on the scalar structure. Any deviation from SMEFT expectations that rely on the doublet structure of the Higgs field is a hint for a description of the scalar sector completely different to both SM and SMEFT. Thus, these deviations carry information on the UV nature of BSM physics, see *e.g.* Ref. [275] for a review on this regard. Since presently no deviation from the SM indicates that the Higgs is not part of an $SU(2)_L$ doublet, we use the SMEFT framework throughout this work.

3.5 EFTfitter: fitting effective theories to data

Constraining SMEFT Wilson coefficients requires a consistent treatment of both correlations between uncertainties of the various measurements included in the fit. To do so, we employ a new implementation of the EFTfitter tool [164] based on the *Bayesian Analysis Toolkit BAT.jl* [276, 277] to derive constraints on the SMEFT Wilson coefficients in the form of posterior probability distributions using a Bayesian interpretation.

In Bayesian statistics, information about free parameters $\boldsymbol{\lambda}$ of a physical model M is expressed in terms of the posterior distribution $p(\boldsymbol{\lambda}|\mathbf{x})$ for a given dataset \mathbf{x} . Following the equation of Bayes and Laplace [278], the posterior distribution can be expressed as

$$p(\boldsymbol{\lambda}|\mathbf{x}) = \frac{p(\mathbf{x}|\boldsymbol{\lambda}) \cdot p(\boldsymbol{\lambda})}{p(\mathbf{x})}, \quad (3.5.1)$$

where $p(\mathbf{x}|\boldsymbol{\lambda})$ is the likelihood, $p(\boldsymbol{\lambda})$ is the prior probability distribution of the parameters $\boldsymbol{\lambda}$ and $p(\mathbf{x})$ is the normalization

$$p(\mathbf{x}) = \int d\boldsymbol{\lambda} p(\mathbf{x}|\boldsymbol{\lambda}) \cdot p(\boldsymbol{\lambda}). \quad (3.5.2)$$

Throughout this work, we consider a uniform distribution for the prior. In EFTfitter, constraints on the parameters are derived from a set of physical observables $\mathbf{y} = \mathbf{y}(\boldsymbol{\lambda})$, which are formulated as functions of the parameters $\boldsymbol{\lambda}$, given a set of measurements \mathbf{x} of these observables. For a set of N observables y_i ($i = 1, \dots, N$) based on n measurements x_i ($i = 1, \dots, n$), the likelihood $p(\mathbf{x}|\mathbf{y})$ reads

$$-2 \ln p(\mathbf{x}|\boldsymbol{\lambda}) = \sum_{i,j=1}^n (\mathbf{x} - U\mathbf{y}(\boldsymbol{\lambda}))_i \mathcal{M}_{ij}^{-1} (\mathbf{x} - U\mathbf{y}(\boldsymbol{\lambda}))_j. \quad (3.5.3)$$

Here, the $n \times N$ matrix U is unity if x_i is a measurement of y_j and zero otherwise, and \mathcal{M} is the positive-semidefinite covariance matrix

$$M_{ij} = \text{cov}(x_i, x_j) = \sum_{k=1}^L \text{cov}^{(k)}(x_i, x_j), \quad (3.5.4)$$

where k iterates over all L sources of uncertainties considered. In EFTfitter, the posterior distribution is evaluated using *Markov Chain Monte Carlo* (MCMC) sampling in *BAT.jl* and marginalization which yields the distributions shown in this thesis.

4 Global fit to top-quark data

Global fits in the SMEFT framework offer a systematic and model-independent way to test for signatures of BSM physics in a variety of observables simultaneously. In recent years, the top-quark sector of the SMEFT Lagrangian has been studied in various analyses, as discussed in Sec. 3.3. It builds the starting point for our analysis of BSM signatures in processes involving third-generation quarks aiming to link top-quark data to present flavor anomalies in the beauty sector, see Sec. 2.3.3. As a first proof of concept of our fit setup, we consider the example of t -channel single top-quark production and top-quark decay. This set of processes has the benefit that only a small number of SMEFT coefficients generates leading contributions at $\mathcal{O}(\Lambda^{-2})$. However, the reasons for considering this dataset goes way beyond constructing a simple fit setup and presenting a first toy example for a global fit: Firstly, as this sector has been considered in previous analyses [18, 163, 230–232, 234–237], it gives us the opportunity to validate results from our analysis. Secondly, as the number of operators is rather small, we can study in detail the impact of quadratic terms in the EFT expansion. These are formally of higher order in the EFT expansion, $\mathcal{O}(\Lambda^{-4})$, and should give negligible contributions in regions where the EFT is valid. Finally, the dataset of single top-quark production and top-quark decay data allows to study the impact of yet undetermined correlations of uncertainties, since it covers multiple experiments as well as total rates and differential distributions. As shown recently in Ref. [279], measurements at different energies and by different energies can have sizable correlation coefficients, which have yet to be determined and included in global fits. While the determination of such correlations cannot be performed without exact knowledge of the experimental setups, it is a key task to work out how these correlations can affect the fit, and if they can safely be neglected. We demonstrate the interplay of constraints on SMEFT Wilson coefficients obtained from different datasets. Modeling BSM contributions with different parametrizations, we investigate the impact of higher-order terms in the EFT expansion on the outcome of the fit. Furthermore, we consider different scenarios for the correlation of uncertainties to study their impact on the fit results.

This chapter, which is based on Ref. [25], is organized as follows: We describe which dimension-six operators contribute to single top-quark production and top-quark decay, and identify the coefficients to be constrained in this fit in Sec. 4.1. In Sec. 4.2, we describe our fit setup. We detail on the computation of both SM and BSM contributions for observables and outline our fitting procedure. Special care is devoted to the parametrization of BSM contributions and the different correlation setups studied in this chapter. In Sec. 4.3, we present results from various fits, and show how changes in the correlation setup affect constraints on SMEFT coefficient. We summarize our results in Sec. 4.4.

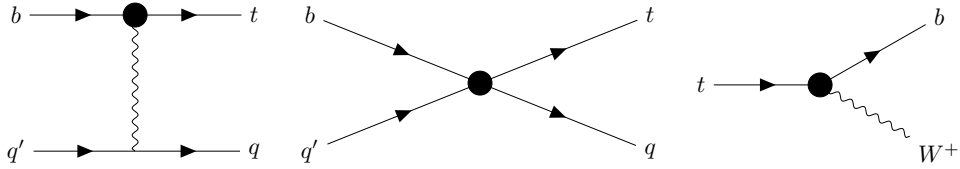


Figure 4.1: Contributions from two-fermion coefficients $\tilde{C}_{\varphi q}^{(3)}$ and \tilde{C}_{uW} (left, middle) and the four-quark coefficient \tilde{C}_{qq} to single top-quark production and top-quark decay.

4.1 Effective operators

Leading BSM contributions to single top-quark production with the SM process arise at dimension six from the following operators:

$$\begin{aligned} O_{\varphi q}^{(3)} &= i \left(\varphi^\dagger \overleftrightarrow{D}_\mu^I \varphi \right) (\bar{q}_L \gamma^\mu \tau^I q_L), & O_{uW} &= (\bar{q}_L \sigma^{\mu\nu} \tau^I u_R) \tilde{\varphi} W_{\mu\nu}^I, \\ O_{qq}^{(1)} &= (\bar{q}_L \gamma_\mu q_L) (\bar{q}_L \gamma^\mu q_L), & O_{qq}^{(3)} &= (\bar{q}_L \gamma_\mu \tau^I q_L) (\bar{q}_L \gamma^\mu \tau^I q_L), \end{aligned} \quad (4.1.1)$$

where u_R and q_L denote $SU(2)_L$ singlet and doublet quarks, respectively, of the third generation in $O_{\varphi q}^{(3)}$, O_{uW} , and first and third generation ones in $O_{qq}^{(1)}$, $O_{qq}^{(3)}$. The quark flavor is specified in the additional superscripts on Wilson coefficients in Eq. (4.1.2). In this analysis, three linear combinations of coefficients can be constrained:

$$\tilde{C}_{\varphi q}^{(3)}, \quad \tilde{C}_{uW}, \quad \tilde{C}_{qq} = \tilde{C}_{qq}^{(3)1133} + \frac{1}{6} \left(\tilde{C}_{qq}^{(1)1331} - \tilde{C}_{qq}^{(3)1331} \right), \quad (4.1.2)$$

where we introduced, as is custom, the rescaled coefficients

$$\tilde{C}_i = \hat{C}_i v^2 / \Lambda^2. \quad (4.1.3)$$

Note that, as outlined in Sec. 3.2.3, we work in the up-mass basis, in which up-quark flavor and mass bases are identical, and additional CKM-matrix elements arise in interactions involving down-type quarks. In addition, O_{uW} is not hermitian, and thus \tilde{C}_{uW} can be complex valued. Since only the real part generates contributions $\mathcal{O}(\Lambda^{-2})$ to observables considered here, we make the simplifying assumption that \tilde{C}_{uW} is real. Contributions from the three coefficients to single top-quark production and top-quark decay are illustrated in Fig. 4.1.

4.2 Fit setup

In our analysis, we include data from ATLAS [280–285], CMS [286–293], CDF, and D0 [294–296], given in Tab. 4.1. Each bin of differential distributions is considered as an independent observable. In total, we include 55 measurements of 41 different observables. If differential cross sections are presented in terms of normalized distributions, we reconstruct absolute distributions by multiplying with total cross sections.

Following Eq. (3.3.1), observables such as total cross sections can be expressed as

$$\sigma = \sigma^{\text{SM}} + \sum_i \tilde{C}_i \sigma_i^{\text{int}} + \sum_{i \leq j} \tilde{C}_i \tilde{C}_j \sigma_{ij}^{\text{BSM}}, \quad (4.2.1)$$

where σ_i^{int} and σ_{ij}^{BSM} denote interference terms between SM and dimension-six operators and

Process	\sqrt{s}	Luminosity	Experiment	Observable	Reference
Single top	7 TeV	4.59 fb ⁻¹	ATLAS	$\sigma(tq/\bar{t}q), d\sigma(tq/\bar{t}q)/dp_T$	[280]
		1.17 fb ⁻¹ (μ)	CMS	$\sigma(tq + \bar{t}q)$	[286]
		1.56 fb ⁻¹ (e)	CMS	$\sigma(tq + \bar{t}q)$	[286]
Single top	8 TeV	20.2 fb ⁻¹	ATLAS	$\sigma(tq/\bar{t}q), d\sigma(tq/\bar{t}q)/dp_T$	[281]
		19.7 fb ⁻¹	CMS	$\sigma(tq/\bar{t}q/tq + \bar{t}q)$	[287]
		19.7 fb ⁻¹	CMS	$d\sigma/d y(t/\bar{t}) $	[289]
Single top	13 TeV	3.2 fb ⁻¹	ATLAS	$\sigma(tq), \sigma(\bar{t}q)$	[282]
		2.2 fb ⁻¹	CMS	$\sigma(tq/\bar{t}q/tq + \bar{t}q)$	[288]
		2.3 fb ⁻¹	CMS	$d\sigma/d y(t/\bar{t}) $	[290]
Top decay	1.96 TeV	2.7 fb ⁻¹	CDF	F_0	[294]
		8.7 fb ⁻¹	CDF	F_0	[295]
		5.4 fb ⁻¹	D0	F_0	[296]
Top decay	7 TeV	1.04 fb ⁻¹	ATLAS	F_0, F_L	[284]
		5.0 fb ⁻¹	CMS	F_0, F_L	[291]
Top decay	8 TeV	20.2 fb ⁻¹	ATLAS	Γ_t	[283]
		20.2 fb ⁻¹	ATLAS	F_0, F_L	[285]
		19.7 fb ⁻¹	CMS	F_0, F_L	[292]
Top decay	13 TeV	19.8 fb ⁻¹	CMS	F_0, F_L	[293]

Table 4.1: The experimental measurements of top-quark production and decay considered in this analysis. For both processes, we indicate the center of mass energy \sqrt{s} , the integrated luminosity, the experiment, the observables included in the analysis and the publication reference.

purely BSM terms, respectively. Using cross sections computed for different values of Wilson coefficients (4.1.2) as sampling points we perform an interpolation according to Eq. (4.2.1) to obtain numerical values for the σ_i terms. This allows us to compute a parametrization for all cross sections as a function of the three coefficients. Computations of total and differential cross sections follow the general guideline presented in Sec. D.3. We employ the `dim6top_L0` [163] *Universal FeynRules Output* (UFO) model [297] and interface it with the *Monte Carlo* (MG) generator `MadGraph5_aMC@NLO` [298]. This allows us to compute total and differential cross sections at parton level at LO QCD for different values of Wilson coefficients. As measurements in Tab. 4.1 are at parton level, a simulation of events at parton level is sufficient and neither hadronization nor detector simulation is needed. For BSM contributions, we allow for only one insertion of an effective operator at a time. For each cross section computed with `MadGraph5_aMC@NLO` we generate 50000 events. In all computations we use the `MSTW20081o` [299] *parton distribution function* (PDF) set (see also App. D.2).

In Fig. 4.2 we give examples for sampling points together with the interpolation calculated at all sampling points. Aiming to reduce the impact of higher-order QCD corrections we include NLO contributions to the SM predictions. In the case of differential distributions, we apply k -factors taken from the experimental analyses presented in Refs. [280, 281, 289, 290]. NLO corrections to total cross sections are computed in `MadGraph5_aMC@NLO` with the `MSTW2008n1o` [299] PDF set and validated with the `CT10n1o` [300] and `MNPFD23_n1o` [301] sets. The same PDF sets are used to reproduce the k -factors of the differential distributions. In the computation, renormalization and factorization scales are set to $\mu_{R,F} = m_t$ and varied in the interval $m_t/2 \leq \mu_{R,F} \leq 2m_t$ to estimate higher-order effects neglected here.

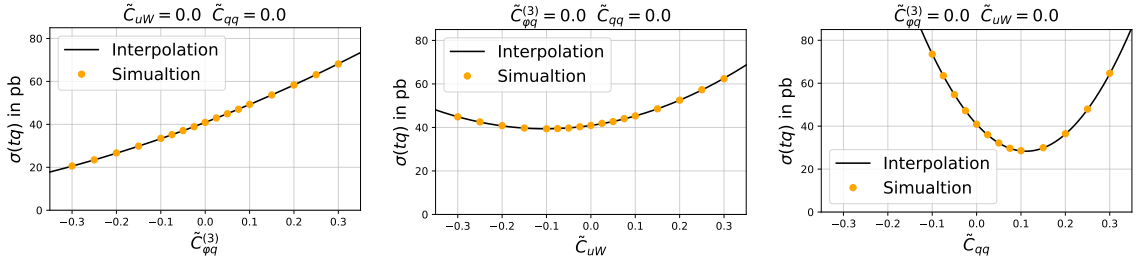


Figure 4.2: Examples for sampling points and the interpolation for the single-top productions cross section at $\sqrt{s} = 7$ TeV. We show slices of the parameter space where two coefficients are set to zero and the remaining one is varied.

The maximal variation is taken as the uncertainty. PDF uncertainties are computed within `MadGraph5_aMC@NLO` with the PDF sets mentioned previously. In our analysis, central values obtained with `MadGraph5_aMC@NLO` are considered as the theory estimate for the observables. The theory uncertainty is calculated by adding statistical, PDF uncertainties and scale variation uncertainties in quadrature.

Top-quark decay observables impose additional constraints on the Wilson coefficients considered here. We include measurements of the decay width Γ_t and the W boson helicity fractions $F_{0,L}$. We only consider operators affecting the Wtb vertex (O_{uW} and $O_{\varphi q}^{(3)}$), as contributions from four-quark operators are suppressed. Since the helicity fractions are defined as ratios and $Q_{\varphi q}^{(3)}$ simply rescales the SM contributions, the F_i depend only on contributions from \tilde{C}_{uW} . In principle, four-fermion operators can also affect $t \rightarrow bl^+\nu_\ell$ and $t \rightarrow bq\bar{q}'$ transitions. However, contributions are very small due to on-shell production of the W boson in the SM process [302]. In addition, in measurements of the helicity fractions only events where the invariant mass of the two jets or the lepton and the neutrino equals m_W are considered. This results in an additional suppressions of four-fermion operators. In our analysis, we include SM and BSM contributions at NNLO [303, 304] and LO [305], respectively. In contrast to Ref. [305], we also include quadratic contributions from \tilde{C}_{uW} to the helicity fractions F_0 and F_L .

For the fit, we employ `EFTfitter` to determine constraints on the three coefficients using a Bayesian ansatz, as described in Sec. 3.5. As a prior, we choose a uniform distribution over the interval $-1 \leq \tilde{C}_i \leq 1$. We consider three different parametrizations of BSM contributions to study the impact of higher-order EFT corrections, $\mathcal{O}(\Lambda^{-4})$, on the fit: a linear ansatz, a quadratic ansatz, and a third one called 'linear + δ_{EFT} '. In the following, we discuss each ansatz at the example of a total cross section. In the linear ansatz we parametrize BSM observables as

$$\sigma = \sigma_{\text{SM}} + \sum_i \tilde{C}_i \sigma_i, \quad (\text{'linear'}), \quad (4.2.2)$$

where we consider only LO interference terms at $\mathcal{O}(\Lambda^{-2})$ between SM and BSM and omit quadratic BSM contributions induced by dimension-six operators. The quadratic ansatz reads

$$\sigma = \sigma_{\text{SM}} + \sum_i \tilde{C}_i \sigma_i + \sum_{i \leq j} \tilde{C}_i \tilde{C}_j \sigma_{ij}, \quad (\text{'quadratic'}), \quad (4.2.3)$$

where we include the purely BSM contributions, which are formally of higher order in the EFT expansion. In the third ansatz ('linear + δ_{EFT} ') we aim at estimating the quadratic contributions neglected in the linear ansatz, and model higher order EFT effects by adding a relative uncertainty δ_{EFT} to each observable. The numerical value of this uncertainty is the measured value times $\delta_{\text{EFT}} = v^2/\Lambda^2 \sim 0.06$, where we consider $\Lambda = 1$ TeV as a conservatively small value for the scale of BSM physics.

In our fit, we consider three different types of uncertainties: statistical uncertainties, systematic uncertainties and theory uncertainties, where the first two types correspond to experimental uncertainties. In the case of statistical uncertainties, correlations arise if different observables are measured from the same dataset. For the measurements in Tab. 4.1, this is the case for differential distributions and helicity fractions. These correlations are typically provided by the experimental collaborations and can be included in the fit without further assumptions. In contrast, correlation matrices of both systematic and theory uncertainties are mostly undetermined. Due to the large number of undetermined entries in the 55×55 dimensional matrices, a simple parametrization of the correlation setup is needed to study the impact of undetermined correlations on the fit results. We model these matrices by introducing effective correlation coefficients ρ_{sys} and ρ_{th} which parametrize correlations from all sources of systematic and theory uncertainties, respectively. The exact choice of the correlation coefficients as well as the parametrization of the matrices is motivated by a recent combined analysis by ATLAS and CMS [279].

Starting with the systematic uncertainties, we expect strong correlations between measurements performed by the same experiment and at the same energy as these uncertainties are expected to stem from the same source. Therefore, we set the corresponding entries in the correlation matrix to ρ_{sys} . For measurements by the same experiment but at different energies, we expect smaller correlations of uncertainties and set the corresponding entries to $\rho_{\text{sys}}/2$. This aims at modeling changes in the detector and Monte-Carlo (MC) settings as well as energy-depend uncertainties (*e.g.* energy resolution). We consider all bins of differential distributions with the same correlation coefficient. This is a simplifying assumption since bin-to-bin migration effects can appear making the situation very complicated. A complete parametrization of these effects clearly requires input from experiments and should ideally be provided to take these effects into account. Here, we aim for a first simplistic ansatz, and thus the inclusion of bin-to-bin migration effects goes beyond the scope of this work.

Theory uncertainties are expected to be mostly independent of the experiment and to depend only on the energy of the process considered. Therefore, we correlate all measurements at the same energy with a coefficient ρ_{th} . For uncertainties of measurements at different energies, we assume a weaker correlation of $\rho_{\text{th}}/2$. This represents energy dependence in both theoretical results and MC uncertainties. We neglect a more profound energy dependence of uncertainties for the sake of a simplistic parametrization. In general, correlations of theory uncertainties depend on the energy of the collision and become weaker when the energy separation becomes larger. However, without input from the experiments it is not possible to exactly estimate this dependence. Numerically, we find that these correlations have a very small impact on the results relative to correlations of systematic uncertainties. Therefore, we simplify our ansatz by considering only two kinds of coefficients, ρ_{th} and $\rho_{\text{th}}/2$. In fits with the 'linear + δ_{EFT} ' ansatz an additional correlation matrix for the EFT uncertainties has to be considered. We use the same ansatz as for the theory uncertainties, since a similar reasoning applies, and parametrize the entries with ρ_{EFT} and $\rho_{\text{EFT}}/2$. However, note that this ansatz only parametrizes the energy dependence of the correlation coefficients and does not aim to describe correlations between observables in different physical processes. An explicit

example considering five measurements is discussed in App. E.

In contrast to the other observables, the two helicity fractions F_0 and F_L are always considered to be anticorrelated, since they are required to add up to $1 - F_R$. Because of the $V - A$ structure of the weak interactions, the SM prediction reads $F_R = 0 + \mathcal{O}(m_b^2/m_t^2)$, and contributions from O_{uW} are also suppressed by m_b^2/m_t^2 . Additional contributions from dimension-six operators not considered here are suppressed by a factor m_b/m_t . Therefore, we neglect these contributions in our fit, and consider only F_0 and F_L .

We demonstrate the impact of correlations on results of SMEFT fits by varying ρ_{sys} and ρ_{th} independently in the interval $[0, 1]$. Typically, we expect correlations to be positive but we also explore the possibility of negative values. We find that for values $\rho_{\text{sys,th}} < -0.075$ the correlation matrix remains no longer positive semi-definite, and thus do not consider this part of the parameter space in the following. While we scan the complete parameter space for the correlation coefficients we highlight two benchmark scenarios: In the first scenario, called 'no correlation' scenario, we neglect all undetermined correlations, similar Refs. [231, 233, 234]

$$\rho_{\text{sys}} = \rho_{\text{th}} = 0. \quad (\text{'no correlation'}) \quad (4.2.4)$$

The second scenario is the 'best guess' scenario with

$$\rho_{\text{sys}} = 0.9, \quad \rho_{\text{th}} = 0.9, \quad (\text{'best guess'}). \quad (4.2.5)$$

where we assume very strong correlations [279], similarly to Ref. [279]. In this analysis by ATLAS and CMS, correlations of systematic uncertainties between ATLAS and CMS are set to zero (except for the integrated luminosity) while correlations of theory uncertainties are assumed to be maximal. In a similar matter, we neglect correlations of systematic uncertainties between different experiments. We have checked numerically that their impact is negligible by replacing all zeros in the correlation matrices of systematic uncertainties with ρ_z and varying this parameter between $-0.25 \neq \rho_z \neq 0.25$. Shifts in the results of the 'best guess' scenario are at the level of few percent and covered by the smallest intervals containing 95% of the posterior probability.

We do not assume maximal correlation of theory uncertainties for observables measured at the same energy, because the effects of such uncertainties depend on the experiment. In particular, the exact impact depends on the detector simulation and varies between different experiments. We do not make any attempts to address the issue of EFT contributions to background processes. This topic would require a reanalysis of the data, since the measurements are performed with SM assumptions for the background processes and goes beyond the scope of this work. In order to demonstrate our parametrization, we consider in App. E an example of five measurements and present correlation matrices for all kinds of uncertainties.

4.3 Fits to data

In the following, we present constraints on the coefficients (4.1.2) obtained from fits to data in Tab. 4.1. Fits are repeated multiple times, with the quadratic ansatz (4.2.3), the linear ansatz (4.2.2), and the 'linear + δ_{EFT} ' ansatz. We consider constraints in both the 'no correlation' scenario (4.2.4) and the 'best guess' scenario (4.2.5), and compare results from both fits.

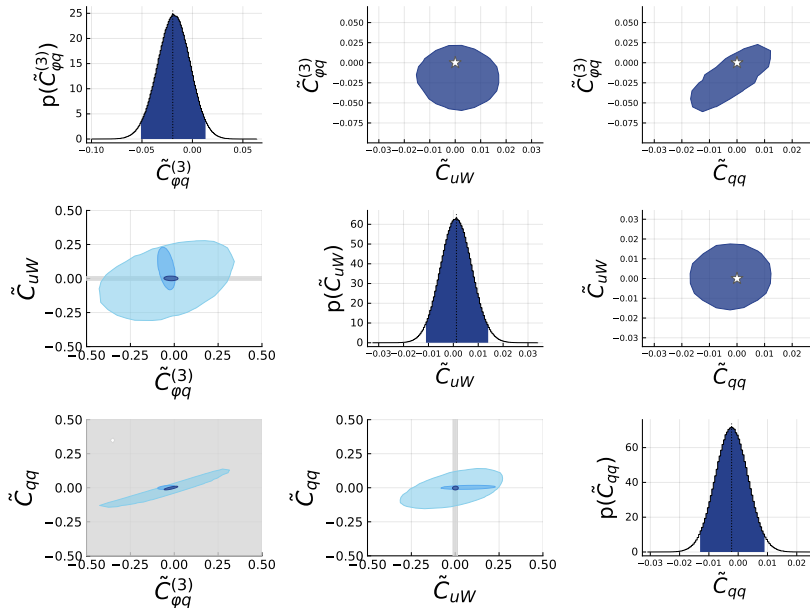


Figure 4.3: Results from the fit with the quadratic ansatz in the ‘no correlation’ scenario (4.2.4). Plots on the diagonal show the one-dimensional posterior distribution for each coefficient. Plots on the lower left show the two-dimensional posterior distributions from fits to total cross sections only (light blue), differential cross sections only (blue), helicity fractions only (grey) and the combined dataset (dark blue). Plots in the upper right show the two-dimensional posterior distributions from the fit to the combined dataset but zoomed in. Stars denote the SM point. Colored areas correspond to the smallest intervals containing 95 % of the posterior probability.

4.3.1 Constraints on Wilson coefficients

In Fig. 4.3 we show the smallest intervals containing 95 % of the posterior probability obtained in a fit with the quadratic ansatz (4.2.3) to the data in Tab. 4.1 in the ‘no correlation’ scenario (4.2.4). The different colors denote results derived from different subsets of observables. We find that the SM is included in the smallest intervals containing 95 % of the posterior probability in all projections. As shown in the three plots in the lower left, the W boson helicity fractions strongly constrain \tilde{C}_{uW} to a level of $\mathcal{O}(10^{-2})$. In contrast, $\tilde{C}_{\varphi q}^{(3)}$ and \tilde{C}_{qq} are not probed by measurements of $F_{0,L}$. Instead, these two coefficients are strongly constrained by measurements of differential cross sections, especially \tilde{C}_{qq} . This is expected since four-fermion contact interactions generate a distribution completely different from the SM one, while $\tilde{C}_{\varphi q}^{(3)}$ simply rescales the SM distribution. \tilde{C}_{qq} is constrained at the level of $\mathcal{O}(10^{-2})$, similar to \tilde{C}_{uW} . Constraints on $\tilde{C}_{\varphi q}^{(3)}$ are slightly weaker, about 5×10^{-2} . In the plots in the upper right we see that $\tilde{C}_{\varphi q}^{(3)}$ and \tilde{C}_{qq} are correlated, which stems from interference of linear contributions. We obtain very similar results for both the linear and the ‘linear + δ_{EFT} ’ ansatz, as shown in Figs. F.1 and F.2, respectively, in App. F.1.

In Fig. 4.4 we show results obtained in fits to data in Tab. 4.1 using the quadratic ansatz (4.2.3) in the ‘best guess’ scenario (4.2.5). Similarly to the ‘no correlation’ scenario, \tilde{C}_{uW} is strongly constrained at the level of $\mathcal{O}(10^{-2})$ by measurements of the helicity fractions. Results for \tilde{C}_{qq} are dominated by differential cross sections and about $\mathcal{O}(10^{-2})$. In contrast,

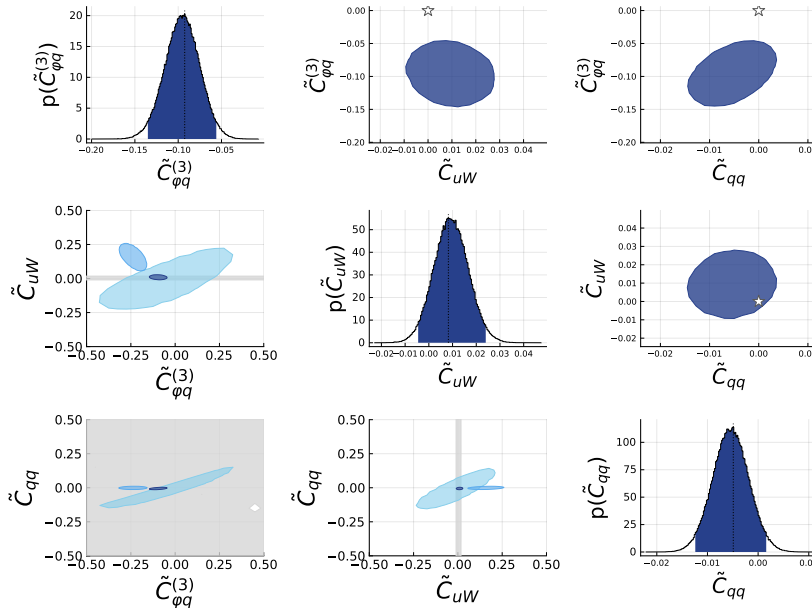


Figure 4.4: Same as Fig. 4.3, but in the 'best guess' scenario (4.2.5).

for $\tilde{C}_{\varphi q}^{(3)}$ the size of the interval is about 8×10^{-2} and the central value shows discrepancies with the SM at the level of 4.7σ . As can be seen in the two-dimensional projections, deviations stem from measurements of differential cross sections. Conversely, constraints from helicity fractions and total cross sections include the SM point. This is understood, as differential cross sections can be strongly correlated, and thus results for coefficients can change significantly depending on the correlation scenario. Similarly, in the fit to differential cross sections \tilde{C}_{uW} shows deviations from the SM, but in the combined fit helicity fractions fix \tilde{C}_{uW} to be close to the SM value. In the case of \tilde{C}_{qq} , constraints are stronger and deviations due to additional correlations are less pronounced.

Again, results with the linear and the 'linear + δ_{EFT} ' ansatz are qualitatively very similar and are shown in Figs. F.3 and F.4 in App. F.2, respectively.

In Fig. 4.5 compare results of fits in both the 'no correlation' (4.2.4) (left) and the 'best guess' scenario (4.2.5) (right) to data in Tab. 4.1 using different parametrizations of BSM contributions. Numerical values of these results are given in Tab. 4.2. The central value (*i.e.* the global mode) lies for all coefficients in the center of the intervals.

In the 'no correlation' scenario we find agreement with the SM for all three parametrizations. The linear and the quadratic ansatz give very similar results for all coefficients, while those obtained with the 'linear + δ_{EFT} ' ansatz show differences. For \tilde{C}_{qq} , this ansatz yields the same constraints as the linear and quadratic ansatz, while for \tilde{C}_{uW} the central value has a different sign and the interval is slightly larger. In general, for these two coefficients the results from all three fits are in agreement at the level of 95% intervals. In the case of $\tilde{C}_{\varphi q}^{(3)}$, constraints obtained with the 'linear + δ_{EFT} ' ansatz differ from those obtained with the linear and the quadratic ones by about 1.2σ . The central value is shifted away from the SM and the size of the interval grows.

In the 'best guess' scenario fits with the quadratic and linear ansatz show good agreement with each other. Conversely, the 'linear + δ_{EFT} ' shows differences: The intervals of \tilde{C}_{uW} and $\tilde{C}_{\varphi q}^{(3)}$ are larger, and the central value of $\tilde{C}_{\varphi q}^{(3)}$ is shifted away from the SM. For $\tilde{C}_{\varphi q}^{(3)}$, this

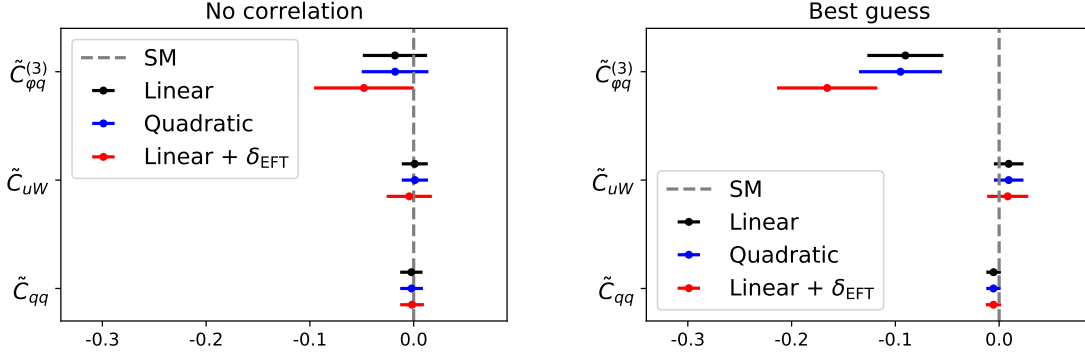


Figure 4.5: The one-dimensional posterior distribution of the coefficients \tilde{C}_i obtained in fits with the 'no correlation' scenario(4.2.4) (left) and the 'best guess' scenario (4.2.5) (right). Dots and lines denote the central value (*i.e.* the global mode) and the smallest intervals containing 95 % of the posterior probability, respectively. The SM is indicated by the vertical dashed line.

Operators	Linear	Linear + δ_{EFT}	Quadratic
'No correlation'			
$\tilde{C}_{\varphi q}^{(3)}$	[-0.049, 0.014]	[-0.096, 0.000]	[-0.050, 0.013]
\tilde{C}_{uW}	[-0.012, 0.014]	[-0.026, 0.018]	[-0.012, 0.014]
\tilde{C}_{qq}	[-0.013, 0.009]	[-0.013, 0.010]	[-0.013, 0.009]
'Best guess'			
$\tilde{C}_{\varphi q}^{(3)}$	[-0.127, -0.055]	[-0.214, -0.118]	[-0.135, -0.056]
\tilde{C}_{uW}	[-0.011, 0.029]	[-0.012, 0.029]	[-0.005, 0.024]
\tilde{C}_{qq}	[-0.012, 0.002]	[-0.013, 0.002]	[-0.012, 0.002]

Table 4.2: Marginalized smallest intervals containing 95 % of the posterior probability obtained in fits in the 'no correlation' scenario Eq. (4.2.4) and the 'best guess' scenario Eq. (4.2.5) to the data in Tab. 4.1 shown in Fig. 4.5. The central value is in the center of these intervals.

results in deviations from the other two parametrizations of about 3σ . This shows that for both correlation scenarios the quadratic terms are only a subleading source of uncertainty in the fit, and that an overall EFT uncertainty overestimates their impact.

Comparing results in the 'no correlation' scenario with those in the 'best guess' scenario we find that correlations have a significant impact on results of the fit. For \tilde{C}_{qq} , correlations affect the constraints only slightly by shifting the central value towards negative values and shrinking the size of the interval. Similarly, additional correlations shift the central value of \tilde{C}_{uW} slightly towards positive values. While these two coefficients are less affected, and results in the 'best guess' scenario still show good agreement with those in the 'no correlation' scenario, we find significant changes in the case of $\tilde{C}_{\varphi q}^{(3)}$. In all three BSM parametrizations the central value is shifted away from the SM towards negative values while the width of the interval grows by about 10 %. This results in deviations of about 4.7σ (linear/quadratic) and 6.6σ ('linear + δ_{EFT} '). The aforementioned differences can be understood as follows:

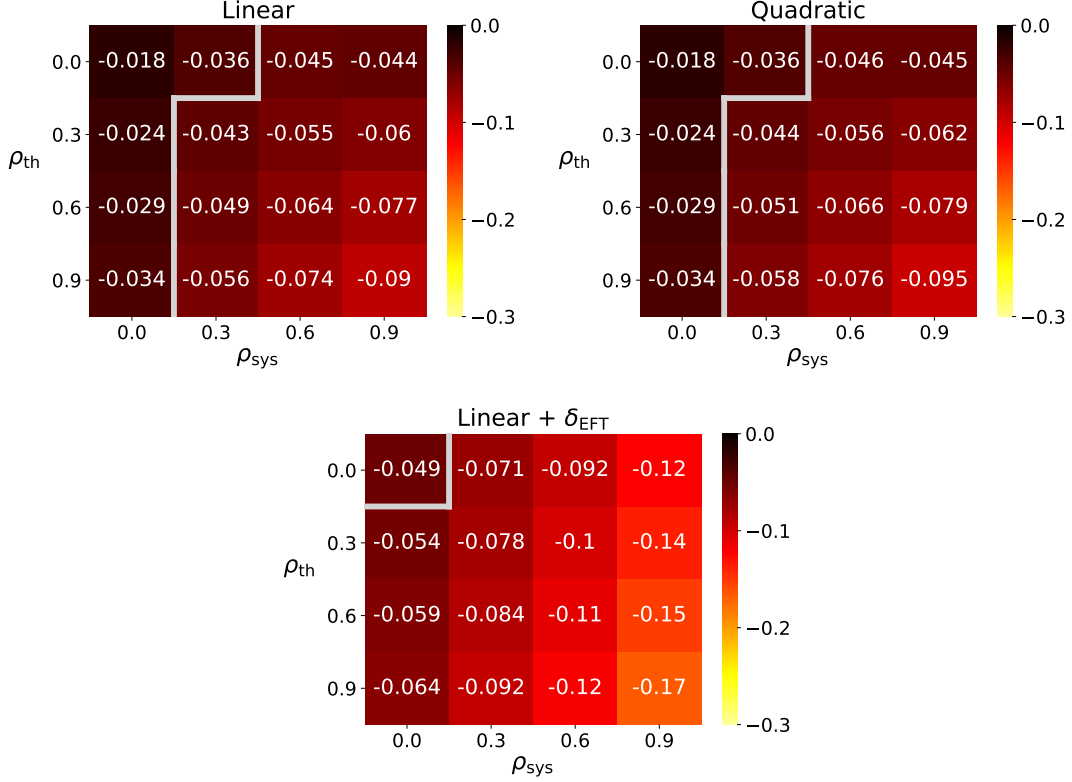


Figure 4.6: Central values of $\tilde{C}_{\varphi q}^{(3)}$ for correlation parameters $\rho_{\text{sys}}, \rho_{\text{th}} = 0.0, 0.3, 0.6, 0.9$ in the three EFT-implementations from a fit to the data given in Tab. 4.1. We vary both correlation parameters independently of each other. The upper-left and lower-right corner correspond to the 'no correlation' (4.2.4) and the 'best guess' scenario (4.2.5), respectively. Central values below and to the right of the grey line are in conflict with the SM at more than 2σ .

Large discrepancies in $\tilde{C}_{\varphi q}^{(3)}$ stem from differential cross sections, as shown in Fig. 4.4. In contrast, considering \tilde{C}_{uW} we find that the intervals are only slightly shifted away from the SM towards positive values, since helicity fractions strongly impose strong constraints. Finally, the shrinking of the interval of \tilde{C}_{qq} is understood, because additional correlations deform the posterior distribution in the three-dimensional parameter space: while the intervals for $\tilde{C}_{\varphi q}^{(3)}$ and \tilde{C}_{uW} grow, the interval for C_{qq} shrinks; an effect which typically arises when correlations are included.

Exploring the parameter space of the correlation coefficients ρ_{sys} and ρ_{th} beyond the two benchmark scenarios, we give in Fig. 4.6 the central value of $\tilde{C}_{\varphi q}^{(3)}$ for different values $\rho_{\text{sys}}, \rho_{\text{th}} = 0.0, 0.3, 0.6, 0.9$. We consider only this coefficient, since it shows by far the strongest effects when additional correlations are turned on. Over the range of the different correlation coefficients the size of the 95% interval varies by a factor of up to 1.5, which we do not show for the sake of legibility. Instead, we indicate with a grey line central values which deviate by more than 2σ from the SM. The linear and quadratic BSM parametrizations show very similar results. Increasing values of the ρ_i leads to stronger deviations from the SM. In

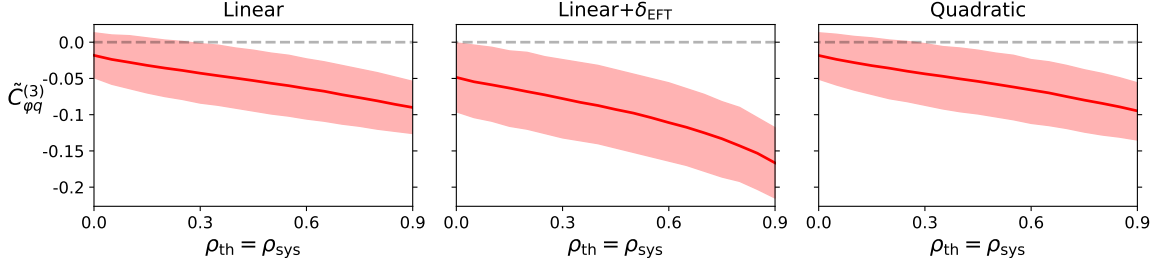


Figure 4.7: Central values (red line) and 95% intervals (red band) of $\tilde{C}_{\varphi q}^{(3)}$ in the different EFT-implementations for correlation parameters $\rho_{\text{sys}} = \rho_{\text{th}} \in [0, 0.9]$ from a fit to the data given in Tab. 4.1.

the 'linear + δ_{EFT} ' scenario we find the same behavior but deviations from the SM are more pronounced and all values besides $\rho_{\text{sys}} = \rho_{\text{th}} = 0$ do not agree with the SM at the 2σ level. Comparing both kinds of uncertainties we find that correlations of systematic uncertainties have a larger impact on the results of the fit. This can be seen by considering $\rho_{\text{sys}} = 0$, where we find for all four values of ρ_{th} agreement with the SM. In contrast, for $\rho_{\text{th}} = 0$ the central value deviates by more than 2σ from the SM for $\rho_{\text{sys}} \geq 0.6$. In general, deviations from the SM are stronger for rising values of ρ_{sys} than for ρ_{th} , as indicated by the central values.

Considering the main diagonal of the heatmaps in more detail, we give in Fig. 4.7 the central value of $\tilde{C}_{\varphi q}^{(3)}$ for $\rho_{\text{sys}} = \rho_{\text{th}}$ varied in the interval $[0, 0.9]$. Over the whole range we see a consistent and continuous behavior where stronger correlations lead to stronger deviations from the SM.

Within our parametrizations of correlation matrices larger values of the correlation coefficients lead to stronger deviations from the SM. The strongest deviations can be found in the 'best guess' scenario. To validate our results, we alter the 'best guess' scenario by adding uniformly distributed random numbers u with $|u| \leq 0.03$ to all non-zero entries in the correlation matrices. We vary each element individually requiring the matrices to remain positive semi-definite, and perform 1000 fits to the data in Tab. 4.1. The results obtained in fits with the linear BSM implementation are shown as histograms in Fig. 4.8 for $\tilde{C}_{\varphi q}^{(3)}$. We find that the distribution of the central value is symmetric and slightly shifted towards values closer to the SM with a clear peak close to the result of the 'best guess scenario'. In the case of the width of the interval, the distribution is asymmetric favoring smaller values and the peak is slightly shifted away from the 'best guess' scenario towards smaller intervals. Both distributions show a sharp peak around the values of the best 'best guess' scenario, indicating that our fit is stable against small perturbations. Very similar results are obtained for the quadratic and 'linear + δ_{EFT} ' parametrizations and are not shown.

To summarize, correlations among uncertainties alter the results of the fit. For \tilde{C}_{uW} and \tilde{C}_{qq} effects are small, and shifts in the central value are covered by the smallest intervals containing 95% of the posterior probability. In contrast, shifts in $\tilde{C}_{\varphi q}^{(3)}$ are significantly larger: we found agreement with the SM in the 'no correlation' scenario, but strong deviations of about 4.7σ (linear and quadratic fit) and 6.6σ ('linear + δ_{EFT} ') arise in the 'best guess' scenario due to strong correlations among differential cross sections. While we consider large values $\rho_i = 0.9$ in the 'best guess' scenario (4.2.5), discrepancies larger than 2σ arise already for fairly small values $\rho_i \sim 0.3$ (see Fig. 4.7). Lastly, from the various fits considered here

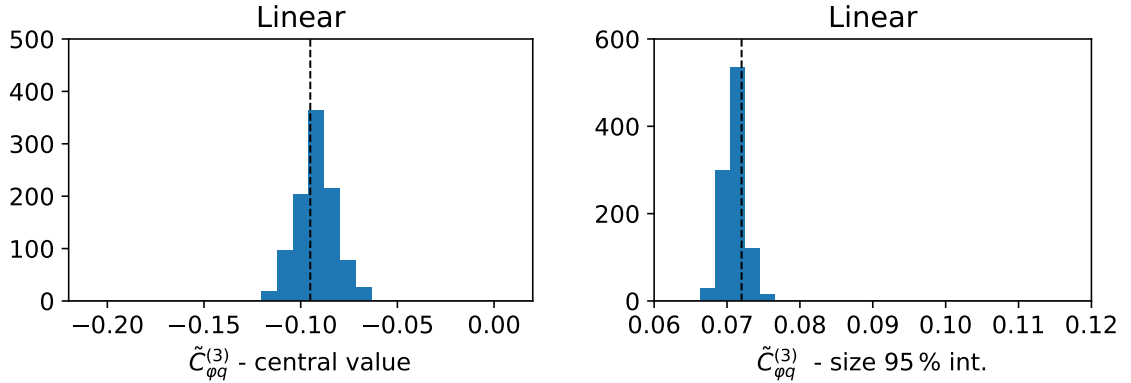


Figure 4.8: Histograms of the central value and the size of the smallest intervals containing 95 % of the posterior probability of $\tilde{C}_{\varphi q}^{(3)}$ for correlation parameters varied randomly around the 'best guess' scenario from a fit to data given in Tab. 4.1. Black lines denote results from the 'best guess' scenario in Eq. (4.2.5). We show as an example results in the linear EFT-implementation.

we learn that quadratic and linear parametrizations of BSM contributions give very similar results indicating that quadratic dimension-six contributions are indeed a subleading source of uncertainty, as expected in regions where the EFT expansion is valid. Conversely, the 'linear + δ_{EFT} ' with a relative uncertainty of $\sim 6\%$ clearly overestimates the effect of quadratic terms.

4.3.2 Comparison to literature

To validate our results in the different BSM parametrizations, we compare constraints obtained in fits with the 'no correlation' scenario to a recent global SMEFT analysis [237], in which 95 % confidence level intervals (CL) from a fit to single top-quark production and top-quark decay data are derived for the coefficients in Eq. (4.1.2). The dataset used in Ref. [237] is comparable to our set in Tab. 4.1 but differs in two points: differential cross sections of single-top production are not considered, and additional s -channel, tW -channel, and tZ -channel cross sections are included in Ref. [237]. In addition, NLO QCD corrections are included for the BSM contributions while we compute them at LO. In order to compare the results of this analysis with ours, we repeat our fits in the 'no correlation' scenario without including differential cross sections. However, note that smallest intervals containing 95 % of the posterior probability in a Bayesian fit do not necessarily agree with 95 % confidence level intervals, as they are obtained using different statistical frameworks. Nevertheless, we expect them to give at least comparable results regarding the order of magnitude.

Results from both the analysis in Ref. [237] and our fits are shown in Tab. 4.3. Note that constraints in Ref. [237] are derived employing a quadratic ansatz. In contrast, we show results within all three parametrizations of BSM physics and find that they are in good agreement with each other, especially when comparing the linear and quadratic ansatz. For all three coefficients, we find that the intervals are almost symmetric around the SM value, except for \tilde{C}_{uW} in the 'linear + δ_{EFT} ' scenario. Here, the interval is shifted towards negative values and is larger by about 50 % compared to the other scenarios due the additional EFT

Operators	95 % CL [237]	Linear	Linear + δ_{EFT}	Quadratic
$\tilde{C}_{\varphi q}^{(3)}$	[-0.29, 0.081]	[-0.30, 0.27]	[-0.30, 0.28]	[-0.33, 0.25]
\tilde{C}_{uW}	[-0.029, 0.029]	[-0.013, 0.013]	[-0.029, 0.015]	[-0.013, 0.013]
\tilde{C}_{qq}	[-0.031, 0.0069]	[-0.115, 0.095]	[-0.12, 0.095]	[-0.112, 0.090]

Table 4.3: Constraints on the coefficients in Eq. (4.1.2) presented as 95 % confidence levels from Ref. [237] from a fit to single top-quark total cross sections and top-quark decay data together with the smallest intervals containing 95 % of the posterior probability obtained in fits in the ‘no correlation’ scenario (4.2.4) to the data in Tab. 4.1 excluding differential cross sections.

uncertainties and their correlations. In case of the helicity fractions $F_{0,L}$, which yield strong constraints on \tilde{C}_{uW} , this additional uncertainty can be larger than both experimental and SM theory uncertainties. Thus, it can dominate the total uncertainty, which is the case for measurements in Refs. [285, 292, 293].

Comparing results obtained in our fits to those derived in Ref. [237] we find differences for all three coefficients, but overall the results are in reasonable agreement. For $\tilde{C}_{\varphi q}^{(3)}$ the 95 % CL in Ref. [237] is both antisymmetric favoring negative values (similar to results in our best-guess scenario) while the size of the interval is smaller by about 35 % compared to our results. As $\tilde{C}_{\varphi q}^{(3)}$ rescales the SM, we expect that additional NLO QCD corrections have a very strong impact on constraints on this coefficient. In addition, this coefficient also contributes to observables from s -channel single top-quark production. Constraints on \tilde{C}_{uW} in Ref. [237] are weaker by a factor of two compared to our results. This can be explained by the additional measurements of the helicity fractions included in our analysis, namely those by CDF, DO and CMS. In particular, we find that the measurement by CMS in Ref. [293] imposes strong constraints. Excluding these measurements from our fit with the quadratic ansatz we obtain an interval about 50 % larger than the one reported in Tab. 4.3. Considering constraints on \tilde{C}_{qq} we find that results in Ref. [237] are stronger by a factor of five relative to ours. However, in Ref. [237] a global $U(2)_q \times U(2)_u \times U(2)_d$ symmetry for the first two generations is assumed, and thus contributions from second-generation quarks are included in \tilde{C}_{qq} . In contrast, in our analysis we only consider couplings to first-generation quarks. In addition, s -channel observables are very sensitive to contributions from \tilde{C}_{qq} due to an energy enhancement when compared to the t -channel process [237]. The additional QCD corrections also affect the constraints on this coefficient. In total, we expect that these reasons explain the stronger constraints reported in Ref. [237].

Overall, results from our fit and results in Ref. [237] show reasonable agreement. Differences can be explained by additional s -channel observables and NLO QCD corrections considered in Ref. [237], the additional measurements of the helicity fractions, and the overestimated BSM contributions in our ‘linear + δ_{EFT} ’ scenario. Note again that we did not expect to find exactly the same results as we are comparing the smallest intervals containing 95 % of the posterior probability obtained in a Bayesian fit with 95 % confidence-level limits.

4.3.3 Future scenarios

As shown in Fig. 4.5 correlations have a major impact on the results. At future experiments theoretical and systematic uncertainties and their correlations will become even more important since statistical uncertainties will be further suppressed at higher integrated luminosity.

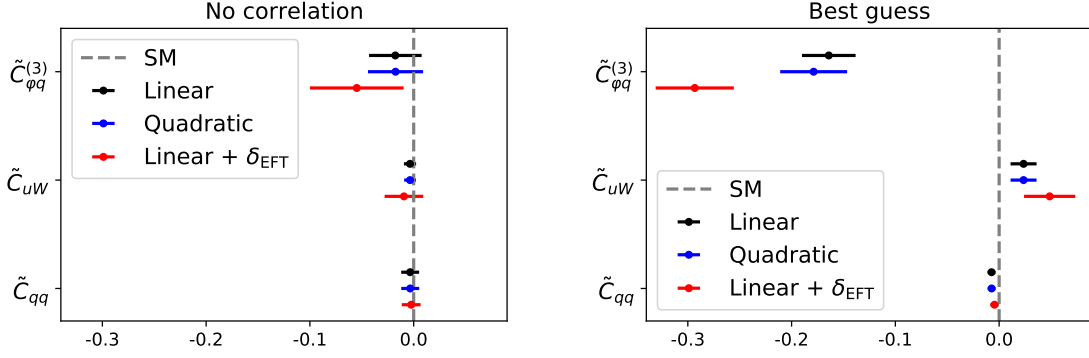


Figure 4.9: Same as Fig. 4.5, but with statistical uncertainties of the data in Tab. 4.1 scaled to 300 fb^{-1} and assuming present central values, systematic uncertainties and theory uncertainties.

Operators	Linear	Linear + δ_{EFT}	Quadratic
'No correlation'			
$\tilde{C}_{\varphi q}^{(3)}$	$[-0.043, 0.009]$	$[-0.100, -0.012]$	$[-0.044, 0.009]$
\tilde{C}_{uW}	$[-0.009, 0.002]$	$[-0.028, 0.010]$	$[-0.009, 0.002]$
\tilde{C}_{qq}	$[-0.012, 0.005]$	$[-0.012, 0.007]$	$[-0.012, 0.005]$
'Best guess'			
$\tilde{C}_{\varphi q}^{(3)}$	$[-0.190, -0.138]$	$[-0.331, -0.256]$	$[-0.211, -0.148]$
\tilde{C}_{uW}	$[0.011, 0.036]$	$[0.024, 0.074]$	$[0.011, 0.036]$
\tilde{C}_{qq}	$[-0.011, -0.004]$	$[-0.009, 0.000]$	$[-0.011, 0.004]$

Table 4.4: Results from fits in the 'no correlation' scenario Eq. (4.2.4) and the 'best guess' scenario Eq. (4.2.5) to the data in Tab. 4.1 with statistical uncertainties scaled to 300 fb^{-1} (see Fig. 4.9). Constraints are shown as smallest intervals containing 95 % of the posterior probability obtained in fits within the different parametrizations of BSM contributions. The central value is in the center of these intervals.

To demonstrate this, we repeat the fit to the data in Tab. 4.1 but scale all statistical uncertainties according to the luminosity of two future scenarios: LHC Run 3 and *High-Luminosity* (HL-)LHC with integrated luminosities of 300 fb^{-1} and 3000 fb^{-1} [306], respectively. Results are shown in Fig. 4.9 for the 300 fb^{-1} scenario, with numerical values given in Tab. 4.4. We find that constraints become stronger when changing the luminosity of the measurements in Tab. 4.1 from up to 20 fb^{-1} to 300 fb^{-1} and scaling statistical uncertainties accordingly. Increasing the luminosity further by one order of magnitude does not improve the constraints significantly (see Fig. F.5 in App. F.3) as systematic and theory uncertainties already dominate at 300 fb^{-1} . Numerically, constraints on all coefficients are the same up to percent level when comparing results with 300 fb^{-1} with those from 3000 fb^{-1} in the 'no correlation' scenario. In the 'best guess' scenario the results change by up to 5 % for $\tilde{C}_{\varphi q}^{(3)}$ and up to 15 % for \tilde{C}_{uW} and \tilde{C}_{qq} . The only exception is the 'linear + δ_{EFT} ' scenario, where we find larger changes for \tilde{C}_{uW} , see App. F.3. In the light of higher integrated luminosity results for the three coefficients depend strongly on the correlation scenario, even more than in fits to present data. In the 'no correlation' scenario the constraints remain almost the same: Compared to

Fig. 4.5 central values are slightly shifted while the size of the intervals shrinks by a factor of 1.2, 3, and 1.3 for $\tilde{C}_{\varphi q}^{(3)}$, \tilde{C}_{uW} , and \tilde{C}_{qq} , respectively. In contrast, in the 'best guess' scenario $\tilde{C}_{\varphi q}^{(3)}$, \tilde{C}_{uW} , and \tilde{C}_{qq} deviate from the SM by up to 3.8σ (4σ), 5σ (5σ), and about 12.5σ (16.0σ) in the linear and quadratic ('linear + δ_{EFT} ') fit, respectively.

To further estimate the impact of correlations in the light of higher integrated luminosities we repeat the analysis in Fig. 4.6 and vary the two correlation parameters independently in the interval $\rho_{\text{sys}}, \rho_{\text{th}} = 0.0, 0.3, 0.6, 0.9$. Again, we find that correlations of systematic uncertainties have a stronger impact on the results of the fit than correlations of theory uncertainties. The heatmaps are shown in App. F.3.

4.4 Summary

In this chapter, we performed a global fit to the top-quark sector of SMEFT considering t -channel single top-quark production and top-quark decay. We have detailed both our procedure to compute BSM contributions to cross sections at the LHC as well as angular distributions, *i.e.* the W boson helicity fractions, and outlined the setup of our fitting procedure. Going beyond a simple first toy example for our fitting procedure, we studied in detail the impact of higher-order corrections, $\mathcal{O}(\Lambda^{-4})$, in the EFT expansion on the constraints on Wilson coefficients employing three different parametrizations: a linear ansatz (4.2.2) including only interference terms at $\mathcal{O}(\Lambda^{-2})$ between SM and BSM contributions, a quadratic ansatz, in which we also consider purely BSM contributions $\tilde{C}_i \tilde{C}_j$, and a third ansatz ('linear + δ_{EFT} '), in which we model higher order corrections with an additional relative uncertainty $\delta_{\text{EFT}} = (v/1 \text{ TeV})^2$. We found that both the linear and quadratic ansatz give almost identical results. Conversely, the 'linear + δ_{EFT} ' ansatz yields deviations from the other two scenarios, see Fig. 4.5. This indicates that quadratic contributions from dimension-six operators are indeed negligible, and that an additional EFT uncertainty overestimates their impact.

Going beyond present global fits available in literature, the dataset of single top-quark production and top-quark decay observables gave us the opportunity to investigate the impact of yet undetermined correlations of measurements on results of global fits. To do so, we parametrized corresponding correlation matrices using two parameters: ρ_{sys} and ρ_{th} for correlations of systematic experimental and theory uncertainties, respectively. Studying the concrete examples of two benchmark scenarios with either vanishing ('no correlation' (4.2.4)) or strong ('best guess' (4.2.5)) correlations, we saw that correlations can alter results significantly. While we found agreement with the SM in the 'no correlation' scenario, one coefficient, $\tilde{C}_{\varphi q}^{(3)}$, showed deviations of about 5σ from the SM in the 'best guess' scenario, see Fig. 4.5. We further investigated these effects in the context of higher integrated luminosity experiments, scaling present data according to the expected integrated luminosities of 300 fb^{-1} (LHC Run 3) 3000 fb^{-1} (HL-LHC). In these projections, even stronger deviations of up to 16σ from the SM are present.

Our findings highlight the importance of opening new ways to improve fits to the top-quark sector of SMEFT by linking it to beauty physics, even without considering the presence of the flavor anomalies. In Chapter 5, we explore implications of a combined fit of top-quark and B -physics data in the SMEFT framework and investigate the feasibility of this approach.

5 Exploring combinations of top and beauty

As we saw in Chapter 4, global fits to the top-quark sector of SMEFT allow to search for BSM signatures in top-quark data in a model-independent and systematic way. However, applying the SMEFT framework goes way beyond fits to a single sector of physics, and additional constraints on effective operators with third-generation up-type quarks arise from processes involving beauty quarks [222, 307, 308]. In particular, FCNCs like $b \rightarrow s$ transitions allow to test BSM physics with high precision [121–127] since they are suppressed in the SM by the Fermi constant, small CKM matrix elements, and loop-factors. As we saw in Sec. 4.3, including additional uncorrelated observables and measurements in the fit is desired to reduce the impact of undetermined correlations. This alone already motivates the inclusion of additional observables from beauty physics. However, the inclusion of $b \rightarrow s$ data has an even stronger physical motivation, which goes way beyond simply making global fits more model-independent: Present data hints at anomalies in the B -physics sector, see Sec. 2.3.3, as well as in interactions of beauty quarks with Z bosons [309], indicating that the third generation might be special, and that charged leptons might not be as equal as assumed in the SM [310].

In this chapter, which is based on Ref. [23], we perform a first combined fit to top-quark and B -physics data at the example of $t\bar{t}\gamma$ cross section and $\bar{B} \rightarrow X_s \gamma$ branching ratio measurements. In the following, we present the steps necessary for a combined fit of BSM contributions to top-quark interactions. We highlight possible pitfalls of the procedure and provide a detailed analysis of the dependence of the observables on the Wilson coefficients. To do so, we introduce in Sec. 5.1 the SMEFT operators considered in this analysis. In Sec. 5.2, we detail on the matching of the SMEFT Lagrangian onto the WET Lagrangian, which is employed to parametrize SM and BSM contributions to B -physics observables. In Sec. 5.3, we present the measurements included in the fit. We discuss the computation of the theory predictions in Sec. 5.4. The results of the fit to the different observables are discussed in detail in Sec. 5.5. In Sec. 5.6, we summarize our findings.

5.1 Effective theories at different scales

In order to derive constraints on SMEFT coefficients from measurements of observables below the EW scale μ_W , different EFTs have to be employed and linked with each other. In the following, we identify dimension-six operators relevant for $t\bar{t}\gamma$ production and describe the EFT approach used to describe $b \rightarrow s$ transitions in terms of SMEFT coefficients.

In Fig. 5.1 we give examples for Feynman diagrams for $t\bar{t}\gamma$ production in the SM (top row) and including insertions of an effective operator (bottom row). We consider only operators involving third generation quarks and bosonic fields affecting the $t\bar{t}\gamma$ production:

$$\begin{aligned}
 O_{uB} &= (\bar{q}_L \sigma^{\mu\nu} u_R) \tilde{\varphi} B_{\mu\nu}, \\
 O_{uG} &= (\bar{q}_L \sigma^{\mu\nu} T^A u_R) \tilde{\varphi} G_{\mu\nu}^A, \\
 O_{uW} &= (\bar{q}_L \sigma^{\mu\nu} \tau^I u_R) \tilde{\varphi} W_{\mu\nu}^I.
 \end{aligned}
 \tag{5.1.1}$$

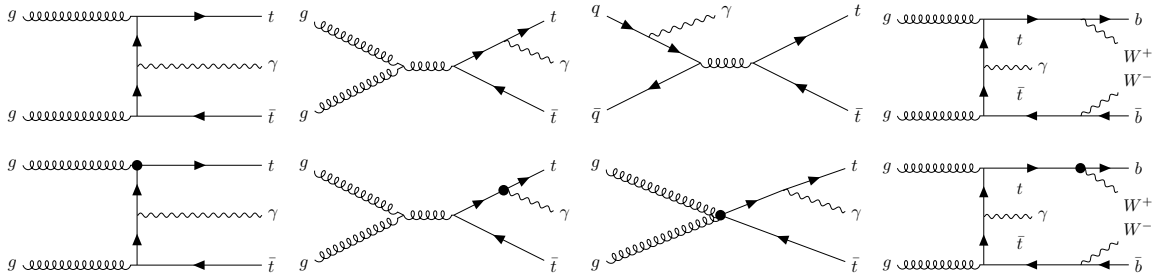


Figure 5.1: Examples for lowest order Feynman diagrams contributing to $t\bar{t}\gamma$ production in pp -collisions in the SM (upper row) and including dimension-six operators (lower row). We denote insertion of an effective operator from Eq. (5.1.1) with a black dot.

The operator O_{uW} has already been defined in Eq. (4.1.1) and is given here for the sake of completeness. Contributions from dipole operators with right-handed b quarks are suppressed by a factor of m_b/m_t compared to those with right-handed top-quark fields. Therefore, we neglect contributions from down-type dipole operators in this analysis. Since all operators in Eq. (5.1.1) are non-hermitian, the corresponding Wilson coefficients can be complex valued. However, only the real part can contribute to the observables at $\mathcal{O}(\Lambda^{-2})$, and thus we assume all coefficients to be real for simplicity. In principle, four-quark operators can also affect $t\bar{t}\gamma$ productions via diagrams similar to the third diagram in the second row in Fig. 5.1 replacing gluons with a quark and an antiquark. At the LHC, $t\bar{t}$ production is dominated by the gluon-gluon channel (75% at 8 TeV and 90% at 13 TeV [231]), and thus we neglect contributions from four-fermion operators. Note that we explicitly allow for BSM contributions to the top-quark decay¹ from O_{uW} (see Fig. 5.1).

As described in Sec. 3.1, to describe both SM and BSM physics at energies below $\mu_W \sim m_W$ a low-energy EFT is used, which parametrizes possible BSM deviations in effective operators invariant under the $SU(3)_C \times U(1)_Q$ gauge group. In our analysis, we consider contributions of operators (5.1.1) to $b \rightarrow s\gamma$ transitions. Therefore, the SMEFT operators have to be matched onto the WET Lagrangian in Eq. C.1.1 in App. C. Here, we neglect contributions suppressed by small CKM matrix elements V_{ub} as well as the strange-quark mass.

5.2 Matching at the electroweak scale

SMEFT contributions to physics below the electroweak scale μ_W are described by matching the SMEFT Lagrangian onto the WET Lagrangian. The general procedure for a combined analysis of top-quark and B measurements is visualized in Fig. 5.2. SMEFT Wilson coefficients at the scale $\mu_t \sim m_t$ are constrained by top-quark measurements. Similarly, WET coefficients are constrained by B measurements at the scale $\mu_b \sim m_b$. In order to translate these results into constraints on SMEFT Wilson coefficients, three steps have to be performed, extending the formalism described in Ref. [221]: Firstly, the SMEFT RGEs are employed to evolve SMEFT Wilson coefficients from the scale μ_t to the scale μ_W . Secondly, the SMEFT Lagrangian is matched onto the WET Lagrangian. As a last step, WET RGE evolution from the scale μ_W to μ_b is performed. This procedure allows to express BSM contributions to WET coefficients at the scale μ_b in terms of SMEFT coefficients $C_i(\mu_t)$ at the scale μ_t . With

¹The operator $O_{\varphi q}^{(3)}$ can generate BSM contributions only to the top-quark decay and is neglected here because this operator merely rescales the SM decay width without changing angular distributions.

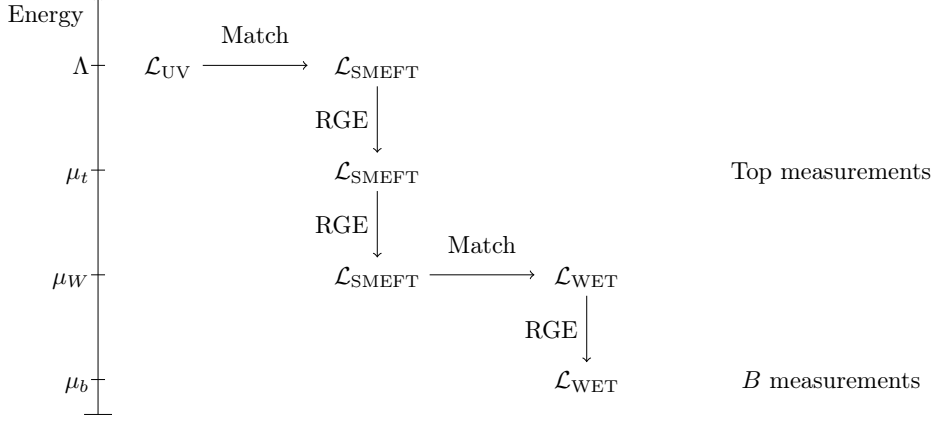


Figure 5.2: Illustration of the energy scales, effective theories and measurements relevant for the combined analysis of top-quark and B measurements. At the high energy scale Λ , the UV theory is matched onto the SMEFT Lagrangian. Measurements of the top quark are described by evolving the dimension-six Wilson coefficients in \mathcal{L}_{SMEFT} to the scale $\mu_t \sim m_t$ using the SMEFT RGEs. For comparison with measurements of B physics, the SMEFT is matched onto the WET at the scale $\mu_W \sim m_W$. To describe BSM contributions to B -physics measurements at the scale $\mu_b \sim m_b$ the WET coefficients are evolved using the WET RGEs.

this, BSM contributions to observables such as $\text{BR}(\bar{B} \rightarrow X_s \gamma)$ can be parametrized using SMEFT Wilson coefficients $C_i(\mu_t)$.

In order to describe the running and mixing of the operators in Eq. (5.1.1) we include the following operators:

$$O_{u\varphi} = \left(\varphi^\dagger \varphi\right) (\bar{q}_L u_R \tilde{\varphi}), \quad O_{\varphi G} = \left(\varphi^\dagger \varphi\right) G_{\mu\nu}^A G^{A\mu\nu}, \quad O_{\varphi\tilde{G}} = \left(\varphi^\dagger \varphi\right) \tilde{G}_{\mu\nu}^A G^{A\mu\nu}. \quad (5.2.1)$$

To identify LO contributions at $\mathcal{O}(\alpha_s)$ in the ADM we rescale the coefficient according to the procedure described in Sec. 3.2.1:

$$\begin{aligned} O'_{uB} &= yg' (\bar{q}_L \sigma^{\mu\nu} u_R) \tilde{\varphi} B_{\mu\nu}, & O'_{uW} &= yg (\bar{q}_L \sigma^{\mu\nu} \tau^I u_R) \tilde{\varphi} W_{\mu\nu}^I, \\ O'_{uG} &= yg_s (\bar{q}_L \sigma^{\mu\nu} T^A u_R) \tilde{\varphi} G_{\mu\nu}^A, & O'_{\varphi G} &= g_s^2 \left(\varphi^\dagger \varphi\right) G_{\mu\nu}^A G^{A\mu\nu}, \\ O'_{u\varphi} &= y \left(\varphi^\dagger \varphi\right) (\bar{q}_L u_R \tilde{\varphi}), & O'_{\varphi\tilde{G}} &= g_s^2 \left(\varphi^\dagger \varphi\right) \tilde{G}_{\mu\nu}^A G^{A\mu\nu}. \end{aligned} \quad (5.2.2)$$

Similarly, the Wilson coefficients are rescaled with inverse powers of the couplings. We can now write the RGE at LO as [188–192]

$$\frac{d}{d \ln \mu} \begin{pmatrix} C'_{uG} \\ C'_{uW} \\ C'_{uB} \\ C'_{u\varphi} \\ C'_{\varphi G} \\ C'_{\varphi\tilde{G}} \end{pmatrix} = \frac{\alpha_s}{4\pi} \frac{4}{3} \begin{pmatrix} 1 & 0 & 0 & 0 & -3 & -3i \\ 2 & 2 & 0 & 0 & 0 & 0 \\ \frac{10}{3} & 0 & 2 & 0 & 0 & 0 \\ -24 & 0 & 0 & -6 & 0 & 0 \\ 0 & 0 & 0 & 0 & 0 & 0 \\ 0 & 0 & 0 & 0 & 0 & 0 \end{pmatrix} \begin{pmatrix} C'_{uG} \\ C'_{uW} \\ C'_{uB} \\ C'_{u\varphi} \\ C'_{\varphi G} \\ C'_{\varphi\tilde{G}} \end{pmatrix} = \frac{\alpha_s}{4\pi} \gamma^{(0)} \begin{pmatrix} C'_{uG} \\ C'_{uW} \\ C'_{uB} \\ C'_{u\varphi} \\ C'_{\varphi G} \\ C'_{\varphi\tilde{G}} \end{pmatrix}. \quad (5.2.3)$$

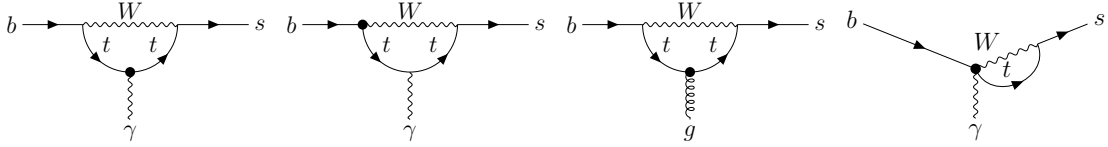


Figure 5.3: Examples of one-loop diagrams for $b \rightarrow s\gamma$ and $b \rightarrow sg$ transitions. Black dots denote the insertion of a SMEFT operator.

Note that $\gamma^{(0)}$ is not closed: both $O'_{\varphi G}$ and $O'_{\varphi \tilde{G}}$ give mixing contributions to the running of

$$O'_{dG} = yg_s (\bar{q}_L \sigma^{\mu\nu} T^A d_R) \varphi G_{\mu\nu}^A, \quad (5.2.4)$$

while O'_{uG} contributes to

$$O'_{quqd}^{(1)} = (q_L^i u_R) \epsilon_{ij} (q_L^j d_R), \quad O'_{quqd}^{(8)} = (q_L^i T^A u_R) \epsilon_{ij} (q_L^j T^A d_R), \quad (5.2.5)$$

where i, j are isospin indices. The corresponding entries in the ADM are neglected here as they are suppressed by small down-type Yukawa couplings. In addition, we see from Eq. (5.2.3) that $C'_{\varphi G}$ and $C'_{\varphi \tilde{G}}$ do not run at $\mathcal{O}(\alpha_s)$. As these operators have no sizable effect on the observables considered here [231], we assume them to be vanishing and consider only effective operators including a top quark. Similarly, the operator $O'_{u\varphi}$ does not generate phenomenologically relevant contributions to the observables. In NLO calculations this operator has to be included to absorb UV divergences in top-quark mass corrections stemming from O'_{uG} [302]. Since we consider SMEFT contributions at LO only, we neglect $O'_{u\varphi}$ in the following. The RGE are solved following the algorithm in App. B.5.

To match the SMEFT operators onto the WET Lagrangian we use the results presented in Ref. [221]:

$$\Delta C_7^{(0)} = \frac{\sqrt{2}m_t}{m_W} \left[\tilde{C}_{uW} E_7^{uW}(x_t) + \tilde{C}_{uW}^* F_7^{uW}(x_t) + \frac{\cos \theta_w}{\sin \theta_w} \left(\tilde{C}_{uB} E_7^{uB}(x_t) + \tilde{C}_{uB}^* F_7^{uB}(x_t) \right) \right], \quad (5.2.6)$$

$$\Delta C_8^{(0)} = \frac{\sqrt{2}m_t}{m_W} \left[\tilde{C}_{uW} E_8^{uW}(x_t) + \tilde{C}_{uW}^* F_8^{uW}(x_t) - \frac{g}{g_s} \left(\tilde{C}_{uG} E_8^{uG}(x_t) + \tilde{C}_{uG}^* F_8^{uG}(x_t) \right) \right], \quad (5.2.7)$$

with $x_t = m_t^2/m_W^2$. With ΔC_i we denote BSM contributions to WET coefficients in (C.1.1) and \tilde{C}_i are the rescaled SMEFT coefficients defined in Eq. (4.1.3). The x_t -dependent functions E_7^{uW} , F_7^{uW} , E_8^{uW} , and F_8^{uW} are taken from Ref. [221] and listed in App. A.2. Examples for corresponding one-loop Feynman diagrams are shown in Fig. 5.3.

Similarly to BSM contributions from dimension-six operators, the SM is also matched onto the WET Lagrangian at the scale μ_W . Using the WET RGEs we evolve the coefficients \tilde{C}_i from μ_W to μ_b resumming large logarithms to all orders in perturbation theory. In order to

Observable	Measurement	SM prediction
$\sigma_{\text{ATLAS}}^{\text{fid}}(t\bar{t}\gamma, 1\ell)$	521 ± 9 (stat.) ± 41 (syst.) fb [313]	495 ± 99 fb [313, 314]
$\sigma_{\text{ATLAS}}^{\text{fid}}(t\bar{t}\gamma, 2\ell)$	69 ± 3 (stat.) ± 4 (syst.) fb [313]	63 ± 9 fb [313, 314]
$\text{BR}(\bar{B} \rightarrow X_s\gamma)$	$(332 \pm 15) \times 10^{-6}$ [315]	$(336 \pm 23) \times 10^{-6}$ [316]

Table 5.1: Measurements and SM predictions of the fiducial cross sections of $t\bar{t}\gamma$ production and the $\bar{B} \rightarrow X_s\gamma$ branching ratio with a minimal photon energy of $E_\gamma \geq 1.6$ GeV.

compute the $\bar{B} \rightarrow X_s\gamma$ branching ratio we use the effective coefficients [311, 312]

$$C_i^{\text{eff}} = \begin{cases} \bar{C}_i & \text{for } i = 1, \dots, 6 \\ \bar{C}_7 + \sum_{j=1}^6 y_j \bar{C}_j & \text{for } i = 7 \\ \bar{C}_8 + \sum_{j=1}^6 z_j \bar{C}_j & \text{for } i = 8 \end{cases}, \quad (5.2.8)$$

with $y = (0, 0, -1/3, -4/9, -20/3, -80/9)$ and $z = (0, 0, 1, -1/6, 20, -10/3)$ [152] in the \overline{MS} scheme with fully anticommuting γ_5 . The WET RGEs for the effective coefficients

$$\frac{d}{d \ln \mu} C_i^{\text{eff}}(\mu) = \gamma_{ji}^{\text{eff}}(\mu) C_j^{\text{eff}}(\mu), \quad (5.2.9)$$

are solved expanding both γ^{eff} and C_i^{eff} in powers of α_s , according to Eqs. (3.1.12) and (3.1.13):

$$\gamma^{\text{eff}}(\mu) = \frac{\alpha_s(\mu)}{4\pi} \gamma^{(0)\text{eff}} + \frac{\alpha_s^2(\mu)}{(4\pi)^2} \gamma^{(1)\text{eff}} + \frac{\alpha_s^3(\mu)}{(4\pi)^3} \gamma^{(2)\text{eff}} + \dots, \quad (5.2.10)$$

$$C_i^{\text{eff}}(\mu) = C_i^{(0)\text{eff}}(\mu) + \frac{\alpha_s(\mu)}{4\pi} C_i^{(1)\text{eff}}(\mu) + \frac{\alpha_s^2(\mu)}{(4\pi)^2} C_i^{(2)\text{eff}}(\mu) + \dots. \quad (5.2.11)$$

The matrices $\gamma^{(0,1)\text{eff}}$ are given in Ref. [152], and $\gamma^{(2)\text{eff}}$ is specified in Ref. [153]. SM values for the coefficients C_i^{eff} at the scale μ_W are calculated at up to NNLO in QCD [154–156]. Again, we employ the procedure in App. B.5 to solve the RGEs.

Note that, obviously, considering simply the matching at the scale μ_b without RGE evolution leads to completely different and wrong results: prefactors of \bar{C}_i in the matching conditions change by a factor of up to 40, and mixing effects are not included at all.

5.3 Measurements included in the analysis

Both ATLAS and CMS have measured the $t\bar{t}\gamma$ production cross section [313, 317–319] at different center-of-mass energies. In this analysis, we include the latest ATLAS measurements of fiducial cross sections for final states containing one or two leptons at 13 TeV [313], referred to as single-lepton and dilepton channel, respectively. Here, leptons are either muons or electrons (and their antiparticles). Both measurements agree well with the SM prediction at NLO [313, 314].

In the case of $\text{BR}(\bar{B} \rightarrow X_s\gamma)$, multiple measurements by Belle [320–322], BaBar [323–325], and Cleo [326] are combined in an averaged value by the *Heavy Flavor Averaging Group* (HFLAV) [327]. In this combination, differences in the minimal photon energy E_γ are taken into account by performing an interpolation according to Ref. [328]. The combined value is given at the minimal photon energy $E_\gamma \geq 1.6$ GeV and is in good agreement with the SM

prediction computed at NNLO [316].

5.4 Computation of observables

The computation of $t\bar{t}\gamma$ production cross sections follows the principle described in Sec. 4.2 and is presented in detail in App. G. Cross sections at parton level are parametrized according to Eq. (4.2.1). Sampling points for the interpolation are computed with the `dim6top_L0` UFO model using `MadGraph5_aMC@NLO`. Samples are generated as $2 \rightarrow 7$ processes for both the single-lepton and dilepton channel with a phase space similar to the one described in Ref. [313], allowing for one insertion of a dimension-six operator at a time.

Following the general procedure outlined in App. D.3, we employ `PYTHIA 8` [329] and apply parton showering to the events and perform an event selection at particle-level using `MadAnalysis` [330–332] in order to compute the fiducial acceptance. Jets (see App. D.1) are clustered with the anti- k_t algorithm [333] using `FastJet` [334]. BSM contributions also affect the fiducial acceptance A and not just the production cross section. Including effects of dimension-six operators the acceptance can be written as

$$A = \frac{A^{\text{SM}}\sigma^{\text{SM}} + \sum_i \tilde{C}_i A_i^{\text{interf.}} \sigma_i^{\text{interf.}} + \sum_{i \leq j} \tilde{C}_i \tilde{C}_j A_{ij}^{\text{BSM}} \sigma_{ij}^{\text{BSM}}}{\sigma^{\text{SM}} + \sum_i \tilde{C}_i \sigma_i^{\text{interf.}} + \sum_{i \leq j} \tilde{C}_i \tilde{C}_j \sigma_{ij}^{\text{BSM}}}. \quad (5.4.1)$$

The denominator is simply the parametrization of the total cross section σ . Including BSM effects in A accounts for changes in the kinematics due to BSM contributions. As the σ_i are already determined, a least squares fit using fiducial acceptances from the generated events as sampling points can be performed. The results of the interpolation are discussed in App. G.

In order to include NLO corrections to SM cross sections we apply k factors to the LO SM result. Parametrizations of fiducial cross sections in the single-lepton and dilepton channel are shown in Fig. 5.4. For both channels, the results look very similar and cross sections show a comparable sensitivity to all three coefficients.

We consider the most recent calculation at NNLO [316] following the general procedure described in Ref. [156] to compute the branching ratio $\text{BR}(\bar{B} \rightarrow X_s \gamma)$. In addition to SM contributions we also include BSM contributions at LO. The branching ratio can be written as

$$\text{BR}(\bar{B} \rightarrow X_s \gamma) = \text{BR}(\bar{B} \rightarrow X_c e \bar{\nu})_{\text{exp}} \left| \frac{V_{ts}^* V_{tb}}{V_{cb}} \right|^2 \frac{6\alpha_e}{\pi C} (P(E_0) + N(E_0)), \quad (5.4.2)$$

where $E_0 = 1.6$ GeV is the minimal photon energy, and $P(E_0)$ and $N(E_0)$ denote perturbative and non-perturbative corrections, respectively. The prefactor C is defined as

$$C = \left| \frac{V_{ub}}{V_{cb}} \right|^2 \frac{\Gamma(\bar{B} \rightarrow X_c e \bar{\nu})}{\Gamma(\bar{B} \rightarrow X_u e \bar{\nu})}, \quad \text{with } C_{\text{exp}} = 0.568 \pm 0.007 \pm 0.01 \text{ [335]}. \quad (5.4.3)$$

The perturbative part $P(E_0)$ can be parametrized as

$$P(E_0) = \sum_{i,j=1}^8 C_i^{\text{eff}}(\mu_b) C_j^{\text{eff}}(\mu_b) K_{ij}(E_0, \mu_b), \quad (5.4.4)$$

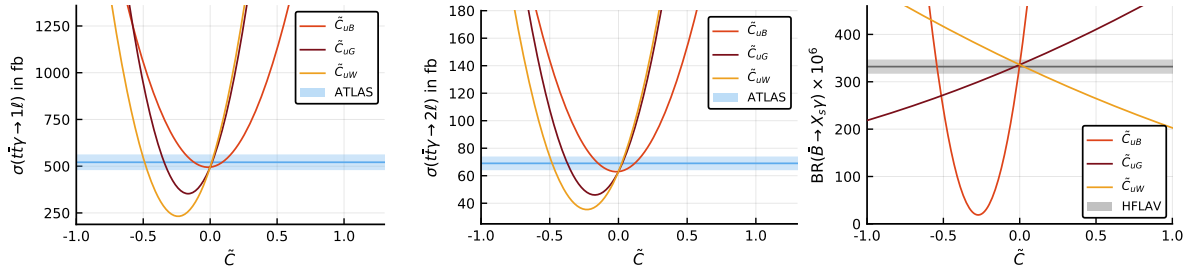


Figure 5.4: Parametrizations of observables included in the analysis: fiducial $t\bar{t}\gamma$ cross sections for the single-lepton channel (left) and the dilepton channel (middle) and $\text{BR}(\bar{B} \rightarrow X_s\gamma)$. (right) We show slices of the phase space varying only one of the Wilson coefficient at a time, while the other coefficients are set to zero. The blue and grey bands indicate the experimental measurements (see Tab. 5.1).

where the matrix K can be perturbatively expanded in powers of α_s :

$$K_{ij}(E_0, \mu_b) = \delta_{i7}\delta_{j7} + \frac{\alpha_s(\mu_b)}{4\pi} K_{ij}^{(1)} + \frac{\alpha_s^2(\mu_b)}{(4\pi)^2} K_{ij}^{(2)} + \mathcal{O}(\alpha_s^3(\mu_b)). \quad (5.4.5)$$

The coefficients $K_{ij}^{(i)}$ are known at approximate NNLO [156, 336–343]. For the computation of non-perturbative corrections $N(E_0)$ we include results from [344–346].

The branching ratio for different values of SMEFT coefficients $\tilde{C}_i(\mu_t)$ is shown in the plot on the right side of Fig. 5.4. We find that \tilde{C}_{uB} has a significantly larger impact compared to the other two. This is expected, as we find numerically that $\Delta\tilde{C}_7^{(0)} = 0.093\tilde{C}_{uW}(\mu_W) - 2.354\tilde{C}_{uB}(\mu_W)$, while \tilde{C}_{uG} is of higher order in α_s . We validate our results using `flavio` [347] together with the `wilson` [348] package and the matching in Eqs. (5.2.6) and (5.2.7) and find good agreement for all three coefficients.

5.5 Constraints on SMEFT coefficients

We fit the parametrizations of the fiducial cross sections and the branching ratio to the data in Tab. 5.1 to derive constraints on the SMEFT Wilson coefficients. We employ `EFTfitter` to obtain marginalized posterior probability distribution and include experimental as well as theory uncertainties. As our focus lies on combining observables at different energy scales, we assume all uncertainties to be uncorrelated for simplicity. This assumption is reasonable for correlations between top-quark and B -physics observables as well as for statistical uncertainties between the two top-quark observables. However, correlations between systematic and theory uncertainties of top-quark observables can arise. Following the reasoning in Sec. 4, we investigate the impact of unknown correlations performing several fits varying entries in the correlation matrices. We assume a uniform distribution over the interval $-1 \leq \tilde{C}_i \leq 1$ as the default prior.

In Fig. 5.5 we give the posterior probability distributions obtained in fits of all SMEFT Wilson coefficients to B -physics observables (left) and top-quark observables (middle, right). In the fit to $\text{BR}(\bar{B} \rightarrow X_s\gamma)$ only \tilde{C}_{uB} can be constrained while the other two coefficients remain unconstrained. This behavior can be understood considering the dependence of $\text{BR}(\bar{B} \rightarrow X_s\gamma)$ on the three coefficients (see Fig. 5.4). Contributions from \tilde{C}_{uB} have a significantly larger impact on the branching ratio than the other two coefficients. In the posterior distribution of

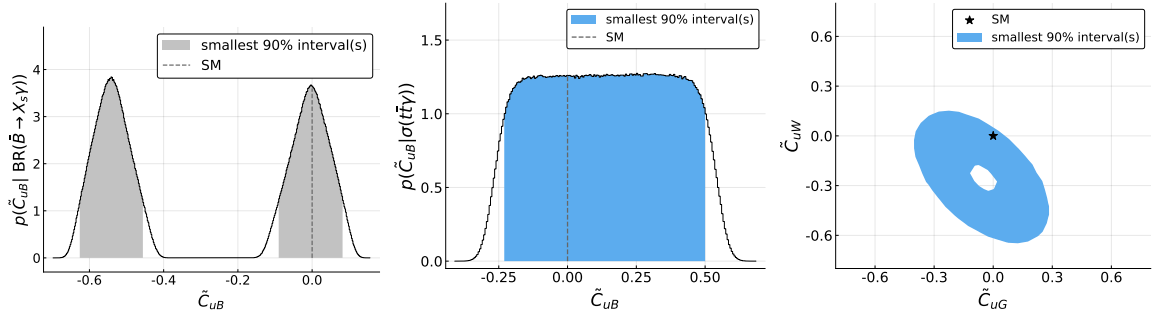


Figure 5.5: Posterior probability distributions for the fit of all three Wilson coefficients using only measurements of $\text{BR}(\bar{B} \rightarrow X_s \gamma)$ (left) and $\sigma(t\bar{t}\gamma)$ (middle, right). Shown are (left, middle) the distribution of \tilde{C}_{uB} together with the corresponding smallest interval containing 90% of the probability (colored region) and (right) the smallest interval containing 90% of the posterior probability for the two-dimensional marginalized distribution in the \tilde{C}_{uG} - \tilde{C}_{uW} plane. The SM values are indicated.

\tilde{C}_{uB} we find two regions around $\tilde{C}_{uB} \sim 0$ and $\tilde{C}_{uB} \sim -0.5$ to be allowed by data, as expected considering Fig. 5.4. Without further input this ambiguity cannot be resolved.

Fitting the coefficients to top-quark data yields comparable constraints on all three coefficients, as shown in Fig. 5.5 in the one-dimensional posterior distribution of \tilde{C}_{uB} (second plot) and the two-dimensional distribution in the \tilde{C}_{uG} - \tilde{C}_{uW} plane (rightmost plot). The smallest intervals containing 90% of the posterior probability are comparable for all three coefficients, as expected considering Fig. 5.4. We validate our results performing fits to either the single-lepton of the dilepton channel and obtain very similar results in both cases.

In Fig. 5.6 we compare two-dimensional projections of the posterior distribution obtained in fits to different datasets. For the sake of a better legibility of the plots, the 90% interval from the fit to top-quark data are shown as contours. Most noticeably, we find that combining top-quark and B -physics data allows to remove the ambiguity in \tilde{C}_{uB} present in the fit to $\text{BR}(\bar{B} \rightarrow X_s \gamma)$ only: in the combined fit the non-SM branch is excluded. Even though the fit to the branching ratio constrains only \tilde{C}_{uB} , the combination with $t\bar{t}\gamma$ cross sections imposes significantly stronger constraints on all three coefficients compared to top-quark data only. The size of the posterior region is reduced by one order of magnitude in the \tilde{C}_{uB} - \tilde{C}_{uG} and \tilde{C}_{uB} - \tilde{C}_{uW} planes, see Fig. 5.6 (upper row). This significant reduction stems from the orthogonality of the constraints from the different observables. Even in the \tilde{C}_{uG} - \tilde{C}_{uW} plane (lower row), where no constraints from $\text{BR}(\bar{B} \rightarrow X_s \gamma)$ are present, we observe a reduction of the size of the smallest intervals. In the combined fit, the region shrinks by a factor of 1.9 relative to results from top-quark data only. This effect is understood as the smallest intervals of the posterior distribution are reduced in the three-dimensional parameter space, and Fig. 5.6 shows only two-dimensional projections.

In Fig. 5.7 we show an alternative representation of the results of our fits in terms of the one-dimensional projections of the smallest intervals. In the individual fit, in which only one coefficient is varied at a time, constraints show a behavior similar to the fit with all three coefficients. Overall, constraints are stronger since no interferences between the linear terms of different coefficients occur. It is recognizable that the combination of top-quark and B -physics data does not only remove the second solution for \tilde{C}_{uB} present in the fit to $\text{BR}(\bar{B} \rightarrow X_s \gamma)$ but also removes a second solution for \tilde{C}_{uW} present in the fit to $\sigma(t\bar{t}\gamma)$. In both cases, the close-to-SM branch is supported in the combination. Conversely, the second

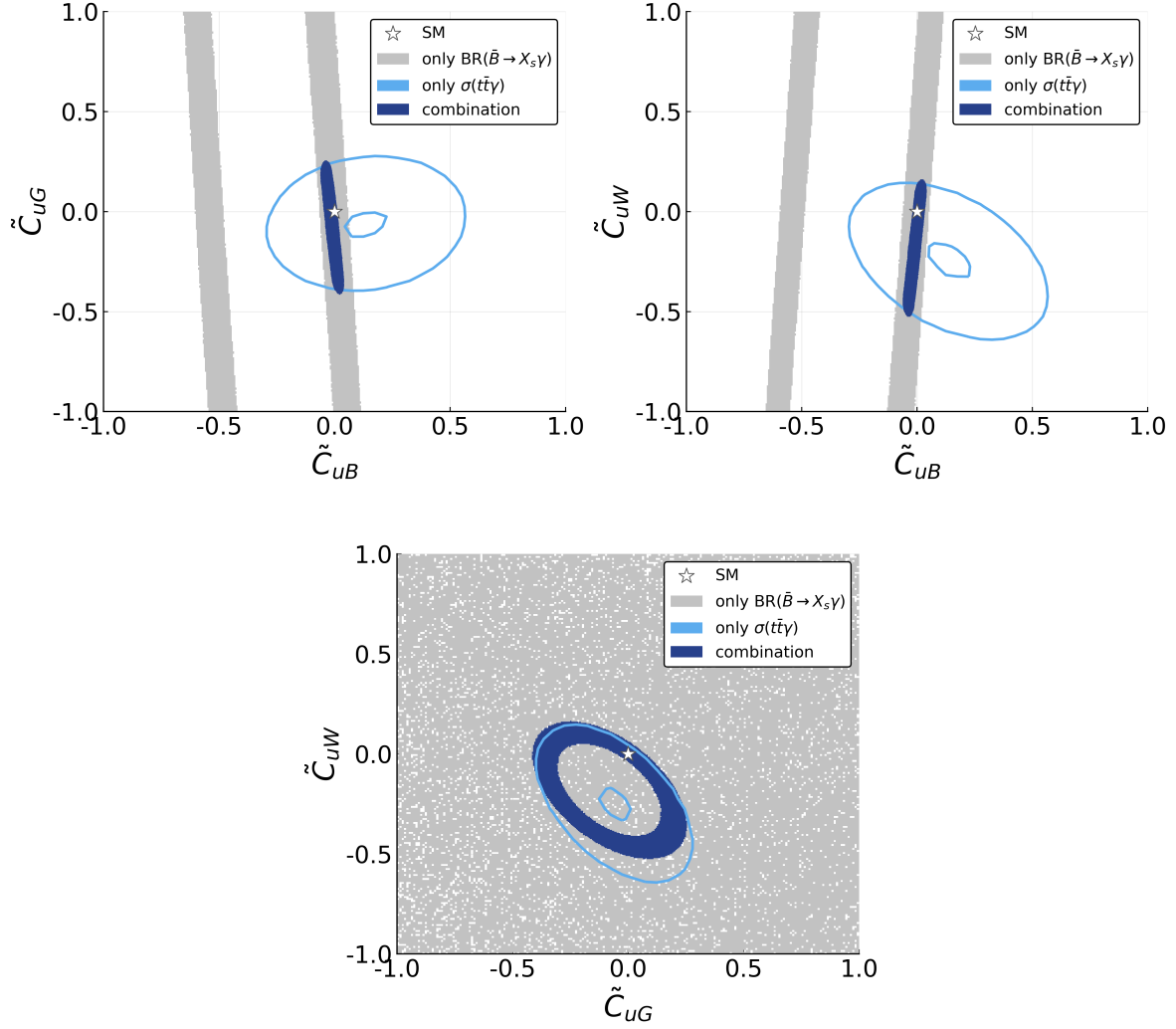


Figure 5.6: The two-dimensional projections of the smallest intervals containing 90 % of the posterior probability distributions for the fits of all three Wilson coefficients using only the measurement of $\text{BR}(\bar{B} \rightarrow X_s \gamma)$ (grey), only the measurements of $\sigma(t\bar{t}\gamma)$ (light blue) and for the combination (blue). The SM values are indicated.

solution for \tilde{C}_{uG} remains even in the combination of both datasets.

As mentioned above, we estimate the impact of correlations between systematic and theory uncertainties of the single-lepton and dilepton channels of $\sigma(t\bar{t}\gamma)$ by varying corresponding entries in the correlation matrices. In the case of systematic uncertainties, the entries are varied between -0.9 and 0.9 , as in principle negative correlations could occur. For theoretical uncertainties, we do not expect any negative correlations and consider coefficients up to 0.9 . Comparing the sizes of the smallest regions in the different correlation scenarios we observe only minor changes in the distributions in the \tilde{C}_{uB} - \tilde{C}_{uG} and \tilde{C}_{uB} - \tilde{C}_{uW} planes, about 4 %. In contrast, the distribution in the \tilde{C}_{uG} - \tilde{C}_{uW} plane shows larger effects, about 30 %. This is expected, since constraints from top-quark data dominate. From these findings we conclude that correlations leave our general findings unchanged.

Note that we focus here on demonstrating the steps necessary for a combined analysis using only two different observables as a proof of concept. Thus, we do not obtain the

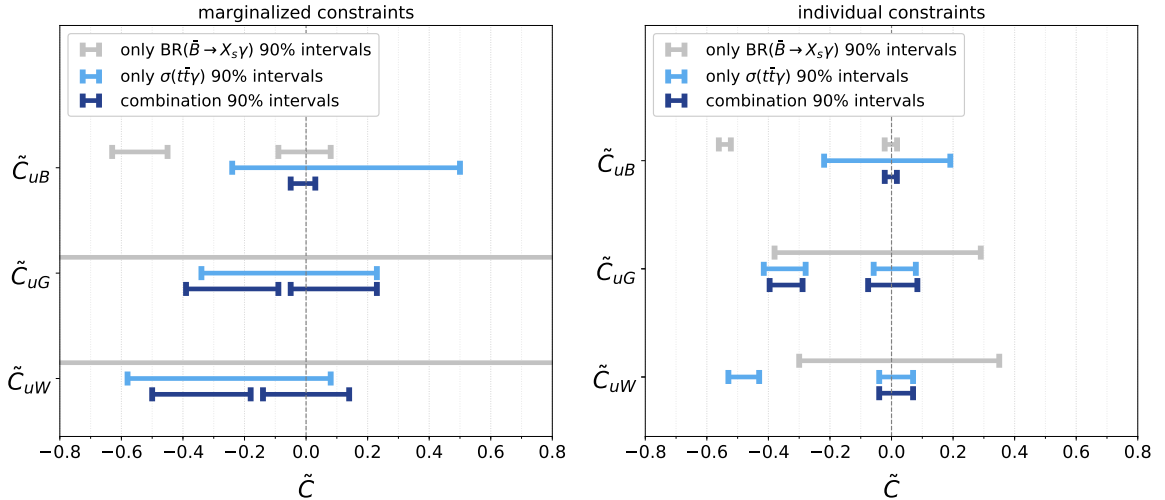


Figure 5.7: The smallest intervals containing 90% probability of the one-dimensional marginalized posterior distribution for the fits using only $\text{BR}(\bar{B} \rightarrow X_s \gamma)$ (grey), only $\sigma(t\bar{t}\gamma)$ (light blue) and using their combination (blue). Shown are the intervals for (left) the one-dimensional marginalized posterior distributions and (right) for individual fits of each Wilson coefficient where the other two coefficients are fixed to zero.

strongest constraints on the coefficients considered (compared to global fits, *e.g.* in Ref. [237]). Including additional observables and measurements would certainly allow to derive stronger constraints on BSM contributions. For example, $t\bar{t}$ production and the W boson helicity fractions strongly constrain \tilde{C}_{uG} and \tilde{C}_{uW} , respectively. Similarly, $b \rightarrow s\ell^+\ell^-$ transitions constrain \tilde{C}_{uB} and remove the ambiguity present in fits to $\text{BR}(\bar{B} \rightarrow X_s \gamma)$ only. We study these effect in Chapter 6.

5.6 Summary

In the SMEFT framework, measurements from both the precision-flavor and the high-energy frontiers can be combined in one analysis. In this chapter, we demonstrated this by exploiting synergies between B -physics and top-quark measurements from flavor factories and the LHC, respectively. To do so, we considered measurements of the $\bar{B} \rightarrow X_s \gamma$ branching ratio and fiducial $t\bar{t}\gamma$ production cross sections. We combined these measurements within the SMEFT framework detailing the steps required to connect measurements at different energy scales. We pointed out that matching beyond tree level is necessary for the analysis. We employed MC generators together with an event selection at particle level to compute cross sections of $t\bar{t}\gamma$ production and the fiducial acceptance for different values of Wilson coefficients. This allowed us to perform an interpolation, which parametrizes the dependence of both cross sections and acceptance on the coefficients.

We highlighted how the different sensitivities of the observables on the dimension-six operators allow to significantly improve constraints on the Wilson coefficients. In particular, their combination removed ambiguities present in fits to either the branching ratio or the fiducial cross sections due to the complementarity of the constraints from the different observables (see Fig. 5.6). Our findings demonstrate the benefits of global analyses combining top-quark and flavor physics measurements. They motivate us to link top-quark and beauty physics,

in particular in the context of several anomalies in the beauty sector, in a global fit. This is present in detail in Chapter 6.

6 Synergies of top and beauty

In Chapter 5, we highlighted how top-quark and B -physics observables can be combined in a single analysis in order to constrain BSM contributions to top-quark physics. We found that top-quark and B -physics observables offer complementary sensitivities to the three Wilson coefficients considered. This significantly tightens the constraints. Motivated by the success of this analysis, we extend our setup to analyze sensitivities to four-fermion operators. We link the top-quark sector of SMEFT to the flavor anomalies, which presently hint at BSM physics in semileptonic $b \rightarrow s$ decays [310, 349]. In addition, semileptonic operators give rise to contact interactions of top-quarks and leptons, which are only very weakly constrained by present data [27]. Conversely, they could be studied with high precision at future lepton colliders [350–361], such as the *International Linear Collider* (ILC) [362, 363], the *Compact Linear Collider* (CLIC) [364], or the *Future Circular Collider* (FCC) [365].

To study the interplay of top-quark and beauty physics in the context of the flavor anomalies, we work out constraints on two-fermion and four-fermion operators. The former are operators with gauge bosons, while the later introduce contact interactions. We consider top-quark pair-production processes, $Z \rightarrow b\bar{b}$ transitions, and $b \rightarrow s$ FCNCs for three different stages. Firstly, we study present data, considering measurements at the LHC¹, the *Large Electron-Positron Collider* (LEP), and B factories. Secondly, we consider a near-future scenario, further including projections for measurements at HL-LHC and Belle II. Thirdly, we add in a far-future scenario measurements at a lepton collider at the concrete example of CLIC. We investigate how such measurements at a future lepton collider affect constraints on SMEFT coefficients and open up new directions in the hunt for BSM physics.

This chapter, which is based on Ref. [24], is structured as follows. In Sec. 6.1, we specify the dimension-six operators considered in this analysis, and detail on the matching conditions and RGEs used to express B -physics observables in terms of SMEFT coefficients. In Sec. 6.2, we present the observables included in our fits and discuss their sensitivity to the different SMEFT operators. The analysis of the measurements of top-quark and B -physics data as well as the constraints on the SMEFT coefficients derived from fits to these datasets are shown in Sec. 6.3. In Sec. 6.4, we determine how the projections for the different future colliders affect the constraints on the coefficients. In Sec. 6.5, we summarize our results.

6.1 Dimension-six operators

We focus on operators which give leading contributions at $\mathcal{O}(\Lambda^{-2})$ to one of the following processes: top-quark pair-production processes at the LHC, top-quark decay, and $t\bar{t}$ production at a future electron-positron collider. We consider operators that affect interactions of

¹Further including CMS data on $t\bar{t}\ell^+\ell^-$ production in Ref. [27] is desirable, but requires detector-level simulations and is beyond the scope of this work.

third-generation quarks with the gauge bosons:

$$\begin{aligned}
O_{\varphi q}^{(1)} &= \left(\varphi^\dagger i \overleftrightarrow{D}_\mu \varphi \right) (\bar{q}_L \gamma^\mu q_L) , & O_{\varphi q}^{(3)} &= \left(\varphi^\dagger i \overleftrightarrow{D}_\mu^I \varphi \right) (\bar{q}_L \tau^I \gamma^\mu q_L) , \\
O_{uB} &= (\bar{q}_L \sigma^{\mu\nu} u_R) \tilde{\varphi} B_{\mu\nu} , & O_{uW} &= (\bar{q}_L \sigma^{\mu\nu} \tau^I u_R) \tilde{\varphi} W_{\mu\nu}^I , \\
O_{uG} &= (\bar{q}_L \sigma^{\mu\nu} T^A u_R) \tilde{\varphi} G_{\mu\nu}^A , & O_{\varphi u} &= \left(\varphi^\dagger i \overleftrightarrow{D}_\mu \varphi \right) (\bar{u}_R \gamma^\mu u_R) ,
\end{aligned} \tag{6.1.1}$$

as well as semileptonic four-fermion operators:

$$\begin{aligned}
O_{lq}^{(1)} &= (\bar{l}_L \gamma_\mu l_L) (\bar{q}_L \gamma^\mu q_L) , & O_{lq}^{(3)} &= (\bar{l}_L \gamma_\mu \tau^I l_L) (\bar{q}_L \gamma^\mu \tau^I q_L) , \\
O_{qe} &= (\bar{q}_L \gamma_\mu q_L) (\bar{e}_R \gamma^\mu e_R) , & O_{eu} &= (\bar{e}_R \gamma_\mu e_R) (\bar{u}_R \gamma^\mu u_R) , \\
O_{lu} &= (\bar{l}_L \gamma_\mu l_L) (\bar{u}_R \gamma^\mu u_R) .
\end{aligned} \tag{6.1.2}$$

Here, we repeat the definitions of dipole operators and $O_{\varphi q}^{(3)}$, which are already defined in Eqs. (4.1.1) and (5.1.1), respectively, for the sake of completeness. Dipole operators O_{dX} with $X = B, W, G$ and right-handed down-type quarks contribute only at subleading order, *i.e.* contributions are suppressed by a factor m_b/m_t relative to up-type dipole operators. We neglect such contributions as well as those that arise from other operators with right-handed down-type quarks. Scalar and tensor four-fermion operators $O_{lequ}^{(1,3)}$ and O_{ledq} (see Tab. B.2), which do not generate contributions at $\mathcal{O}(\Lambda^{-2})$ to the processes considered here [18, 21, 361, 366], are not included in our analysis. Contributions from four-quark operators to top-quark pair-production processes are neglected in our approach since pair production is dominated by the gluon-gluon channel (90 % at 13 TeV LHC [231]). Note that this argument only holds for total cross sections, since four-quark operators can dominate in tails of distributions due to an energy enhancement [237]. However, bin-to-bin correlations are not available, yet important for the fit [25], and thus we do not consider such observables. Furthermore, lepton dipole operators, which alter interactions of leptons with the Z boson, are not considered since they are already strongly constrained by Z data [309].

Note that dipole operators are non-hermitian and can in general have complex-valued Wilson coefficients. However, only the real part contributes to the leading interference terms, and thus we consider only real-valued coefficients for the sake of simplicity.

6.1.1 Coefficients in the mass basis

As discussed in Sec. 3.2.3, the operators in Eqs. (6.1.1) and (6.1.2) are written in the flavor basis. Quark flavor $q_{L/R}^i$ and mass basis $q_{L/R}^l$ are connected via the rotation matrices $S_{L/R}^q$ with $q = u, d$ and flavor indices $i = 1, 2, 3$, see Eq. (2.1.42). As shown in Sec. 3.2.3, rotation matrices S_R^q can simply be absorbed in the flavor basis coefficients C_i . This gives rise to the coefficients in the mass basis, denoted by \hat{C}_i (3.2.7). Conversely, rotations S_L^q of quark doublets relate different physical processes by $SU(2)_L$ symmetry (3.2.8). As an example, consider the $C_{\varphi q}^{(1)} O_{\varphi q}^{(1)}$ terms, which involve a quark doublet current. With quark flavor indices written explicitly the terms read

$$C_{\varphi q}^{(1)ij} O_{\varphi q}^{(1)ij} = \hat{C}_{\varphi q}^{(1)kl} \left(\varphi^\dagger i \overleftrightarrow{D}_\mu \varphi \right) \left(\bar{u}_L^k \gamma^\mu u_L^l + V_{mk}^\dagger V_{ln} \bar{d}_L^m \gamma^\mu d_L^n \right) , \tag{6.1.3}$$

where we work in the up-mass basis, in which flavor mixing is entirely in the down-sector. In general, $C_{\varphi q}^{(1)ij}$, and similarly all operators with quark-doublet currents, induce contributions

to both $u^i - u^j$ and $d^i - d^j$ transitions irrespective of the choice of mass basis. In the up-mass basis, the latter are proportional to CKM matrix elements. Operators such as $C_{\varphi q}^{(3)} O_{\varphi q}^{(3)}$, which have a triplet structure, involve an additional minus sign between up- and down-sector currents:

$$C_{\varphi q}^{(3)ij} O_{\varphi q}^{(3)ij} = \hat{C}_{\varphi q}^{(3)kl} \left(\varphi^\dagger_i \overleftrightarrow{D}_\mu \varphi \right) \left(\bar{u}_L^k \gamma^\mu u_L^l - V_{mk}^\dagger V_{ln} \bar{d}_L^m \gamma^\mu d_L^n \right). \quad (6.1.4)$$

Thus, up-type and down-type quarks receive contributions from different linear combinations of $C_i^{(1)}$ and $C_i^{(3)}$, which has already been exploited recently in the context of lepton flavor universality and transitions involving neutrinos [223]. Further information on the definition of Wilson coefficients and operators in the mass basis are given in App. H.1.

In this analysis, we consider only BSM contributions proportional to coefficients with third generation up-type quarks, \hat{C}_i^{33} . Such hierarchies can arise in top-philic scenarios where BSM particles couple dominantly to third-generation quarks [163]. As can be seen in Eq. (6.1.3), flavor mixing relates contributions from coefficients \hat{C}_i^{33} to top-quark production and $d_L^i \rightarrow d_L^j$ transitions with $i \neq j$. These are proportional to $V_{ti} V_{tj}^*$, similar to the SM. Here, we focus on BSM contributions to $b \rightarrow s$ FCNC data. Additional $s \rightarrow d$ data does presently not yield significantly stronger constraints [21], and is not considered further. This leaves eleven coefficients for our fit:

$$\hat{C}_{uB}^{33}, \hat{C}_{uG}^{33}, \hat{C}_{uW}^{33}, \hat{C}_{\varphi q}^{(1)33}, \hat{C}_{\varphi q}^{(3)33}, \hat{C}_{\varphi u}^{33}, \hat{C}_{eu}^{33}, \hat{C}_{lu}^{33}, \hat{C}_{qe}^{33}, \hat{C}_{lq}^{(1)33}, \hat{C}_{lq}^{(3)33}. \quad (6.1.5)$$

Considering fits to present data, no assumptions regarding lepton universality are needed as B -physics data is dominated by distributions with muons. Belle II is expected to test both $b \rightarrow s e^+ e^-$ and $b \rightarrow s \mu^+ \mu^-$ distributions, and thus provides further insights in the present hints for lepton flavor non-universality, see Sec. 2.3. Even further in the future, $t\bar{t}$ data from an $e^+ e^-$ collider can be combined with results from $b \rightarrow s e^+ e^-$, while B -physics data with muons can be combined with data from a muon collider. This allows to perform lepton-specific fits. In addition, lepton flavor violating contributions could be included in the future. Conversely, assumptions regarding lepton flavor are needed when dineutrino data is included in the fit because branching ratios are measured flavor-inclusively:

$$\text{BR}(b \rightarrow s \nu \bar{\nu}) = \sum_{i,j=1}^3 \text{BR}(b \rightarrow s \nu_i \bar{\nu}_j). \quad (6.1.6)$$

Assuming universality, the total branching ratio is simply given by $\text{BR}(b \rightarrow s \nu \bar{\nu}) = 3\text{BR}(b \rightarrow s \nu_i \bar{\nu}_i)$ with flavor indices fixed. We assume lepton flavor universality for fits in future scenarios including dineutrino data.

Similarly to Chapters 4 and 5, we use rescaled Wilson coefficients $\tilde{C}_i = v^2/\Lambda^2 \hat{C}_i^{33}$. In addition, we introduce the linear combinations

$$\tilde{C}_{\varphi q}^\pm = \tilde{C}_{\varphi q}^{(1)} \pm \tilde{C}_{\varphi q}^{(3)}, \quad \tilde{C}_{lq}^\pm = \tilde{C}_{lq}^{(1)} \pm \tilde{C}_{lq}^{(3)}, \quad (6.1.7)$$

to highlight the $SU(2)_L$ complementarity of top and beauty, which is illustrated in Fig. 6.1.

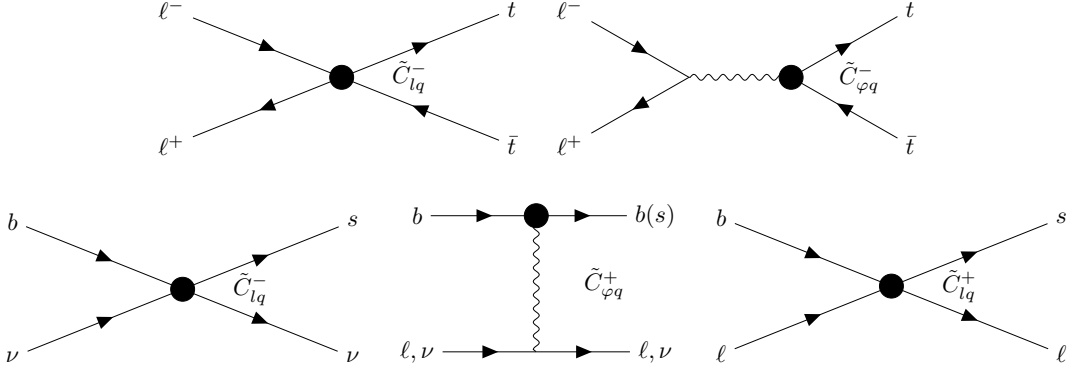


Figure 6.1: Sensitivities to \tilde{C}_{lq}^{\pm} and $\tilde{C}_{\varphi q}^{\pm}$ in top-quark (upper row) and down-type quark (lower row) interactions. The black circles denote insertion of dimension-six operators.

6.1.2 Matching conditions

In order to describe physics below the EW scale μ_W in terms of SMEFT coefficients, the SMEFT Lagrangian has to be matched onto the WET Lagrangian describing the corresponding process. In addition, the RGEs of both SMEFT and WET have to be employed to include the effects of running and mixing. The exact procedure is described in detail in Ref. [23] and Sec. 5.2 and adapted here. In contrast to fits in Chapters 4 and 5, we determine constraints on Wilson coefficients at the scale $\mu = 1$ TeV. We choose this scale to include RGE effects, which have to be considered when matching a concrete UV model with particles at the TeV scale onto the SMEFT and can have a significant impact on the results of the fit. In the following, we summarize the steps necessary for our analysis.

We consider the RGEs of the SMEFT coefficients (6.1.5) at leading order in the strong coupling α_s given in Refs. [188–190]. For the coefficients \tilde{C}_{uB} , \tilde{C}_{uW} , and \tilde{C}_{uG} , the running at $\mathcal{O}(\alpha_s)$ is discussed in detail in Sec. 5.2. Here, we include the complete running at one-loop level by employing the `wilson` package [348].

Operators which include two $SU(2)_L$ quark doublets contribute at tree level to $b \rightarrow s$ transitions due to the flavor rotations. At tree level, contributions from $O_{\varphi q}^{(1)}$, $O_{\varphi q}^{(3)}$, O_{qe} , $O_{lq}^{(1)}$, and $O_{lq}^{(3)}$ to coefficients of semileptonic WET operators $O_{9,10,L}$, given in App. C, arise [21, 221, 367]:

$$\begin{aligned}
\Delta C_9^{\text{tree}} &= \frac{\pi}{\alpha} \left[\tilde{C}_{lq}^{(1)} + \tilde{C}_{lq}^{(3)} + \tilde{C}_{qe} + (-1 + 4 \sin^2 \theta_w) \left(\tilde{C}_{\varphi q}^{(1)} + \tilde{C}_{\varphi q}^{(3)} \right) \right] \simeq \frac{\pi}{\alpha} \left[\tilde{C}_{lq}^+ + \tilde{C}_{qe} \right], \\
\Delta C_{10}^{\text{tree}} &= \frac{\pi}{\alpha} \left[-\tilde{C}_{lq}^{(1)} - \tilde{C}_{lq}^{(3)} + \tilde{C}_{qe} + \left(\tilde{C}_{\varphi q}^{(1)} + \tilde{C}_{\varphi q}^{(3)} \right) \right] = \frac{\pi}{\alpha} \left[-\tilde{C}_{lq}^+ + \tilde{C}_{qe} + \tilde{C}_{\varphi q}^+ \right], \\
\Delta C_L^{\text{tree}} &= \frac{\pi}{\alpha} \left[\tilde{C}_{lq}^{(1)} - \tilde{C}_{lq}^{(3)} + \tilde{C}_{\varphi q}^{(1)} + \tilde{C}_{\varphi q}^{(3)} \right] = \frac{\pi}{\alpha} \left[\tilde{C}_{lq}^- + \tilde{C}_{\varphi q}^+ \right],
\end{aligned} \tag{6.1.8}$$

where we neglected in the second step for ΔC_9 the suppressed Z contributions because of the smallness of the Z 's vector coupling ($\sin^2 \theta_w = 0.223$) to charged leptons [368].

In addition to dominant tree-level contributions, SMEFT operators contribute at one-loop level to WET dipole operators $O_{7,8}$, semileptonic operators $O_{9,10,L}$, and B_s mixing (see

App. C) [21, 221, 366, 369–371]:

$$\Delta C_7^{\text{loop}} = \frac{\sqrt{2}m_t}{m_W} \left[\tilde{C}_{uW} E_7^{uW}(x_t) + \tilde{C}_{uW}^* F_7^{uW}(x_t) + \frac{\cos \theta_w}{\sin \theta_w} \left(\tilde{C}_{uB} E_7^{uB}(x_t) + \tilde{C}_{uB}^* F_7^{uB}(x_t) \right) \right] + E_7^{\varphi q}(x_t) \tilde{C}_{\varphi q}^{(1)} + E_7^{\varphi q(3)}(x_t) \tilde{C}_{\varphi q}^{(3)} \quad (6.1.9)$$

$$\Delta C_8^{\text{loop}} = \frac{\sqrt{2}m_t}{m_W} \left[\tilde{C}_{uW} E_8^{uW}(x_t) + \tilde{C}_{uW}^* F_8^{uW}(x_t) - \frac{g}{g_s} \left(\tilde{C}_{uG} E_8^{uG}(x_t) + \tilde{C}_{uG}^* F_8^{uG}(x_t) \right) \right] + E_8^{\varphi q}(x_t) \tilde{C}_{\varphi q}^{(1)} + E_8^{\varphi q(3)}(x_t) \tilde{C}_{\varphi q}^{(3)}, \quad (6.1.10)$$

$$\Delta C_9^{\text{loop}} = \sqrt{2} \frac{m_t}{m_W} \left[\left(\frac{Y_{uW}(x_t)}{\sin^2 \theta_w} - Z_{uW}(x_t) \right) \text{Re}(\tilde{C}_{uW}) - \frac{\cos \theta_w}{\sin \theta_w} Z_{uB}(x_t) \text{Re}(\tilde{C}_{uB}) \right] + \frac{1}{\sin^2 \theta_w} \left\{ I_1(x_t) \left[\tilde{C}_{eu} + \tilde{C}_{lu} + (-1 + 4 \sin^2 \theta_w) \tilde{C}_{\varphi u} \right] + I_2(x_t) \left[\tilde{C}_{qe} + \tilde{C}_{lq}^{(1)} \right] + I^{lq}(x_t) \tilde{C}_{lq}^{(3)} + \left[(-1 + 4 \sin^2 \theta_w) I_2(x_t) \tilde{C}_{\varphi q}^{(1)} + I_1^{\varphi q}(x_t) \tilde{C}_{\varphi q}^{(3)} \right] \right\} \quad (6.1.11)$$

$$\Delta C_{10}^{\text{loop}} = - \frac{\sqrt{2}}{\sin^2 \theta_w} \frac{m_t}{m_W} Y_{uW}(x_t) \text{Re}(\tilde{C}_{uW}) + \frac{1}{\sin^2 \theta_w} \left\{ I_1(x_t) \left[\tilde{C}_{eu} - \tilde{C}_{lu} + \tilde{C}_{\varphi u} \right] + I_2(x_t) \left[\tilde{C}_{qe} - \tilde{C}_{lq}^{(1)} \right] - I^{lq}(x_t) \tilde{C}_{lq}^{(3)} + \left[I_2(x_t) \tilde{C}_{\varphi q}^{(1)} + I_2^{\varphi q}(x_t) \tilde{C}_{\varphi q}^{(3)} \right] \right\} \quad (6.1.12)$$

$$\Delta C_L^{\text{loop}} = I_{uW}^{\nu} \text{Re}(\tilde{C}_{uW}) + I_{\varphi q}^{\nu(1)} \tilde{C}_{\varphi q}^{(1)} + I_{\varphi q}^{\nu(3)} \tilde{C}_{\varphi q}^{(3)} + I_{lu}^{\nu} (\tilde{C}_{\varphi u} + \tilde{C}_{lu}) + I_{lq}^{\nu(1)} \tilde{C}_{lq}^{(1)} + I_{lq}^{\nu(3)} \tilde{C}_{lq}^{(3)}, \quad (6.1.13)$$

$$\Delta C_{1,tt}^{\text{mix, loop}} = + \sqrt{2} \frac{m_t}{m_W} \text{Re}(\tilde{C}_{uW}) \frac{9x_t}{4} \left(\frac{x_t + 1}{(x_t - 1)^2} - \frac{2x_t}{(x_t - 1)^3} \log x_t \right) + 4S_0(x_t) \tilde{C}_{\varphi q}^{(3)} + H_1(x_t) \tilde{C}_{\varphi q}^{(1)} + H_2(x_t) \tilde{C}_{\varphi q}^{(3)}, \quad (6.1.14)$$

where $x_t = m_t^2/m_W^2$. The expressions for the functions can be found in Refs. [221, 369–371]. In addition, we give them in App. A.2 for the sake of completeness.

Note that contributions at loop level are present also in the absence of CKM-mixing. We find sensitivity at one-loop level to contributions from semileptonic operators O_{lu} and O_{eu} with up-type quark singlets. However, such contributions are parametrically suppressed compared to those of semileptonic operators with quark doublets. Numerical values of the matching conditions at $\mu_W = m_W$ are given in App. H.2. In the actual analysis, RGE effects both in SMEFT and WET are taken into account as well.

In order to compute the WET coefficients at the scale μ_b , we employ `flavio` [347] together with the `wilson` package. Exceptions are the operators describing the B_s mixing, since the observables are formulated in terms of coefficients $C_i(\mu_W)$ [372], and those needed for $b \rightarrow s\nu\bar{\nu}$ transitions, whose running is negligible.

6.2 Observables

In the following, we discuss the contributions from dimension-six operators to the different observables. In Sec. 6.2.1, we present the computation of observables for top-quark pair-production processes, top-quark decay, $Z \rightarrow b\bar{b}$ transitions, and $b \rightarrow s$ FCNCs. In Sec. 6.2.2, we discuss the sensitivities of the different sets to contributions from SMEFT coefficients.

6.2.1 Computation of observables

We follow the procedure already employed in Secs. 4.2 and 5.4 to compute cross sections for top-quark pair-production processes at the LHC. Inclusive cross sections of $t\bar{t}$ and $t\bar{t}Z$ production at the LHC and $t\bar{t}$ production at CLIC are computed using `MadGraph5_aMC@NLO` together with the `dim6top_L0` UFO model. BSM contributions are parametrized with a quadratic ansatz (see Eq. (4.2.3))

$$\sigma = \sigma^{\text{SM}} + \sum_i \tilde{C}_i \sigma_i^{\text{int}} + \sum_{i \leq j} \tilde{C}_i \tilde{C}_j \sigma_{ij}^{\text{BSM}}, \quad (6.2.1)$$

where σ^{int} and σ^{BSM} denote interference and purely BSM terms, respectively. Fiducial cross sections of $t\bar{t}\gamma$ production are computed according to Sec. 5.4 as 2 \rightarrow 7 processes and include BSM contributions in the top-quark decay. The forward-backward asymmetry in $t\bar{t}$ production considered at CLIC is defined as

$$A_{\text{FB}} = \frac{\sigma_{\text{FB}}}{\sigma}, \quad \sigma_{\text{FB}} = \int_{-1}^1 d \cos \theta \text{sign}(\cos \theta) \frac{d\sigma}{d \cos \theta}, \quad (6.2.2)$$

with θ denoting the angle between the top-quark and positron three-momenta defined in the center-of-mass frame. BSM contributions are parametrized according to Eq.(4.2.1) and are included in both numerator and denominator.

Helicity fractions are computed according to Ref. [305] including also quadratic terms. As discussed in Sec. 4.2, only \tilde{C}_{uW} gives contributions at $\mathcal{O}(\Lambda^{-2})$. Similarly, the top-quark decay width is computed following Ref. [302] including contributions from quadratic terms.

For $Z \rightarrow b\bar{b}$ observables we employ `MadGraph5_aMC@NLO` and the `dim6top_L0` UFO model for the computation. We consider the forward-backward asymmetry $A_{FB}^{0,b}$ and the ratio of partial width for $Z \rightarrow f\bar{f}$

$$R_b = \frac{\Gamma_{b\bar{b}}}{\Gamma_{\text{had}}}, \quad \Gamma = \Gamma^{\text{SM}} + \sum_i \tilde{C}_i \Gamma_i^{\text{int}} + \sum_{i \leq j} \tilde{C}_i \tilde{C}_j \Gamma_{ij}^{\text{BSM}}. \quad (6.2.3)$$

BSM contributions to $A_{FB}^{0,b}$ are computed using Eq. 6.2.2, and for R_b we include BSM contributions in both numerator and denominator.

In the case of $b \rightarrow s$ transitions, the matching conditions in Eqs. (6.1.8)-(6.1.14) together with SMEFT RGE evolution from the scale μ to μ_W enable us to compute B -physics observables in terms of SMEFT Wilson coefficients $\tilde{C}_i(\mu)$ with $\mu = 1$ TeV. For $b \rightarrow s\gamma$ and $b \rightarrow s\ell^+\ell^-$ transitions we employ `flavio` and `wilson` to compute SM predictions and BSM contributions in terms of the WET coefficients ΔC_i at the scale $\mu_W = m_W$. We consider BSM contributions at LO in α_s and employ `wilson` to run the coefficients from the scale μ_W down to the scale μ_b . In the case of $b \rightarrow s\nu\bar{\nu}$ transitions, the branching ratio of $B \rightarrow K^{(*)}\nu\bar{\nu}$

amounts to [367]

$$\text{BR}(B \rightarrow K^{(*)}\nu\bar{\nu}) = \text{BR}(B \rightarrow K^{(*)}\nu\bar{\nu})_{\text{SM}} \frac{|\Delta C_L(\mu_b) - C_L(\mu_b)_{\text{SM}}|}{C_L(\mu_b)_{\text{SM}}}. \quad (6.2.4)$$

The SM values are given as [367]

$$\text{BR}(B^+ \rightarrow K^+\nu\bar{\nu})_{\text{SM}} = (4.0 \pm 0.5) \times 10^{-6}, \quad (6.2.5)$$

$$\text{BR}(B^0 \rightarrow K^{*0}\nu\bar{\nu})_{\text{SM}} = (9.2 \pm 1.0) \times 10^{-6}, \quad (6.2.6)$$

where $C_L(\mu_b)_{\text{SM}} = \frac{X_s}{\sin^2\theta_w}$ and $X_s = 1.469 \pm 0.017$. For $B_s - \bar{B}_s$ mixing we consider the mass difference between the two mass eigenstates [372]

$$\Delta M_s = \Delta M_s^{\text{SM}} \left| 1 + \frac{\Delta C_{1,tt}^{\text{mix}}(\mu_W)}{S_0(x_t)} \right|, \quad (6.2.7)$$

where S_0 denotes the Inami–Lim function [373], and ΔM_s^{SM} is the SM value, for which we consider $\Delta M_s^{\text{SM}} = (18.4_{-1.2}^{+0.7}) \text{ ps}^{-1}$ [372].

6.2.2 Sensitivity to Wilson coefficients

In Tab. 6.1 we summarize BSM contributions to the different observables included in our analysis. We illustrate the order at which contributions arise with the following notation: contributions at tree level are denoted by \tilde{C}_i , contributions at one-loop level are indicated via $[\tilde{C}_i]$, and $\{\tilde{C}_i\}$ shows contributions arising via mixing at $\mathcal{O}(\alpha_s)$. Furthermore, with additional asterisks $\tilde{C}_i^{(*)}$ and $\tilde{C}_i^{(**)}$ we identify coefficients whose tree-level definitions are altered when including loop-level effects. Such effects are suppressed by at least one order of magnitude, see Eqs.(6.2.8),(6.2.9), and App. H.2.

At the LHC, observables from top-quark pair-production processes and top-quark decay allow to constrain the three dipole coefficients \tilde{C}_{uX} with $X = B, G, W$, $\tilde{C}_{\varphi q}^{(1)}$, $\tilde{C}_{\varphi q}^{(3)}$, and $\tilde{C}_{\varphi u}^2$. Interestingly, measurements of $t\bar{t}Z$ production allow to test the only the linear combination $\tilde{C}_{\varphi q}^-$. Thus, inclusion of the top-quark decay width, which is sensitive to \tilde{C}_{uW} and $\tilde{C}_{\varphi q}^{(3)}$, is paramount to constrain $\tilde{C}_{\varphi q}^{(1)}$ and $\tilde{C}_{\varphi q}^{(3)}$ simultaneously. Note that \tilde{C}_{uG} contributes only through mixing and running to B -physics and lepton-collider observables.

For $Z \rightarrow b\bar{b}$, BSM contributions arise through $\tilde{C}_{\varphi q}^+$. The remaining coefficients in (6.1.5) do not contribute to this process as they do not alter the $Zb\bar{b}$ vertex.

BSM contributions to $b \rightarrow s\gamma$ transitions do not arise at tree level, and are induced only at one-loop level through \tilde{C}_{uB} , \tilde{C}_{uG} , \tilde{C}_{uW} , and $\tilde{C}_{\varphi q}^{(3)}$. Observables measured in $b \rightarrow s\ell^+\ell^-$ processes receive BSM contributions at tree level from \tilde{C}_{lq}^+ , $\tilde{C}_{\varphi q}^+$, and \tilde{C}_{qe} . For the later operator, contributions cancel in the left-chiral combination $\Delta C_9 - \Delta C_{10}$, which dominates the interference term with the SM in semileptonic B decays. Conversely, $B_s \rightarrow \mu^+\mu^-$ is sensitive to ΔC_{10} , which highlights the importance of including this process. At one-loop level, all eleven coefficients (6.1.5) contribute to $\Delta C_{9,10}$ (\tilde{C}_{uG} only through RGE mixing). Contributions from \tilde{C}_{lu} , \tilde{C}_{eu} , \tilde{C}_{qe} , \tilde{C}_{lq}^+ , $\tilde{C}_{\varphi q}^{(1)}$, and partially $\tilde{C}_{\varphi q}^{(3)}$ can be absorbed in the tree-

²Additional constraints arise from single-top production, see Chapter 4 and Ref. [237]. However, bin-to-bin correlations can be sizable [25], but are yet unknown, and thus we do not consider these observables here.

Process	Observable	Two-fermion operators	Four-fermion operators
$pp \rightarrow t\bar{t}$	σ^{inc}	\tilde{C}_{uG}	-
$pp \rightarrow t\bar{t}\gamma$	σ^{fid}	$\tilde{C}_{uB}, \tilde{C}_{uW}, \tilde{C}_{uG}$	-
$pp \rightarrow t\bar{t}Z$	σ^{inc}	$\tilde{C}_{uB}, \tilde{C}_{uW}, \tilde{C}_{uG}, \tilde{C}_{\varphi q}^-, \tilde{C}_{\varphi u}$	-
$t \rightarrow bW$	$F_{0,L}$	\tilde{C}_{uW}	-
Top decay	Γ_t	$\tilde{C}_{\varphi q}^{(3)}, \tilde{C}_{uW}$	-
$Z \rightarrow b\bar{b}$	$A_{FB}^b, R_b, \sigma_{\text{had}}$	$\tilde{C}_{\varphi q}^+$	-
$b \rightarrow s\gamma$	BR	$[\tilde{C}_{uB}], [\tilde{C}_{uW}], \{\tilde{C}_{uG}\}, [\tilde{C}_{\varphi q}^{(3)}]$	-
$b \rightarrow s\ell^+\ell^-$	BR, $A_{FB}, P_i^{(\prime)}, S_i, F_L, d\text{BR}/dq^2$	$[\tilde{C}_{uB}], [\tilde{C}_{uW}], \{\tilde{C}_{uG}\}, \tilde{C}_{\varphi q}^{+(*)}, [\tilde{C}_{\varphi q}^{(3)}]$	$\tilde{C}_{lq}^{+(*)}, \tilde{C}_{qe}^{(*)}$
$b \rightarrow s\nu\bar{\nu}$	BR	$\tilde{C}_{\varphi q}^{+(**)}$	$\tilde{C}_{lq}^{-(*)}$
Mixing	ΔM_s	$[\tilde{C}_{uW}], \{\tilde{C}_{uG}\}, [\tilde{C}_{\varphi q}^{(1)}], [\tilde{C}_{\varphi q}^{(3)}]$	-
$e^+e^- \rightarrow t\bar{t}$	σ, A_{FB}	$\tilde{C}_{uB}, \tilde{C}_{uW}, \{\tilde{C}_{uG}\}, \tilde{C}_{\varphi q}^-, \tilde{C}_{\varphi u}$	$\tilde{C}_{eu}, \tilde{C}_{qe}, \tilde{C}_{lu}, \tilde{C}_{lq}^-$

Table 6.1: Sensitivity to SMEFT coefficients for the various processes considered. Coefficients \tilde{C}_i without any additional markings denote contributions at tree level. With additional parentheses $[\tilde{C}_i]$ and $\{\tilde{C}_i\}$ we mark coefficients that contribute at one-loop level and through RGE mixing at $\mathcal{O}(\alpha_s)$ only, respectively. Asterisks $\tilde{C}_i^{(*)}$ and $\tilde{C}_i^{(**)}$ show for which coefficients additional contributions at one-loop level alter their tree-level definitions, see Eqs. (6.2.8) and (6.2.9).

level definitions of the fit degrees of freedom

$$\begin{aligned}
\tilde{C}_{lq}^{+(*)} &= \tilde{C}_{lq}^+ + \frac{\alpha}{\pi \sin^2 \theta_w} \left(I_1(x_t) \tilde{C}_{lu} + I_2(x_t) \tilde{C}_{lq}^+ \right), \\
\tilde{C}_{qe}^{(*)} &= \tilde{C}_{qe} + \frac{\alpha}{\pi \sin^2 \theta_w} \left(I_1(x_t) \tilde{C}_{eu} + I_2(x_t) \tilde{C}_{qe} \right), \\
\tilde{C}_{\varphi q}^{+(*)} &= \tilde{C}_{\varphi q}^+ + \frac{\alpha}{\pi \sin^2 \theta_w} \left(I_1(x_t) \tilde{C}_{\varphi u} + I_2(x_t) \tilde{C}_{\varphi q}^+ \right).
\end{aligned} \tag{6.2.8}$$

Further contributions from $\tilde{C}_{\varphi q}^{(3)}$, \tilde{C}_{uB} , \tilde{C}_{uG} , and \tilde{C}_{uW} cannot be absorbed and additional degrees of freedom arise, see Eqs. (6.1.9)-(6.1.12). However, such contributions are parametrically suppressed by at least one order of magnitude compared to tree-level ones. Considering $b \rightarrow s\nu\bar{\nu}$ transitions, contributions at tree level are proportional to $\tilde{C}_{lq}^- + \tilde{C}_{\varphi q}^+$. One-loop matching gives rise to contributions from \tilde{C}_{uW} , $\tilde{C}_{\varphi q}^{(1)}$, $\tilde{C}_{\varphi q}^{(3)}$, $\tilde{C}_{\varphi u}$, $\tilde{C}_{lq}^{(1)}$, $\tilde{C}_{lq}^{(3)}$, and \tilde{C}_{lu} , which can be absorbed into $\tilde{C}_{\varphi q}^{+(**)}$ and $\tilde{C}_{lq}^{-(*)}$

$$\begin{aligned}
\tilde{C}_{\varphi q}^{+(**)} &= \tilde{C}_{\varphi q}^+ - \sqrt{2} \frac{\alpha m_t}{\pi m_W} I_{uW}^\nu \tilde{C}_{uW} - \frac{\alpha}{\pi} I_{\varphi q}^{\nu(3)}(x_t) \tilde{C}_{\varphi q}^{(3)} + \frac{\alpha}{\pi} \left(I_{lu}^\nu(x_t) \tilde{C}_{\varphi u} + I_{\varphi q}^{\nu(1)} \tilde{C}_{\varphi q}^{(1)} \right), \\
\tilde{C}_{lq}^{-(*)} &= \tilde{C}_{lq}^- + \frac{\alpha}{\pi} \left(I_{lu}^\nu(x_t) \tilde{C}_{lu} + I_{lq}^{\nu(1)}(x_t) \tilde{C}_{lq}^{(1)} \right) + \frac{\alpha}{\pi} I_{lq}^{\nu(3)}(x_t) \tilde{C}_{lq}^{(3)}.
\end{aligned} \tag{6.2.9}$$

In the case of B_s mixing, BSM contributions from \tilde{C}_{uW} , \tilde{C}_{uG} (through $\mathcal{O}(\alpha_s)$ SMEFT RGE evolution only), $\tilde{C}_{\varphi q}^{(1)}$, and $\tilde{C}_{\varphi q}^{(3)}$ arise at one-loop level (6.1.14). EW RGE effects both within

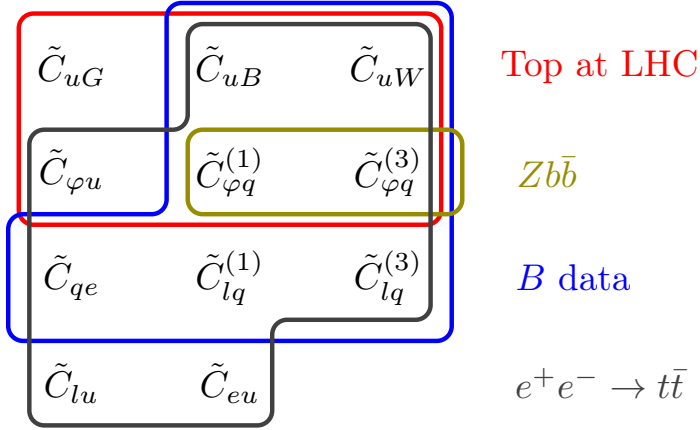


Figure 6.2: Schematic overview of dominant contributions from SMEFT coefficients to the different sets of observables considered here. Subleading one-loop contributions as well as mixing-induced ones from \tilde{C}_{uG} are neglected.

WET [374] and SMEFT are taken into account in the numeric fits but omitted here for the sake of clarity.

To summarize, while all eleven coefficients contribute to the B -physics observables considered here, most of these effects arise at one-loop level. The only exceptions are contributions at tree level from $\tilde{C}_{\varphi q}^+$, \tilde{C}_{lq}^+ , \tilde{C}_{qe} , and \tilde{C}_{lq}^- , which stem from flavor rotations. In addition, effects from \tilde{C}_{uB} are important as they dominate in ΔC_7 [23]. Thus, we expect strong constraints on these operators from B physics, while others are expected to be much less constrained.

Top-quark physics at a future lepton collider is sensitive to contributions from nine SMEFT coefficient. These comprise five two-fermion coefficients \tilde{C}_{uB} , \tilde{C}_{uG} (through mixing only), \tilde{C}_{uW} , $\tilde{C}_{\varphi q}^-$, and $\tilde{C}_{\varphi u}$, as well as four four-fermion ones: \tilde{C}_{eu} , \tilde{C}_{lu} , \tilde{C}_{qe} , and \tilde{C}_{lq}^- . Two-fermion operators affect both the ttZ and $tt\gamma$ vertices, while four-fermion operators introduce contact interactions. Combining $\ell^+\ell^- \rightarrow t\bar{t}$ observables with top-quark ones at LHC, $Z \rightarrow b\bar{b}$ transition observables, and B -physics ones allows to test the complete eleven-dimensional parameter space. This combination is particularly beneficial for \tilde{C}_{eu} and \tilde{C}_{lu} , which remain only poorly constrained by Belle II and (HL-)LHC, even when considering the recent analysis by CMS [27]. The sensitivities to dominant BSM contributions are illustrated in Fig. 6.2.

6.3 Fits to present data

We employ *EFTfitter* to constrain SMEFT and WET Wilson coefficients using a Bayesian interpretation. For all fits, we assume a uniform distribution over the interval $-1 \leq \tilde{C}_i \leq 1$ as the prior, unless otherwise specified. We include both experimental uncertainties, for which we add statistical and systematic uncertainties in quadrature, and theory uncertainties. In our fits, all uncertainties are assumed to follow a Gaussian distribution, see Sec. 3.5 and Refs.[23, 25, 164] for details. Contributions of dimension-six operators are parametrized according to Sec. 6.2. Purely BSM contributions $\sim \tilde{C}_i\tilde{C}_j$ are formally of higher order in the EFT expansion, $\mathcal{O}(\Lambda^{-4})$. However, it has been shown in Chapter 4 as well as Ref. [234] that these contributions are only a subleading source of uncertainty as long as the linear terms in the EFT expansion dominate, as expected in regions where the EFT is valid.

We include measurements of observables from top-quark pair-production processes, top-

Process	Observable	\sqrt{s}	Int. luminosity	Experiment	Ref.	SM Ref.
$t\bar{t}\gamma$	$\sigma^{\text{fid}}(t\bar{t}\gamma, 1\ell)$	13 TeV	36.1 fb $^{-1}$	ATLAS	[313]	[313, 314]
	$\sigma^{\text{fid}}(t\bar{t}\gamma, 2\ell)$					
$t\bar{t}Z$	$\sigma^{\text{inc}}(t\bar{t}Z)$	13 TeV	77.5 fb $^{-1}$	CMS	[376]	[377–379]
$t\bar{t}$	$\sigma^{\text{inc}}(t\bar{t})$	13 TeV	36.1 fb $^{-1}$	ATLAS	[380]	[381]
	F_0, F_L	8 TeV	20.2 fb $^{-1}$	ATLAS	[285]	[303]
	Γ_t	8 TeV	20.2 fb $^{-1}$	ATLAS	[283]	[304]

Table 6.2: List of observables and measurements for top-quark processes at the LHC together with the references of the experimental analyses and the SM predictions.

quark decay, $Z \rightarrow b\bar{b}$ transitions, and $b \rightarrow s$ transitions. Measurements of the same observable from different experiments and at different energies can in principle be correlated [279]. If correlations are provided, they are included, comprising bin-to-bin correlations in $b \rightarrow s$ angular distributions and those between W boson helicity fractions. Unknown correlations can alter the results of fits significantly, as discussed in Ref. [25] and Chapter 4. Hence, in order to minimize the impact of these unknown correlations, we follow the approach in Refs. [18, 237] and include only the most precise measurement of an observable in the fit. In particular, as no complete correlation matrices for kinematic distributions measured in top-quark processes are provided by experiments, we do not include them. Instead, we consider only measurements of total cross sections in the analysis, as well as measurements of W -boson helicity fractions. For angular distributions of $b \rightarrow s\mu\mu$ transitions complete correlation matrices of experimental uncertainties are provided. Therefore, we include these measurements in our analysis. In addition, various measurements of B -physics observables have been combined by the HFLAV collaboration. Wherever possible, we include these averaged experimental values in our analysis. One notable exception is the $B_s \rightarrow \mu^+\mu^-$ branching ratio for which we consider the latest measurement by LHCb instead [375] presented at 55th Rencontres de Moriond 2021. For all remaining unknown correlations we make the simplifying assumption that the measurements are uncorrelated.

In Sec. 6.3.1, we present constraints from fits to individual sets of top-quark measurements, $Z \rightarrow b\bar{b}$ data, and B -physics measurements. In Sec. 6.3.2, we perform a global fit, and discuss how different sensitivities of individual observables enhance the constraints.

6.3.1 Fits to individual sets

In Tab. 6.2 we summarize the observables and measurements of top-quark processes at the LHC considered in this analysis. We include measurements of fiducial cross sections $\sigma^{\text{fid}}(t\bar{t}\gamma, 1\ell)$ and $\sigma^{\text{fid}}(t\bar{t}\gamma, 2\ell)$ of $t\bar{t}\gamma$ production in the single lepton and dilepton channel, respectively. We further add inclusive cross sections $\sigma^{\text{inc}}(t\bar{t}Z)$ and $\sigma^{\text{inc}}(t\bar{t})$ of $t\bar{t}Z$ and $t\bar{t}$ production, respectively, measurements of the W boson helicity fractions $F_{0,L}$, and data on the top-quark decay width. SM predictions at NLO for $t\bar{t}\gamma$ cross sections are taken from Refs. [313, 314], and predictions for $t\bar{t}Z$ cross sections include are computed at NLO QCD including EQ corrections [377–379]. The SM predictions for $t\bar{t}$ cross sections, W boson helicity fractions, and the total decay width at NNLO QCD are taken from Refs. [380, 381], Ref. [303], and Ref. [304] respectively.

In Fig. 6.3 we show results obtained in a fit to the data in Tab. 6.2, which allows to test six SMEFT coefficients. The strongest constraints are found for \tilde{C}_{uG} and \tilde{C}_{uW} , whose width

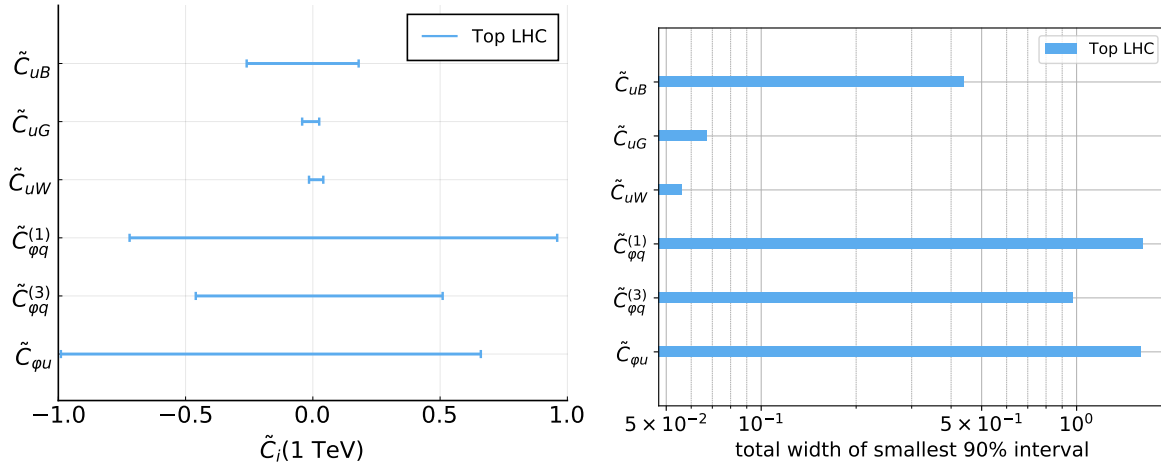


Figure 6.3: Constraints on SMEFT coefficients \tilde{C}_i from a fit of six coefficients to top-quark data in Tab. 6.2. Shown are the position (left) and the total width (right) of the marginalized smallest intervals containing 90 % of the posterior probability.

of the smallest intervals is about $(6 - 7) \times (10^{-2})$. In case of \tilde{C}_{uG} , constraints arise from the $t\bar{t}$ production cross section, while for \tilde{C}_{uW} they are dominated by measurements of the helicity fractions. Constraints on \tilde{C}_{uB} stem mostly from $t\bar{t}\gamma$ cross sections and are at the level of $\mathcal{O}(10^{-1})$. While measurements of the top-quark decay width allow to test $\tilde{C}_{\varphi q}^{(3)}$, the constraints are very weak, $\mathcal{O}(1)$, and are currently limited by experimental uncertainties. In contrast, both $\tilde{C}_{\varphi q}^{(1)}$ and $\tilde{C}_{\varphi u}$ are barely constrained by $t\bar{t}Z$ measurements, $\mathcal{O}(1)$, due to sizable correlations between their contributions. Additional information on the shape of the posterior distribution is shown in Fig. H.1 in App. H.3 where we show one-dimensional and two-dimensional projections of the posterior distribution.

Precision measurements of Z -pole observables have been performed at LEP1 and SLC [309, 382]. We consider observables sensitive to BSM contributions to the $Zb\bar{b}$ vertex, *i.e.* measurements of the forward-backward asymmetry and the ratio of partial $Z \rightarrow f\bar{f}$ width [382]

$$A_{FB}^{0,b \text{ Exp}} = 0.0996 \pm 0.0016, \quad R_b^{\text{Exp}} = 0.21629 \pm 0.00066. \quad (6.3.1)$$

Corresponding SM predictions read [309, 382]

$$A_{FB}^{0,b \text{ SM}} = 0.1030 \pm 0.0002, \quad R_b^{\text{SM}} = 0.21581 \pm 0.00002. \quad (6.3.2)$$

The results of a fit of one ($\tilde{C}_{\varphi q}^+$) and two ($\tilde{C}_{\varphi q}^{(1)}, \tilde{C}_{\varphi q}^{(3)}$) coefficients to $Z \rightarrow b\bar{b}$ data are shown in Fig. 6.4 for $\tilde{C}_{\varphi q}^+$ (left) and in the $\tilde{C}_{\varphi q}^{(1)} - \tilde{C}_{\varphi q}^{(3)}$ plane (right). The dataset constraint $\tilde{C}_{\varphi q}^+$ to about 10^{-3} , and we observe deviations from the SM at the 2σ level induced by the discrepancy in $A_{FB}^{0,b}$. As expected, when considering results in the $\tilde{C}_{\varphi q}^{(1)} - \tilde{C}_{\varphi q}^{(3)}$ plane, we observe a flat direction and strong correlations between the coefficients. Only a very small slice of the two-dimensional parameter space (corresponding to $\tilde{C}_{\varphi q}^{(1)} \sim -\tilde{C}_{\varphi q}^{(3)}$) is allowed by data.

In Tab. 6.3 we summarize measurements of observables for $b \rightarrow s$ transitions considered in our analysis. This set comprises inclusive and exclusive branching ratios of $b \rightarrow s\gamma$ processes, total and differential branching ratios, angular distributions in $b \rightarrow s\mu^+\mu^-$ transitions, and

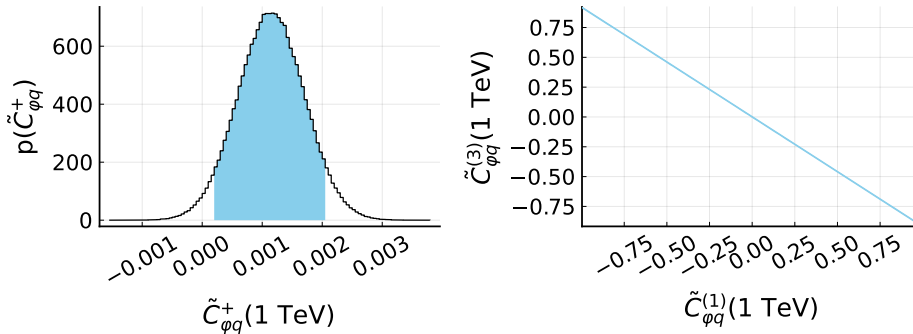


Figure 6.4: Results of fits to $Zb\bar{b}$ data considering $\tilde{C}_{\varphi q}^+$ (left) and $\tilde{C}_{\varphi q}^{(1)}$ and $\tilde{C}_{\varphi q}^{(3)}$ (right) as degrees of freedom. Shown are the one-dimensional (left) and two-dimensional (right) projection of the posterior distribution obtained in fits of one and two coefficients, respectively. Colored areas correspond to the smallest intervals containing 90% of the posterior distribution.

Process	Observable	q^2 bin [GeV ²]	Experiment	Ref.	SM Ref.
$\bar{B} \rightarrow X_s \gamma$	$\text{BR}_{E_\gamma > 1.6 \text{ GeV}}$	-	HFLAV	[315]	[316]
$B^0 \rightarrow K^* \gamma$	BR	-	HFLAV	[315]	[347]
$B^+ \rightarrow K^{*+} \gamma$	BR	-	HFLAV	[315]	[347]
$\bar{B} \rightarrow X_s \ell^+ \ell^-$	BR	[1, 6]	BaBar	[385]	[386]
	A_{FB}	[1, 6]	Belle	[387]	[386]
$B_s \rightarrow \mu^+ \mu^-$	BR	-	LHCb	[375]	[347]
$B^0 \rightarrow K^* \mu^+ \mu^-$	$F_L, P_1, P_2, P_3, P_4, P_5', P_6', P_8'$	[1, 1, 6]	LHCb	[90]	[347]
$B^0 \rightarrow K \mu^+ \mu^-$	$d\text{BR}/dq^2$	[1, 6]	LHCb	[84]	[347]
$B^+ \rightarrow K^+ \mu^+ \mu^-$	$d\text{BR}/dq^2$	[1, 6]	LHCb	[84]	[347]
$B^+ \rightarrow K^{*+} \mu^+ \mu^-$	$d\text{BR}/dq^2$	[1, 6]	LHCb	[84]	[347]
$B_s \rightarrow \phi \mu^+ \mu^-$	F_L, S_3, S_4, S_7	[1, 6]	LHCb	[85]	[347]
$\Lambda_b \rightarrow \Lambda \mu^+ \mu^-$	$d\text{BR}/dq^2$	[15, 20]	LHCb	[388]	[347]
$B_s - \bar{B}_s$ mixing	ΔM_s	-	HFLAV	[315]	[372]

Table 6.3: B -physics measurements included in the fit. For observables measured in q^2 bins (where q^2 denotes the squared invariant dilepton mass), we include only one bin due to unknown correlations between different bins.

inclusive branching ratios and asymmetries of $b \rightarrow \ell^+ \ell^-$ transitions. Corresponding SM predictions and theory uncertainties are computed with `flavio`. Furthermore, we include the $B_s - \bar{B}_s$ mass difference ΔM_s , whose SM prediction is taken from Ref. [372]. In addition to these measurements, upper limits on $B \rightarrow K^{(*)} \nu \bar{\nu}$ branching ratios have been derived by Belle[383] and BaBar[384]. However, as there is currently no possibility to include such upper limits in `EFTfitter`, we do not consider them at this point.

In Fig. 6.5 we give results for the WET coefficients $\Delta C_i(\mu_W)$ at the matching scale (upper plots) derived from a fit to data in Tab. 6.3. As can be seen, the strongest constraints are obtained for ΔC_7 and ΔC_1^{mix} , where the size of the interval is about $(4 - 6) \times 10^{-1}$. In contrast, \tilde{C}_8 is only very weakly constrained, $\mathcal{O}(1)$, since this coefficient contributes only via mixing with ΔC_7 . Thus, we find a strong correlation between these two coefficients. In the

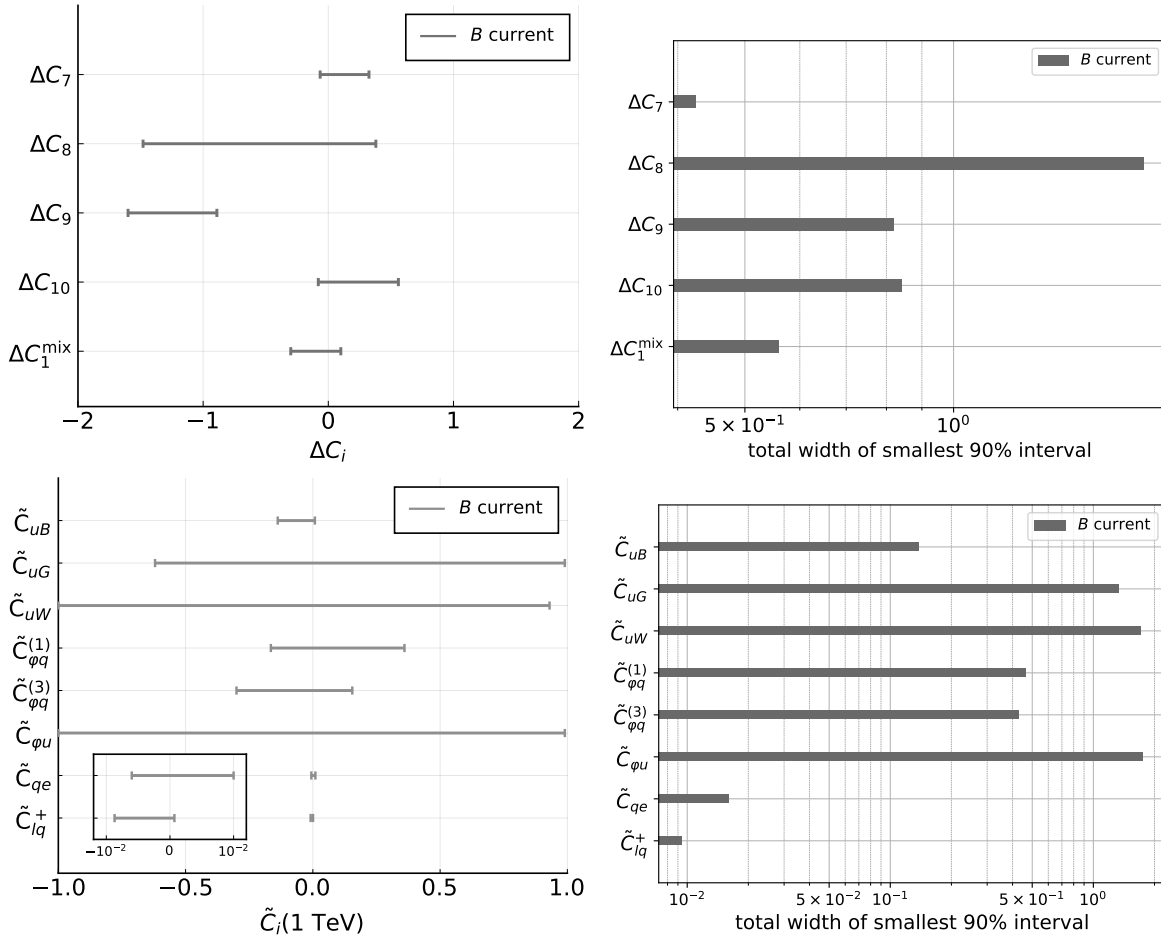


Figure 6.5: Results for WET coefficients ΔC_i at the scale μ_W (upper plots) and SMEFT coefficients (lower plots) from a fit of five WET and eight SMEFT coefficients to B data in Tab. 6.3. Shown are the position (left) and the total width (right) of the smallest intervals containing 90% of the posterior probability. The results are obtained assuming a uniform distribution over the interval $-2 \leq \Delta C_i \leq 2$ ($-1 \leq \tilde{C}_i \leq 1$) as the prior for the WET (SMEFT) coefficients.

case of ΔC_{10} , weaker constraints are imposed compared to those on ΔC_7 and ΔC_1^{mix} and the size of the interval is about 1.8 times larger. For ΔC_9 , we find a similar size of the 90% interval, about 8×10^{-1} . However, in contrast to the remaining WET coefficients, we find deviations from the SM in ΔC_9 . This effect can be traced back to the measurements of angular distributions included in our fit. Especially P'_5 shows deviations from the SM, which is widely known and discussed in the literature, see *e.g.* Ref. [389] for a detailed discussion. Results for WET coefficients can be translated into constraints on SMEFT coefficients, which turn out to be strongly correlated due to matching conditions, see Eqs. 6.1.8-(6.1.14). The results from a fit of eight SMEFT coefficients (compare Tab. 6.1 and Eq. (6.3.3)) to B data in Tab. 6.3 are shown in Fig. 6.5 (lower plots). Strong constraints at the level of $\mathcal{O}(10^{-2})$ are obtained for the semileptonic four-fermion coefficients \tilde{C}_{qe} and \tilde{C}_{lq}^+ . Constraints on the remaining coefficients are about one to two orders of magnitude weaker. Note that deviations from the SM, which are present in ΔC_9 in Fig. 6.5, can not be seen in the one-dimensional

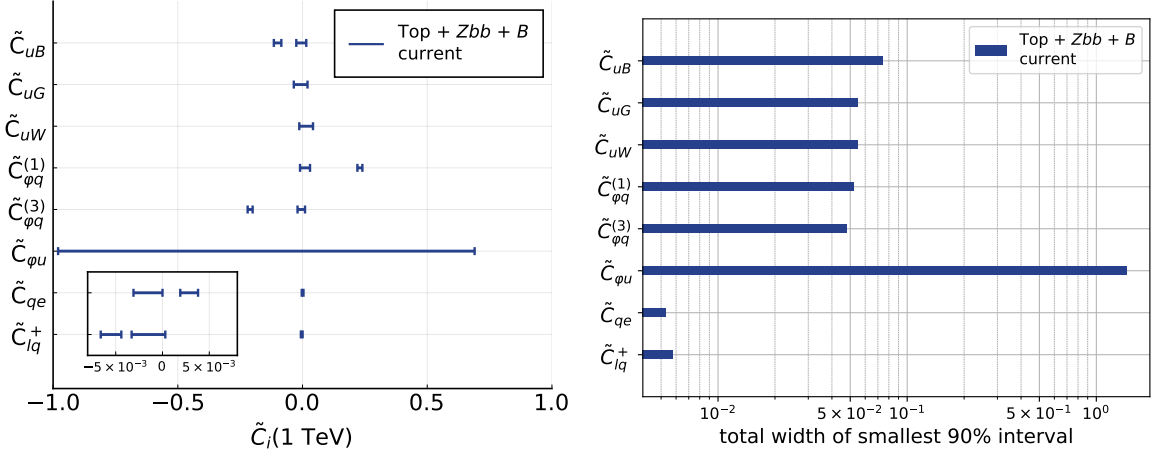


Figure 6.6: Results from a fit of eight SMEFT coefficients (6.3.3) to data in Tabs. 6.2 and 6.3 and Zbb data. Shown are the position (left) and the total width (right) of the marginalized smallest intervals containing 90 % of the posterior probability.

projections of the SMEFT coefficients due to the correlations induced by matching conditions.

6.3.2 Combined fit to present data

Fits to the combined set of top-quark, $Z \rightarrow b\bar{b}$, and B -physics data allow to test a larger number of coefficients compared to fits to the individual datasets. Here, measurements in Tabs. 6.2 and 6.3 together with Zbb data constrain eight coefficients:

$$\tilde{C}_{uB}, \quad \tilde{C}_{uG}, \quad \tilde{C}_{uW}, \quad \tilde{C}_{\varphi q}^{(1)}, \quad \tilde{C}_{\varphi q}^{(3)}, \quad \tilde{C}_{\varphi u}, \quad \tilde{C}_{qe}, \quad \tilde{C}_{lq}^+. \quad (6.3.3)$$

Results of the fit are shown in Fig. 6.6. Additional information on the two-dimensional projections of the posterior distribution is provided in Fig. H.3. The strongest constraints are found for \tilde{C}_{qe} and \tilde{C}_{lq}^+ , whose width of the interval is around $(5 - 6) \times 10^{-3}$. Such strong constraints are expected, as both coefficients give sizable contributions to $\Delta C_{9,10}$ at tree level (6.1.8), see also Fig. 6.5 (lower plots). As can be seen, the SM is not included in the interval of \tilde{C}_{qe} . This is shown in more detail for both four-fermion coefficients in Fig. 6.8. In the case of \tilde{C}_{uB} , \tilde{C}_{uG} , \tilde{C}_{uW} , $\tilde{C}_{\varphi q}^{(1)}$, and $\tilde{C}_{\varphi q}^{(3)}$, constraints are about one order of magnitude weaker, $(5 - 7) \times 10^{-2}$. Results for \tilde{C}_{uG} and \tilde{C}_{uW} coincide with those obtained from fits to top-quark data only. Conversely, for the other coefficients we see a significant tightening of the constraints. For \tilde{C}_{uB} , this enhancement stems from the orthogonal sensitivities of top-quark and B data, as already seen in Sec. 5.5. Here, the effect is more pronounced due to the additional observables included in the fit. The effect of the different sensitivities is exemplified in Fig. 6.7 (left plot) where we compare constraints in the \tilde{C}_{uB} - \tilde{C}_{uW} plane obtained in fits to different datasets. Similarly, the combination of Zbb data, which strongly constraints $\tilde{C}_{\varphi q}^+$ (see Fig. 6.4), with top-quark and B -physics observables, which strongly constrain $\tilde{C}_{\varphi q}^{(3)}$ as shown in Fig. 6.7 (right), significantly tightens the constraints. For both $\tilde{C}_{\varphi q}^{(1)}$ and $\tilde{C}_{\varphi q}^{(3)}$, the combined set yields constraints of about 5×10^{-2} , and the SM is included in the smallest interval, see Fig. H.4. Conversely, constraints on $\tilde{C}_{\varphi u}$ are significantly weaker, $\mathcal{O}(1)$, since $t\bar{t}Z$ data provides only a limited sensitivity and contributions to B -physics observables are strongly suppressed. The fit yields two solutions for \tilde{C}_{uB} , $\tilde{C}_{\varphi q}^{(1)}$, $\tilde{C}_{\varphi q}^{(3)}$, \tilde{C}_{qe} , and \tilde{C}_{lq}^+ , one of

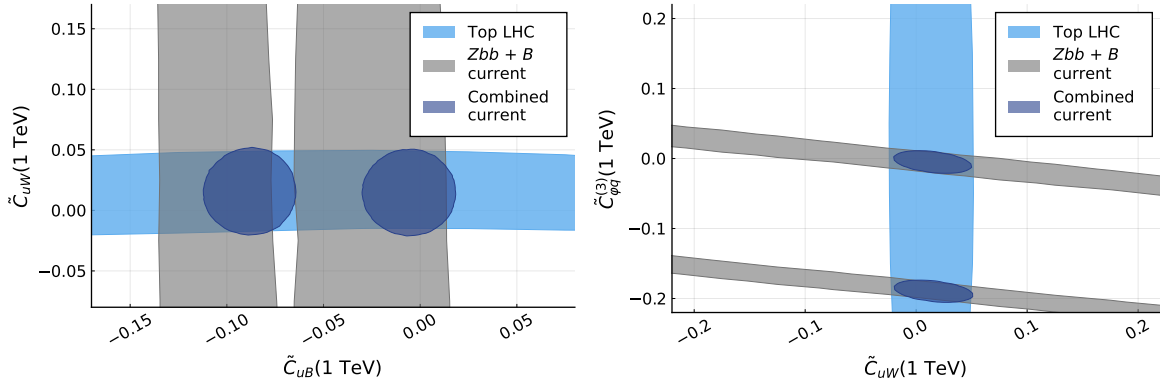


Figure 6.7: Two examples for two-dimensional projections of the posterior distribution from fits of eight coefficients to top-quark data in Tab. 6.2 (light blue), B -physics data in Tab. 6.3 (grey) and the combined dataset (blue) in the \tilde{C}_{uW} - \tilde{C}_{uB} plane (left) and \tilde{C}_{uW} - $\tilde{C}_{\varphi q}^{(3)}$ plane (right). Shown are the marginalized smallest regions containing 90% of the posterior probability of coefficients in Eq. (6.3.3).

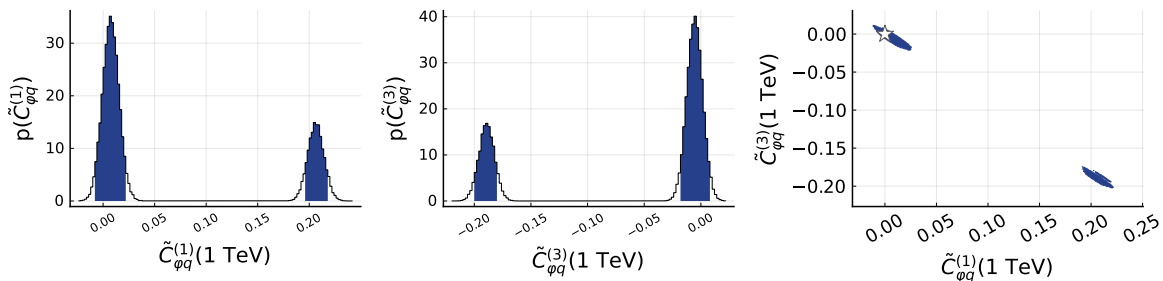


Figure 6.8: One-dimensional (left, middle) and two-dimensional (right) projections of the posterior distribution for \tilde{C}_{qe} and \tilde{C}_{lq}^+ (lower row). Results are obtained for a fit to the combined set of present top-quark, $Zb\bar{b}$, and B -physics data. The star in the rightmost plot denotes the SM point.

which is SM like, while the other deviates from the SM. The reason for two solutions is the quadratic ansatz (4.2.3), which in general allows for two solutions, as we already saw in Sec. 5.5. In addition, correlations among several coefficients arise from the matching of SMEFT onto WET. Since the number of degrees of freedom in WET is smaller than in SMEFT these correlations can not be completely removed. Without inclusion of further observables with a different sensitivity, this ambiguity can not be resolved. To validate our fit, we compare our result to a recent study of $b \rightarrow s\mu^+\mu^-$ data in Ref. [390]. In this analysis, operators are defined in the basis with diagonal down-type Yukawa couplings, and thus an additional factor $1/(V_{tb}V_{ts}^*)$ has to be included. Taking this factor into account, the results in Ref. [390] correspond to $\tilde{C}_{qe}, \tilde{C}_{lq}^+ \sim 10^{-3}$, which is consistent with our results in Fig. 6.6. As a different number of degrees of freedom is considered in this analysis, we repeated our fit considering \tilde{C}_{qe} and \tilde{C}_{lq}^+ only and found agreement with Ref. [390].

Additional constraints, particularly on four-fermion operators, arise from Drell–Yan processes. Amongst the operators considered here, this affects $\tilde{C}_{\varphi q}^+$, \tilde{C}_{qe} , and \tilde{C}_{lq}^+ , similar to $b \rightarrow sl^+\ell^-$ and $Zb\bar{b}$ data. Constraints on semileptonic four-fermion operators with b quarks

derived from present Drell–Yan data and a future 3000 fb^{-1} projection are at the level of $\mathcal{O}(10^{-2})$ [22, 391], and weaker compared to our combined fit, see Fig. 6.6. Note also that the flavor of the initial quark in the pp collision is undetermined, which permits an actual measurement of flavor-specific coefficients. A detailed study of the impact of Drell–Yan data in the context of global fits is beyond the scope of this work.

6.4 Constraints at future colliders

In the future, both HL-LHC at 14 TeV and 3000 fb^{-1} and Belle II at 50 ab^{-1} are going to test the SM with significantly higher precision. In Sec. 6.4.1, we investigate the impact of measurements at these future facilities on constraints on SMEFT Wilson coefficients.

In addition, measurements of top-quark observables at a future lepton collider provide additional tests of SMEFT coefficients [361]. A first projection of the expected precision at the CLIC has been provided in Ref. [364]. CLIC is a proposed electron-positron collider with a longitudinal polarization of $\pm 80\%$ for the electron beam and an unpolarized positron beam. This collider is intended to operate at three different center-of-mass energies: 380 GeV, 1.4 TeV, and 3 TeV. We consider the foreseen precision of top-quark pair-production measurements at such a collider, and investigate the impact of these measurements on the SMEFT coefficients in Sec. 6.4.2.

In Sec. 6.4.3, we combine projections for HL-LHC, Belle II, and CLIC with existing data and work out constraints on the Wilson coefficient in a global fit.

6.4.1 Constraints in the near-future scenario

For the expected experimental uncertainties at HL-LHC and Belle II we adopt estimates by ATLAS, CMS and Belle II [392–396]. If no estimate of the expected systematic uncertainties are given, we assume that they shrink by a factor of two relative to present data. For the observables considered here, this is the case for $t\bar{t}$ and $t\bar{t}Z$ cross sections, the W boson helicity fractions, and the top-quark decay width. Similarly, in order to simulate improvements of MC predictions and higher-order calculations, we assume that theory uncertainties shrink by a factor of two compared to current SM computations. Observables and references for expected experimental and theory precision are given in Tab. 6.4. To investigate the impact of the hints for BSM physics in present $b \rightarrow s\mu^+\mu^-$ angular distributions in the light of higher luminosity runs at future experiments, we consider central values of present data for the future projections. If no measurement is available, we consider the SM value instead.

For measurements of fiducial cross sections of $t\bar{t}\gamma$ production, the analysis in Refs. [392, 393] provides expected uncertainties for different final-state channels. For both the single-lepton and dilepton cross sections we estimate the precision considering the channel with the largest experimental uncertainty. In the case of $t\bar{t}Z$ production, we assume that statistical uncertainties scale according to the integrated luminosity, following the analysis in Refs. [393, 394]. For simplicity, systematic uncertainties are assumed to shrink by a factor of two, as a more profound estimate requires detector-level simulations which are beyond the scope of this work. To estimate the expected precision of $t\bar{t}$ production cross sections we consider the study of differential $t\bar{t}$ cross sections in Refs. [393, 395], and use the same assumptions for the uncertainties as for $t\bar{t}Z$. Since no projections for W boson helicity fractions and the top-quark decay width are provided, we follow the procedure for $t\bar{t}$ and $t\bar{t}Z$ cross sections.

Our future projection for $b \rightarrow s$ measurements is based on Ref. [396]. For inclusive branching ratios of $b \rightarrow s\gamma$, we consider the expected precision of $\text{BR}(\bar{B} \rightarrow X_s\gamma)_{E_\gamma > 1.9 \text{ GeV}}$ and

Process	Observable	q^2 bin [GeV ²]	Experiment	Ref.	SM Ref.
$t\bar{t}\gamma$	$\sigma^{\text{fid}}(t\bar{t}\gamma, 1\ell), \sigma^{\text{fid}}(t\bar{t}\gamma, 2\ell)$	-	ATLAS	[392, 393]	[313, 314]
$t\bar{t}Z$	$\sigma^{\text{inc}}(t\bar{t}Z)$	-	CMS	[393, 394]	[377–379]
$t\bar{t}$	$\sigma^{\text{inc}}(t\bar{t})$	-	CMS	[393, 395]	[381]
	F_0, F_L	-	-	-	[303]
	Γ_t	-	-	-	[304]
$\bar{B} \rightarrow X_s \gamma$	$\text{BR}_{E_\gamma > 1.6 \text{ GeV}}$	-	Belle II	[396]	[316]
$B^0 \rightarrow K^* \gamma$	BR	-	Belle II	[396]	[347]
$B^+ \rightarrow K^{*+} \gamma$	BR	-	Belle II	[396]	[347]
$\bar{B} \rightarrow X_s \ell^+ \ell^-$	BR, A_{FB}	[3.5, 6]	Belle II	[396]	[386]
$B^0 \rightarrow K^* \mu^+ \mu^-$	$F_L, P_1, P_2, P_3, P'_4, P'_5, P'_6, P'_8$	[1.1, 2.5], [2.5, 4], [4, 6]	Belle II	[396]	[347]
$B^0 \rightarrow K^{(*)} \nu \bar{\nu}$	BR	-	Belle II	[396]	[347]

Table 6.4: Overview of future HL-LHC and Belle II projections for observables included in our analysis. For each process, we give the references for the experimental projection and the SM prediction. For the $1.1 \text{ GeV}^2 \leq q^2 \leq 2.5 \text{ GeV}^2$ bin in $B^0 \rightarrow K^* \mu^+ \mu^-$ angular observables, we consider the Belle II estimate for the experimental precision for the $1.0 \text{ GeV}^2 \leq q^2 \leq 2.5 \text{ GeV}^2$ bin.

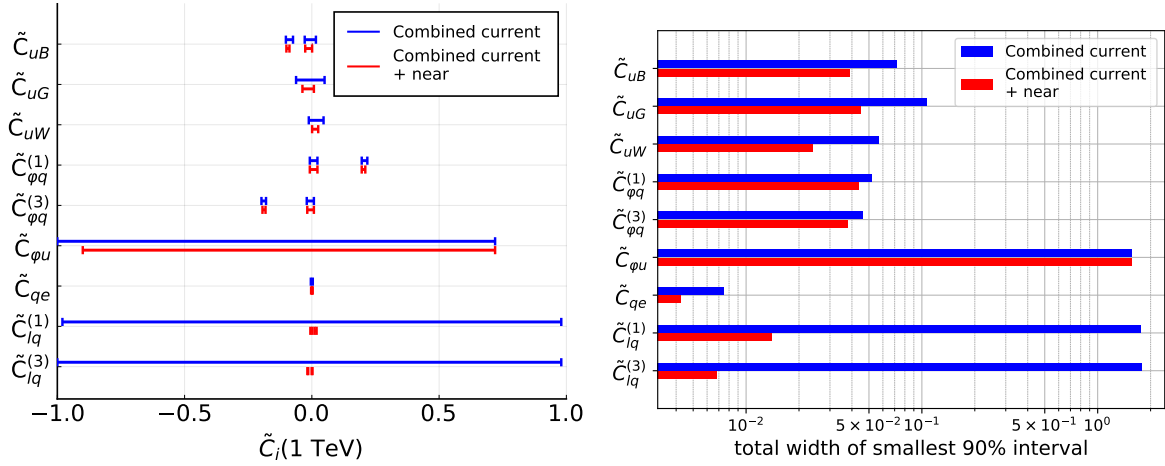


Table 6.5: Constraints on coefficients \tilde{C}_i obtained from fits of nine coefficients to present measurements in Tabs. 6.2 and 6.3 (blue) and from present measurements and projections of top-quark and B observables in Tabs. 6.2-6.4 (red). Shown are the position (left) and the total width (right) of the marginalized smallest intervals containing 90% of the posterior probability.

assume that the same uncertainty applies for $E_\gamma > 1.6 \text{ GeV}$. For exclusive branching ratios, we take into account estimates for $B^{(+)} \rightarrow K^{*(+)}\gamma$, and include projections for the $3.5 \text{ GeV}^2 \leq q^2 \leq 6 \text{ GeV}^2$ bin for both the branching ratio and the forward-backward asymmetry of $\bar{B} \rightarrow X_s \ell^+ \ell^-$ transitions. For the latter, we explicitly checked that other bins offer a very comparable sensitivity. For $B \rightarrow K^* \mu^+ \mu^-$ observables, we include projections for the angular distribution observables in three different q^2 bins, and investigate implications of anomalies found within present data.

The combined fit to present data and projections for top-quark and B -physics observables at HL-LHC and Belle II, respectively, allows to probe nine SMEFT coefficients, as shown

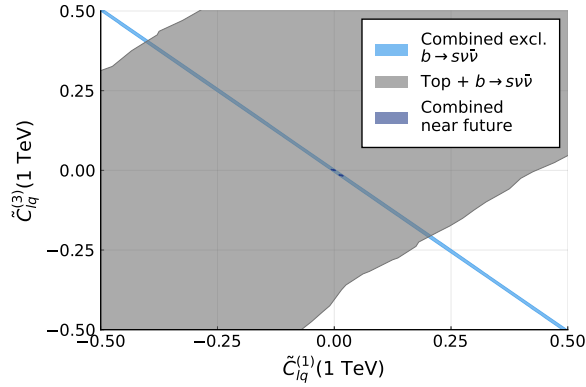


Figure 6.9: Two-dimensional projection of the posterior distribution in the $\tilde{C}_{lq}^{(1)}$ - $\tilde{C}_{lq}^{(3)}$ plane obtained in fits of nine coefficients in the near future projection including top-quark observables and all beauty observables except $b \rightarrow s\nu\bar{\nu}$ ones (light blue), top-quark observables and only $b \rightarrow s\nu\bar{\nu}$ ones (grey), and the combined set (dark blue). Colored areas correspond to the smallest intervals containing 90% of the posterior distribution.

in Fig. 6.5. To obtain these constraints, we used a smaller interval $-0.1 \leq \tilde{C}_i \leq 0.1$ for the prior of the four-fermion coefficients. A larger interval would lead to convergence issues due to the small size of the posterior distribution. We explicitly checked that no solutions are lost using this ansatz. At this point, we do not include subleading contributions of \tilde{C}_{lu} and \tilde{C}_{eu} , which are studied in Sec. 6.4.3. As can be seen in Fig. 6.5, the observables at HL-LHC and Belle II data yield strong constraints on all coefficients with the exception of $\tilde{C}_{\varphi u}$. This coefficient is only weakly constrained, $\mathcal{O}(1)$, due to low sensitivities in both $t\bar{t}Z$ and B -physics observables. In contrast, the projections yield strong constraints on the four-fermion coefficient, about $(4-14) \times 10^{-3}$, where the strongest ones are obtained for \tilde{C}_{qe} . In particular, $\tilde{C}_{lq}^{(1)}$ and $\tilde{C}_{lq}^{(3)}$ can be tested simultaneously because the inclusion of $b \rightarrow s\nu\bar{\nu}$ observables provides a orthogonal sensitivity compared to $b \rightarrow s\ell^+\ell^-$ observables. This is shown in Fig. 6.9 where it also becomes obvious that constraints in the combined fit are significantly stronger than expected from simply overlaying constraints from individual sets. The reason for this enhancement is not directly visible in two-dimensional projections of the posterior distribution: Constraints from different observables are combined in the multi-dimensional parameter space, which removes flat directions present in fits to individual datasets and reduces correlations between coefficients, as already seen in Sec. 5.5. Interestingly, we find two solutions for both $\tilde{C}_{lq}^{(1)}$ and $\tilde{C}_{lq}^{(3)}$; one of which is SM-like, while the other one implies $\tilde{C}_{lq}^{(1)} \sim -\tilde{C}_{lq}^{(3)} \sim 10^{-3}$ and deviates strongly from the SM. This is shown in more detail in Fig. H.5 in App. H.4 where we give the one- and two-dimensional projections of the posterior distribution for both coefficients. Without further input, this ambiguity cannot be resolved. Constraints on the remaining coefficients \tilde{C}_{uB} , \tilde{C}_{uG} , \tilde{C}_{uW} , $\tilde{C}_{\varphi q}^{(1)}$, and $\tilde{C}_{\varphi q}^{(3)}$ are about $(2.5-4.5) \times 10^{-2}$. For \tilde{C}_{uB} (\tilde{C}_{uW}) the improved precision of $t\bar{t}\gamma$ and $b \rightarrow s\gamma$ observables (helicity fractions) enhances the constraints by a factor of 1.5 (2.2), and for the remaining coefficients constraints remain mostly unchanged compared to Fig. 6.6.

\sqrt{s}	Observable	Polarization (e^-, e^+)	Ref. experiment	SM Ref.
380 GeV	$\sigma_{t\bar{t}}$	($\pm 80\%$, 0)	[364]	[361]
	A_{FB}	($\pm 80\%$, 0)	[364]	[361]
1.4 TeV	$\sigma_{t\bar{t}}$	($\pm 80\%$, 0)	[364]	[361]
	A_{FB}	($\pm 80\%$, 0)	[364]	[361]
3 TeV	$\sigma_{t\bar{t}}$	($\pm 80\%$, 0)	[364]	[361]
	A_{FB}	($\pm 80\%$, 0)	[364]	[361]

Table 6.6: Observables at different energies and polarizations for $t\bar{t}$ production at CLIC [364]. The SM prediction considered in this analysis are taken from [361].

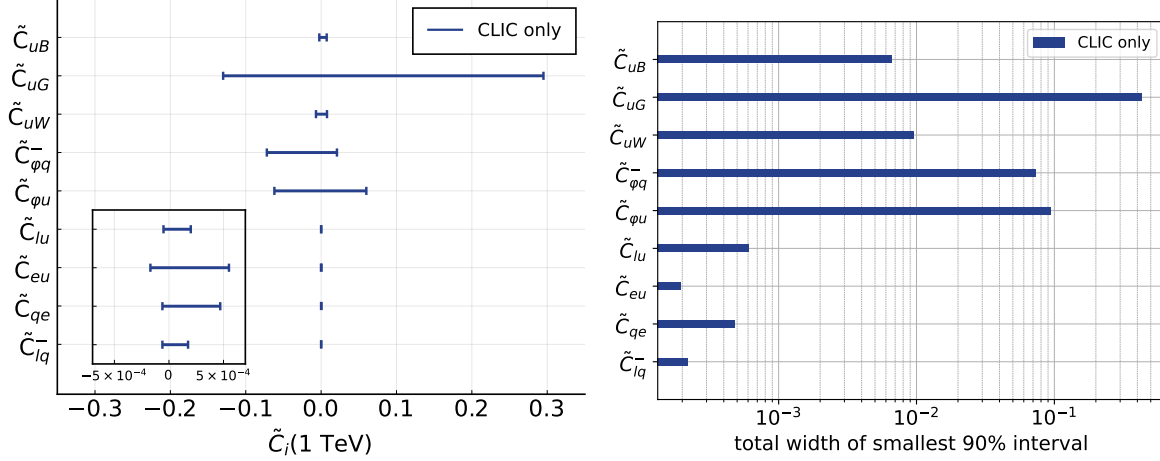


Table 6.7: Results from a fit of nine coefficients to CLIC future projections in Tab. 6.6. Constraints on the coefficients \tilde{C}_i are shown as the position (left) and the total width (right) of the smallest intervals containing 90% of the posterior probability.

6.4.2 Constraints in the far-future scenario

Top-quark observables for CLIC projections are listed in Tab. 6.6. This set includes total cross sections of top-quark pair production and forward-backward asymmetries for different beam polarizations and energy stages [364]. SM predictions are computed at NLO [361], and we use these predictions as nominal values for the observables.

The results of the fit to observables in Tab. 6.6 are shown in Fig. 6.7. The constraints are derived using a smaller interval $|\tilde{C}_i| \leq 0.1$ for the prior distribution of the four-fermion coefficients in order to avoid convergence issues. These arise due to the small size of the posterior region, and we explicitly checked that no solution is lost when applying a smaller interval. As can be seen, the strongest constraints are found for the four-fermion coefficients, whose width of the smallest interval is $(2-6) \times 10^{-4}$. Constraints on the remaining coefficients are weaker, as expected, since contributions from four-fermion operators receive an energy enhancement compared to both the SM and other operators. For \tilde{C}_{uB} and \tilde{C}_{uW} the width of the interval is 7×10^{-3} and 10^{-2} , respectively. Constraints on $\tilde{C}_{\varphi q}^-$ and $\tilde{C}_{\varphi u}$ are about one order of magnitude weaker due to interference between their contributions. The weakest constraints of about 4×10^{-1} are found for \tilde{C}_{uG} , whose contributions are mixing-induced only.

Note that $\tilde{C}_{lq}^{(1)}$ and $\tilde{C}_{lq}^{(3)}$ evolve differently under the RGE flow. This introduces corrections at the level of $\mathcal{O}(1)\%$. This allows to constrain both coefficients simultaneously at the level

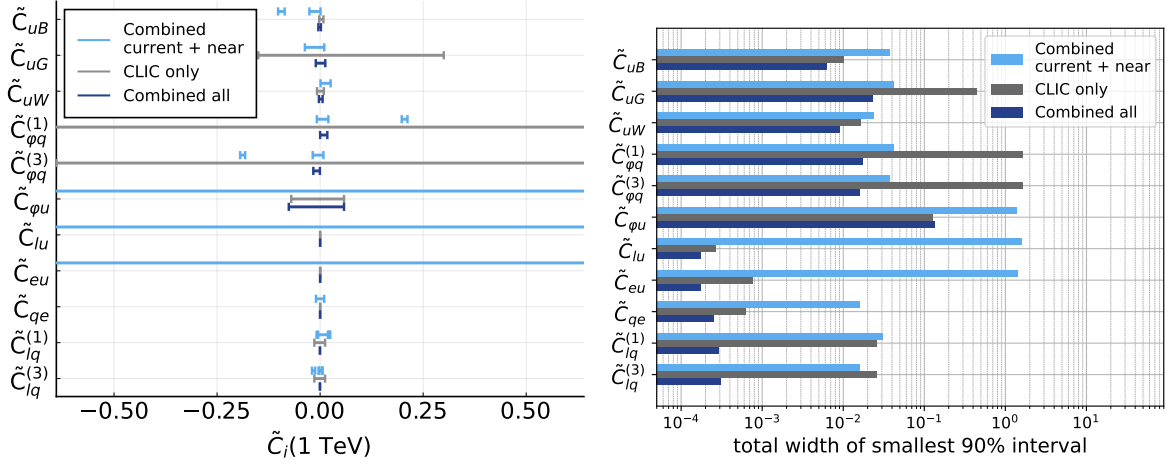


Figure 6.10: Constraints on coefficients \tilde{C}_i from fits of eleven coefficients to top-quark and B -physics data and near-future projections in 6.2-6.4 (light blue), to CLIC projections in Tab. 6.6 (grey) and the combined set (blue). For all fits, we give the marginalized smallest intervals containing 90% of the posterior probability.

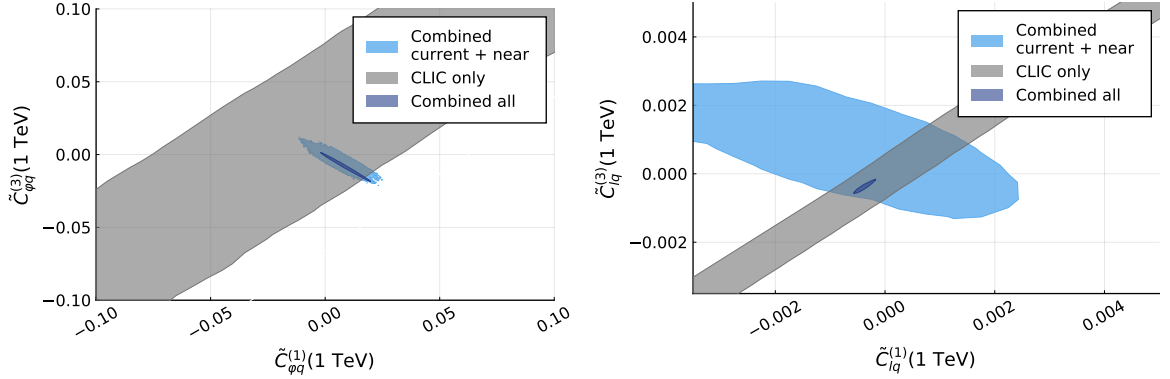


Figure 6.11: Two examples for two-dimensional projections of the posterior distribution from fits of eleven coefficients to top-quark and B -physics data and near-future projections in Tabs. 6.2-6.4 (light blue), CLIC projections in Tab. 6.6 (grey) and the combined set (blue) in the $\tilde{C}_{\varphi q}^{(1)} - \tilde{C}_{\varphi q}^{(3)}$ plane (left) and the $\tilde{C}_{lq}^{(1)} - \tilde{C}_{lq}^{(3)}$ plane (right). Shown are the marginalized smallest regions containing 90% of the posterior probability.

of $\mathcal{O}(10^{-2})$ using only CLIC observables, see Fig. 6.10 for details.

6.4.3 Combined fit

Combining present data (Tabs. 6.2 and 6.3 and Zbb data), near-future projections for HL-LHC and Belle II (Tab. 6.4), and far-future projections for CLIC (Tab. 6.6) allows to constrain all SMEFT Wilson coefficients considered in this analysis. In Fig. 6.10 we compare results from three fits: a fit to present data and HL-LHC and Belle II projections (light blue), a fit to CLIC projections (grey), and a fit to the combined set (blue). All eleven coefficients can be constrained in the combined fit and flat directions in the posterior distribution are removed. The strongest constraints are obtained for the four-fermion coefficient, $\mathcal{O}(10^{-4})$. Constraints

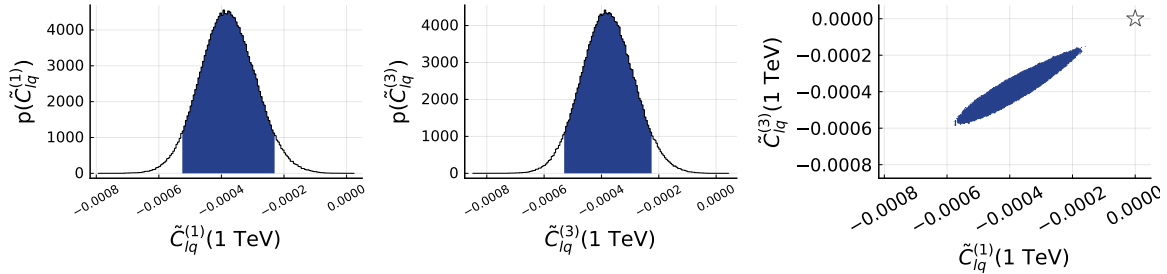


Figure 6.12: One-dimensional (left, middle) and two dimensional (right) projections of the posterior distribution of $\tilde{C}_{lq}^{(1)}$ and $\tilde{C}_{lq}^{(3)}$ obtained in the fit of eleven coefficients to the combined set of present data, HL-LHC and Belle II projections, and CLIC projections. The colored areas show the smallest intervals containing 90% of the posterior distribution, and the star denotes the SM.

on the remaining coefficients are at the level of $\mathcal{O}(10^{-2})$ for \tilde{C}_{uB} , \tilde{C}_{uG} , \tilde{C}_{uW} , $\tilde{C}_{\varphi q}^{(1)}$, and $\tilde{C}_{\varphi q}^3$, and $\mathcal{O}(10^{-1})$ for $\tilde{C}_{\varphi u}$.

As already seen in Sec. 6.3.2, stronger constraints arise in the combination of different observables. For both $\tilde{C}_{\varphi q}^{(1)}$ and $\tilde{C}_{\varphi q}^{(3)}$, which are already strongly constrained by present data and near future projections, CLIC observables yield constraints that are orthogonal to those from the remaining observables, see Fig. 6.11 (left). This complementarity strengthens the constraints by a factor of two and allows to remove the non-SM branch leaving only one region in the posterior distribution. However, a strong correlation between both coefficients remains. The combined fit yields particularly strong constraints on $\tilde{C}_{lq}^{(1)}$ and $\tilde{C}_{lq}^{(3)}$, whose intervals shrink by almost two orders of magnitude compared to the fit in the near-future scenario (see Fig. 6.5). Again, the second solution is excluded. While $b \rightarrow s\nu\bar{\nu}$ and $b \rightarrow s\ell^+\ell^-$ observables allow to probe both coefficients simultaneously, the inclusion of CLIC observables is paramount to remove the second solution around $\tilde{C}_{lq}^{(1)} \sim -\tilde{C}_{lq}^{(3)} \sim 10^{-2}$, as shown in detail in Fig. 6.11 (right). Again, constraints are significantly stronger in the combined fit than expected considering the overlay of constraints from individual sets. The reason is that the combined fit removes flat directions in the parameter space and Fig. 6.11 shows only two-dimensional projections. Correlations between $\tilde{C}_{lq}^{(1)}$ and $\tilde{C}_{lq}^{(3)}$, which stem from CLIC observables, are still present in the combined fit and sizeable deviations from the SM can be found. This is shown in more detail in Fig. 6.12. These deviations arise due to deviations in angular distributions of $b \rightarrow s\mu^+\mu^-$, in particular from assuming that Belle II confirms central values of LHCb data. While CLIC observables yield strong constraints on \tilde{C}_{lq}^- (assuming SM predictions for central values), the position of the smallest interval in the $\tilde{C}_{lq}^{(1)} \sim \tilde{C}_{lq}^{(3)}$ subspace depends on results from Belle II, see Fig. 6.12. Assuming SM values for Belle II observables, we find agreement with the SM in $\tilde{C}_{lq}^{(1)}$ and $\tilde{C}_{lq}^{(3)}$, see Fig. H.6.

As discussed in Sec. 6.1.1, results in the global fit including present data, HL-LHC and Belle II projections, and CLIC projections are obtained assuming lepton flavor universality. In BSM scenarios with different couplings to the lepton generations, our results cannot be applied directly, however, the findings on the orthogonality of the constraints from different datasets as well as the synergies between top and beauty continue to hold.

6.5 Summary

In this chapter, we performed fits within the SMEFT framework to observables from top-quark pair-production processes, Zbb data, and $b \rightarrow s$ transitions. We pointed out how each individual set of observables constrains a different subset of coefficients (See Fig. 6.2) affecting top-quark physics (6.1.5) at present and future colliders. We extended the work presented in Chapter 5, and included semileptonic four-fermion operators. These are strongly connected to the flavor anomalies seen in current B data, see Sec. 2.3.3, and are only weakly constrained by present top-quark data [27]. Exploiting $SU(2)_L$ invariance of the SMEFT Lagrangian, we related top-quark and beauty physics, a well-known procedure with recent application in other semileptonic processes [223], and applied this link to top-quark and beauty observables at present and future colliders. A global fit to top-quark data in Tab. 6.2, Zbb data, and B -physics data in Tab. 6.3 yields constraints on eight SMEFT Wilson coefficients, see Fig. 6.6. The complementarity of constraints from individual datasets significantly improves the fits, as shown in Fig. 6.7, and removes flat directions in the parameter space. Considering future scenarios beyond present data, we studied implications of measurements at HL-LHC, BelleII, and a future lepton collider at the example of CLIC. Measurements of top-quark observables at HL-LHC test the same set of coefficients already probed by present data. In contrast, qualitative improvements are implied by additional measurements of $b \rightarrow s\nu\bar{\nu}$ transitions at Belle II, which, assuming lepton flavor universality, allow to test four-fermion operators in new ways. Constraints derived from these transitions are orthogonal to those obtained from $b \rightarrow s\mu^+\mu^-$, and offer a sensitivity similar to contact interactions of charged leptons and top quarks, see Fig. 6.1. Including these future projections allows to test nine SMEFT coefficient with a sensitivity shown in Fig. 6.5. Further including top-quark observables at a future lepton collider, which probe $\tilde{C}_{\varphi u}$, $\tilde{C}_{l u}$, and $\tilde{C}_{e u}$, see Fig. 6.7, allows to test all eleven coefficients considered here 6.1.5, as shown in Fig. 6.10. In particular, the second solution for $\tilde{C}_{l q}^{(1)}$ and $\tilde{C}_{l q}^{(3)}$ present in fits in the near future scenario can be removed when including lepton-collider measurements, as shown in Fig. 6.11. Expected constraints on coefficients of four-fermion operators are at the level of $\mathcal{O}(10^{-4})$. Interestingly, despite the strong constraints derived from CLIC observables, the fate of deviations from the SM in $\tilde{C}_{l q}^{(1)}$ and $\tilde{C}_{l q}^{(3)}$ implied by present LHCb data depends on measurements at Belle II, as shown in Fig. 6.12. Again, this is due to the complementarity of the constraints derived from the different sets of observables.

To summarize, $SU(2)_L$ relations between top and beauty as well as different collider setups have to be employed to derive the strongest constraints on SMEFT coefficients relevant for top-quark physics and anomalies found in beauty data. This procedure allows to remove flat directions in the parameter space and to test all possible sources of BSM contributions simultaneously. In particular, this analysis highlights the strong BSM physics impact of a future lepton collider.

7 Asymptotic safety confronts collider physics

The SMEFT framework allows to search for deviations from the SM in a systematic way, which is both efficient and (almost) model independent. In this bottom-up approach, the SMEFT Lagrangian is constructed assuming that BSM particles are significantly heavier than energy scales available in present experiments. As not necessarily all extensions of the SM feature particles with masses of about 1 TeV or above, the SMEFT framework cannot always be employed to constrain BSM models. Furthermore, experimental analyses designed to explicitly test specific features of extensions of the SM are typically more sensitive to contributions of such BSM models. Thus, constraints on the parameters of these models are typically stronger compared to those derived in global SMEFT fits.

Additional guidance from top-down theory frontiers allows to extend the SM to accommodate a specific set of its theoretical shortcomings and to explain anomalies observed in AMMs of both electron and muon, see Sec. 2.3.3. In this regard, asymptotic safety has raised new opportunities for model building, keeping the theory fundamental and predictive at arbitrarily high energy scales. Asymptotically safe extensions of the SM include new flavorful scalars and vector-like leptons (VLLs)[63, 64], which can be searched for at colliders. The new scalars are special in the sense that they transform as singlets under the SM gauge group and carry two flavor indices. This makes them a matrix in flavor space, and allows for distinct flavorful signatures when connected to the SM via Yukawa interactions. As shown in Refs. [28–30], asymptotically safe models predicting three generations of VLLs and a BSM sector including flavor and Higgs portals to the SM leptons can explain the AMMs of both the electron and the muon. Most noticeably, these models do not necessarily introduce lepton flavor non-universality and explain both anomalies for regions of the parameter space where the VLLs can have masses as light as a few hundred GeV while passing bounds from several precision observables. Therefore, it is promising to search for such VLLs at colliders. First analyses at LEP [397] have excluded heavy leptons with masses below 100 GeV, while a search by ATLAS [398] for VLLs transforming as singlets under $SU(2)_L$ excluded masses in the range 114-176 GeV at 95 % CL. Constraints on a simple extension of the SM featuring one generation of $SU(2)_L$ doublet VLLs with couplings to third-generation leptons only are found to be even stronger by a recent CMS analysis [399], where VLLs within the mass region of 120-790 GeV are excluded at 95 % CL [400].

However, these constraints are derived considering simplified models and do not directly translate into constraints on the singlet and doublet models in [28–30]. Thus, in this chapter, which is based on Ref. [26], we present the phenomenological implications of these models in Sec. 7.1. We compare signatures of VLLs to present data [400] in Sec. 7.2. We highlight how specific features such as lepton-flavor-violating-like decays enable us to construct new observables, which allow for null tests of the SM, in Sec. 7.3. We consider the distributions of these observables at the expected integrated luminosity of the complete LHC Run 2 (150 fb^{-1}), and discuss implications for HL-LHC (3000 fb^{-1}) [306]. In addition, we study regions in the parameter space that do not accommodate the muon AMM. In Sec. 7.4 we summarize our results.

7.1 Asymptotically safe vector-like leptons

The models considered in the following are presented in detail in Ref. [28–30] and feature three generations of colorless VLLs $\psi_{L,R}$, which are either $SU(2)_L$ doublets with hypercharge $Y = -1/2$ (*doublet model*) or $SU(2)_L$ singlets with $Y = -1$ (*singlet model*). In the doublet model components of the $SU(2)$ doublet are referred to as

$$\psi_{L,R} = (\psi_{L,R}^0, \psi_{L,R}^-)^T. \quad (7.1.1)$$

In both models, the VLLs carry a lepton flavor index $i = 1, 2, 3$. In addition to the VLLs, the models include a set of nine singlet complex scalars S_{ij} carrying two flavor indices $i, j = 1, 2, 3$. In the interaction basis, the BSM Yukawa sectors can be written as

$$\begin{aligned} \mathcal{L}_Y^{\text{singlet}} &= -\kappa \bar{l}_L \varphi \psi_R - \kappa' \bar{e}_R S^\dagger \psi_L - y \bar{\psi}_L S \psi_R + \text{h.c.}, \\ \mathcal{L}_Y^{\text{doublet}} &= -\kappa \bar{e}_R \varphi^\dagger \psi_L - \kappa' \bar{e}_R S \psi_R - y \bar{\psi}_L S \psi_R + \text{h.c.}, \end{aligned} \quad (7.1.2)$$

where flavor and gauge indices are contracted implicitly. As can be seen, both the singlet and the doublet model provide Higgs and BSM scalar portal interactions. Following [28], we assume an $SU(3)$ flavor symmetry and identify the symmetry of the leptons with the one of the VLLs. This leads to conservation of lepton flavor and universal couplings with BSM Yukawas y, κ, κ' , which become single couplings instead of tensors. While the coupling y is crucial in the asymptotically safe framework [30, 65], its implications for phenomenology are less relevant and neglected here. Instead, we focus on interactions connecting the SM and BSM sectors via the portal couplings κ and κ' . As discussed in Refs. [28, 30], the VLLs and SM leptons mix after SSB. In the singlet model, mass eigenstates are defined as

$$\begin{pmatrix} \psi_{L,R}^m \\ e_{L,R}^m \end{pmatrix} = \begin{pmatrix} \cos \theta_{L,R} & \sin \theta_{L,R} \\ -\sin \theta_{L,R} & \cos \theta_{L,R} \end{pmatrix} \begin{pmatrix} \psi_{L,R} \\ e_{L,R} \end{pmatrix}, \quad (7.1.3)$$

with mixing angles $\theta_{L,R}$. Mass eigenstates in the doublet model are defined similarly with rotation angles $\theta_{L,R}^-$ (θ_L^0) for the charged (neutral) leptons. In the following, we drop the additional superscripts on the mass eigenstates, and continue to use our notion referring to the three light mass eigenstates as leptons and the three heavy eigenstates as VLLs. Since mixing affects the couplings of the Z boson to leptons, measurements of the decay $Z \rightarrow \ell^+ \ell^-$ [13] constrain the mixing angles [30], see [401] for recent fits. In the singlet (doublet) model, the Z -decay data demands mixing angles of left-handed (right-handed) leptons as small as $\theta_{L(R)} \simeq kv/(\sqrt{2}M_F) < \mathcal{O}(10^{-2})$, where we assume that all VLLs (all flavor and $SU(2)_L$ components) have approximately the same mass M_F . Since we find that $\theta, \kappa \ll 1$, we can employ a small-angle approximation. At leading order in κ the interactions in the mass basis in the singlet model read

$$\begin{aligned} \mathcal{L}_{\text{int}}^{\text{singlet}} &= -e \bar{\psi} \gamma^\mu \psi A_\mu + \frac{g}{\cos \theta_w} \bar{\psi} \gamma^\mu Z_\mu + \left(-\frac{\kappa}{\sqrt{2}} \bar{e}_L \psi_R h - \kappa' \bar{e}_R S^\dagger \psi_L \right. \\ &\quad \left. + g_S \bar{e}_R S^\dagger e_L + g_Z \bar{e}_L \gamma^\mu \psi_L Z_\mu + g_W \bar{\nu} \gamma^\mu \psi_L W_\mu^+ + \text{h.c.} \right), \end{aligned} \quad (7.1.4)$$

where the couplings g_i are defined as

$$g_S = \frac{\kappa' \kappa}{\sqrt{2}} \frac{v}{M_F}, \quad g_Z = -\frac{\kappa g}{2\sqrt{2} \cos \theta_w} \frac{v}{M_F}, \quad g_W = \frac{\kappa g}{2} \frac{v}{M_F}. \quad (7.1.5)$$

Similarly, the interactions in the doublet model are given as

$$\begin{aligned} \mathcal{L}_{\text{int}}^{\text{doublet}} = & -e\bar{\psi}^- \gamma^\mu \psi^- + \frac{g}{2 \cos \theta_w} [(2 \sin^2 \theta_w - 1)\bar{\psi}^- \gamma^\mu \psi^- + \bar{\psi}^- \gamma^\mu \psi^0] Z_\mu \\ & + \left(\frac{g}{\sqrt{2}} \bar{\psi}^- \gamma^\mu \psi^0 W_\mu^- - \frac{\kappa}{\sqrt{2}} \bar{e}_R \psi_L^- h - \kappa' \bar{e}_L S \psi_R^- - \kappa' \bar{\nu} S \psi_R^0 \right. \\ & \left. + g_S \bar{e}_L S e_R + g_Z \bar{e}_R \gamma^\mu \psi_R^- Z_\mu + g_W \bar{e}_R \gamma^\mu \psi_R^0 W_\mu^- + \text{h.c.} \right), \end{aligned} \quad (7.1.6)$$

with couplings

$$g_S = \frac{\kappa' \kappa}{\sqrt{2}} \frac{v}{M_F}, \quad g_Z = \frac{\kappa g}{2\sqrt{2} \cos \theta_w} \frac{v}{M_F}, \quad g_W = -\frac{\kappa g}{2} \frac{v}{M_F}. \quad (7.1.7)$$

The $\bar{\nu} \psi_L^- W^+$ vertex is present only at higher order and is not considered here, see Ref. [30] for details. As shown in Refs. [28, 30], these models accommodate both the muon and the electron $g-2$ anomalies (2.3.13) and (2.3.14), respectively. In the case of the muon anomaly, the experimental result can be explained via

$$\Delta a_\mu = \frac{\kappa'^2}{32\pi^2} \frac{m_\mu^2}{M_F^2} f\left(\frac{M_S^2}{M_F^2}\right), \quad (7.1.8)$$

with $f(t) = (2t^3 + 3t^2 - 6t^2 \ln t - 6t + 1)/(t-1)^4$ being positive for any t , and $f(0) = 1$. In order to accommodate Δa_e at one-loop level the coupling κ is mandatory. However, since Δa_e also depends on parameters of the scalar sector, κ is less constrained. Here, in order to prevent large contributions to Z -decay observables and to accommodate both AMMs, we choose to set $\kappa = 10^{-2} \kappa'$ for simplicity.

The scalar sector [28, 30, 402] includes in total four interaction terms with three quartic couplings and a Higgs portal one $\delta S^\dagger S \varphi^\dagger \varphi$. This allows for EWSB as well as non-trivial VEVs v_s for the flavor-diagonal scalars S_{ii} with two different configurations: a universal ground state, where all three diagonal scalars obtain the same VEV, and a configuration where only one flavor direction obtains a VEV, see [28, 30] for details. The phenomenological implications of δ and v_s at a pp collider are negligible, and thus we do not include them in this analysis. In total, the singlet (doublet) model comprise three flavors of VLL singlets (7.1.4) (doublets (7.1.6)) and nine scalar singlets. Assuming VLLs (scalars) to have degenerate masses M_F (M_S) and neglecting small isospin splitting $\Delta M = M_{\psi^{-1}} - M_{\psi^0} = g^2/4\pi \sin^2 \theta_w M_Z/2 \approx 0.4$ GeV [30] between ψ^0 and ψ^- in the doublet model (induced by electromagnetic interactions), our set of parameters reads

$$M_F, \quad M_S, \quad \kappa', \quad \kappa = 10^{-2} \kappa', \quad (7.1.9)$$

where we use Eq. (7.1.8) together with the muon AMM data (2.3.13) to express κ' as a function of M_F and M_S , $\kappa' = \kappa'(M_F, M_S)$. This enables us to compute the numerical predictions for collider signatures in terms of the two masses of the BSM sector. A more general scenario,

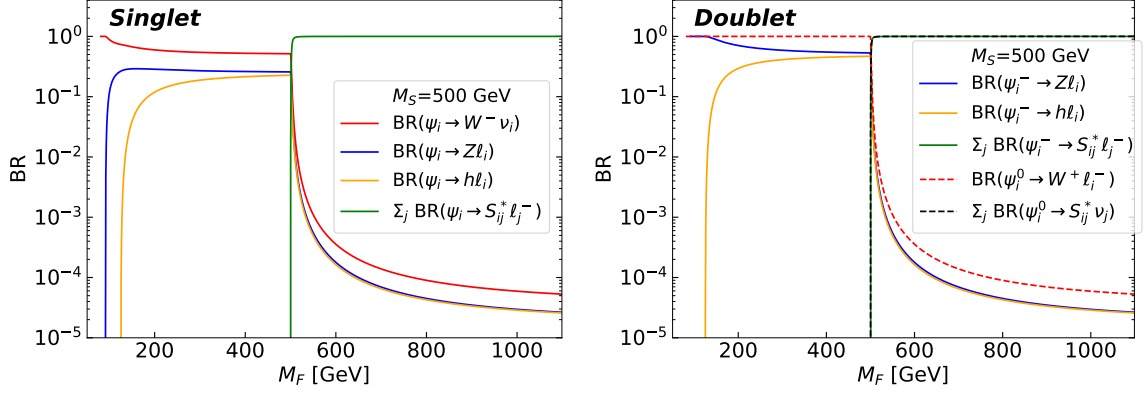


Figure 7.1: Branching ratios of the on-shell decays of the VLLS in the singlet model (left) and the doublet model (right) as a function of the mass, with $M_S = 500$ GeV. For $M_F < M_S$, only electroweak decays are possible. As we fix $\kappa = 10^{-2} \kappa'$ branching ratios are independent of κ' . Larger values of κ/κ' lead to larger branching ratios for the electroweak decays.

where we consider κ' as a free parameter, is discussed in Sec. 7.3.4.

Note that the simplified version (7.1.9) of the complete higher-dimensional parameter space succeeds in describing the leading signatures of the model relevant for a pp -collider study. For a complete investigation of the stability of the RGE flow to the Planck scale a dedicated analysis of the couplings and their interplay has to be provided. In Ref. [30], a detailed study is provided for a wide range of BSM coupling parameters and $M_F = 1000$ GeV, $M_S = 500$ GeV. While not every point in the complete BSM parameter space is necessarily asymptotically safe, the initial conditions on M_F and M_S in the range 100-1000 GeV have only a subleading effect on the RGE evolution. Hence, specific choices of BSM Yukawas and quartic couplings allow to find Planck safe trajectories using the methods described in [28, 30].

The phenomenology of VLL production at a hadron collider is outlined in Ref. [30] (together with implications for a lepton collider) and discussed in more detail in App. I.1. At the LHC, VLLs can be produced through electroweak and Yukawa interactions via single and pair production. Considering a benchmark scenario with $M_S = 500$ GeV, we find that pair-production cross sections are, in both models, about three orders of magnitude larger than single-production ones, regardless of M_F . The reason is that pair production depends only on the quantum numbers of the VLLs and is completely independent of κ and κ' . In contrast, single production is only induced by mixing (7.1.3) and is strongly suppressed due to the aforementioned Z -decay constraints.

The VLLs can decay into SM particles via mixing-induced terms or via portal interactions in Eqs. (7.1.4) and (7.1.6). If the VLLs are lighter than the BSM scalars ($M_F < M_S$), they decay either into an electroweak or Higgs boson and a charged or neutral lepton. In contrast, if kinematically allowed by the mass hierarchy of the BSM sector ($M_F > M_S$), decays into new scalars and a SM lepton dominate due to large values of κ' needed to accommodate Δa_μ . In the singlet model the VLL decay rates are given as [30]:

$$\Gamma(\psi_i \rightarrow h l_i^-) = \kappa^2 \frac{M_F}{64\pi} (1 - r_h^2)^2, \quad (7.1.10a)$$

$$\Gamma(\psi_i \rightarrow S_{ij}^* l_j^-) = \kappa'^2 \frac{M_F}{32\pi} (1 - r_S^2)^2 \quad (j \text{ fixed}), \quad (7.1.10b)$$

$$\Gamma(\psi_i \rightarrow W^- \nu_i) = g_W^2 \frac{M_F}{32\pi} (1 - r_W^2)^2 (2 + 1/r_W^2), \quad (7.1.10c)$$

$$\Gamma(\psi_i \rightarrow Z \ell_i^-) = g_Z^2 \frac{M_F}{32\pi} (1 - r_Z^2)^2 (2 + 1/r_Z^2), \quad (7.1.10d)$$

with $r_X = M_X/M_F$. Similarly, decay rates in the doublet model read

$$\Gamma(\psi_i^- \rightarrow h \ell_i^-) = \kappa^2 \frac{M_F}{64\pi} (1 - r_h^2)^2, \quad (7.1.11a)$$

$$\Gamma(\psi_i^- \rightarrow S_{ji} \ell_j^-) = \kappa'^2 \frac{M_F}{32\pi} (1 - r_S^2)^2 \quad (j \text{ fixed}), \quad (7.1.11b)$$

$$\Gamma(\psi_i^0 \rightarrow S_{ji} \nu_j) = \kappa'^2 \frac{M_F}{32\pi} (1 - r_S^2)^2 \quad (j \text{ fixed}), \quad (7.1.11c)$$

$$\Gamma(\psi_i^- \rightarrow Z \ell_i^-) = g_Z^2 \frac{M_F}{32\pi} (1 - r_Z^2)^2 (2 + 1/r_Z^2), \quad (7.1.11d)$$

$$\Gamma(\psi_i^0 \rightarrow W^+ \ell_i^-) = g_W^2 \frac{M_F}{32\pi} (1 - r_W^2)^2 (2 + 1/r_W^2). \quad (7.1.11e)$$

As can be seen, in both the singlet and doublet model the decays into S_{ij} are proportional to κ' and dominate over decays into Higgs bosons (electroweak bosons) for $\kappa' \gtrsim \kappa/\sqrt{6}$ ($\kappa' \gtrsim \kappa/\sqrt{3}$). The corresponding branching ratios are shown in Fig. 7.1 for a benchmark scenario with $M_S = 500$ GeV. The enhancement of the BSM scalar channel is caused by the potentially large values of the coupling κ' needed to accommodate the muon AMM (7.1.8), since matrix elements of the processes $\psi_i^{(-)} \rightarrow S_{ij}^* \ell_j^-$ and $\psi_i^0 \rightarrow S_{ij}^* \nu_j$ are proportional to κ' . Conversely, matrix elements for decays into SM bosons are proportional to $\kappa = 10^{-2} \kappa'$.

Decays into BSM scalars are a distinct feature of the models and set them apart from other theories with VLLs, *e.g.* [399, 403–405]. In particular, we highlight the cascade decays

$$\psi_i \rightarrow S_{ij}^* \ell_j^- \rightarrow \ell_i^- \ell_j^+ \ell_j^-, \quad (7.1.12)$$

in the singlet model and

$$\psi_i^- \rightarrow S_{ji} \ell_j^- \rightarrow \ell_i^- \ell_j^+ \ell_j^-, \quad \psi_i^0 \rightarrow S_{ji} \nu_j \rightarrow \ell_i^- \ell_j^+ \nu_j. \quad (7.1.13)$$

in the doublet model. If VLLs are heavier than the scalars on-shell decays in Eqs. (7.1.12) and (7.1.13) allow for final states with three leptons, and in particular a different-flavor dilepton pair with opposite sign and an invariant mass centered at M_S . While this signature seems to be flavor violating, the decay $S_{ji} \rightarrow \ell_i^- \ell_j^+$ is actually flavor conserving, since the BSM scalars carry two flavor indices. These flavor-violating-like decays of the BSM scalars are a distinct feature of the models (7.1.4) and (7.1.6), and provide a clean signature of BSM physics. Note that the scalars can also decay into diboson final states at one-loop level and, depending on the mass hierarchy of the BSM sector, into two VLLs or one VLL and a SM lepton at tree level, see Ref. [30]. Here, these channels are considered to be negligible due to loop suppression and the fact that scalars are only produced in decays of VLLs which kinematically forbids a decay of BSM scalars into VLLs.

State	Decay modes
$\psi_1^{(-)}$	$e^-e^+e^-, e^-\mu^+\mu^-, e^-\tau^+\tau^-$
$\psi_2^{(-)}$	$\mu^-\mu^+\mu^-, \mu^-e^+e^-, \mu^-\tau^+\tau^-$
$\psi_3^{(-)}$	$\tau^-e^+e^-, \tau^-\mu^+\mu^-$
ψ_1^0	$e^-e^+\nu_e, e^-\mu^+\nu_\mu$
ψ_2^0	$\mu^-\mu^+\nu_\mu, \mu^-e^+\nu_e$

Table 7.1: Decay modes of the VLLs (see Eqs. (7.1.12) and (7.1.13)) which can give rise to a final state with four light leptons after the VLLs are pair produced. Pair production of ψ_3^0 cannot generate such a 4L final state due to the presence of either four neutrinos or two neutrinos and two taus.

7.2 Present tests of parameter space

We focus on constraints from CMS data [400] on both the singlet (7.1.4) and the doublet (7.1.6) model. In Ref. [400], different final states with two light leptons, three light leptons, and at least four light leptons are considered in order to search for deviations from the SM. To do so, the missing transverse momentum p_T^{miss} and the scalar sum of the transverse momenta of the light leptons (e, μ) with the highest transverse momentum L_T are used as a discriminator. Dominant background processes arise in the form of diboson, $t\bar{t}$, $t\bar{t}Z$, and triboson production, which are generated using MC generators. Distributions at particle level are computed applying a full detector simulation and additional reweighting, which accounts for differences between data and simulation. Several control regions are defined for each of the final-state channels allowing for fits of the distributions to the data taken in these regions. The fitted background distributions are applied to the signal regions of the L_T distributions, and the statistical analysis of the data in these regions allows to set constraints on the simplified models in Ref. [399].

In our work, we focus on final states with at least four light leptons, referred to as $4L$, because we expect the largest contributions from decays of three generations of VLLs in both models in this channel. The reason is that non-trivial flavor structure of the BSM sector allows for various VLL production channels with at least for light leptons (see Tab. 7.1), enriching contributions from BSM processes to the signal regions of the CMS analysis. Hence, the dataset taken by CMS allows to constrain both the singlet and doublet models considered here.

In order to generate events and study production and decay of VLLs at the LHC, we employ the steps outlined in Sec. D.3. In particular, SM background processes, including ZZ , $t\bar{t}Z$ and triboson production, are generated at LO using `MadGraph5_aMC@NLO`. We also consider contributions from ZZj final states using multijet merging with `PYTHIA 8`, since programs describe parton radiation using MCMC techniques, which is formally only correct in the limit of soft and collinear emissions. For production of hard jets the complete tree-level matrix elements have to be included, which diverge for soft or collinear partons. Hence, both techniques have to be employed together and, to avoid double counting, multijet merging has to be used [406, 407]. Contributions from virtual photons via $pp \rightarrow \gamma^*\gamma^*, \gamma^*Z$ are taken into account at LO. We require pairs of leptons (regardless of their charge or flavor) to have an invariant mass of at least $m_{\ell\ell} \geq 12$ GeV to suppress contributions from quarkonia resonances and to reproduce the CMS settings. Furthermore, we include gluon-induced ZZ production $gg \rightarrow ZZ$ at one-loop level to the total cross section of ZZ production. Higher-

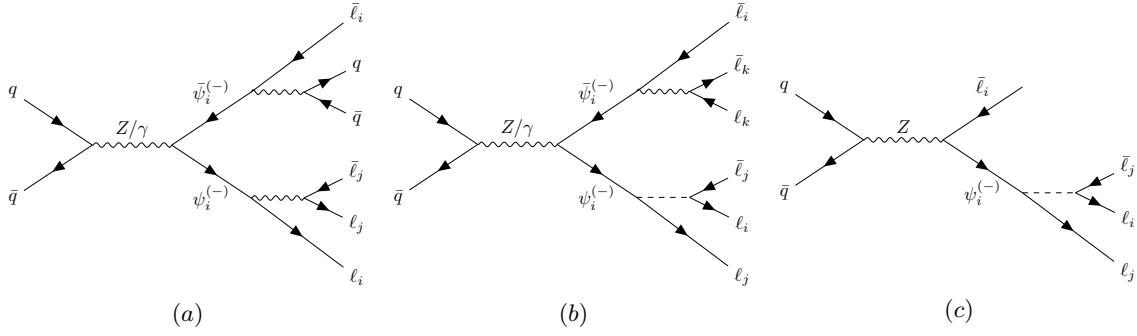


Figure 7.2: Examples for Feynman diagrams for production of final states with at least four light leptons in the singlet (7.1.4) and doublet (7.1.6) model. Single-production contributions (c) and final states with jets (a) are only possible for first and second generation vector-like leptons.

order corrections for the cross sections are taken into account applying k -factors [377, 378, 408–413]. Signal processes are generated at LO with `MadGraph5_aMC@NLO`. In all cases, we employ `PYTHIA 8` for showering and `DELPE3 3` [414] for the fast detector simulation. For all samples we use a set of cuts to define a signal region very similar to the one considered in the CMS analysis, see Tab. I.1. The settings and details on the generation process are listed in App. I.2.

7.2.1 Production of final states with at least four light leptons

In both models single and pair production of VLLs allows for 4L final states. Examples for Feynman diagrams are shown in Fig. 7.2. In the singlet model, 4L final states can be generated via the following processes:

$$pp \rightarrow \psi_i \bar{\psi}_i \rightarrow \ell_i^- \ell_i^+ \ell_j^+ \ell_j^- \ell_k^+ \ell_k^- \quad \text{for } i, j, k = 1, 2, 3, \quad (20) \quad (7.2.1a)$$

$$pp \rightarrow \psi_i \bar{\psi}_i \rightarrow \ell_i^- \ell_i^+ q_j \bar{q}_j \ell_k^+ \ell_k^- \quad \text{for } i, k = 1, 2, \quad (15 \times 4) \quad (7.2.1b)$$

$$pp \rightarrow \psi_i \bar{\psi}_i \rightarrow \ell_i^- \ell_i^+ \ell_j^+ \ell_j^- \nu_k \bar{\nu}_k \quad \text{for } i, j = 1, 2, k = 1, 2, 3, \quad (12) \quad (7.2.1c)$$

$$pp \rightarrow \psi_i \bar{\psi}_i \rightarrow \nu_i \ell_i^+ \ell_j^+ \ell_j^- \ell_k^- \bar{\nu}_k \quad \text{for } i, j, k = 1, 2, \quad (8) \quad (7.2.1d)$$

$$pp \rightarrow \psi_i \bar{\psi}_i \rightarrow \ell_i^- \bar{\nu}_i \ell_j^+ \ell_j^- \ell_k^+ \nu_k \quad \text{for } i, j, k = 1, 2, \quad (8) \quad (7.2.1e)$$

$$pp \rightarrow \psi_i \ell_i^+ \rightarrow \ell_i^- \ell_j^+ \ell_j^- \ell_i^+ \quad \text{for } i, j = 1, 2, \quad (4) \quad (7.2.1f)$$

$$pp \rightarrow \bar{\psi}_i \ell_i^- \rightarrow \ell_i^+ \ell_j^+ \ell_j^- \ell_i^- \quad \text{for } i, j = 1, 2, \quad (4) \quad (7.2.1g)$$

where i, j, k denote flavor indices and q_l denotes all quarks except the top quark (quarks stem from decays of SM bosons only). Between parentheses we give the number of 4L final states for each decay chain (summed over all indices). In the first decay chain, 4L final states occur only if at most one of the three flavor indices is equal to 3 (see Tab. 7.1).

In the doublet model, the negatively charged VLLs decay as in Eq. (7.2.1) except for decays with multiplicity eight in Eq. 7.2.1 (from $\psi_i^- \rightarrow \nu_i \ell_j^- \bar{\nu}_j$) because the $\psi^- \nu W$ vertex is only subleading. Additional contributions from the neutral VLLs via the following decay chains arise:

$$pp \rightarrow \psi_i^0 \bar{\psi}_i^0 \rightarrow \nu_j \bar{\nu}_k \ell_j^+ \ell_i^- \ell_i^+ \ell_k^- \quad \text{for } i, j, k = 1, 2, \quad (8) \quad (7.2.2a)$$

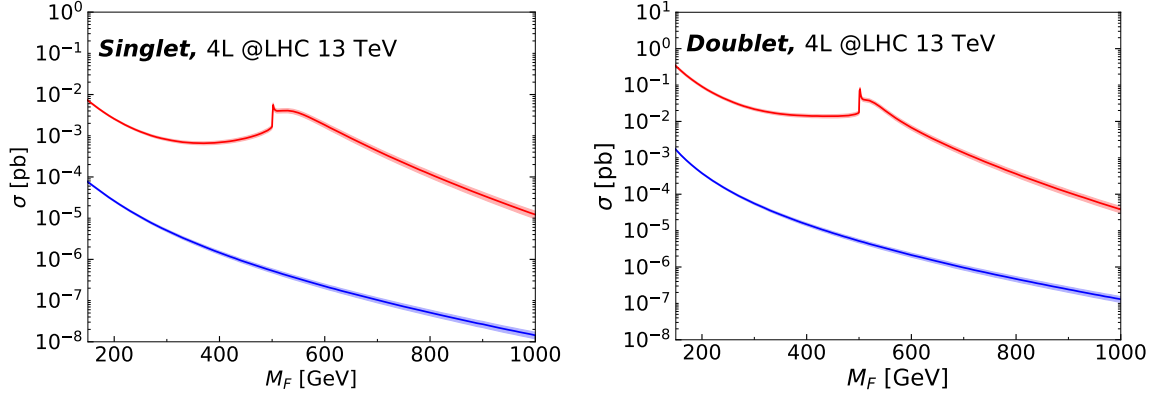


Figure 7.3: Cross sections for BSM production of final states with at least four light leptons at a pp collider with $\sqrt{s} = 13$ TeV in the singlet (left) and the doublet (right) model for different VLL masses with $M_S = 500$ GeV. The red curves correspond to the VLL models (7.1.4) and (7.1.6), while the blue curves correspond to third-generation VLL models such as in [399]

$$pp \rightarrow \psi_i^- \bar{\psi}_i^0 \rightarrow \ell_i^- \ell_i^+ \bar{\nu}_j \ell_j^- \ell_k^+ \ell_k^- \quad \text{for } i, j, k = 1, 2, \quad (7.2.2b)$$

$$pp \rightarrow \psi_i^0 \psi_i^+ \rightarrow \ell_i^- \ell_i^+ \ell_j^+ \nu_j \ell_k^+ \ell_k^- \quad \text{for } i, j, k = 1, 2, \quad (7.2.2c)$$

$$pp \rightarrow \psi_i^- \bar{\psi}_i^0 \rightarrow \ell_i^- \ell_i^+ \bar{q}_j q_j \ell_k^+ \ell_k^- \quad \text{for } i, k = 1, 2, \quad (15 \times 4) \quad (7.2.2d)$$

$$pp \rightarrow \psi_i^0 \psi_i^+ \rightarrow \ell_i^- \ell_i^+ \bar{q}_j q_j \ell_k^+ \ell_k^- \quad \text{for } i, k = 1, 2. \quad (15 \times 4) \quad (7.2.2e)$$

Note that third-generation VLLs $\psi_3^{(-)}$ can generate 4L final states only via the first process in Eq. (7.2.1) since a $\tau^+ \tau^-$ pair has to be produced due to flavor conservation.

In Fig. 7.3 we illustrate cross sections for production of 4L final states at 13 TeV via processes in Eqs. (7.2.1) and (7.2.2). Shown are results for both the singlet model (left) and the doublet model (right) for $M_S = 500$ GeV as a function of M_F . We compare cross sections computed for the models in Eqs. (7.1.4) and (7.1.6) (red) with results from the models in Ref. [399] featuring one generation of VLLs with couplings to third-generation leptons only. In general, models (7.1.4) and (7.1.6) with an enriched flavor structure generate cross sections about two ($M_F < M_S$) to four orders ($M_F \gtrsim M_S$) of magnitude larger when compared to those in Ref. [399]. Reasons for this enhancement are the additional generation of the VLLs as well as the on-shell production of the new scalars: Production of $\psi_{1,2}$ allows for additional 4L final states, while the decay into BSM scalars, which produces two leptons and increases the number of 4L states, dominates if kinematically allowed (see Fig. 7.1).

7.2.2 Constraints from transverse momentum distributions

Distributions of the scalar sum of the transverse momenta have been studied in the CMS analysis [400] to test the doublet model in Ref. [399]. In order to derive constraints on the $M_F - M_S$ parameter space of the singlet and doublet model (with κ' fixed according to Eq. (7.1.8)), we perform an event generation at detector level and compare the resulting L_T distributions to CMS data for 4L final states with $p_T^{\text{miss}} < 50$ GeV. Distributions are computed for various values of M_F and M_S and fixed BSM couplings. We also consider the SM background processes of ZZ , ttZ and triboson production. We include the control region veto of two dilepton pairs (same flavor) with invariant masses $76 \text{ GeV} < m_{2\ell} < 106 \text{ GeV}$ and

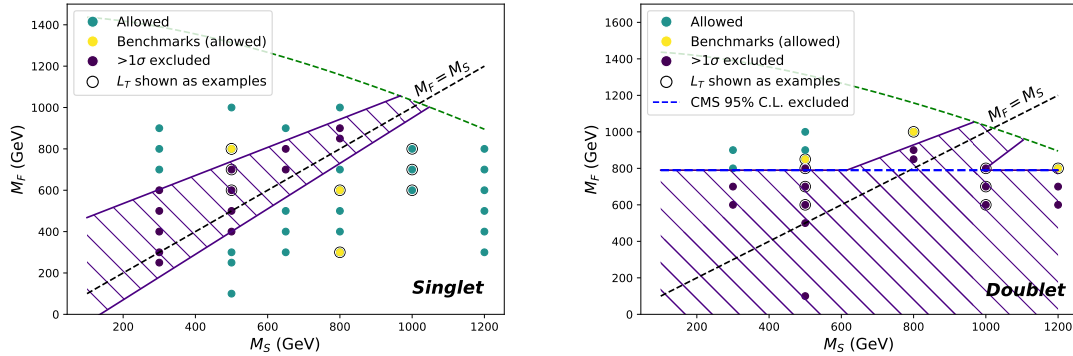


Figure 7.4: Different benchmark values of the VLL mass M_F and the BSM scalar mass M_S with κ' fixed to explain the $(g - 2)_\mu$ anomaly using Eq. (7.1.8). Points are marked as 'allowed' (green, yellow) if all bins in the sum of transverse momenta L_T of the 4L final states fall within 1σ of central values measured by CMS [400]. Points marked in yellow serve as benchmark scenarios in our study of the collider signatures and observables defined in Sec. 7.3. For scenarios highlighted with a black circle, we show L_T distributions in Figs. 7.5 and I.3. Values above the green line denote scenarios where κ' is non-perturbative.

set the L_T bin width to 150 GeV matching settings in [400].

We find that our SM simulation for the L_T distribution shows small differences relative to the CMS background. This is expected, since we perform an event generation at LO and only a fast detector simulation is publicly available. In addition, we cannot perform a fit of the SM background to a control region similar to the CMS analysis. Thus, even though a recasting of CMS data in the context of the models (7.1.2) is desired, these differences prohibit at detailed interpretation, which can only be obtained from a dedicated experiment analysis. Nevertheless, we find that our simulation reproduce both the shape of the L_T distribution and the number of events in each of the bins reasonably well. Considering the differences in the SM background, we refer to scenarios as 'excluded' if the L_T distributions rise above the 1σ range of the CMS data in at least one of the bins.

The findings are summarized in Fig. 7.4 where we show which points in the parameter space are allowed by CMS data (green and yellow circles) or excluded (purple circles) together with illustrative exclusion limits (purple area). Furthermore, the green dashed line indicates mass configurations for which the coupling κ' computed via Eq. (7.1.8) becomes non-perturbative. This line presents an upper limit on the parameter space. While a complete scan over the whole parameter space is beyond the scope of this analysis, we find the following pattern. In both models points with $M_F \sim M_S$ are excluded. This is a result of the enhancement of cross sections around the S resonance (see peak in red curves in Fig. 7.3). In the singlet model, most of the parameter space departing from the $M_F \sim M_S$ line remains unconstrained, and VLLs can be as light as a few hundred GeV. In contrast, in the doublet model points with $M_F < 800$ GeV are excluded due to the larger production cross sections (see Fig. 7.3) regardless of M_S in addition to the $M_F \sim M_S$ area, as already expected from the CMS analysis. Still, areas with both light ($M_S \lesssim 600$ GeV) and heavy scalars ($M_S \gtrsim 1000$ GeV) are still in agreement with CMS data for $M_F \gtrsim 800$ GeV. In general, constraints on the parameter space of the singlet model are weaker relative to the doublet one, since cross sections are smaller by at least one order of magnitude.

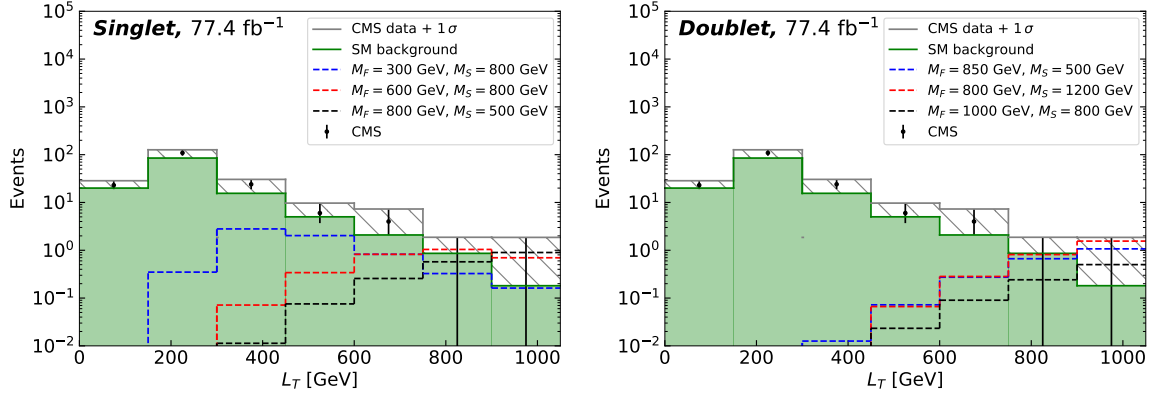


Figure 7.5: Scalar sum of transverse momenta L_T in the singlet (left) and the doublet model (right). Shown are distributions for SM background processes and different benchmark scenarios with different configurations of M_F and M_S . The observables are computed for an integrated luminosity of 77.4 fb^{-1} with subsequent detector simulation and the bin width is set to 150 GeV. CMS data from [400] is indicated as black dots and the upper limit of the 1σ interval is shown by the grey line.

In the following, we consider for each model three representative scenarios marked as benchmarks in Fig. 7.4 (yellow dots), which serve as examples for our analysis procedure. We give the L_T distributions obtained in these benchmark scenarios in Fig. 7.5 together with the SM background and the CMS data. In both models, we include at least one case with $M_F > M_S$ and one with $M_S < M_F$. As can be seen, the VLL contributions do not rise above the experimental 1σ range in any of the benchmark scenarios, regardless of the mass hierarchy. To illustrate the L_T distribution for further hierarchies in the BSM sector, we present L_T distributions for additional mass configurations (see Fig. 7.4, black rings) in App. I.3.

In summary, while both models can explain the electron and muon AMM anomalies within a very similar parameter space [28, 30], CMS data already excludes a large part of the parameter space of the doublet model. In contrast, the singlet model remains mostly untested by the L_T distributions of the 4L channel.

7.3 Additional observables with null test potential

While L_T distributions allows to probe the parameter space of both the singlet and the doublet model, they are not sensitive to mass hierarchies of the BSM sector. Thus, we design novel observables targeting specific flavor features of the models. These offer new ways to search for flavorful scalars and VLLs and can serve as null tests of the SM. The observables represent invariant masses which aim to reconstruct the masses of BSM scalars and VLLs. The latter are reconstructed via their decay into a neutral SM boson or, if kinematically allowed, into the new scalars. As final states with neutrinos offer only a very limited resolution when reconstructing invariant masses they are discarded by cuts on the missing transverse energy (see Tab. I.1). Given $M_F > M_S$, the decay of VLLs into BSM scalars becomes the dominant mode (see Fig. 7.1). However, due to large values of κ' contributions from BSM scalars can

be sizable even in the case of off-shell decays. In this regard, the production modes

$$\begin{aligned}\psi_i \bar{\psi}_i &\rightarrow \ell_j^- S_{ij}^* \ell_k^+ S_{ik} \rightarrow \ell_j^- \ell_j^+ \ell_i^- \ell_k^+ \ell_k^- \ell_i^+ \quad (\text{singlet}), \\ \psi_i^- \psi_i^+ &\rightarrow \ell_j^- S_{ji} \ell_k^+ S_{ki}^* \rightarrow \ell_j^- \ell_j^+ \ell_i^- \ell_k^+ \ell_k^- \ell_i^+ \quad (\text{doublet})\end{aligned}\tag{7.3.1}$$

in the singlet and doublet model, respectively, allow for a reconstruction of the new scalars from two leptons with *opposite charge and same flavor* (OCSF) as well as leptons with *opposite charge and different flavor* (OCDF). Combining these two leptons with a third charged lepton allows us to reconstruct the VLLs. This additional lepton is required to carry opposite charge and same flavor as one of the leptons in the initial pair. Similarly to the S_{ij} , SM Higgs and Z bosons can be reconstructed from both dilepton and dijet pairs. We refer to masses reconstructed from two and three final-state particles as $m_{2\ell}$ and $m_{3\ell}$, respectively. The subsets of these invariant masses reconstructed from OCDF leptons are referred to as $m_{2\ell_diff}$ and $m_{3\ell_diff}$, respectively.

In order to reconstruct the BSM scalars S_{ij} with $i \neq j$ we consider only OCDF leptons. We include invariant masses from events where we find two invariant masses which are the same within a small window $\Delta M_S = 5$ GeV (see Tab. I.1) assuming a rather narrow width for BSM scalars. With this procedure we are able to find on-shell contributions from BSM scalars. If two scalars are found, the VLLs can be reconstructed by requiring flavor-conservation. Assuming perfect reconstruction of final-state particles these flavor conditions allow to suppress SM background processes. Therefore, processes in Eq. (7.3.1) are the 'golden channels' of our analysis.

7.3.1 Definition of observables

In the following, we discuss the algorithm employed to compute the masses $m_i(_diff)$. We start with the reconstruction of SM bosons and new scalars by computing all possible sets of invariant dijet and dilepton (combinations of leptons with opposite charge only) masses. For each event, we include at most one pair of invariant masses in the observable $m_{2\ell}$. In order to be included, the dilepton or dijet masses must fulfill one of the following requirements:

- a) We find two invariant masses reconstructed from different dijet or OCSF dilepton pairs that are equal to either $m_Z \pm \Delta m_Z$ or $m_h \pm \Delta m_h$ (see Tab. I.1). This allows to reconstruct SM Z and Higgs bosons.
- b) Two invariant OCSF dilepton masses (reconstructed from different lepton pairs) differ by less than ΔM_S (see Tab. I.1). This allows to reconstruct S_{ii} scalars. If multiple combinations fulfill this criteria, only the pair with the smallest difference is included.
- c) Two invariant dilepton masses differ by less than ΔM_S (see Tab. I.1) where at least one of them is reconstructed from a OCDF lepton pair. This step reconstructs S_{ij} scalars with $i, j = 1, 2, 3$.

We test for each of these conditions in the order ($a \rightarrow b \rightarrow c$). If one of the conditions is fulfilled, we stop and consider the next event. The observable $m_{2\ell_diff}$ contains the subset of masses found in step c). Note that the conditions are designed in a way that they are only sensitive to scalar contributions if two scalars are found within the same event. However, as the VLL pair-production cross section is significantly larger than the single-production one (see Fig. I.2) and VLLs decay almost exclusively into BSM scalars (as soon as kinematically allowed, see Fig. 7.1), this is an excellent approximation.

After we found suitable candidates of two-particle states, we reconstruct VLLs by adding an additional lepton to the dilepton and dijet states. Within each event, we search for a pair of three-particle states and add them to $m_{3\ell}$ if they pass one of the following conditions:

- 1) We add an additional lepton to each of the invariant masses reconstructed in step *a*). The invariant masses of the two three-particle states are required to agree within a mass window ΔM_F (see Tab. I.1). If multiple combinations are found, we consider only the one with the smallest mass difference.
- 2) Additional leptons are added to the two dilepton states reconstructed in step *b*). The additional leptons are required to have the same flavor as the leptons in the dilepton pair. The two invariant masses reconstructed from these lepton combinations are required to have the same mass within a mass window ΔM_F (see Tab. I.1). Again, only the combination with the smallest mass difference is included in $m_{3\ell}$.
- 3) For dilepton masses reconstructed in step *c*) we add a third lepton depending on the flavor structure of the dilepton state. If the state contains two OCSF leptons, the third lepton is required to have the same flavor as the other two leptons. If the state is a OCDF dilepton state, the third lepton is required to have the same flavor but different charge than one of the leptons in the dilepton state. Furthermore, considering the six leptons we require flavor conservation. For all events, at most one combination fulfills these requirements and is added to $m_{3\ell}$ and $m_{3\ell_diff}$.

In the last two steps flavor requirements representing flavor conservation in decays of BSM scalars allow to reconstruct the VLLs. In particular, in the last step no assumption about the width of the VLLs has to be made. This requirement allows to reconstruct VLLs even in the case $M_F \gg M_S$ where the width of the VLLs becomes significantly larger than ΔM_F . As this flavor requirement cannot be fulfilled by SM processes (given perfect reconstruction), the m_{i_diff} observables present null tests of the SM. Thus, they offer the opportunity to detect deviations from the SM even if only a few events are detected at the LHC.

7.3.2 Distributions at Run 2

We study the distributions of the observables $m_{2\ell}(_diff)$ and $m_{3\ell}(_diff)$ for the benchmark scenarios shown in Fig. 7.5. For each scenario, we generate 5×10^4 events and rescale the distributions to an integrated luminosity of 150 fb^{-1} (this leads to small statistical fluctuations in the distributions).

The distributions of the invariant masses $m_i(_diff)$ at parton level in the singlet model are shown in Figs. 7.6. Corresponding distributions in the doublet model are very similar and are given in Fig. I.4 in App. I.4. In general, the number of events is larger compared to the singlet model due to enhanced cross sections. The main features are that m_{i_diff} observables are significantly cleaner compared to the m_i ones, since the SM background is, as expected, suppressed. In particular, this can be seen at the rejection of invariant masses around the Z mass in the $m_{2\ell_diff}$ distribution (plot in the upper right), and at the fact that the $m_{3\ell_diff}$ distribution (plot in the lower right) is free of any SM background. In both the $m_{2\ell}$ and $m_{2\ell_diff}$ distributions, scalar resonances appear as narrow peaks for scenarios with $M_F > M_S$ (black curve in Fig. 7.6), with $\mathcal{O}(10^1)$ events in the peak bins. In contrast, the $m_{3\ell}(_diff)$ distributions present very broad resonances, with $\mathcal{O}(1)$ events per bin. In the inverse scenario with $M_F < M_S$, the $m_{2\ell}$ distributions show peaks with $\mathcal{O}(10^2)$ events per bin at the mass of the Z boson. These peaks are strongly depleted by about two orders of

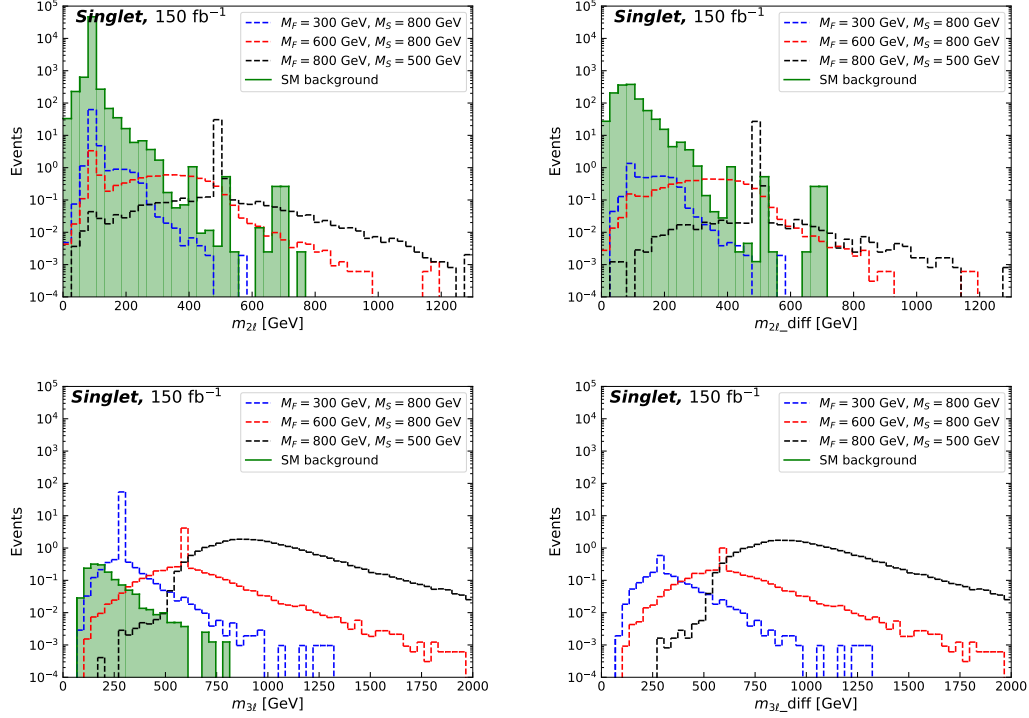


Figure 7.6: Parton-level distributions of invariant masses $m_{2\ell}$, $m_{2\ell_diff}$, $m_{3\ell}$, and $m_{3\ell_diff}$ for the singlet model for different benchmark masses of the VLLs and the BSM scalars at a luminosity of 150 fb^{-1} and $\sqrt{s} = 13 \text{ TeV}$. The coupling κ' is fixed according to Eq. (7.1.8).

magnitude in the $m_{2\ell_diff}$ distributions, similar to the SM background. While the peaks fall below the SM background in both distributions, BSM signatures can in principle be detected in the tails for $m_{2\ell}(_diff) \gtrsim 500 \text{ GeV}$. However, the number of events is at the level of $\mathcal{O}(10^{-1})$ only. VLL resonance appear as narrow peaks in $m_{3\ell}$ distributions with $\mathcal{O}(10^2)$ ($\mathcal{O}(10^1)$) events per bin for $M_F = 300 \text{ GeV}$ ($M_F = 600 \text{ GeV}$) (blue (red) curves in Fig. 7.6). These peaks are again strongly suppressed by more than an order of magnitude in the $m_{3\ell_diff}$ distribution, since the S cannot contribute on shell in the decay of the VLLs.

In order to estimate the effects of both hadronization and a finite detector resolution, we apply parton showering with `PYTHIA 8` and a fast detector simulation using `Delphes 3` with the CMS default card to the events at parton level. The corresponding distributions of the $m_i(_diff)$ observables at particle level are shown in Figs. 7.7 and 7.8 for the singlet and the doublet model, respectively. A general feature of the particle-level distributions is the depletion of all distributions, which is more pronounced in the peaks than in the rest of the distributions. Depending on the mass hierarchy of the BSM sector and the observables considered, the number of events in the peaks bins is reduced by around one to two orders of magnitude. In particular, peak bins in the $m_{2\ell}$ and $m_{2\ell_diff}$ distributions at the masses of the electroweak bosons and the new scalars become broader, and the number of events in the peak bins is reduced by around one order of magnitude to a level of up to a few events in the signal peaks. Similarly, we find that peaks in the $m_{3\ell}(_diff)$ distributions become both smaller and broader, similar to the $m_{2\ell}(_diff)$ ones. Given $M_F < M_S$, which is the case for $M_F = 300 \text{ GeV}$, 600 GeV (blue and red curves) and $M_F = 800 \text{ GeV}$ (red curve) in the

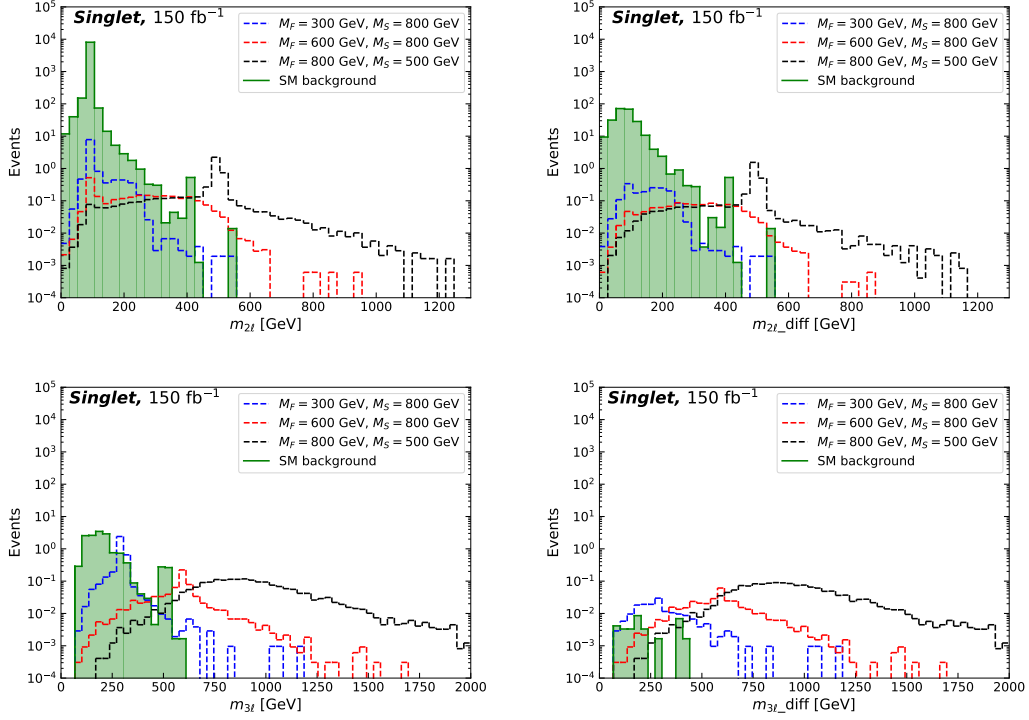


Figure 7.7: Distributions of invariant masses $m_{2\ell}$, $m_{2\ell_diff}$, $m_{3\ell}$, and $m_{3\ell_diff}$ at 150 fb^{-1} and $\sqrt{s} = 13 \text{ TeV}$ in the singlet model for selected benchmark scenarios after detector simulation.

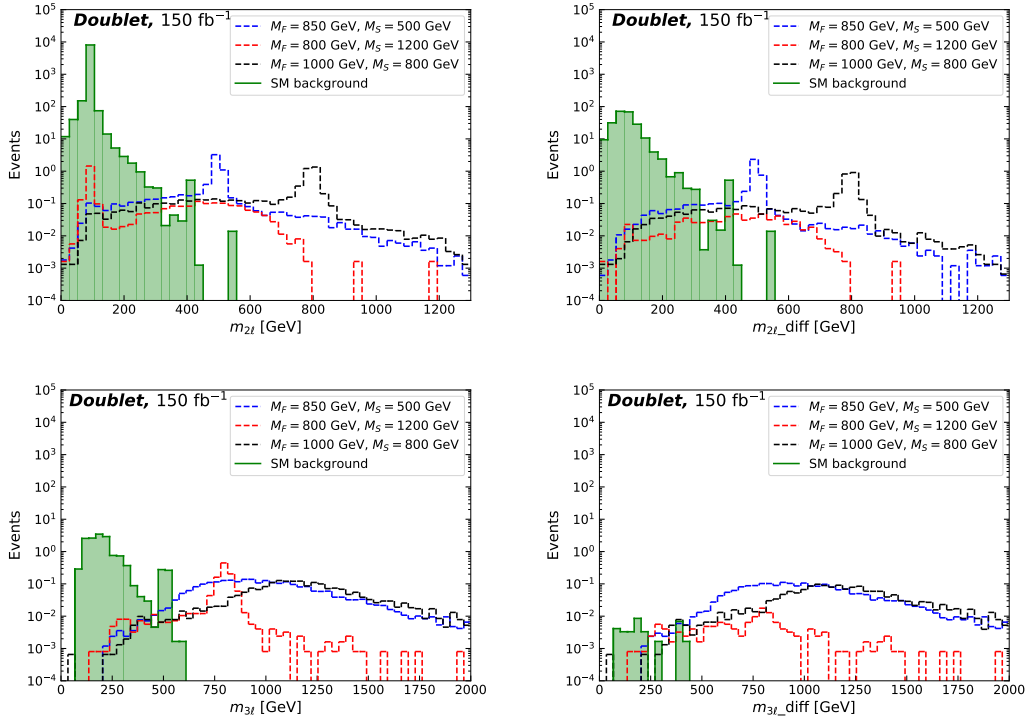


Figure 7.8: Same as Fig. 7.7 but for the doublet model.

Model	M_F (GeV)	M_S (GeV)	$m_{2\ell}$	$m_{2\ell_diff}$	$m_{3\ell}$	$m_{3\ell_diff}$
Singlet	300	800	1/8*	1/3*	1/22	1/19
Singlet	600	800	1/6*	1/5*	1/18	1/16
Singlet	800	500	1/12	1/17	1/17**	1/19**
Doublet	850	500	1/14	1/17	1/16**	1/20**
Doublet	800	1200	1/16*	1/6*	1/60	1/15
Doublet	1000	800	1/36	1/48	1/27**	1/34**

Table 7.2: Scaling factors $f = N_{\text{peak, det}}/N_{\text{peak}}$ for the different benchmarks of our models. We denote by $N_{\text{peak, det}}$ (N_{peak}) the number of events at the peaks after (before) detector simulation and compute the scaling factors for all four observables. The values correspond to observables computed at $\sqrt{s} = 13$ TeV and a luminosity of 150 fb^{-1} . Peaks which fall below the SM background (resonances are broad) are marked with * (**).

singlet and doublet model, respectively, the number of events in the peak bins in the $m_{3\ell}$ distributions is suppressed by roughly one order of magnitude. For low VLLs masses, which is the case for $M_F = 300$ GeV in the singlet model (blue curve), we find $\mathcal{O}(1)$ events in the peak bins. For the other two scenarios with heavier VLLs and scalars the number of events in the peak bin is at the level of $\mathcal{O}(10^{-1})$. Benchmark scenarios with the inverse hierarchy $M_F > M_S$ show a similar suppression of the number of events, about one order of magnitude. For $M_F = 800$ GeV in the singlet model (black curve) and $M_F = 850$ GeV, 1000 GeV in the doublet model (red and black curves), we find $\mathcal{O}(10^{-1})$ events in the peak bins. In contrast to distributions with a narrow peak, the suppression is an overall rescaling of the resonances and their width is unaffected.

The findings for the suppression of the number of events in the peak bins are summarized in Tab. 7.2 in the form of scaling factors $f = N_{\text{peak, det}}/N_{\text{peak}}$, which are defined as the ratio of numbers of events in the peaks after ($N_{\text{peak, det}}$) and before (N_{peak}) detector simulation. The scaling factors are at the level of $\mathcal{O}(10^{-1} - 10^{-2})$ and are typically larger in the $m_{2\ell}$ and $m_{2\ell_diff}$ distributions in the case $M_F < M_S$. This pattern, as well as the strong suppression of peaks compared to the rest of the distributions, is understood. The detector energy resolutions scales like $\Delta E \sim \sqrt{E}$, and thus the high- $m_{2(3)\ell}(_diff)$ bins show larger differences when comparing distributions before and after detector simulation. Similarly, peaks of distributions become broader due to bin-to-bin migration and are more affected, since more events propagate out of the peak bins than into them from adjacent bins due to the significantly larger number of events in the peak bins. As the resolution depends on the energy of the particles, effects of bin-to-bin migration are asymmetric and have a stronger effect on the high-energy region. Therefore, the distributions are shifted towards smaller values of $m_i(_diff)$ and the bins around peaks show an asymmetric shape. The scaling factors in Tab. 7.2 reflect the energy dependence. For example, the $M_F = 1000$ GeV scenario in the doublet model shows a stronger suppression than the $M_F = 850$ GeV one. Similarly, scaling factors for the $M_F = 850$ GeV benchmark point in the doublet model do almost coincide with those of the $M_F = 800$ GeV scenario in the singlet model.

7.3.3 Distributions at higher luminosities

As we have shown in Sec. 7.3.2, the discovery of VLLs and new scalars featuring a non-trivial flavor structure is a challenging task given present detector resolution and the integrated luminosity collected in LHC Run 2. Future measurements at the HL-LHC will benefit from

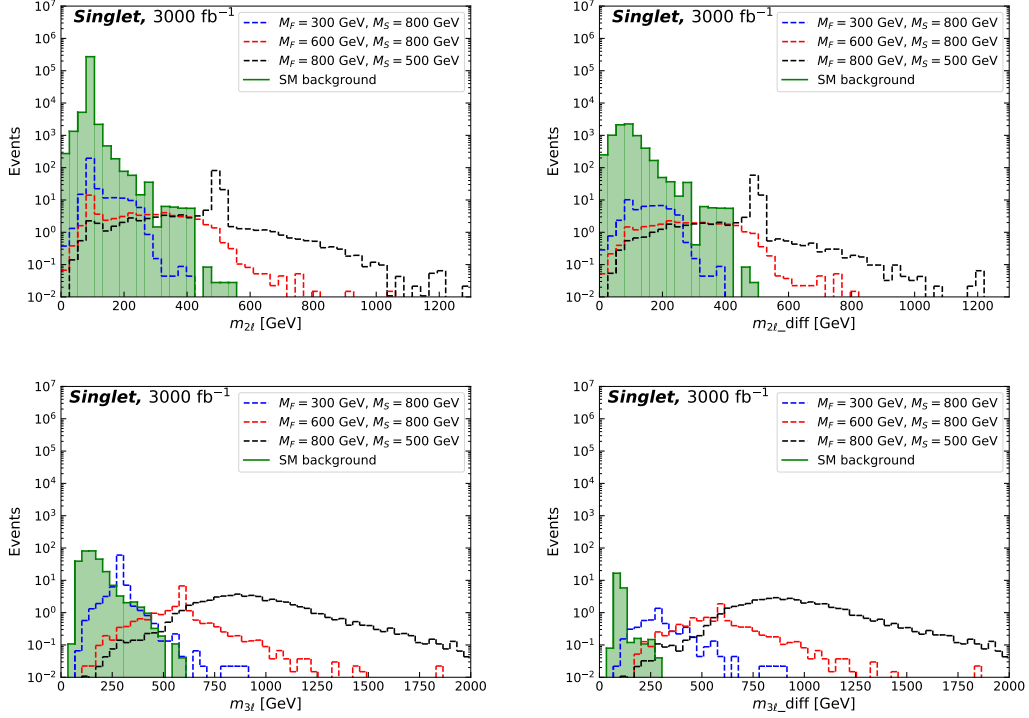


Figure 7.9: Distributions of the observables $m_{2\ell}$, $m_{2\ell_diff}$, $m_{3\ell}$, and $m_{3\ell_diff}$ after detector simulation for the singlet model. We show results for different benchmark scenarios at a luminosity of 3000 fb^{-1} and $\sqrt{s} = 14 \text{ TeV}$. The coupling κ' is fixed according to Eq. (7.1.8).

both upgraded detectors and a higher integrated luminosity, and thus they provide a peerless opportunity for BSM searches. In order to estimate the potential of the observables $m_i(_diff)$ in future analyses, we study distributions of the previously discussed benchmark scenarios at the HL-LHC at $\sqrt{s} = 14 \text{ TeV}$ and 3000 fb^{-1} [306]. For the fast detector simulation, we employ Delphes 3 with the HL-LHC default card instead of the CMS one. The distributions of the new observables $m_i(_diff)$ at particle level are shown in Figs. 7.9 and 7.10 for benchmark scenarios in the singlet and doublet model, respectively. The corresponding parton-level distributions are given in Figs. I.5 and I.6.

As expected, we find a significantly higher rate of events due to the higher integrated luminosity at HL-LHC, which enhances event rates by a factor of about $3000/150 = 20$. Despite the differences in center of mass energies and detector settings, distributions at 3000 fb^{-1} look like scaled-up version of the 150 fb^{-1} distributions in Figs. 7.7 and 7.8. Similarly, the scaling factors given in Tab. I.2 are also comparable to the LHC Run 2 ones in Tab. 7.2. In general, HL-LHC scaling factors are slightly larger due to improved detector settings.

In both mass hierarchies, the number of events in the peaks in the $m_{2\ell}$ distributions is at the level of $\mathcal{O}(10^1 - 10^2)$. In the $m_{2\ell_diff}$ distributions, peaks around masses of SM bosons are strongly suppressed, while at scalar masses contain $\mathcal{O}(10^1 - 10^2)$ events. For both hierarchies, bins with $m_{2\ell}(_diff) \gtrsim 500 \text{ GeV}$ allow to distinguish BSM signals from SM background and to search for on- and off-shell production of BSM scalars. The $m_{3\ell}$ and $m_{3\ell_diff}$ distributions show a sizable number of events for all benchmark scenarios. The $m_{3\ell}$ distributions of benchmark scenarios with $M_F < M_S$ show peaks with $\mathcal{O}(10^1)$ events per bin

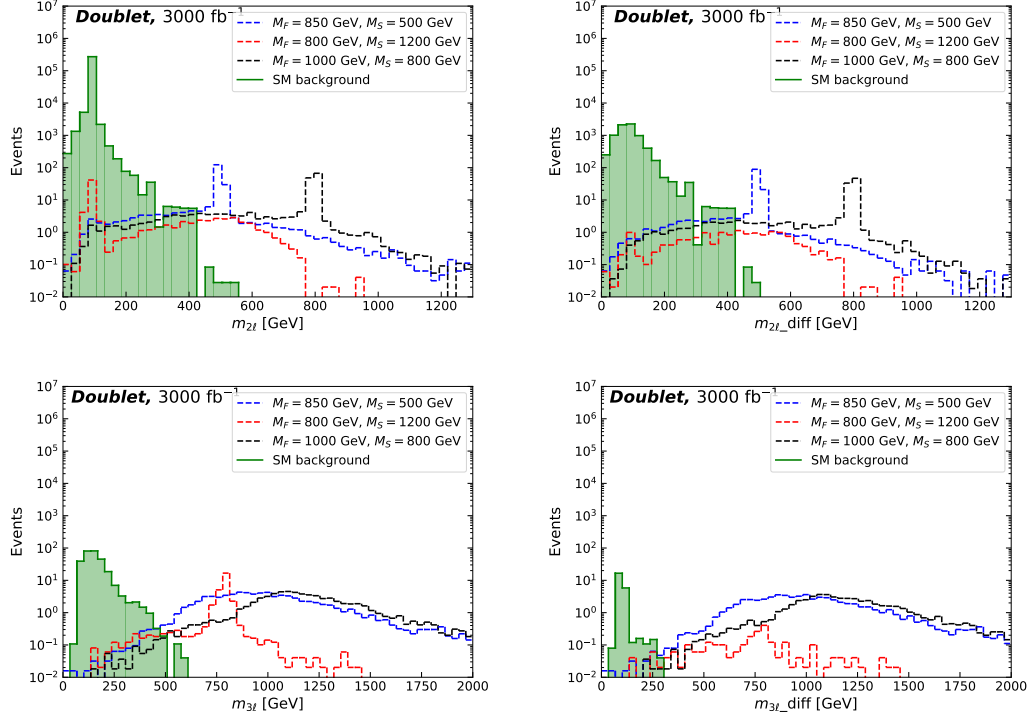


Figure 7.10: Same as Fig. 7.9 but for the benchmark scenarios in the doublet model.

for $M_F = 600$ GeV (singlet) and $M_F = 800$ GeV (doublet), and $\mathcal{O}(10^2)$ events in the peak bin for $M_F = 300$ GeV (singlet). In all cases, peaks are strongly depleted in the $m_{3\ell_diff}$ distributions with up to single events in the peak bins for light VLLS ($M_F = 300$ GeV, 600 GeV in the singlet model). In contrast, benchmark scenarios with the inverse hierarchy $M_F > M_S$ have broad resonances in both the $m_{3\ell}$ and $m_{3\ell_diff}$ distributions, with $\mathcal{O}(1)$ events in the peak bins. In these scenarios, which are the ones with $M_F = 800$ GeV (black curves) and $M_F = 800$ GeV, 1000 GeV (blue, black curves) in the singlet and doublet models, respectively, the $m_{3\ell_diff}$ distributions turn out to be the ideal probe for VLL signatures. To summarize, data at LHC Run 2 can in principle allow for a detection of specific points in the $M_F - M_S$ plane, and HL-LHC will allow to further probe the parameter space and to extract mass hierarchies.

7.3.4 Benchmark scenarios beyond $g - 2$

While κ is necessarily small due to bounds from measurements of Z -decay properties, the exact size of κ' is unconstrained by electroweak data. In order to explain the muon AMM, we fixed κ' according to Eq. (7.1.8). Since the deviations in the muon AMM are subject to debate in the literature [130–132], we investigate the possibility that the tension between SM prediction and data is reduced in the future. Therefore, we drop the condition in Eq. (7.1.8) and consider κ' as a free parameter. Since values of κ' needed to accommodate Δa_μ tend to be rather large, we study a more moderate value $\kappa' = 1$. This scenario implies a less pronounced dominance of decays into BSM scalars plus SM leptons. We consider distributions in the singlet model only as in this model the M_F, M_S parameter space is largely untested by present CMS data (see Fig 7.4). However, when fixing $\kappa' = 1$ the constraints on the parameter space change

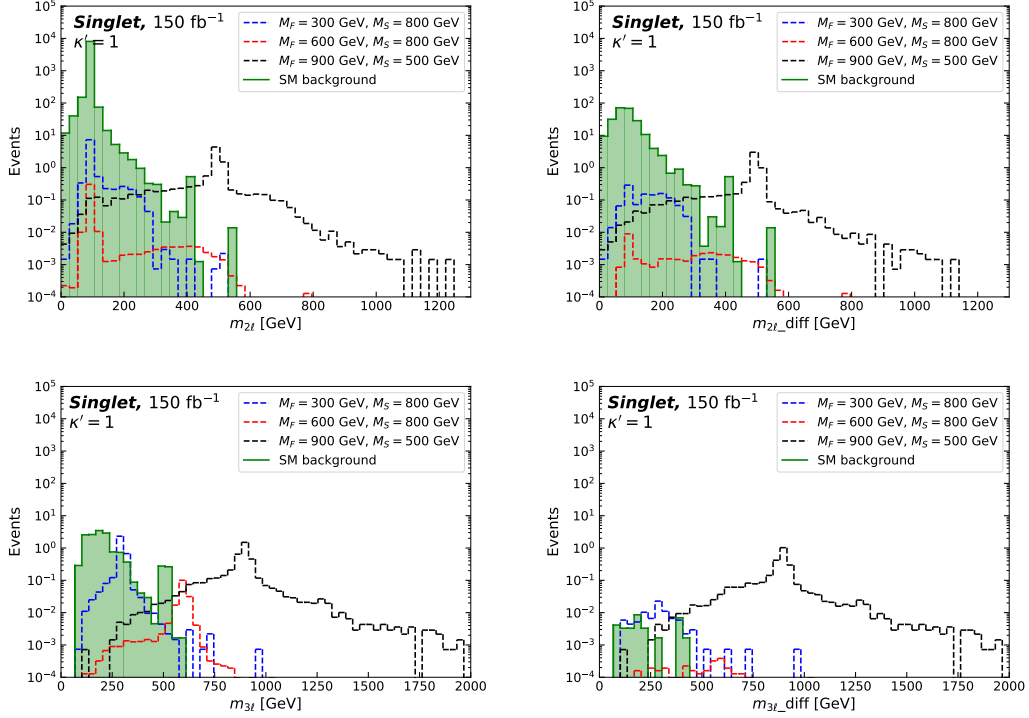


Figure 7.11: Distributions of invariant masses $m_{2\ell}$, $m_{2\ell_diff}$, $m_{3\ell}$ and $m_{3\ell_diff}$ for the singlet model with fixed $\kappa' = 1$ and including the effects of parton shower and detector simulation. The observables are computed for the different benchmark scenarios for a luminosity of 150 fb^{-1} and $\sqrt{s} = 13 \text{ TeV}$.

slightly. For example, the benchmark scenario with $M_F = 800 \text{ GeV}$, $M_S = 500 \text{ GeV}$ is now in conflict with data distributions provided by CMS, and we choose to replace this scenario with the $M_F = 900 \text{ GeV}$, $M_S = 500 \text{ GeV}$ scenario (see Fig. I.7).

The distributions of the $m_i(_diff)$ observables after detector simulation at 150 fb^{-1} and $\sqrt{s} = 13 \text{ TeV}$ are shown in Fig. 7.11. Both the $m_{2\ell}$ and $m_{2\ell_diff}$ distributions turn out to be very similar to the $g - 2$ benchmarks, shown in the upper row of Fig. 7.7. For $M_F < M_S$ ($M_F > M_S$), we find peaks at the masses of electroweak bosons (BSM scalars S) in the $m_{2\ell}$ distribution. For the latter (black curve), the $m_{2\ell_diff}$ distribution shows a peak with a few events, while for $M_F < M_S$ peaks are depleted by about one order of magnitude compared to the $m_{2\ell}$ distributions. The $m_{3\ell}(_diff)$ distributions show a striking difference compared to the $g - 2$ scenarios (lower row of Fig. 7.7): we find peaks in the $m_{3\ell}$ distributions in all three scenarios, regardless of the hierarchy of the BSM sector. The only difference is that the resonance shows a slightly broader peak in the case $M_F > M_S$, as seen at the benchmark point $M_F = 900 \text{ GeV}$ (black curve), compared to the scenarios with the inverse mass hierarchy and $M_F = 300 \text{ GeV}$, 600 GeV (blue and red curves). The $m_{3\ell_diff}$ distributions show peaks for $M_F > M_S$ with a similar number of events compared to the $m_{3\ell}$ one, $\mathcal{O}(1)$. In contrast, for scenarios with $M_F < M_S$ the number of events in the peak is suppressed by about two orders of magnitude relative to the $m_{3\ell}$ distribution.

To conclude, the presence of two peaks in distributions of both $m_{2\ell_diff}$ and $m_{3\ell_diff}$ allows to estimate the size of the aforementioned coupling: if κ' is too large, the peak in the

$m_{3\ell_diff}$ distribution would turn into a very broad resonance. Thus, if two peaks are found simultaneously, the coupling κ' has to be as small as $\kappa' \sim 1$.

Note that in scenarios with $\kappa' = 0$ the models would still provide lepton-flavor-violating-like signatures for $y \neq 0$. In this case, $\psi_i \rightarrow S_{ij}\ell_j$ would happen at order $y\theta$, and the decay $S_{ij} \rightarrow \ell_i^-\ell_j^+$ at order $y\theta^2 v/M_F$ plus additional suppression from small lepton Yukawa couplings to the Higgs boson. As mixing angles are necessarily small due to Z -data constraints, the m_{i_diff} observables would be strongly suppressed down to the level of statistical noise. Similar results apply to scenarios with other representations of VLLs under $SU(2) \times U(1)_Y$ without the $\psi - S - \ell$ coupling, or scenarios with very large values of M_S . Without any SM-BSM portal couplings ($\kappa = \kappa' = 0$) the phenomenology of VLLs would be completely different and is discussed for various scenarios in Ref. [64].

7.4 Summary

The LHC provides a unique opportunity to study signatures of a BSM sector consisting of VLLs and new scalars S_{ij} carrying two flavor indices [28, 30]. Here, we considered models with either $SU(2)_L$ singlet or doublet VLLs (7.1.2) explaining the AMMs of the electron and the muon while providing a UV completion of the SM that is asymptotically safe. The additional BSM Yukawa sector features couplings of the VLLs to new scalars and SM particles via portal couplings κ and κ' . As the BSM scalars carry two flavor indices, the decay $S_{ij} \rightarrow \ell_i^+\ell_j^-$ produces a OCDF dilepton state without explicit lepton flavor violation. This lepton-flavor-violating-like decay provides a signature that allows for the construction of null tests of the SM.

Fixing κ' according to Eq. (7.1.8) in order to explain the AMMs we derived constraints on the M_F - M_S parameter space by comparing distributions of the scalar sum of transverse momenta in the four-light-lepton channel to CMS data [400] (see Fig. 7.4). We found that in the singlet model only scenarios with $M_F \sim M_S$ are in tension with data by CMS due to the enhancement from on-shell scalar production (purple area). Constraints on the doublet model are significantly stronger due the larger cross sections, and VLL masses $M_F < 800$ GeV and scenarios with $M_F \sim M_S$ are already excluded by CMS. Requiring κ' to be small enough to allow for perturbation theory further restricts the parameter space, as it places an upper limit on both M_F and M_S at the level of $\mathcal{O}(1)$ TeV.

To probe the specific signatures of the models we defined new observables $m_{2\ell}$, $m_{2\ell_diff}$, $m_{3\ell}$, and $m_{3\ell_diff}$. These invariant masses allow to search for both scalar (in the dilepton distributions) and for VLL resonances (in the three-particle invariant masses). The $m_{2(3)\ell_diff}$ distributions provide a suppression of the SM background. The suppression is particularly efficient in the case of $m_{3\ell_diff}$, which is in fact a null test of the SM. Fixing κ' according to Eq. (7.1.8) we find that $m_{2\ell}$ distributions after detector simulation normalized to 150 fb^{-1} show peaks at either the mass of the electroweak bosons given $M_F < M_S$, or at the mass of the scalars for $M_F > M_S$. Only in the latter case, we also find peaks in the $m_{2\ell_diff}$ distributions. For both observables, the number of events in the peaks is at the level of $\mathcal{O}(1)$. For $M_S \gtrsim 500$ GeV we can separate SM and BSM signals for both on- and off-shell scalar production. In case of the $m_{3\ell}$ distributions, we find narrow peaks with $\mathcal{O}(1)$ events per bin at the mass of the VLLs as long as the decay into BSM scalars is kinematically forbidden ($M_F < M_S$). If BSM mass hierarchies allow for decays of VLLs into BSM scalars ($M_F > M_S$), the peaks in the $m_{3\ell}(_diff)$ distributions become very broad resonances due to large values of κ' required to explain the muon AMM. . Even though we find similar resonances in the

$m_{3\ell_diff}$ distributions, the number of events in the bins is at the level of $\mathcal{O}(0.1)$ events only.

While the observables allow to distinguish different mass hierarchies of the BSM sector (in contrast to the L_T distribution), present integrated luminosities and detector performance render the discovery of both the singlet and doublet model very challenging. As the distributions would extremely benefit from a higher event count, we considered the potential of experiments at the HL-LHC. We found that the number of events in the peaks rises by more than one order of magnitude for all benchmark scenarios considered. This would allow to detect BSM signatures and to infer information on the mass hierarchy of the BSM sector.

Dropping the explanation of the muon AMM allowed us to choose κ' with more freedom. In the case of $\kappa' = 1$, narrow peaks in the $m_{3\ell}$ and $m_{3\ell_diff}$ distributions (see Fig. 7.11) are present also for $M_F > M_S$ with again $\mathcal{O}(1)$ events per bin after detector simulation.

Thus, the observables considered here do not only allow to search for direct-detection signatures of VLLs, but provide a method to distinguish between different mass hierarchies of the BSM sector. In addition, they also allow to estimate the size of the coupling κ' .

8 Conclusion

This thesis presents opportunities for searches for BSM physics in both the framework of EFTs as well as a specific model for BSM physics motivated by flavor anomalies. We focused on the top-quark sector of the SMEFT Lagrangian, and studied synergies of top-quark and beauty observables related by $SU(2)_L$ invariance.

To set up our model-independent analysis in the SMEFT framework, we started in Chapter 4 with a global fit of three Wilson coefficients to data from t -channel single top-quark production and top-quark decay. Originally intended as a testing ground for our fit setup, it further enabled us to tackle two questions in the context of global fits in SMEFT. These comprise the impact of quadratic contributions of dimension-six operators, $\mathcal{O}(\Lambda^{-4})$, and of undetermined correlations of uncertainties on the fit. The former turned out to be a sub-leading source of uncertainty only, as fits with linear and quadratic ansatz are found to be in agreement. Conversely, correlations have a significant impact on the fit: Results for the coefficients can either show agreement with the SM (neglecting correlations (4.2.4)) or deviate by around 5σ from the SM (strong correlations (4.2.5)), see Fig. 4.5.

With our fit setup in place, we proceeded to link top-quark physics to the beauty sector. This allows us to circumvent the issue of undetermined correlations, and, more importantly, to include the hints for BSM physics in $b \rightarrow s$ transitions in our global analysis. In this regard, we presented in Chapter 5 a first step in the direction of combined fits to top-quark and B -physics data. We considered $t\bar{t}\gamma$ production cross sections and $B \rightarrow X_s\gamma$ branching ratios and constrained three SMEFT coefficients of top-quark dipole operators given in (5.1.1). The constraints on the SMEFT Wilson coefficients were found to be significantly enhanced in the fit to the combined dataset due to the complementarity of sensitivities of the individual observables. The size of the posterior regions is reduced by up to one order of magnitude compared to the individual fit to top-quark or B -physics data (see Fig. 5.6). In addition, ambiguous solutions present in individual fits can be removed in the combined fit.

In Chapter 6, we extended our setup and turned our attention to semileptonic four-fermion operators. These are of special interest regarding their relation to the flavor anomalies seen within present data on $b \rightarrow s$ transitions. In addition, they provide top-quark contact interactions with leptons which could be studied at future lepton colliders. Up-type and down-type quark sectors are related via $SU(2)_L$ symmetry, and exploiting this link we combined top-quark and beauty observables at present colliders as well as future scenarios for HL-LHC, Belle II, and CLIC. We highlighted how combining data of top-quark pair production, $Z \rightarrow b\bar{b}$ transitions, and $b \rightarrow s$ transitions enables us to constrain eight SMEFT Wilson coefficients, including two four-fermion ones that indicate deviations from the SM, see Figs. 6.3 and 6.8. Going beyond present data, we studied several future scenarios with projections for measurements at HL-LHC, Belle II, and CLIC. While inclusion of Belle II measurements already increases the sensitivity, see Fig. 6.9, a combination with observables at a future lepton collider is paramount to constrain the complete eleven-dimensional parameter space, see Fig. 6.10. In addition, we found that the fate of deviations from the SM found within present $b \rightarrow s\mu^+\mu^-$ data is decided by Belle II measurements, even if CLIC data confirms the SM predictions. This is due to the orthogonality of the sensitivities, see Fig. 6.11.

Anomalies in present flavor data drive the hunt for BSM physics, and not in all cases BSM physics is required to be at the TeV scale or above. Thus, direct detection of new physics can be in the reach of experiments at the LHC offering an approach complementary to indirect searches. In this regard, we considered in Chapter 7 an asymptotically safe extension of the SM [28–30] featuring vector-like leptons and new scalars with a non-trivial flavor structure. This model is again related to flavor anomalies, in this case the AMMs of the electron and the muon. Considering two $SU(2)_L$ realizations of this model, we found that present data only excludes a small region of the parameter space given that vector-like leptons transform as $SU(2)_L$ singlets. In contrast, the doublet model is already strongly constrained, see Fig. 7.4. To improve searches for these models, we proposed new observables exploiting the flavor structure of the BSM sector. We showed that luminosities of Run 2 can, depending on the mass hierarchy of the BSM sector and the values of the coupling constants (see Figs. 7.7 and 7.8), be sufficient to find signals of BSM physics in distributions of the observables. In the future, the higher integrated luminosity at HL-LHC allows to discern hierarchies in the BSM sector, see Fig. 7.9.

To conclude this thesis, our work opens up a new route for global fits to the top-quark sector of SMEFT by combining data from top-quark and beauty physics, linking top-quark physics to the flavor anomalies. We highlighted how this combination of observables improved constraints on several SMEFT operators, and how it enabled us to test additional coefficients removing ambiguities and flat directions present in fits to individual datasets. Especially in the light of future measurements at (HL-)LHC and Belle II or proposed high-energy lepton colliders, the increased precision will allow to pursue the quest for BSM physics with global searches in top-quark and flavor-physics data. Furthermore, it will shed light on the question whether BSM physics truly has the properties hinted at by present anomalies. However, indirect searches are just one of two pillars of wisdom: Despite the versatility and model-independence of global fits, direct searches for BSM physics have to be employed to test for new particles whenever they are light enough to be directly produced. As anomalies within data of electron and muon AMMs hint at the possibility that BSM physics can be just around the corner, direct searches for new particles offer a complementary approach. Even though standard tools in direct searches may already be pushed to their limits, novel observables exploiting flavor-specific features of BSM physics open new directions in the pursuit of BSM physics. In the era of searches for BSM signatures, only the combination of these two approaches - direct and indirect searches - will ultimately drive our fundamental understanding of nature into new territories.

A Parameters and loop functions

In the following, we summarize the default values for SM parameters used in the analysis and list analytic formulas of loop functions.

A.1 Input parameters

In our analysis, we use the following numerical values for the SM parameters [13]

$$\begin{aligned} m_t &= (173.1 \pm 0.4) \text{ GeV} , \\ m_t(m_t) &= (160_{-4}^{+5}) \text{ GeV} , \\ m_b(m_b) &= (4.18_{-0.03}^{+0.04}) \text{ GeV} , \\ m_c(m_c) &= (1.275_{-0.035}^{+0.025}) \text{ GeV} , \\ m_s(2 \text{ GeV}) &= (0.095_{-0.008}^{+0.009}) \text{ GeV} , \\ m_Z &= 91.188 \text{ GeV} , \\ m_W &= 80.4 \text{ GeV} , \\ \alpha_s(m_Z) &= 0.1181 , \\ \alpha_e &= 7.29735257 \times 10^{-3} , \\ \sin^2 \theta_w(m_Z) &= 0.2313 , \\ G_F &= 1.166379 \times 10^{-5} \text{ GeV}^{-2} . \end{aligned}$$

The relevant CKM matrix elements are given in Refs. [415, 416]

$$\begin{aligned} V_{tb} &= 0.999097 \pm 0.000024 , \\ V_{ts} &= (-0.04156 \pm 0.00056) \exp[(1.040 \pm 0.035)^\circ] , \\ V_{cb} &= 0.04255 \pm 0.00069 . \end{aligned}$$

In addition, the experimental input for our explicit computation of $\text{BR}(\bar{B} \rightarrow X_s \gamma)$ reads [335, 417]

$$\begin{aligned} C &= 0.568 \pm 0.007 \pm 0.01 , \\ \text{BR}(\bar{B} \rightarrow X_c e \bar{\nu})_{\text{exp}} &= 0.1061 \pm 0.0017 . \end{aligned}$$

Note that these values are the default values for our analyses. However, for some computations we use numerical values slightly different from the ones specified above to match experimental analyses. In addition, whenever we employ tools such as `MadGraph5_aMC@NLO`, `flavio`, or `DELPHES 3` we apply the default values used in these tools if not stated otherwise.

A.2 Loop functions

The functions E_7^{uW} , F_7^{uW} , E_8^{uW} , and F_8^{uW} relevant for the matching of the SMEFT operators O_{uB} , O_{uB} , and O_{uB} (see Eq. (5.1.1)) onto O_7 and O_8 (see Eq. (C.1.2)) are given as [221]

$$E_7^{uW}(x_t) = \frac{-9x_t^3 + 63x_t^2 - 61x_t + 19}{48(x_t - 1)^3} + \frac{(3x_t^4 - 12x_t^3 - 9x_t^2 + 20x_t - 8) \ln(x_t)}{24(x_t - 1)^4} + \frac{1}{8} \ln\left(\frac{m_W^2}{\mu_W^2}\right), \quad (\text{A.2.1a})$$

$$F_7^{uW}(x_t) = \frac{x_t(2 - 3x_t) \ln(x_t)}{4(x_t - 1)^4} - \frac{3x_t^3 - 17x_t^2 + 4x_t + 4}{24(x_t - 1)^3}, \quad (\text{A.2.1b})$$

$$E_7^{uB}(x_t) = -\frac{1}{8} \ln\left(\frac{m_W^2}{\mu_W^2}\right) - \frac{(x_t + 1)^2}{16(x_t - 1)^2} - \frac{x_t^2(x_t - 3) \ln(x_t)}{8(x_t - 1)^3}, \quad (\text{A.2.1c})$$

$$F_7^{uB}(x_t) = -\frac{1}{8}, \quad (\text{A.2.1d})$$

$$E_8^{uW}(x_t) = \frac{3x_t^2 - 13x_t + 4}{8(x_t - 1)^3} + \frac{(5x_t - 2) \ln(x_t)}{4(x_t - 1)^4}, \quad (\text{A.2.1e})$$

$$F_8^{uW}(x_t) = \frac{x_t^2 - 5x_t - 2}{8(x_t - 1)^3} + \frac{3x_t \ln(x_t)}{4(x_t - 1)^4}, \quad (\text{A.2.1f})$$

$$E_8^{uG}(x_t) = E_7^{uB}(x_t), \quad (\text{A.2.1g})$$

$$F_8^{uG}(x_t) = F_7^{uB}(x_t), \quad (\text{A.2.1h})$$

with $x_t = m_t^2/m_W^2$.

The following functions relevant for the matching of up-type dipole operators on C_9 and C_{10} are taken from Ref. [221] and read

$$Y_{uW}(x_t) = \frac{3x_t}{4(x_t - 1)} - \frac{3x_t}{4(x_t - 1)^2} \ln(x_t), \quad (\text{A.2.2})$$

$$Z_{uW}(x_t) = \frac{99x_t^3 - 136x_t^2 - 25x_t + 50}{36(x_t - 1)^3} - \frac{24x_t^3 - 45x_t^2 + 17x_t + 2}{6(x_t - 1)^4} \ln(x_t), \quad (\text{A.2.3})$$

$$Z_{uB}(x_t) = -\frac{x_t^2 + 3x_t - 2}{4(x_t - 1)^2} + \frac{3x_t - 2}{2(x_t - 1)^3} \ln(x_t). \quad (\text{A.2.4})$$

The following functions parametrize contributions from both four-fermion operators and operators with two Higgs bosons [371]

$$K_0(x, \mu) = -\frac{x}{32} \left[\ln \frac{\mu^2}{m_W^2} + \frac{3(x+1)}{2(x-1)} - \frac{x^2 - 2x + 4}{(x-1)^2} \ln x \right], \quad (\text{A.2.5})$$

$$K_1(x, \mu) = \frac{x}{16} \left[\ln \frac{\mu^2}{m_W^2} + \frac{x-7}{2(x-1)} - \frac{x^2 - 2x - 2}{(x-1)^2} \ln x \right], \quad (\text{A.2.6})$$

$$K_2(x, \mu) = -\frac{x}{8} \left[\ln \frac{\mu^2}{m_W^2} + 1 - \ln x \right], \quad (\text{A.2.7})$$

$$J_2(x) = \frac{x}{8}, \quad (\text{A.2.8})$$

$$J_3(x, \mu) = -\frac{3}{16}x_t \left[\ln \frac{\mu^2}{m_W^2} + \frac{x_t + 3}{2(x_t - 1)} - \frac{x_t^2 + 1}{(x_t - 1)^2} \ln x_t \right], \quad (\text{A.2.9})$$

$$B(x) = \frac{3}{16}x \left[\frac{1}{x-1} - \frac{1}{(x-1)^2} \ln x \right], \quad (\text{A.2.10})$$

$$D(x) = -\frac{2}{9} \ln x - \frac{x}{72} \left[\frac{82x^2 - 151x + 63}{(x-1)^3} - \frac{10x^3 + 59x^2 - 138x + 63}{(x-1)^4} \ln x \right]. \quad (\text{A.2.11})$$

With these definitions, functions relevant for the matching of SMEFT to C_9 and C_{10} read [371]

$$\begin{aligned} I_1(x_t) &= -J_2(x_t) - 2K_0(x_t, \mu_W) \\ &= \frac{x_t}{16} \left[\ln \frac{\mu^2}{m_W^2} - \frac{x_t - 7}{2(x_t - 1)} - \frac{x_t^2 - 2x_t + 4}{(x_t - 1)^2} \ln x_t \right]. \end{aligned} \quad (\text{A.2.12})$$

$$\begin{aligned} I_2(x_t) &= J_2(x_t) + K_2(x_t, \mu_w) + K_0(x_t, \mu) \\ &= -\frac{x_t}{32} \left(5 \ln \frac{\mu_W^2}{m_W^2} + \frac{3(x_t + 1)}{2(x_t - 1)} - \frac{5x_t^2 - 10x_t + 8}{(x_t - 1)^2} \ln x_t \right), \end{aligned} \quad (\text{A.2.13})$$

$$\begin{aligned} I^{lq}(x_t) &= -J_2(x_t) + K_2(x_t, \mu_w) + K_0(x_t, \mu) \\ &= -\frac{x_t}{32} \left(8 + 5 \ln \frac{\mu_W^2}{m_W^2} + \frac{3(x_t + 1)}{2(x_t - 1)} - \frac{5x_t^2 - 10x_t + 8}{(x_t - 1)^2} \ln x_t \right), \end{aligned} \quad (\text{A.2.14})$$

$$\begin{aligned} I_1^{\varphi q}(x_t) &= (-1 + 4 \sin^2 \theta_w) (J_2(x_t) + 2J_3(x_t) - K_1(x_t) - 3K_0(x_t, \mu)) \\ &\quad + 2(B(x_t) + 2 \sin^2 \theta_w D(x_t)) \\ &= (-1 + 4 \sin^2 \theta_w) \frac{x_t}{32} \left(4 - 11 \ln \frac{\mu_W^2}{m_W^2} - \frac{5x_t + 13}{2(x_t - 1)} + \frac{11x_t^2 + 2x_t - 4}{(x_t - 1)^2} \ln x_t \right) \\ &\quad + \frac{3}{8}x \left[\frac{1}{x_t - 1} - \frac{1}{(x_t - 1)^2} \ln x_t \right] + \sin^2 \theta_w \left\{ -\frac{8}{9} \ln x_t \right. \\ &\quad \left. - \frac{x_t}{18} \left[\frac{82x_t^2 - 151x_t + 63}{(x_t - 1)^3} - \frac{10x_t^3 + 59x_t^2 - 138x_t + 63}{(x_t - 1)^4} \ln x_t \right] \right\}, \end{aligned} \quad (\text{A.2.15})$$

$$\begin{aligned} I_2^{\varphi q}(x_t) &= (J_2(x_t) + 2J_3(x_t) - K_1(x_t) - 3K_0(x_t, \mu)) + 2B(x_t) \\ &= \frac{x_t}{32} \left(4 - 11 \ln \frac{\mu_W^2}{m_W^2} - \frac{5x_t + 37}{2(x_t - 1)} + \frac{11x_t^2 + 2x_t + 8}{(x_t - 1)^2} \ln x_t \right), \end{aligned} \quad (\text{A.2.16})$$

where we neglected CKM-suppressed contributions $\sim |V_{ts}|^2, \sim |V_{td}|^2$, which are smaller by a factor of at least $\sim 10^{-3}$.

Contributions from $\tilde{C}_{\varphi q}^{(1)}$ and $\tilde{C}_{\varphi q}^{(3)}$ to C_1^{mix} are parametrized with the functions H_i as [369]

$$H_1(x_t) = -\frac{x_t - 7}{4(x_t - 1)} - \frac{x_t^2 - 2x_t + 4}{2(x_t - 1)^2} \ln x_t, \quad (\text{A.2.17})$$

$$H_1(x_t) = +\frac{7x_t - 25}{4(x_t - 1)} - \frac{x_t^2 - 14x_t + 4}{2(x_t - 1)^2} \ln x_t. \quad (\text{A.2.18})$$

Finally, functions relevant for the matching of SMEFT coefficients onto C_L at one-loop level are taken from [370]. In the following, we give results with evanescent coefficients set to

1:

$$I_{uW}^\nu = \frac{m_t}{m_W \sin^2 \theta_w} \left(-\frac{3(x_t - 2)}{4\sqrt{2}(x_t - 1)} - \frac{3x_t \ln x_t}{\sqrt{2}(x_t - 1)^2} \right), \quad (\text{A.2.19})$$

$$I_{\varphi q}^{\nu(1)} = \frac{1}{\sin^2 \theta_w} \left(\frac{x_t}{8} - \frac{3x_t(x_t + 1)}{32(x_t - 1)} - \frac{x_t(x_t^2 - 2x_t + 4) \ln \frac{\mu_W^2}{m_t^2}}{16(x_t - 1)^2} + \frac{3x_t \ln \frac{\mu_W^2}{m_W^2}}{16(x_t - 1)^2} \right. \\ \left. + \frac{(2m_W^2 + m_Z^2)}{8m_W^2} - \frac{3x_t \ln \frac{\mu_W^2}{m_t^2}}{8} \right), \quad (\text{A.2.20})$$

$$I_{\varphi q}^{\nu(3)} = \frac{1}{\sin^2 \theta_w} \left(-\frac{x_t}{8} + \frac{5x_t(x_t - 7)}{32(x_t - 1)} + \frac{x_t(7x_t^2 - 2x_t - 20) \ln \frac{\mu_W^2}{m_t^2}}{16(x_t - 1)^2} - \frac{3x_t(4x_t - 9) \ln \frac{\mu_W^2}{m_W^2}}{16(x_t - 1)^2} \right. \\ \left. + \frac{19m_W^2 + m_Z^2}{8m_W^2} - \frac{3 \ln \frac{m u_W^2}{m_W^2}}{8} + \frac{3m_W^2 \ln \frac{\mu_W^2}{m_W^2}}{4m_W} \right), \quad (\text{A.2.21})$$

$$I_{lu}^\nu = \frac{1}{\sin^2 \theta_w} \left(-\frac{x_t(x_t - 7)}{32(x_t - 1)} + \frac{(x_t^3 - 2x_t^2 + 4x_t) \ln \frac{\mu_w^2}{m_t^2}}{16(x_t - 1)^2} - \frac{3x_t \ln \frac{\mu_w^2}{m_W^2}}{16(x_t - 1)^2} \right), \quad (\text{A.2.22})$$

$$I_{lq}^{\nu(1)} = \frac{1}{\sin^2 \theta_w} \left(\frac{x_t}{8} - \frac{3x_t(x_t + 1)}{32(x_t - 1)} - \frac{x_t(x_t^2 - 2x_t + 4) \ln \frac{\mu_W^2}{m_t^2}}{16(x_t - 1)^2} + \frac{3x_t \ln \frac{\mu_W^2}{m_W^2}}{16(x_t - 1)^2} \right. \\ \left. + \frac{11(2m_W^2 + m_Z^2)}{48m_W^2} + \frac{(2m_W^2 + m_Z^2) \ln \frac{\mu_W^2}{m_Z^2}}{8m_W} \right), \quad (\text{A.2.23})$$

$$I_{lq}^{\nu(3)} = \frac{1}{\sin^2 \theta_w} \left(\frac{x_t}{8} - \frac{3x_t(x_t + 1)}{32(x_t - 1)} - \frac{x_t(x_t^2 - 26x_t + 28) \ln \frac{\mu_W^2}{m_t^2}}{16(x_t - 1)^2} + \frac{3x_t(8x_t - 9) \ln \frac{\mu_W^2}{m_W^2}}{16(x_t - 1)^2} \right. \\ \left. + \frac{-154m_W^2 - 11m_Z^2}{48m_W^2} - \frac{3 \ln \frac{m u_W^2}{m_W^2}}{2} - \frac{(2m_W^2 + m_Z^2) \ln \frac{\mu_W^2}{m_Z^2}}{8m_W} \right). \quad (\text{A.2.24})$$

B SMEFT Lagrangian at dimension six

In this appendix, we provide additional information about the SMEFT Lagrangian at dimension six. In App. B.1, we list the dimension-six operators in the Warsaw basis. In App. B.2, we discuss the redefinitions of SM parameters induced by dimension-six operators at the example of the gauge sector. The relations among the parameters in the SMEFT Lagrangian in the two input schemes $\{\check{\alpha}_e, \check{m}_Z, \check{G}_F\}$ and $\{\check{m}_W, \check{m}_Z, \check{G}_F\}$ are shown in App. B.3 In App. B.4, we discuss implications for the WET Lagrangian which arise when SMEFT is considered as the underlying theory.

B.1 Basis of dimension-six operators

φ^6		$\varphi^4 D^2$		$\psi^2 \varphi^3$	
O_φ	$(\varphi^\dagger \varphi)^3$	$O_{\varphi \square}$	$(\varphi^\dagger \varphi) \square (\varphi^\dagger \varphi)$	$O_{e\varphi}$	$(\varphi^\dagger \varphi) (\bar{l}_L e_R \varphi)$
		$O_{\varphi D}$	$(\varphi^\dagger D^\mu \varphi)^* (\varphi^\dagger D_\mu \varphi)$	$O_{u\varphi}$	$(\varphi^\dagger \varphi) (\bar{q}_L u_R \tilde{\varphi})$
				$O_{d\varphi}$	$(\varphi^\dagger \varphi) (\bar{q}_L d_R \varphi)$
$X^2 \varphi^2$		$\psi^2 X \varphi$		$\psi^2 \varphi^2 D$	
$O_{\varphi G}$	$\varphi^\dagger \varphi G_{\mu\nu}^A G^{A\mu\nu}$	O_{eW}	$(\bar{l}_L \sigma^{\mu\nu} e_R) \tau^I \varphi W_{\mu\nu}^I$	$O_{\varphi l}^{(1)}$	$(\varphi^\dagger i \overleftrightarrow{D}_\mu \varphi) (\bar{l}_L \gamma^\mu l_L)$
$O_{\varphi \tilde{G}}$	$\varphi^\dagger \varphi \tilde{G}_{\mu\nu}^A G^{A\mu\nu}$	O_{eB}	$(\bar{l}_L \sigma^{\mu\nu} e_R) \varphi B_{\mu\nu}$	$O_{\varphi l}^{(3)}$	$(\varphi^\dagger i \overleftrightarrow{D}_\mu^I \varphi) (\bar{l}_L \tau^I \gamma^\mu l_L)$
$O_{\varphi W}$	$\varphi^\dagger \varphi W_{\mu\nu}^I W^{I\mu\nu}$	O_{uG}	$(\bar{q}_L \sigma^{\mu\nu} T^A u_R) \tilde{\varphi} G_{\mu\nu}^A$	$O_{\varphi e}$	$(\varphi^\dagger i \overleftrightarrow{D}_\mu \varphi) (\bar{e}_R \gamma^\mu e_R)$
$O_{\varphi \tilde{W}}$	$\varphi^\dagger \varphi \tilde{W}_{\mu\nu}^I W^{I\mu\nu}$	O_{uW}	$(\bar{q}_L \sigma^{\mu\nu} u_R) \tau^I \tilde{\varphi} W_{\mu\nu}^I$	$O_{\varphi q}^{(1)}$	$(\varphi^\dagger i \overleftrightarrow{D}_\mu \varphi) (\bar{q}_L \gamma^\mu q_L)$
$O_{\varphi B}$	$\varphi^\dagger \varphi B_{\mu\nu} B^{\mu\nu}$	O_{uB}	$(\bar{q}_L \sigma^{\mu\nu} u_R) \tilde{\varphi} B_{\mu\nu}$	$O_{\varphi q}^{(3)}$	$(\varphi^\dagger i \overleftrightarrow{D}_\mu^I \varphi) (\bar{q}_L \tau^I \gamma^\mu q_L)$
$O_{\varphi \tilde{B}}$	$\varphi^\dagger \varphi \tilde{B}_{\mu\nu} B^{\mu\nu}$	O_{dG}	$(\bar{q}_L \sigma^{\mu\nu} T^A d_R) \varphi G_{\mu\nu}^A$	$O_{\varphi u}$	$(\varphi^\dagger i \overleftrightarrow{D}_\mu \varphi) (\bar{u}_R \gamma^\mu u_R)$
$O_{\varphi WB}$	$\varphi^\dagger \tau^I \varphi W_{\mu\nu}^I B^{\mu\nu}$	O_{dW}	$(\bar{q}_L \sigma^{\mu\nu} d_R) \tau^I \varphi W_{\mu\nu}^I$	$O_{\varphi d}$	$(\varphi^\dagger i \overleftrightarrow{D}_\mu \varphi) (\bar{d}_R \gamma^\mu d_R)$
$O_{\varphi \tilde{W}B}$	$\varphi^\dagger \tau^I \varphi \tilde{W}_{\mu\nu}^I B^{\mu\nu}$	O_{dB}	$(\bar{q}_L \sigma^{\mu\nu} d_R) \varphi B_{\mu\nu}$	$O_{\varphi ud}$	$i (\tilde{\varphi}^\dagger D_\mu \varphi) (\bar{u}_R \gamma^\mu d_R)$
X^3					
O_G	$f^{ABC} G_\mu^{A\nu} G_\nu^{B\rho} G_\rho^{C\mu}$				
$O_{\tilde{G}}$	$f^{ABC} \tilde{G}_\mu^{A\nu} G_\nu^{B\rho} G_\rho^{C\mu}$				
O_W	$\epsilon^{IJK} W_\mu^{I\nu} W_\nu^{J\rho} W_\rho^{K\mu}$				
$O_{\tilde{W}}$	$\epsilon^{IJK} \tilde{W}_\mu^{I\nu} W_\nu^{J\rho} W_\rho^{K\mu}$				

Table B.1: List of dimension-six operators other than four-fermion operators in the SMEFT Lagrangian. With \square we denote the contraction $D_\mu D^\mu$ of two covariant derivatives.

$(\bar{R}R)(\bar{R}R)$		$(\bar{L}L)(\bar{R}R)$	
O_{ee}	$(\bar{e}_R \gamma_\mu e_R)(\bar{e}_R \gamma^\mu e_R)$	O_{le}	$(\bar{l}_L \gamma_\mu l_L)(\bar{e}_R \gamma^\mu e_R)$
O_{uu}	$(\bar{u}_R \gamma_\mu u_R)(\bar{u}_R \gamma^\mu u_R)$	O_{lu}	$(\bar{l}_L \gamma_\mu l_L)(\bar{u}_R \gamma^\mu u_R)$
O_{dd}	$(\bar{d}_R \gamma_\mu d_R)(\bar{d}_R \gamma^\mu d_R)$	O_{ld}	$(\bar{l}_L \gamma_\mu l_L)(\bar{d}_R \gamma^\mu d_R)$
O_{eu}	$(\bar{e}_R \gamma_\mu e_R)(\bar{u}_R \gamma^\mu u_R)$	O_{qe}	$(\bar{q}_L \gamma_\mu q_L)(\bar{e}_R \gamma^\mu e_R)$
O_{ed}	$(\bar{e}_R \gamma_\mu e_R)(\bar{d}_R \gamma^\mu d_R)$	$O_{qu}^{(1)}$	$(\bar{q}_L \gamma_\mu q_L)(\bar{u}_R \gamma^\mu u_R)$
$O_{ud}^{(1)}$	$(\bar{u}_R \gamma_\mu u_R)(\bar{d}_R \gamma^\mu d_R)$	$O_{qu}^{(8)}$	$(\bar{q}_L \gamma_\mu T^A q_L)(\bar{u}_R \gamma^\mu T^A u_R)$
$O_{ud}^{(8)}$	$(\bar{u}_R \gamma_\mu T^A u_R)(\bar{d}_R \gamma^\mu T^A d_R)$	$O_{qd}^{(1)}$	$(\bar{q}_L \gamma_\mu q_L)(\bar{d}_R \gamma^\mu d_R)$
		$O_{qd}^{(8)}$	$(\bar{q}_L \gamma_\mu T^A q_L)(\bar{d}_R \gamma^\mu T^A d_R)$
$(\bar{L}L)(\bar{L}L)$		$(\bar{L}R)(\bar{R}L)$	
O_{ll}	$(\bar{l}_L \gamma_\mu l_L)(\bar{l}_L \gamma^\mu l_L)$	O_{ledq}	$(\bar{l}_L^j e_R)(\bar{d}_R q_L^j)$
$O_{qq}^{(1)}$	$(\bar{q}_L \gamma_\mu q_L)(\bar{q}_L \gamma^\mu q_L)$		
$O_{qq}^{(3)}$	$(\bar{q}_L \gamma_\mu \tau^I q_L)(\bar{q}_L \gamma^\mu \tau^I q_L)$		
$O_{lq}^{(1)}$	$(\bar{l}_L \gamma_\mu l_L)(\bar{q}_L \gamma^\mu q_L)$		
$O_{lq}^{(3)}$	$(\bar{l}_L \gamma_\mu \tau^I l_L)(\bar{q}_L \gamma^\mu \tau^I q_L)$		
$(\bar{L}R)(\bar{L}R)$		$(\bar{L}R)(\bar{L}R)$	
$O_{quqd}^{(1)}$	$(\bar{q}_L^j u_R) \epsilon_{jk} (\bar{q}_L^k d_R)$	$O_{lequ}^{(1)}$	$(\bar{l}_L^j e_R) \epsilon_{jk} (\bar{q}_L^k u_R)$
$O_{quqd}^{(8)}$	$(\bar{q}_L^j T^A u_R) \epsilon_{jk} (\bar{q}_L^k T^A d_R)$	$O_{lequ}^{(3)}$	$(\bar{l}_L^j \sigma_{\mu\nu} e_R) \epsilon_{jk} (\bar{q}_L^k \sigma^{\mu\nu} u_R)$

Table B.2: List of dimension-six four-fermion operators in the SMEFT Lagrangian. In some operators we give explicitly the contracted isospin indices j, k .

Assuming baryon number conservation, the SMEFT Lagrangian at dimension six consists of 59 different operators. They are listed in Tabs. B.1 and B.2 in the Warsaw basis [179]. Note that not all of these operators are hermitian, and the hermitian conjugate of the operator is added to the SMEFT Lagrangian together with the conjugated Wilson coefficient.

Many of these operators carry additional flavor indices, especially the four-fermion operators. This dramatically increases the number of operators and Wilson coefficients. In full flavor generality, the SMEFT Lagrangian consists of 2499 different operators (with 1350 CP -even and 1149 CP -odd couplings).

Dropping the assumption of baryon number conservation, four additional four-fermion operators arise. In the Warsaw, basis these operators read

$$O_{udq} = \epsilon^{\alpha\beta\gamma} \epsilon_{jk} \left[(d_R^\alpha)^T C u_R^\beta \right] \left[(q_L^j)^T C l_L^k \right], \quad (\text{B.1.1a})$$

$$O_{quq} = \epsilon^{\alpha\beta\gamma} \epsilon_{jk} \left[(q_L^{\alpha j})^T C q_R^{\beta k} \right] \left[(u_R^\gamma)^T C e_R \right], \quad (\text{B.1.1b})$$

$$O_{qqq} = \epsilon^{\alpha\beta\gamma} \epsilon_{jn} \epsilon_{km} \left[(q_L^{\alpha j})^T C q_L^{\beta k} \right] \left[(q_L^{\gamma m})^T C l_L^n \right], \quad (\text{B.1.1c})$$

$$O_{dww} = \epsilon^{\alpha\beta\gamma} \left[(d_R^\alpha)^T C u_R^\beta \right] \left[(u_R^\gamma)^T C e_R \right], \quad (\text{B.1.1d})$$

where C denotes the charge conjugation matrix.

B.2 Redefinition of SM parameters: the gauge sector

As discussed in detail in Ref. [190], definitions of fields as well as parameters (*i.e.* masses, couplings) in the Lagrangian are modified by the presence of higher-dimensional operators. As an example, we consider here the gauge part of the Lagrangian including contributions from both the SM and higher-dimensional operators:

$$\begin{aligned} \mathcal{L}_{\text{gauge}}^{(6)} = & \frac{C_{\varphi G}}{\Lambda^2} \varphi^\dagger \varphi G_{\mu\nu}^A G^{A\mu\nu} + \frac{C_{\varphi W}}{\Lambda^2} \varphi^\dagger \varphi W_{\mu\nu}^I W^{I\mu\nu} + \frac{C_{\varphi B}}{\Lambda^2} \varphi^\dagger \varphi B_{\mu\nu} B^{\mu\nu} \\ & + \frac{C_{\varphi WB}}{\Lambda^2} \varphi^\dagger \tau^I \varphi W_{\mu\nu}^I B^{\mu\nu} + \frac{C_G}{\Lambda^2} f^{ABC} G_\mu^{A\nu} G_\nu^{B\rho} G_\rho^{C\mu} + \frac{C_W}{\Lambda^2} \epsilon^{IJK} W_\mu^{I\nu} W_\nu^{J\rho} W_\rho^{K\mu}. \end{aligned} \quad (\text{B.2.1})$$

After SSB, these dimension-six operators give additional contributions to the kinetic terms of the gauge fields in the SM Lagrangian in Eq. (2.1.50), and thus the gauge fields are no longer canonically normalized. To solve this issue, the first step is to redefine the gauge fields:

$$G_\mu^A = \mathcal{G}_\mu^A \left(1 + \frac{C_{\varphi G} v_T^2}{\Lambda^2} \right), \quad W_\mu^I = \mathcal{W}_\mu^I \left(1 + \frac{C_{\varphi W} v_T^2}{\Lambda^2} \right), \quad B_\mu = \mathcal{B}_\mu \left(1 + \frac{C_{\varphi B} v_T^2}{\Lambda^2} \right), \quad (\text{B.2.2a})$$

where v_T denotes the SMEFT Higgs VEV:

$$v_T = \left(1 + \frac{3C_H v^2}{8\lambda\Lambda^2} \right) v. \quad (\text{B.2.3})$$

In addition, the gauge couplings are modified as

$$\bar{g}_s = g_s \left(1 + \frac{C_{\varphi G} v_T^2}{\Lambda^2} \right), \quad \bar{g} = g \left(1 + \frac{C_{\varphi W} v_T^2}{\Lambda^2} \right), \quad \bar{g}' = g' \left(1 + \frac{C_{\varphi B} v_T^2}{\Lambda^2} \right). \quad (\text{B.2.4})$$

Note that products such as $g_s G_\mu^A = \bar{g}_s \mathcal{G}_\mu^A$ are unchanged by these redefinitions. While these definitions take care of the gluon terms, the EW terms need additional care due to the additional mixing between B and W^3 introduced in Eq. (B.2.1). We define the mass eigenstates as [418]

$$\begin{pmatrix} \mathcal{W}_\mu^3 \\ \mathcal{B}_\mu \end{pmatrix} = \begin{pmatrix} 1 & -\frac{v_t^2 C_{\varphi WB}}{2\Lambda^2} \\ -\frac{v_t^2 C_{\varphi WB}}{2\Lambda^2} & 1 \end{pmatrix} \begin{pmatrix} \cos \bar{\theta} & \sin \bar{\theta} \\ -\sin \bar{\theta} & \cos \bar{\theta} \end{pmatrix} \begin{pmatrix} \mathcal{Z}_\mu \\ \mathcal{A}_\mu \end{pmatrix}, \quad (\text{B.2.5})$$

where the rotation angle $\bar{\theta}$ is defined as

$$\tan \bar{\theta} = \frac{\bar{g}'}{\bar{g}} + \frac{v_T^2 C_{\varphi WB}}{2\Lambda^2} \left(1 - \frac{\bar{g}'^2}{\bar{g}^2} \right), \quad (\text{B.2.6a})$$

$$\sin \bar{\theta} = \frac{\bar{g}'}{\sqrt{\bar{g}'^2 + \bar{g}^2}} \left(1 + \frac{v_T^2 C_{\varphi WB}}{2\Lambda^2} \frac{\bar{g} \bar{g}^2 - \bar{g}'^2}{\bar{g}' \bar{g}^2 + \bar{g}'^2} \right), \quad (\text{B.2.6b})$$

$$\cos \bar{\theta} = \frac{\bar{g}}{\sqrt{\bar{g}'^2 + \bar{g}^2}} \left(1 - \frac{v_T^2 C_{\varphi WB}}{2\Lambda^2} \frac{\bar{g}' \bar{g}^2 - \bar{g}'^2}{\bar{g} \bar{g}^2 + \bar{g}'^2} \right). \quad (\text{B.2.6c})$$

With these definitions, the gauge boson masses are defined as:

$$m_W^2 = \frac{\bar{g}^2 v_T^2}{4}, \quad m_Z^2 = \frac{v_T^2}{4} (\bar{g}^2 + \bar{g}'^2) + \frac{v_T^4 C_{\varphi D}}{8\Lambda^2} (\bar{g}^2 + \bar{g}'^2) \frac{v_T^4 C_{\varphi WB}}{2\Lambda^2} \bar{g} \bar{g}', \quad (\text{B.2.7})$$

which changes the ρ parameter at tree level to

$$\rho = 1 + \frac{v_T^2 C_{\varphi WB}}{2\Lambda^2}. \quad (\text{B.2.8})$$

The effective couplings of the photon and the Z boson are given as

$$\bar{e} = \bar{g} \sin \bar{\theta} - \bar{g} \cos \bar{\theta} \frac{v_T^2 C_{\varphi WB}}{2\Lambda^2}, \quad \bar{g}_Z = \frac{\bar{e}}{\sin \bar{\theta} \cos \bar{\theta}} \left(1 \frac{\bar{g}^2 + \bar{g}'^2}{2\bar{g}\bar{g}'} \frac{v_T^2 C_{\varphi WB}}{\Lambda^2} \right). \quad (\text{B.2.9})$$

Note that the quantities $\bar{\theta}_i$ coincide with the SM ones θ_i when they are multiplied with a term from the dimension-six Lagrangian up to corrections $\sim \Lambda^{-4}$ which are neglected. For more details regarding this topic as well as the complete list of SMEFT redefinitions see Ref. [190].

B.3 Input scheme dependence

Considering the $\{\alpha_e, m_Z, G_F\}$ scheme the tree level SM relations

$$\begin{aligned} \check{e} &= \sqrt{4\pi\alpha_e}, & \check{g}' &= \frac{\check{e}}{\cos \check{\theta}}, & \check{g} &= \frac{\check{e}}{\sin \check{\theta}}, \\ \check{v}_T^2 &= \frac{1}{\sqrt{2}\check{G}_F}, & \check{m}_W^2 &= \check{m}_Z^2 \cos^2 \check{\theta}, & \sin^2 \check{\theta} &= \frac{1}{2} \left[1 - \sqrt{1 - \frac{4\pi\check{\alpha}_e}{\sqrt{2}\check{G}_F} \check{m}_Z^2} \right], \end{aligned} \quad (\text{B.3.1})$$

receive additional BSM contributions. Using the notation of Ref. [419] we write the shifts in the following way:

$$\delta\theta_i = \bar{\theta}_i - \check{\theta}_i. \quad (\text{B.3.2})$$

The SM limit ($C_i \rightarrow 0$) is identified as $\delta\theta_i \rightarrow 0$. We define short-hand notations for convenience where additional superscripts denote the generation index of the fermion fields in the effective operators:

$$\delta G_F = \frac{1}{2\check{G}_F \Lambda^2} \left(C_{\varphi l}^{(3)11} C_{\varphi l}^{(3)22} - \frac{C_{ll}^{2112} + C_{ll}^{1221}}{2} \right), \quad (\text{B.3.3a})$$

$$\delta m_h^2 = \frac{\check{m}_h^2}{\sqrt{2}\check{G}_F \Lambda^2} \left[-\frac{3C_\varphi}{2\lambda} + 2\sqrt{2}\check{G}_F \check{v}_T^2 \left(C_{\varphi \square} - \frac{1}{4} C_{\varphi D} \right) \right], \quad (\text{B.3.3b})$$

$$\delta m_Z^2 = \frac{1}{2\sqrt{2}} \frac{\check{m}_Z^2 C_{\varphi D}}{\check{G}_F m_Z^2} + \frac{\sqrt{\sqrt{2}\check{\alpha}_e} \check{m}_Z C_{\varphi WB}}{\check{G}_F^{\frac{3}{2}} \Lambda^2}, \quad (\text{B.3.3c})$$

$$\delta m_W^2 = \check{m}_W^2 \left(\sqrt{2}\delta G_F + \frac{2\delta g}{\check{g}} \right). \quad (\text{B.3.3d})$$

Using this notation, we find the following relations:

$$\delta v_T^2 = \frac{\delta G_F}{\check{G}_F}, \quad (\text{B.3.4a})$$

$$\delta g' = \frac{\check{g}'}{2 \cos 2\check{\theta}} \left[\sin^2 \check{\theta} \left(\sqrt{2} \delta G_F + \frac{\delta m_Z^2}{\check{m}_Z^2} \right) + \cos^2 \check{\theta} \sin 2\check{\theta} \check{v}_T^2 \frac{C_{\varphi WB}}{\Lambda^2} \right], \quad (\text{B.3.4b})$$

$$\delta g = \frac{-\check{g}}{2 \cos 2\check{\theta}} \left[\cos^2 \check{\theta} \left(\sqrt{2} \delta G_F + \frac{\delta m_Z^2}{\check{m}_Z^2} \right) + \sin^2 \check{\theta} \sin 2\check{\theta} \check{v}_T^2 \frac{C_{\varphi WB}}{\Lambda^2} \right], \quad (\text{B.3.4c})$$

$$\delta \sin^2 \theta = 2 \cos^2 \check{\theta} \sin^2 \check{\theta} \left(\frac{\delta g}{\check{g}} + \frac{\delta g'}{\check{g}'} \right) + \check{v}_T^2 \sin 2\check{\theta} \cos 2\check{\theta} \frac{C_{\varphi WB}}{2\Lambda^2}. \quad (\text{B.3.4d})$$

In the $\{\check{\alpha}_e, \check{m}_Z, \check{G}_F\}$ we find $\{\bar{\alpha}_e, \bar{m}_Z\} = \{\check{\alpha}_e, \check{m}_Z\}$ while for EW processes \bar{G}_F is defined as $\bar{G}_F = 1/\sqrt{2}\check{v}_T^2$.

In the $\{\check{m}_W, \check{m}_Z, \check{G}_F\}$ scheme the SM relations in Eq. (B.3.1) are altered to

$$\begin{aligned} \check{e} &= 2\check{m}_W \sqrt{\sqrt{2}\check{G}_F \sin \check{\theta}}, & \check{g} &= 2\check{m}_W \sqrt{\sqrt{2}\check{G}_F}, & \sin^2 \check{\theta} &= 1 - \frac{\check{m}_W^2}{\check{m}_Z^2}. \\ \check{g}' &= 2\check{m}_Z \sqrt{\sqrt{2}\check{G}_F \left(1 - \frac{\check{m}_W^2}{\check{m}_Z^2}\right)}, & \check{v}_T^2 &= \frac{1}{\sqrt{2}\check{G}_F}, \end{aligned} \quad (\text{B.3.5})$$

In this input parameter scheme, $\{\delta G_F, \delta m_h^2\}$ are the same as in Eq. (B.3.3). The remaining shifts read:

$$\frac{\delta \alpha_e}{2\check{\alpha}_e} = -\frac{\delta G_F}{\sqrt{2}} + \frac{\delta m_Z^2}{\check{m}_Z^2} \frac{\check{m}_W^2}{2(\check{m}_W^2 - \check{m}_Z^2)} - \sin \check{\theta} \frac{\check{m}_W C_{\varphi WB}}{\sqrt{2}\check{m}_Z \check{G}_F \Lambda^2}, \quad (\text{B.3.6a})$$

$$\delta \sin^2 \check{\theta} = 2 \cos^2 \check{\theta} \sin^2 \check{\theta} \left(\frac{\delta g'}{\check{g}'} - \frac{\delta g}{\check{g}} \right) + \check{v}_T^2 \frac{\sin 2\check{\theta} \cos 2\check{\theta} C_{\varphi WB}}{2\Lambda^2}, \quad (\text{B.3.6b})$$

$$\frac{\delta m_Z^2}{\check{m}_Z^2} = \frac{C_{\varphi D}}{2\sqrt{2}\check{G}_F \Lambda^2} + \frac{\sqrt{2}\check{m}_W C_{\varphi WB}}{\check{G}_F \check{m}_Z \Lambda^2} \sqrt{1 - \frac{\check{m}_W^2}{\check{m}_Z^2}}, \quad (\text{B.3.6c})$$

$$\frac{\delta m_W^2}{\check{m}_W^2} = 0, \quad (\text{B.3.6d})$$

$$\delta g' = -\frac{\check{g}' \delta G_F}{\sqrt{2}} - \check{g}_1 \frac{\delta m_Z^2}{2 \sin^2 \check{\theta} \check{m}_Z^2}, \quad (\text{B.3.6e})$$

$$\delta g = -\frac{\check{g} \delta G_F}{\sqrt{2}}. \quad (\text{B.3.6f})$$

B.4 Implications for the low-energy Lagrangian

In the WET Lagrangian, effective operators arise already at dimension three. In the following, we summarize the number of effective operators in the WET Lagrangian that are added to the Lagrangian in Eq. 3.1.23 in the case of three (one) fermion generation up to dimension six [150].

At dimension three, there are six independent operators plus their hermitian conjugates (1 + 1 for one generation). These operators introduce Majorana mass terms for neutrinos and violate lepton number by $\Delta L = 2$. At dimension five, 35 independent dipole operators

plus their conjugates (5 + 5) with $\Delta B = \Delta L = 0$ can be defined, where ΔB denotes changes of the baryon number. In addition, 3 + 3 (1+1) Majorana-neutrino dipole operators with $\Delta L = 2$ are present. At dimension six, the number of operators is significantly larger in the case of three generations of fermions. There are in total 3631 (80) $\Delta B = \Delta L = 0$ operators, 600 + 600 (14 + 14) $\Delta L = \pm 2$ ones, 6 + 6 (1 + 1) with $\Delta L = \pm 4$, 288 + 288 (9 + 9) operators that have $\Delta B = \Delta L = \pm 1$, and 228 + 228 (7 + 7) operators with $\Delta B = -\Delta L = \pm 1$.

Considering WET as the low-energy limit of the SMEFT Lagrangian allows only for certain operators in the WET Lagrangian. Dimension-three WET operators are induced by dimension-five operators in the SMEFT. From the WET dimension-five operators only those with $\Delta B = \Delta L = 0$ receive contribution from dimension-six SMEFT operators of the class $\psi^2 X \varphi$. Matching SMEFT operators to dimension-six WET operators is done by dividing the ψ^4 into subclasses with different chirality (L/R) and the dirac structure (scalar/vector/tensor). This choice is, however, not unique and operators of one subclass can be converted into operators of another by applying Fierz identities. In the $\delta B = \Delta L = 0$ class, the triple-gluon operators already exist in SMEFT while from the four-fermion operators receive contributions from both SMEFT four-fermion operators as well as contributions from diagrams with the exchange of a heavy boson. Only for some operators with the $(\bar{L}L)(\bar{R}R)$, $(\bar{L}R)(\bar{R}L)$, and $(\bar{L}R)(\bar{L}R)$ chirality structure there are no contributions at dimension-six in the SMEFT. WET $\Delta L = \pm 4$ operators and $\Delta L = \pm 2$ operators are induced in SMEFT after spontaneous symmetry breaking. However, such contributions stem from Higgs exchange diagrams suppressed by small Yukawa couplings and are formally of higher order. In contrast, not all $\Delta B = \Delta L = \pm 1$ operators receive contributions from SMEFT at tree level (in total 36 plus their hermitian conjugates), while $\Delta B = -\Delta L = \pm 1$ operators do not receive any tree-level contributions from SMEFT. The matching results can be found in Tabs. 9-21 of Refs. [150].

B.5 Solving renormalization group equations

The RGEs for Wilson coefficients can be written as

$$\frac{d}{d \ln \mu} C_i = \gamma_{ji}(\mu) C_j, \quad (\text{B.5.1})$$

with the ADM γ . In the following, we consider contributions proportional to the strong coupling α_s only. The perturbative expansion of γ in powers of α_s is given as

$$\gamma(\mu) = \frac{\alpha_s(\mu)}{4\pi} \gamma^{(0)} + \frac{\alpha_s^2(\mu)}{(4\pi)^2} \gamma^{(1)} + \frac{\alpha_s^3(\mu)}{(4\pi)^3} \gamma^{(2)} + \dots \quad (\text{B.5.2})$$

Analogously, the coefficients expanded in powers of α_s read

$$C_i(\mu) = C_i^{(0)}(\mu) + \frac{\alpha_s(\mu)}{4\pi} C_i^{(1)}(\mu) + \frac{\alpha_s^2(\mu)}{(4\pi)^2} C_i^{(2)}(\mu) + \dots \quad (\text{B.5.3})$$

Given the values of the coefficients at a scale μ_0 the RGE are used to evolve the coefficients to the low-energy scale. The solution to Eq. (B.5.1) reads [420]

$$C^{(0)}(\mu) = U^{(0)}(\mu, \mu_0) C^{(0)}(\mu_0), \quad (\text{B.5.4})$$

$$C^{(1)}(\mu) = \frac{4\pi}{\alpha_s(\mu)} \left(U^{(0)}(\mu, \mu_0) \frac{\alpha_s(\mu_0)}{4\pi} C^{(1)}(\mu_0) + \frac{\alpha_s(\mu)}{4\pi} J^{(1)} U^{(0)}(\mu, \mu_0) C^{(0)}(\mu_0) - \frac{\alpha_s(\mu_0)}{4\pi} U^{(0)}(\mu, \mu_0) J^{(1)} C^{(0)}(\mu_0) \right), \quad (\text{B.5.5})$$

$$C^{(2)}(\mu) = \frac{\alpha_s^2(\mu_0)}{\alpha_s^2(\mu)} U^{(0)}(\mu, \mu_0) C^{(2)}(\mu_0) + \frac{\alpha_s(\mu_0)}{\alpha_s(\mu)} J^{(1)} U^{(0)}(\mu, \mu_0) C^{(1)}(\mu_0) - \frac{\alpha_s^2(\mu_0)}{\alpha_s^2(\mu)} U^{(0)}(\mu, \mu_0) J^{(1)} C^{(1)}(\mu_0) + J^{(2)} U^{(0)}(\mu, \mu_0) C^{(0)}(\mu_0) - \frac{\alpha_s^2(\mu_0)}{\alpha_s^2(\mu)} U^{(0)}(\mu, \mu_0) (J^{(2)} - (J^{(1)})^2) C^{(0)}(\mu_0) - \frac{\alpha_s(\mu_0)}{\alpha_s(\mu)} J^{(1)} U^{(0)}(\mu, \mu_0) J^{(1)} C^{(0)}(\mu_0). \quad (\text{B.5.6})$$

and similarly for $C^{(i)}$ with $i > 2$. The matrices $U^{(0)}$, $J^{(1)}$ and $J^{(2)}$ are given as

$$U^{(0)}(\mu, \mu_0) = V \text{diag} \left[\left(\frac{\alpha_s(\mu_0)}{\alpha_s(\mu)} \right)^{a_i} \right] V^{-1}, \quad (\text{B.5.7})$$

$$J^{(i)} = V S^{(i)} V^{-1}, \quad (\text{B.5.8})$$

with

$$\left(V^{-1} \left(\gamma^{(0)\text{eff}} \right)^T V \right)_{ij} = 2\beta_0 a_i \delta_{ij}, \quad (\text{B.5.9})$$

and

$$S_{ij}^{(1)} = \frac{\beta_1}{\beta_0} a_i \delta_{ij} - \frac{G_{ij}^{(1)}}{2\beta_0(1+a_i-a_j)}, \quad (\text{B.5.10})$$

$$S_{ij}^{(2)} = \left(\frac{\beta_2}{2\beta_0} - \frac{\beta_1^2}{2\beta_0} \right) a_i \delta_{ij} + \sum_k \frac{2\beta_1 a_i \delta_{ik} - G_{ik}^{(1)}}{2\beta_0(2+a_i-a_j)} S_{kj}^{(1)} + \frac{\beta_1 G_{ij}^{(1)} - \beta_0 G_{ij}^{(2)}}{2\beta_0^2(2+a_i-a_j)}, \quad (\text{B.5.11})$$

$$G^{(i)} = V^{-1} \left(\gamma^{(i)\text{eff}} \right)^T V. \quad (\text{B.5.12})$$

The coefficients β_i are taken from the expansion of the beta function of the QCD coupling with $\beta_0 = 11 - 2/3n_q$, $\beta_1 = 102 - 38n_q/3$ and $\beta_2 = 2857/2 - 5033/18n_q + 325/54n_q^2$ with n_q being the number of active quarks.

C Weak effective theories

In the following, we list the WET Lagrangians used throughout this work.

C.1 $b \rightarrow s\gamma$ and $b \rightarrow s\ell^+\ell^-$ transitions

The Lagrangian that describes $b \rightarrow s\gamma$ and $b \rightarrow s\ell^+\ell^-$ transitions was originally formulated as the weak effective Hamiltonian [152, 311] and is given as

$$\mathcal{L}_{\text{WET}}^{b \rightarrow s} = \frac{4G_F}{\sqrt{2}} V_{ts}^* V_{tb} \sum_{i=1}^8 \bar{C}_i Q_i. \quad (\text{C.1.1})$$

Here, Q_i are effective operators and \bar{C}_i are the corresponding Wilson coefficients parametrizing both SM and BSM contributions. The operators relevant for $b \rightarrow s$ transitions are [152, 311]

$$\begin{aligned} Q_1 &= (\bar{s}_L \gamma_\mu T^a c_L)(\bar{c}_L \gamma^\mu T^a b_L), & Q_2 &= (\bar{s}_L \gamma_\mu c_L)(\bar{c}_L \gamma^\mu b_L), \\ Q_3 &= (\bar{s}_L \gamma_\mu b_L) \sum_q (\bar{q} \gamma^\mu q), & Q_4 &= (\bar{s}_L \gamma_\mu T^a b_L) \sum_q (\bar{q} \gamma^\mu T^a q), \\ Q_5 &= (\bar{s}_L \gamma_\mu \gamma_\nu \gamma_\sigma b_L) \sum_q (\bar{q} \gamma^\mu \gamma^\nu \gamma^\sigma q), & Q_6 &= (\bar{s}_L \gamma_\mu \gamma_\nu \gamma_\sigma T^a b_L) \sum_q (\bar{q} \gamma^\mu \gamma^\nu \gamma^\sigma T^a q), \\ Q_7 &= \frac{e}{16\pi^2} m_b (\bar{s}_L \sigma^{\mu\nu} b_R) F_{\mu\nu}, & Q_8 &= \frac{g_s}{16\pi^2} m_b (\bar{s}_L \sigma^{\mu\nu} T^a b_R) G_{\mu\nu}^a, \\ Q_9 &= \frac{e^2}{16\pi^2} (\bar{s}_L \gamma_\mu b_L) (\bar{\ell} \gamma^\mu \ell'), & Q_{10} &= \frac{e^2}{16\pi^2} (\bar{s}_L \gamma_\mu b_L) (\bar{\ell} \gamma^\mu \gamma^5 \ell'), \end{aligned} \quad (\text{C.1.2})$$

where L(R) denote chiral left (right) projection operators, and $F_{\mu\nu}$ is the photon field strength tensor.

C.2 $b \rightarrow s\nu\bar{\nu}$ transitions

The effective Lagrangian describing $b \rightarrow s\bar{\nu}\nu$ transitions reads:

$$\mathcal{L}_{\text{WET}}^\nu = \frac{4G_F}{\sqrt{2}} V_{ts}^* V_{tb} (C_L(\mu) Q_L(\mu) + C_R(\mu) Q_R(\mu)), \quad (\text{C.2.1})$$

where the effective operators are defined as

$$Q_L^{\nu\nu'} = \frac{e^2}{16\pi^2} (\bar{s}_L \gamma_\mu b_L) (\bar{\nu} \gamma^\mu (1 - \gamma_5) \nu'), \quad Q_R^{\nu\nu'} = \frac{e^2}{16\pi^2} (\bar{s}_R \gamma_\mu b_R) (\bar{\nu} \gamma^\mu (1 - \gamma_5) \nu'). \quad (\text{C.2.2})$$

C.3 $B_s - \bar{B}_s$ mixing

The last process we consider here is $B_s - \bar{B}_s$ mixing. The part of the Lagrangian relevant for our work reads [366]

$$\mathcal{L}_{\text{WET}}^{\text{mix}} = \frac{G_F^2 m_W^2}{16\pi^2} Q_1^{\text{mix}} |V_{tb} V_{ts}^*|^2 C_{1,tt}^{\text{mix}}, \quad (\text{C.3.1})$$

where

$$Q_1^{\text{mix}} = (\bar{s}\gamma_\mu P_L b) (\bar{s}\gamma^\mu P_L b). \quad (\text{C.3.2})$$

D Search for physics beyond the Standard Model at colliders

Measurement at colliders provide a unique opportunity to test the SM and to search for signatures of BSM physics. In order to compute SM and BSM predictions for observables, a variety of tools has to be employed, regardless of the new-physics model considered. In addition, in order to determine the values of the parameters allowed by experimental measurements, a consistent statistical framework has to be employed.

We present tools employed for the computation of SM and BSM contributions to observables at colliders and the statistical and theoretical framework applied in this work to derive constraints on the parameter space of the model considered in the analysis. We first introduce the concept of jets in Sec. D.1 and discuss why they necessarily arise. Afterwards, we present the theoretical concept of the parton distribution functions used for computation of observables at hadron colliders in Sec. D.2 In Sec. D.3, we give the different steps needed for the computation of observables at colliders.

D.1 Final state radiation and the notion of jets

In computations of higher-order contributions to scattering processes such as $e^+e^- \rightarrow \mu^+\mu^-$ in QED virtual corrections to the tree-level process have to be included in the computation. Consider the virtual vertex corrections to the tree-level process shown in Fig. D.1 (for simplicity, we consider contributions proportional to the muon coupling only). While the counterterm contributions from the second diagram cancel all occurring UV divergences, IR divergences do still occur in the computation. Introducing a photon mass m_γ as a regulator for the divergences we find for the virtual correction to the total cross section [421]:

$$\sigma_V = \frac{e^2}{8\pi^2} \sigma_0 \left(-\ln^2 \frac{m_\gamma^2}{q^2} - 3 \ln \frac{m_\gamma^2}{q^2} - \frac{7}{2} + \frac{\pi^2}{3} \right), \quad (\text{D.1.1})$$

where σ_0 is the tree-level result for the cross section, and e refers to the renormalized coupling. The logarithm $\ln^2(m_\gamma^2/q^2)$ is called *Sudakov double logarithm* [422] and is a characteristic feature of IR divergences. As such, the divergent logarithms $\sim \ln^2$ remain in the computation even when comparing two cross sections at different scales. The solution to this issue is to include final-state radiation from real-emission diagrams as shown in Fig. D.2. Squaring these diagrams gives contributions at the same order in the coupling as interference terms between tree-level diagrams and virtual-correction diagrams. Computing these diagrams we encounter two kinds of divergences which occur when the product of the four-vectors, $p_\gamma p_{\mu^\pm} = E_\gamma E_{\mu^\pm} \cos \theta$, of the emitting particle and the photon vanishes: those with $E_i \rightarrow 0$ are called *soft singularities*, and singularities with $\cos \theta \rightarrow 1$ (photon and emitting particle are in same direction) are referred to as *collinear singularities*. Again, divergences can be regulated with a photon mass, and we find for the real-emission contributions to the cross



Figure D.1: Virtual corrections to the tree level process of $e^- e^+ \rightarrow \mu^- \mu^+$ scattering at NLO in the muon coupling.

section [421]

$$\sigma_R = \frac{e^2}{8\pi^2} \sigma_0 \left(-\ln^2 \frac{m_\gamma^2}{q^2} - 3 \ln \frac{m_\gamma^2}{q^2} + 5 - \frac{\pi^2}{3} \right). \quad (\text{D.1.2})$$

While both the virtual corrections as well as the real-emission contributions are IR divergent their sum is finite:

$$\sigma_V + \sigma_R = \sigma_0 \frac{3e^2}{16\pi^2}. \quad (\text{D.1.3})$$

The physical interpretation of this finding is that a final state particle such as the muon can not be distinguished from a particle with an additional arbitrary number of soft or collinear photons. The reason is that there are always lower limits E_{low} and θ_{low} on the resolution of the energy and the angle between a photon and a particle, respectively. Objects, which describe such final states, are called *jets*. In general, any experimental resolution parameter can act as an IR regulator.

Almost every final state of a scattering process at high-energy colliders contains such a collection of collimated particles. The most prominent example for jets and also the one that is mostly observed experimentally are QCD jets. Here, we would replace the muon with a quark and the photon with a gluon in the example discussed above. The quark radiates gluons which split into additional gluons and quark-antiquark pairs. However, an important difference arises in QCD compared to QED. Due to the different energy dependence of the coupling constants (see also Fig. 2.1) quarks are not observed as free particles at colliders. Instead, at distances larger than the length scale $\Lambda_{\text{QCD}}^{-1}$ (anti-)quarks and gluons hadronize into bound states. These hadrons continue to decay into (meta-)stable particles such as pions which are then measured by the experiment. As the radiation happens dominantly in the direction of the original hard parton, the hadrons are grouped together in a jet. The four-momentum of the jet then serves as an approximation for the four-momentum of the original parton. In experiments, the exact reconstruction of jets, and thus of the hard parton, are defined by the jet algorithm used to cluster the particles into one jet. One example is the anti- k_t algorithm [333], where essentially soft particles within a cone with radius R around a hard particle are clustered together with the hard particle to form a jet.



Figure D.2: Real emission diagrams process of $e^-e^+ \rightarrow \mu^-\mu^+$ scattering.

D.2 Parton distribution functions

Similarly to the higher-order corrections to the final-state particles, IR divergences occur in the case of initial state radiation. Again, the sum of virtual vertex corrections and initial-state radiation contributions is IR finite. The physical interpretation, however, is fundamentally different. These infrared divergences occur in the propagators $\sim 1/(p_e - p_\gamma)^2$ of intermediate states as this propagator can develop soft and collinear divergences. In QED, there are no massless charged particles, and thus the collinear singularities are regulated by the particle mass so that large logarithms $\sim \ln m_e^2/E^2$ appear. In contrast, collinear divergences can appear in QCD as the massless gluons carry charge and can emit other gluons. Such IR divergences can be canceled when a probabilistic distribution of initial states is assumed [423–425].

One example for such a distribution of initial states are PDFs $f_i(x, Q^2)$. These functions parametrize the probability of finding a parton i inside the proton carrying fraction x of the proton momentum, and Q denotes the energy scale of the hard process. PDFs allow to compute observables such as cross sections in terms of partons by convolving cross sections at parton level with the distribution functions. Consider as an example the total cross section of proton-proton scattering

$$\sigma(pp \rightarrow X) = \sum_{q, q'} \int dx_1 dx_2 f_q(x_1, Q^2) f_{q'}(x_2, Q^2) \hat{\sigma}(qq' \rightarrow X), \quad (\text{D.2.1})$$

where $\hat{\sigma}$ denotes the cross section computed at parton level, and q, q' run over all quarks, antiquarks and gluons. As such, making predictions for processes at hadron colliders such as the LHC requires precise knowledge of the PDFs. However, QCD makes no predictions about the parton content of the proton, and as such the PDFs are determined from fits to data. In these fits, observables from a large variety of processes are used employing the *DGLAP evolution equation* [426–429] named after Dokshitzer, Gribov, Lipatov, Altarelli and Parisi. At leading order these equations read

$$\frac{df_i(x, \mu)}{d \ln \mu} = \sum_j \frac{\alpha_s}{\pi} \int_x^1 d \ln \xi f_j(\xi, \mu) P_{ij} \left(\frac{x}{\xi} \right), \quad (\text{D.2.2})$$

where the P_{ij} are DGLAP splitting functions and i, j run over quarks, antiquarks and gluons. The DGLAP evolution equations allow to predict the evolution of the PDFs from a scale μ_0 within perturbative QCD. However, as stated above, solving the DGLAP equations does not make any predictions about the x dependence of the PDFs at a given scale Q^2 . Several groups determine the PDFs from fits to data from fixed-target experiments, HERA, Tevatron and LHC, see Refs. [430–435] for recent examples of PDF determinations at NNLO.

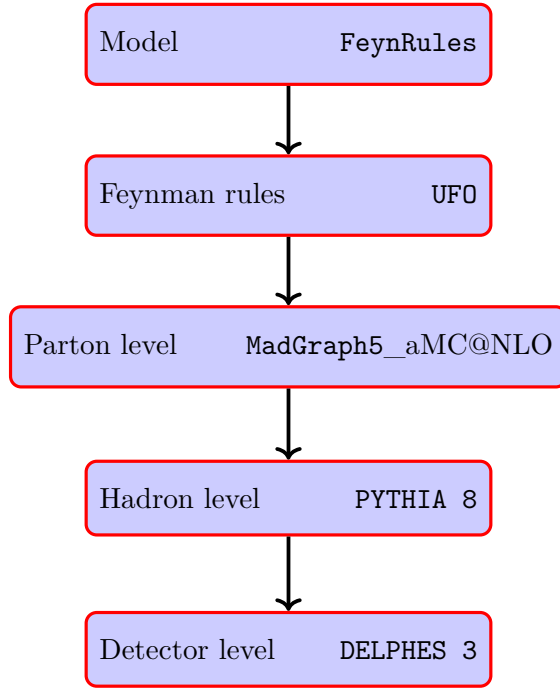


Figure D.3: List of steps and related tool needed in an analysis of collider signatures of a model. See text for details.

D.3 Related tools

Computing observables in scattering processes at colliders requires different steps, as shown in Fig. D.3 In the following, we discuss each of these five steps.

Model: The first step is to provide a definition of a physical model in the form of fields, a Lagrangian, and the parameters of the model. This information can be implemented in `FeynRules` [436] which allows to calculate the Feynman rules.

Feynman rules: The Feynman rules are then provided in the UFO format [297] for automated matrix-element generators. This format is designed to be compatible with a variety of generators. In addition, it is generic in the sense that no assumptions are made about the structures appearing in the model.

Parton level: MC generators are used for a variety of applications, *e.g.* predicting event rates or simulating backgrounds. Especially, MC event generators allow to compute cross sections of the hard scattering processes including initial and final state radiation. An example for such a MC generator is `MadGraph5_aMC@NLO` [298] which allows the automatic computation of tree level and NLO cross sections well as the matching to parton-shower simulations.

Hadron level: After the generation of the parton-level events the effects of final and initial state radiation have to be included, see also App. D.1. As such, the parton configuration is hadronized and followed by decays of the unstable particles. Typically, a MC generator, *e.g.* `PYTHIA 8` [329], is used for this step. This process is, in contrast to the previous step, to the largest part non-perturbative and requires modeling and parameterization of data, especially for the decays. At the end of this step, realistic events which could be observed by a detector are obtained.

Detector level: As a final step of phenomenological studies, the effects of detectors have to be included in the analysis. This is done by performing a detector simulation. Full simulations

performed by experimental collaborations are very time-consuming. An example for a toolkit for such simulations is `Geant4` [437]. Most phenomenological studies, however, do not need a complete detector simulation, and a fast parametrization of the detector response can be employed to obtain a sufficient precision. In this approach, which is used in the software toolbox `DELPES 3` [414], the detector response at the particle level is parametrized allowing to *e.g.* treat pile-up, *b* tagging, or jet and missing energy resolution.

E Toy example for correlation matrices

In order to demonstrate the general shape of the correlation matrices introduced in in Sec. 4.2, we consider an example with five measurements: two measurements of total cross sections at 7 TeV of single-top ($\sigma(tq)_7^A$) and single-antitop production ($\sigma(\bar{t}q)_7^A$) by ATLAS, two measurement of single-top production cross section at 8 TeV by ATLAS ($\sigma(tq)_8^A$) and CMS ($\sigma(tq)_8^C$), and one measurement of the total decay width by ATLAS (Γ_t). Within our parametrization, the correlation matrix of systematic uncertainties reads

$$\begin{matrix} & \sigma(tq)_7^A & \sigma(\bar{t}q)_7^A & \sigma(tq)_8^A & \sigma(tq)_8^C & \Gamma_t \\ \sigma(tq)_7^A & \left(\begin{array}{ccccc} 1 & \rho_{\text{sys}} & \frac{\rho_{\text{sys}}}{2} & 0 & 0 \\ \rho_{\text{sys}} & 1 & \frac{\rho_{\text{sys}}}{2} & 0 & 0 \\ \frac{\rho_{\text{sys}}}{2} & \frac{\rho_{\text{sys}}}{2} & 1 & 0 & 0 \\ 0 & 0 & 0 & 1 & 0 \\ 0 & 0 & 0 & 0 & 1 \end{array} \right) & & & & \\ \sigma(\bar{t}q)_7^A & & & & & \\ \sigma(tq)_8^A & & & & & \\ \sigma(tq)_8^C & & & & & \\ \Gamma_t & & & & & \end{matrix}, \quad (\text{E.0.1})$$

while the matrix for theory uncertainties is given by

$$\begin{matrix} & \sigma(tq)_7^A & \sigma(\bar{t}q)_7^A & \sigma(tq)_8^A & \sigma(tq)_8^C & \Gamma_t \\ \sigma(tq)_7^A & \left(\begin{array}{ccccc} 1 & \rho_{\text{th}} & \frac{\rho_{\text{th}}}{2} & \frac{\rho_{\text{th}}}{2} & 0 \\ \rho_{\text{th}} & 1 & \frac{\rho_{\text{th}}}{2} & \frac{\rho_{\text{th}}}{2} & 0 \\ \frac{\rho_{\text{th}}}{2} & \frac{\rho_{\text{th}}}{2} & 1 & \rho_{\text{th}} & 0 \\ \frac{\rho_{\text{th}}}{2} & \frac{\rho_{\text{th}}}{2} & \rho_{\text{th}} & 1 & 0 \\ 0 & 0 & 0 & 0 & 1 \end{array} \right) & & & & \\ \sigma(\bar{t}q)_7^A & & & & & \\ \sigma(tq)_8^A & & & & & \\ \sigma(tq)_8^C & & & & & \\ \Gamma_t & & & & & \end{matrix}. \quad (\text{E.0.2})$$

As can be seen, we do not include correlations among observables from single top production and top-quark decay. While single-top production is indeed a background process for $t\bar{t}$ production where the decay width of the top quark is measured, we do not include this kind of correlation. The reason is that in all experimental analyses background processes are assumed to be SM like. Thus, in order to include additional correlations the measurements would have to be reanalyzed without assumptions on the background.

In the fit with the 'linear + δ_{EFT} ' ansatz an additional matrix for the EFT uncertainties has to be considered, which has the same structure as the matrix of theory uncertainties:

$$\begin{matrix} & \sigma(tq)_7^A & \sigma(\bar{t}q)_7^A & \sigma(tq)_8^A & \sigma(tq)_8^C & \Gamma_t \\ \sigma(tq)_7^A & \left(\begin{array}{ccccc} 1 & \rho_{\text{EFT}} & \frac{\rho_{\text{EFT}}}{2} & \frac{\rho_{\text{EFT}}}{2} & 0 \\ \rho_{\text{EFT}} & 1 & \frac{\rho_{\text{EFT}}}{2} & \frac{\rho_{\text{EFT}}}{2} & 0 \\ \frac{\rho_{\text{EFT}}}{2} & \frac{\rho_{\text{EFT}}}{2} & 1 & \rho_{\text{EFT}} & 0 \\ \frac{\rho_{\text{EFT}}}{2} & \frac{\rho_{\text{EFT}}}{2} & \rho_{\text{EFT}} & 1 & 0 \\ 0 & 0 & 0 & 0 & 1 \end{array} \right) & & & & \\ \sigma(\bar{t}q)_7^A & & & & & \\ \sigma(tq)_8^A & & & & & \\ \sigma(tq)_8^C & & & & & \\ \Gamma_t & & & & & \end{matrix}. \quad (\text{E.0.3})$$

Note that we do not include correlations between measurements of observables from different physical processes, which are single-top production and top-quark decay since all three coefficients affect t -channel single top-quark production, while only two, namely $\tilde{C}_{\varphi q}^{(3)}$ and \tilde{C}_{uW} , give contributions to top-quark decay observables. Contributions at $\mathcal{O}(\Lambda^{-2})$ from \tilde{C}_{qq} are in principle present for $t \rightarrow bj\bar{j}$ but are strongly suppressed, since the W boson can be produced on-shell [227, 302]. In addition, while quadratic contributions do not suffer from this kind of suppression, their contributions are still negligible, because in experimental analyses the W boson is reconstructed out of its decay particles. Thus, only a small kinematic window for contributions from four-fermion operators remains. In our analysis, the general shape of the correlation matrices serves for a parametrization of the energy dependence of correlation coefficients only. An inclusion of the additional correlation among different observables lies beyond the scope of this ansatz. In all fits with the 'linear + δ_{EFT} ' ansatz we set $\rho_{\text{EFT}} = 0.9$ as strong correlations among the measurements are expected.

F Constraints in different correlation scenarios

In this appendix, we present additional information for fits of the coefficients (4.1.2) to data in Tab. 4.1.

F.1 'No correlation' scenario

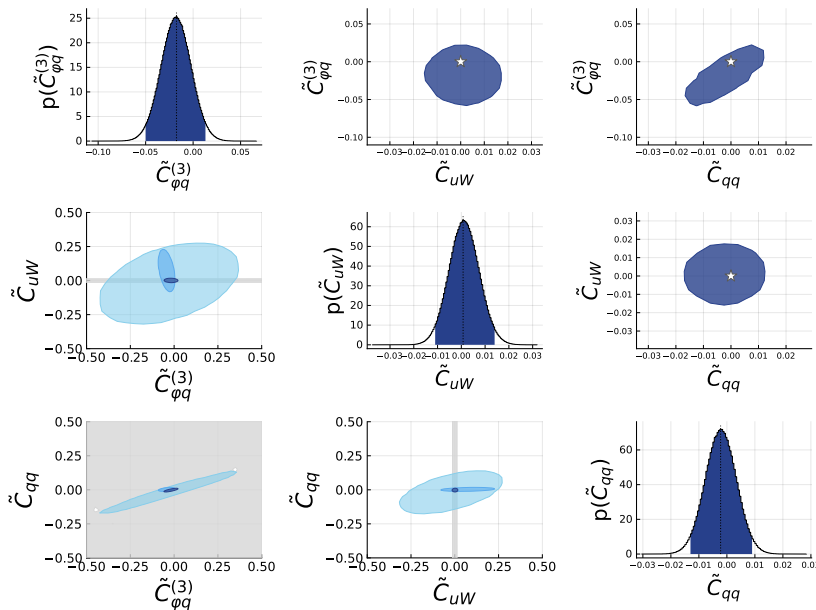


Figure F.1: Results from the fit with the linear ansatz in the 'no correlation' scenario (4.2.4). Plots on the diagonal show the one-dimensional posterior distribution for each coefficient. Plots on the lower left show the two-dimensional posterior distributions from fits to total cross sections only (light blue), differential cross sections only (blue), helicity fractions only (grey) and the combined dataset (dark blue). Plots in the upper right show the two-dimensional projections from the fit to the combined dataset but zoomed in. Stars denote the SM point. Colored areas show the smallest intervals containing 95% of the posterior probability.

Results for fits in the 'no correlation' scenario (4.2.4) with both the linear and 'linear + δ_{EFT} ' ansatz are shown in Figs. F.1 and F.2, respectively. In the fit with the linear ansatz, we obtain results very similar to those found in the fit with the quadratic ansatz (Fig. 4.3). For all coefficients we find agreement with the SM within the smallest intervals containing 95% of the posterior probability. The helicity fractions strongly constrain \tilde{C}_{uW} while constraints on $\tilde{C}_{\varphi q}^{(3)}$ and \tilde{C}_{qq} are dominated by differential cross sections. This also leads to correlations among the coefficients seen in the two-dimensional posterior distributions.

In fits to the different datasets with the 'linear + δ_{EFT} ' ansatz, we find again agreement with the SM within the 95% intervals for all coefficients. However, in the case of $\tilde{C}_{\varphi}^{(3)}$, the

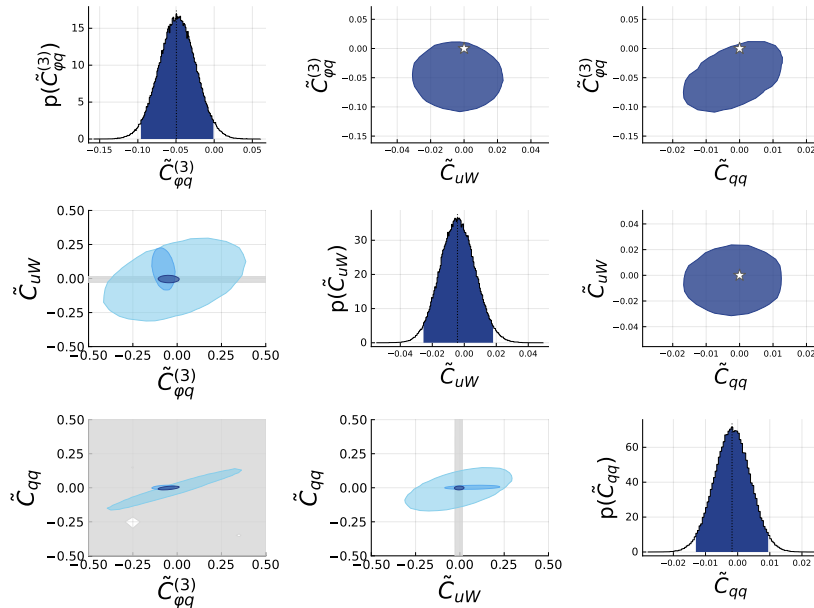


Figure F.2: Same as Fig. F.1 but with the 'linear + δ_{EFT} ' ansatz.

SM point is barely included in the interval. Again, constraints on \tilde{C}_{uW} are driven by helicity-fraction measurements, while differential cross sections dominate constraints on the other two coefficients.

F.2 'Best guess' scenario

In Figs. F.3 and F.4 we show results from fits in the 'best guess' scenario (4.2.5) with the linear and 'linear + δ_{EFT} ' ansatz, respectively. We find that the constraints obtained from differential cross sections deviate from the SM and from results from fits the other two subsets. This leads to deviations from the SM for $\tilde{C}_{\varphi q}^{(3)}$, which are even larger in the 'linear + δ_{EFT} ' scenario due to the additional correlations. In the case of \tilde{C}_{uW} , the fit to differential cross sections shows deviations from the SM. However, constraints are dominated by helicity fraction measurements which result in an interval around the SM value. Interestingly, even though constraints on \tilde{C}_{qq} are dominated by differential cross sections this dataset fixes \tilde{C}_{qq} to values around the SM. The reason is that \tilde{C}_{qq} strongly contributes to these observables and thus only small values are allowed by the data. Again, we observe a correlation between $\tilde{C}_{\varphi q}^{(3)}$ and \tilde{C}_{qq} in the two-dimensional posterior distribution.

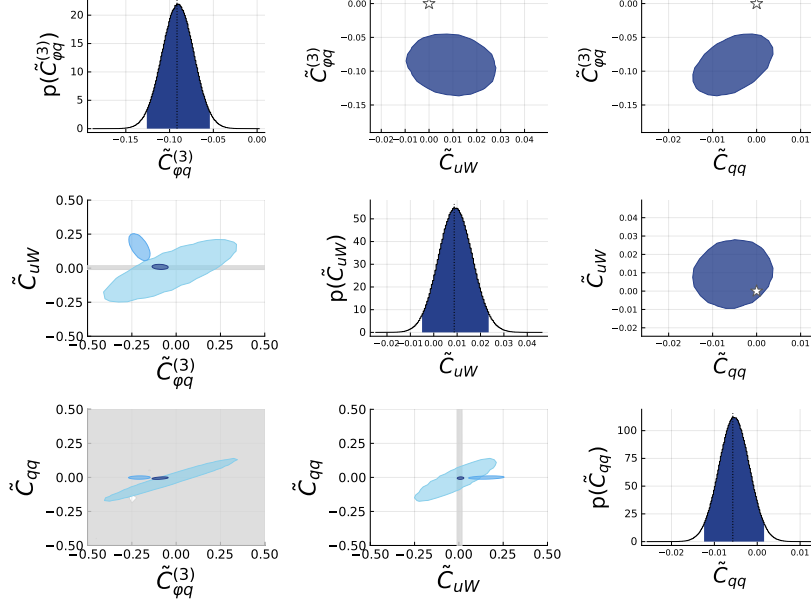


Figure F.3: Results from the fit with the linear ansatz in the 'best guess' scenario (4.2.5). Plots on the diagonal show the one-dimensional projection of posterior distribution for each coefficient. Plots on the lower left show the two-dimensional posterior distributions from fits to total cross sections only (light blue), differential cross sections only (blue), helicity fractions only (grey) and the combined dataset (dark blue). Plots in the upper right show the two-dimensional posterior distributions from the fit to the combined dataset but zoomed in. Stars denote the SM point. Colored areas correspond to the smallest intervals containing 95 % of the posterior probability.

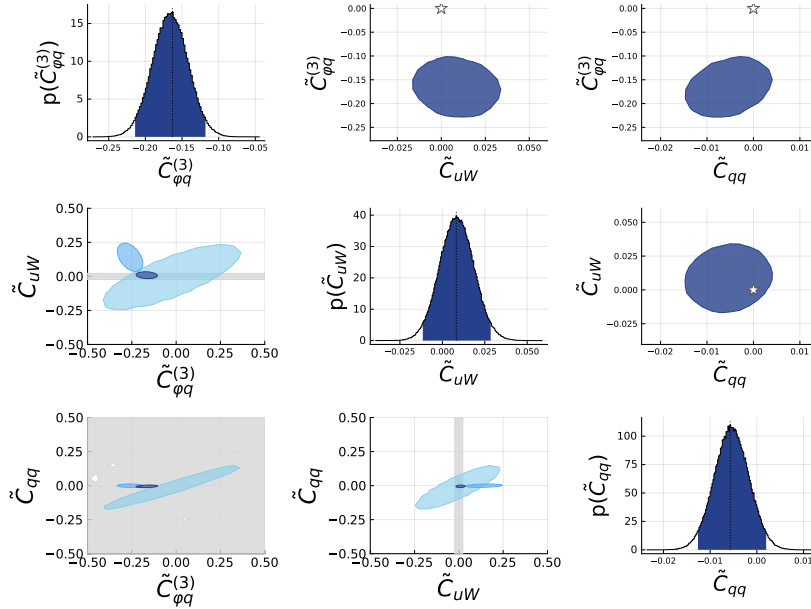


Figure F.4: Same as Fig. F.3 but with the 'linear + δ_{EFT} ' ansatz.

F.3 Constraints in future scenarios

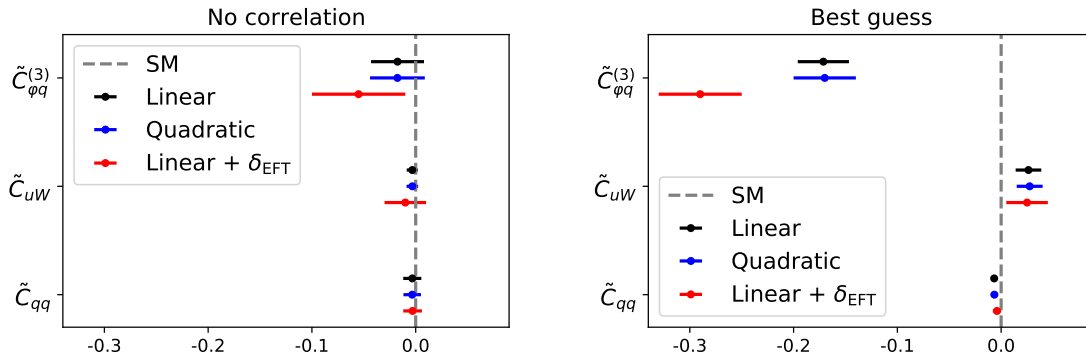


Figure F.5: The one-dimensional representation of the posterior distribution of the coefficients \tilde{C}_i from fits to data in Tab. 4.1 but with statistical uncertainties scaled to 3000 fb^{-1} . We show results in both the 'no correlation' scenario (4.2.4) and the 'best guess' scenario (4.2.5) within different BSM parametrizations. Dots denote the central value and lines the smallest intervals containing 95 % of the posterior probability. The SM is indicated by the vertical dashed line.

Operators	Linear	Linear + δ_{EFT}	Quadratic
'No correlation'			
$\tilde{C}_{\varphi q}^{(3)}$	$[-0.043, 0.008]$	$[-0.100, -0.010]$	$[-0.044, 0.008]$
\tilde{C}_{uW}	$[-0.009, 0.002]$	$[-0.030, 0.010]$	$[-0.009, 0.002]$
\tilde{C}_{qq}	$[-0.012, 0.005]$	$[-0.012, 0.006]$	$[-0.012, 0.005]$
'Best guess'			
$\tilde{C}_{\varphi q}^{(3)}$	$[-0.196, -0.146]$	$[-0.330, -0.250]$	$[-0.20, -0.140]$
\tilde{C}_{uW}	$[0.014, 0.039]$	$[0.005, 0.045]$	$[0.015, 0.040]$
\tilde{C}_{qq}	$[-0.010, -0.004]$	$[-0.008, 0.000]$	$[-0.010, 0.003]$

Table F.1: Numerical values of the smallest intervals containing 95 % of the posterior probability shown in Fig. F.5. The central value lies in the center of these intervals.

In Fig. F.5 we give results obtained in fits to data in Tab. 4.1 but with statistical uncertainties scaled to an integrated luminosity of 3000 fb^{-1} . The numerical values of these intervals are shown in Tab. F.1. In general, in the linear and quadratic fits the constraints on the coefficients do not significantly improve when compared to the 300 fb^{-1} scenario (see Fig. 4.9 and Tab. 4.4). Changes in the 'no correlation' scenario are at the level of a few percent, while those in the 'best guess' scenario are at most around 15 %. In contrast, results obtained in fits within the 'linear + δ_{EFT} ' parametrizations can be different at higher luminosities. While in the 'no correlation' scenario the results agree for all coefficients up to percent-level corrections, large effects are found in the 'best guess' scenario. For $\tilde{C}_{\varphi q}^{(3)}$ and \tilde{C}_{qq} the size of the smallest intervals changes by about 3 % and 10 %, respectively. In contrast, for \tilde{C}_{uW} the size of the intervals shrinks by about 20 %. In addition, the interval is shifted closer to the SM. In the 300 fb^{-1} future scenario the deviation of the central value from the

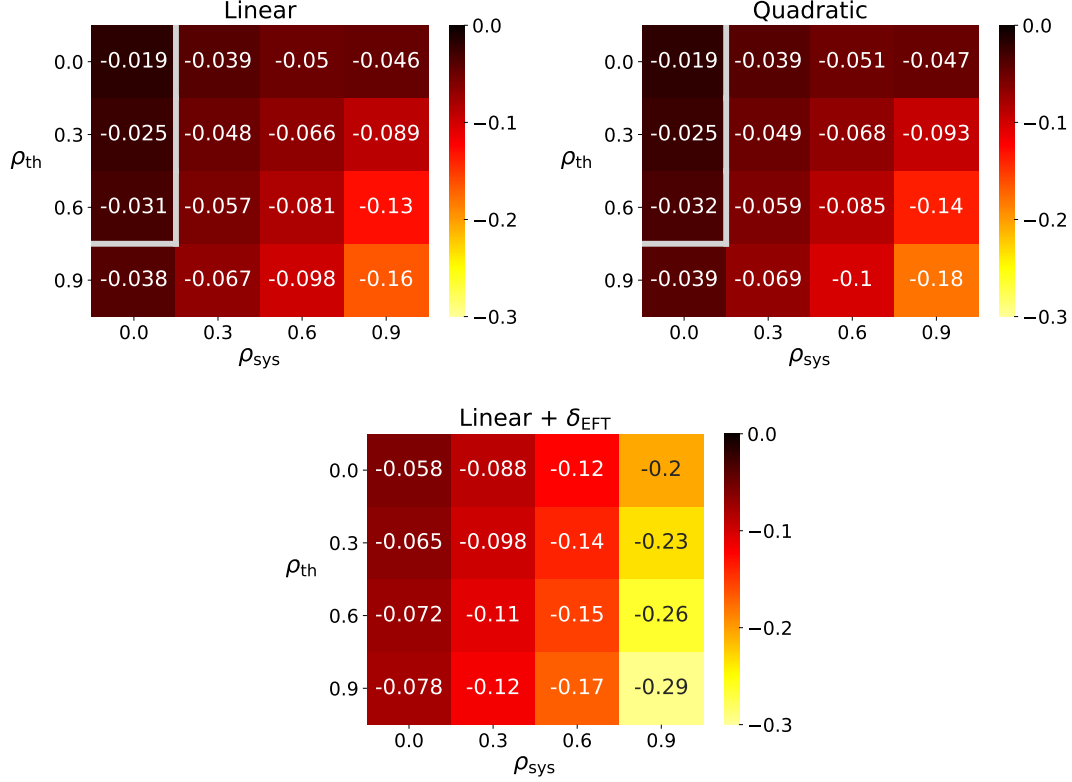


Figure F.6: Central values of $\tilde{C}_{\varphi q}^{(3)}$ for correlation parameters $\rho_{\text{sys}}, \rho_{\text{th}} = 0.0, 0.3, 0.6, 0.9$ in the three EFT-implementations from a fit to the data given in Tab. 4.1 with statistical uncertainties scaled to 300 fb^{-1} , assuming present central values, systematic uncertainties and theory uncertainties. Central values below and to the right of the grey line are in conflict with the SM at more than 2σ .

SM was at the level of 4σ . Conversely, in the 3000 fb^{-1} future scenario this deviation is only at the level of 2.5σ . We expect that this change is due to the fact that constraints on \tilde{C}_{uW} are dominated by helicity fractions, which in turn receive sizable uncertainties (compared to experimental and theory uncertainties) in the 'linear + δ_{EFT} ' fit. While indeed statistical uncertainties are already suppressed in the 300 fb^{-1} future scenario, this suppression is enhanced in the 3000 fb^{-1} scenario, and thus changes in the results of the fit are to be expected.

The central values of $\tilde{C}_{\varphi q}^{(3)}$ obtained in the 300 fb^{-1} scenario are shown in Fig. F.6 for different values of the correlation parameters ρ_{th} and ρ_{sys} . ly to the results from fits to current data (see Fig. 4.6), we find that correlations of systematic uncertainties have a stronger impact on the results of the fit than theory uncertainties. For $\rho_{\text{sys}} \neq 0$ $\tilde{C}_{\varphi q}^{(3)}$ deviates from the SM by more than 2σ in all three EFT implementations regardless of ρ_{th} . In contrast, for $\rho_{\text{sys}} = 0$ and $\rho_{\text{th}} \leq 0.6$ we find agreement with the SM at the level of 2σ in the linear and quadratic ansatz. In the 'linear + δ_{EFT} ' ansatz, all values of the correlation coefficients result in deviations of more than 2σ from the SM. As expected, stronger correlations lead to stronger deviations from the SM.

G Fiducial cross sections within SMEFT

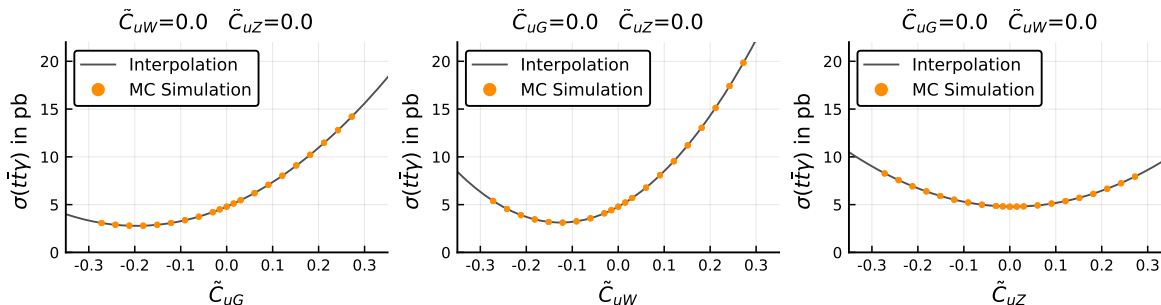


Figure G.1: The $t\bar{t}\gamma$ cross section for different values of the coefficients \tilde{C}_{uG} , \tilde{C}_{uW} , and \tilde{C}_{uZ} (see Eq. G.0.1). For each coefficient we show sampling points and the result of the interpolation represented as slices of the phase space where only one of the Wilson coefficient is varied at a time.

In order to compute the fiducial cross sections of $t\bar{t}\gamma$ production, we parametrize the cross sections at parton level with the ansatz in Eq. (4.2.1). To do so, we use cross sections computed with `MadGraph5_aMC@NLO` for different values of the coefficients \tilde{C}_i in Eq. (5.1.1). The simulations are performed employing the `dim6top_L0` UFO model where, for the sake of the computation, we set $\Lambda = 1$ TeV. To ensure that our computation is suitable for a comparison to the measurement in Ref. [313] we generated samples similar to those described in the experimental analysis. The sampling points are generated with the `dim6top_L0` UFO model varying the three coefficients C_{uG} , C_{uW} , and C_{uZ} . The latter is defined as the linear combination

$$C_{uZ} = \cos\theta_w C_{uW} - \sin\theta_w C_{uB}, \quad (\text{G.0.1})$$

and is used in the UFO model instead of C_{uB} . We first parametrize the cross sections in terms of these three coefficients, and later switch to the equivalent basis formulated in terms of \tilde{C}_{uG} , \tilde{C}_{uW} and \tilde{C}_{uB} .

In total we choose 201 different sampling points and generate 50000 events for each point. The interpolation with the ansatz in Eq. (4.2.1) is performed using a least squared fit with the Levenberg–Marquardt algorithm provided in the `LsqFit.jl` package [438]. Results for the $t\bar{t}\gamma$ cross section at parton level and examples for sampling points are shown in Fig. G.1. We find that the interpolation describes the cross sections simulated at parton level with `MadGraph5_aMC@NLO` very well, as the relative differences between interpolation and sampling points have a standard deviation as small as 0.2%.

Fiducial acceptances are computed by employing `PYTHIA 8` to shower the parton-level events previously generated with `MadGraph5_aMC@NLO` and performing an event selection at particle level with `MadAnalysis`. Jets are clustered with the anti- k_t algorithm with a radius parameter of $R = 0.4$ using the `FastJet` package. Following the selection described in Ref. [313], we apply an event selection with `MadAnalysis` at each sampling point. Comparing

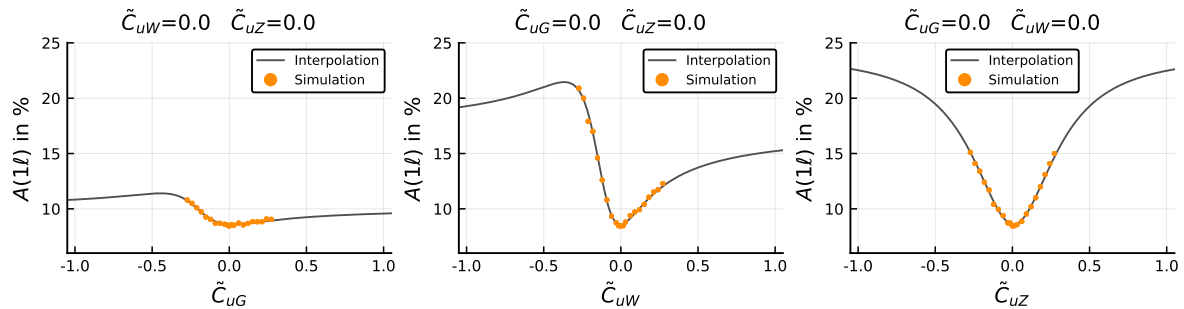


Figure G.2: The fiducial acceptance of the single-lepton channel $A(1\ell)$ for different values of the Wilson coefficients. We show both the sampling points and the result of the interpolation. For each coefficient we consider slices of the parameter space where only one coefficient is considered to be different from zero.

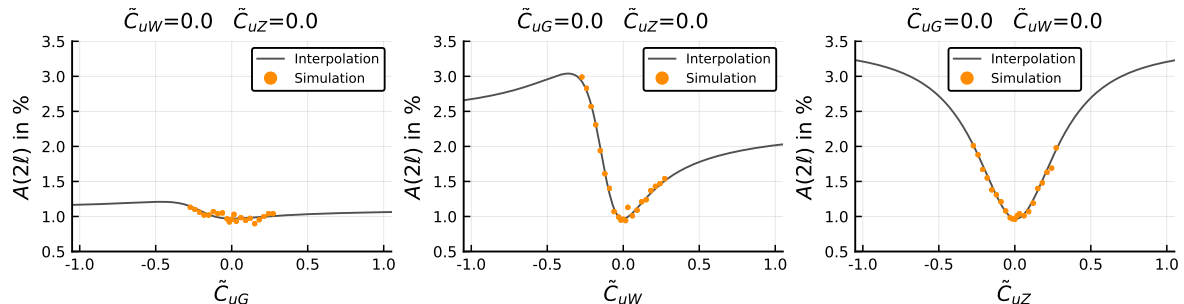


Figure G.3: Same as Fig:G.2 but for the dilepton channel.

our results for the SM with those given in the experimental analysis we find the same value for the dilepton channel and only small deviation of 3% for the single-lepton channel. In addition, we find that applying the fiducial cuts directly to the parton-level simulation does not serve as a first approximation of our results, since the LO SM predictions deviate by 25% and 50% from the values quoted in Ref. [313] for the dilepton and single-lepton channel, respectively.

The fiducial acceptance is parametrized according to Eq. (5.4.1). The results for σ_i can directly be inferred from the interpolation of the total cross section leaving only the acceptances A_i as free parameters. We perform a least squares fit of the ansatz in Eq. (5.4.1) to the fiducial acceptance computed at every sampling point. The results of these interpolations are shown together with the sampling points in Figs. G.2 and G.3 for the single-lepton and dilepton channel, respectively. Comparing the results of the interpolation with the sampling points we find only small deviations in both channels: In the single-lepton channel the standard deviation of the relative difference between sampling points and interpolation is 1.3%, while in the dilepton channel the standard deviation is 3.9%. With these results, the fiducial cross sections at LO are obtained multiplying the interpolations of the fiducial acceptance and the total cross sections. In order to include NLO corrections for the SM predictions we use k -factors [313, 314].

H Linking top and beauty

In this appendix, we give additional information for the analysis of constraints on the top-quark sector of SMEFT derived from observables at present and future colliders. We first discuss the definition of both SMEFT coefficients and effective operators in the mass basis in Sec. H.1. In App. H.2, we give the numerical values of the matching conditions linking SMEFT and WET coefficients. In App. H.3 we provide additional information on the posterior distribution obtained in fits to present data in Sec. 6.3. Results from fits in the far future scenario in Sec. 6.4.3 are shown in more detail in App. H.4.

H.1 Coefficients and operators in the mass basis

As discussed in Sec. 3.2.3, we define Wilson coefficients in the up-mass basis, in which the flavor mixing is entirely in the down-sector. With this convention, the coefficients of the operators (6.1.1) in the mass basis are

$$\begin{aligned}\hat{C}_{\varphi q}^{(1)ij} &= \hat{C}_{\varphi q}^{(1)kl} \left(S_L^{u\dagger} \right)_{ik} \left(S_L^u \right)_{lj}, & \hat{C}_{\varphi q}^{(3)ij} &= \hat{C}_{\varphi q}^{(3)kl} \left(S_L^{u\dagger} \right)_{ik} \left(S_L^u \right)_{lj}, \\ \hat{C}_{uB}^{ij} &= \hat{C}_{uB}^{kl} \left(S_L^{u\dagger} \right)_{ik} \left(S_R^u \right)_{lj}, & \hat{C}_{uW}^{ij} &= \hat{C}_{uW}^{kl} \left(S_L^{u\dagger} \right)_{ik} \left(S_R^u \right)_{lj}, \\ \hat{C}_{uG}^{ij} &= \hat{C}_{uG}^{kl} \left(S_L^{u\dagger} \right)_{ik} \left(S_R^u \right)_{lj}, & \hat{C}_{\varphi u}^{ij} &= \hat{C}_{\varphi u}^{kl} \left(S_R^{u\dagger} \right)_{ik} \left(S_R^u \right)_{lj}.\end{aligned}$$

Similarly, results for the four-fermion operators (6.1.2) read

$$\begin{aligned}\hat{C}_{lq}^{(1)ij} &= C_{lq}^{(1)kl} \left(S_L^{u\dagger} \right)_{ik} \left(S_L^u \right)_{lj}, & \hat{C}_{lq}^{(3)ij} &= C_{lq}^{(3)kl} \left(S_L^{u\dagger} \right)_{ik} \left(S_L^u \right)_{lj}, \\ \hat{C}_{qe}^{ij} &= C_{qe}^{kl} \left(S_L^{u\dagger} \right)_{ik} \left(S_L^u \right)_{lj}, & \hat{C}_{eu}^{ij} &= C_{eu}^{kl} \left(S_R^{u\dagger} \right)_{ik} \left(S_R^u \right)_{lj}, \\ \hat{C}_{lu}^{ij} &= C_{lu}^{kl} \left(S_R^{u\dagger} \right)_{ik} \left(S_R^u \right)_{lj}.\end{aligned}$$

With the definition of the coefficients in the up-mass basis, we find for the effective operators in Eq. (6.1.1)

$$\begin{aligned}\hat{C}_{\varphi q}^{(1)ij} \hat{O}_{\varphi q}^{(1)ij} &= \hat{C}_{\varphi q}^{(1)ij} \left(\varphi^\dagger i \leftrightarrow D_\mu \varphi \right) \left(\bar{u}_L^i \gamma^\mu u_L^j + V_{ki}^\dagger V_{il} \bar{d}_L^k \gamma^\mu d_L^l \right), \\ \hat{C}_{\varphi q}^{(3)ij} \hat{O}_{\varphi q}^{(3)ij} &= \hat{C}_{\varphi q}^{(3)ij} \left(\varphi^\dagger i \leftrightarrow D_\mu^3 \varphi \right) \left(\bar{u}_L^i \gamma^\mu u_L^j - V_{ki}^\dagger V_{jl} \bar{d}_L^k \gamma^\mu d_L^l \right) + \dots, \\ \hat{C}_{uB}^{ij} \hat{O}_{uB}^{ij} &= \hat{C}_{uB}^{ij} \left(\bar{u}_L^i \sigma^{\mu\nu} u_R^j \right) \frac{h+v}{\sqrt{2}} B_{\mu\nu}, \\ \hat{C}_{uW}^{ij} \hat{O}_{uW}^{ij} &= \hat{C}_{uW}^{ij} \left[\left(\bar{u}_L^i \sigma^{\mu\nu} u_R^j \right) \frac{h+v}{\sqrt{2}} W_{\mu\nu}^3 + \left(V_{ki}^\dagger \left(\bar{d}_L^k \sigma^{\mu\nu} u_R^j \right) \frac{h+v}{\sqrt{2}} W_{\mu\nu}^- + \text{h.c.} \right) \right], \\ \hat{C}_{uG}^{ij} \hat{O}_{uG}^{ij} &= \hat{C}_{uG}^{ij} \left(\bar{u}_L^i \sigma^{\mu\nu} T^A u_R^j \right) \frac{h+v}{\sqrt{2}} G_{\mu\nu}^A,\end{aligned}$$

$$\hat{C}_{\varphi u}^{ij} \hat{O}_{\varphi u}^{ij} = \hat{C}_{\varphi u}^{ij} \left(\varphi^\dagger i \leftrightarrow D_\mu \varphi \right) \left(\bar{u}_R^i \gamma^\mu u_R^j \right).$$

Similarly, we find for four-fermion operators:

$$\begin{aligned} \hat{C}_{lq}^{(1)ij} \hat{O}_{lq}^{(1)ij} &= \hat{C}_{lq}^{(1)ij} \left(\bar{l}_L \gamma_\mu l_L \right) \left(\bar{u}_L^i \gamma^\mu u_L^j + V_{ki}^\dagger V_{il} \bar{d}_L^k \gamma^\mu d_L^l \right), \\ \hat{C}_{lq}^{(3)ij} \hat{O}_{lq}^{(3)ij} &= \hat{C}_{lq}^{(3)ij} \left(\bar{l}_L \gamma_\mu \tau^3 l_L \right) \left(\bar{u}_L^i \gamma^\mu u_L^j - V_{ki}^\dagger V_{il} \bar{d}_L^k \gamma^\mu d_L^l \right) + \dots, \\ \hat{C}_{eq}^{ij} \hat{O}_{eq}^{ij} &= \hat{C}_{eq}^{(1)ij} \left(\bar{e}_R \gamma_\mu e_R \right) \left(\bar{u}_L^i \gamma^\mu u_L^j + V_{ki}^\dagger V_{il} \bar{d}_L^k \gamma^\mu d_L^l \right), \\ \hat{C}_{eu}^{ij} \hat{O}_{eu}^{ij} &= \hat{C}_{eu}^{ij} \left(\bar{e}_R \gamma_\mu e_R \right) \left(\bar{u}_R^i \gamma^\mu u_R^j \right), \\ \hat{C}_{lu}^{ij} \hat{O}_{lu}^{ij} &= \hat{C}_{lu}^{ij} \left(\bar{l}_L \gamma_\mu l_L \right) \left(\bar{u}_R^i \gamma^\mu u_R^j \right). \end{aligned}$$

These results are in agreement with Ref. [221].

H.2 Numerical results for matching

The numerical values of the tree-level matching conditions in Eq. (6.1.8) at $\mu_W = m_W$ read:

$$\begin{aligned} \Delta C_9^{\text{tree}} &= 402.1 \left[\tilde{C}_{lq}^1 + \tilde{C}_{lq}^3 + \tilde{C}_{qe} \right] - 44.53 \left(\tilde{C}_{\varphi q}^1 + \tilde{C}_{\varphi q}^3 \right), \\ \Delta C_{10}^{\text{tree}} &= 402.1 \left[-\tilde{C}_{lq}^1 - \tilde{C}_{lq}^3 + \tilde{C}_{qe} + \tilde{C}_{\varphi q}^1 + \tilde{C}_{\varphi q}^3 \right], \\ \Delta C_L^{\text{tree}} &= 402.1 \left[\tilde{C}_{lq}^1 - \tilde{C}_{lq}^3 + \tilde{C}_{\varphi q}^1 + \tilde{C}_{\varphi q}^3 \right]. \end{aligned} \tag{H.2.1}$$

For the contributions at one-loop level presented in Eqs. (6.1.9) to (6.1.14), we obtain

$$\Delta C_7^{\text{loop}} = -2.310 \tilde{C}_{uB} + 0.09251 \tilde{C}_{uW} - 0.0946 \tilde{C}_{\varphi q}^{(1)} + 0.7951 \tilde{C}_{\varphi q}^{(3)}, \tag{H.2.2}$$

$$\Delta C_8^{\text{loop}} = -0.6687 \tilde{C}_{uG} + 0.2709 \tilde{C}_{uW} + 0.2839 \tilde{C}_{\varphi q}^{(1)} + 0.7568 \tilde{C}_{\varphi q}^{(3)}, \tag{H.2.3}$$

$$\begin{aligned} \Delta C_9^{\text{loop}} &= 2.170 \tilde{C}_{uW} + 2.512 \tilde{C}_{uB} - 1.812 \tilde{C}_{\varphi q}^{(1)} - 1.957 \tilde{C}_{\varphi q}^{(3)} + 0.1484 \tilde{C}_{\varphi u} \\ &\quad - 1.898 \left(\tilde{C}_{eu} + \tilde{C}_{lu} \right) - 2.242 \left(\tilde{C}_{lq}^{(1)} - \tilde{C}_{qe} \right) - 4.444 \tilde{C}_{lq}^{(3)}, \end{aligned} \tag{H.2.4}$$

$$\begin{aligned} \Delta C_{10}^{\text{loop}} &= -7.536 \tilde{C}_{uW} + 12.76 \tilde{C}_{\varphi q}^{(1)} - 3.431 \tilde{C}_{\varphi q}^{(3)} - 1.898 \tilde{C}_{\varphi u} - 1.898 \left(\tilde{C}_{eu} - \tilde{C}_{lu} \right) \\ &\quad - 2.242 \left(\tilde{C}_{lq}^{(1)} - \tilde{C}_{qe} \right) 4.444 \tilde{C}_{lq}^{(3)}, \end{aligned} \tag{H.2.5}$$

$$\begin{aligned} \Delta C_L^{\text{loop}} &= -2.876 \tilde{C}_{uW} + 12.76 \tilde{C}_{\varphi q}^{(1)} + 0.3324 \tilde{C}_{\varphi q}^{(3)} - 1.898 \left(\tilde{C}_{\varphi u} + \tilde{C}_{lu} \right) + 4.622 \tilde{C}_{lq}^{(1)} \\ &\quad + 1.033 \tilde{C}_{lq}^{(3)}, \end{aligned} \tag{H.2.6}$$

$$\Delta C_{1,tt}^{\text{mix, loop}} = 4.120 \tilde{C}_{uW} + 14.76 \tilde{C}_{\varphi q}^{(1)} + 11.60 \tilde{C}_{\varphi q}^{(3)} + 3.150 \tilde{C}_{\varphi u}. \tag{H.2.7}$$

Note that these results are just the numerical versions of the matching conditions at the scale $\mu_W = m_W$ in Eqs. (6.1.8)-(6.1.14). On both sides of the equations Wilson coefficients are evaluated at the same scale. For actual predictions for observables the effects of RGE evolution have to be included.

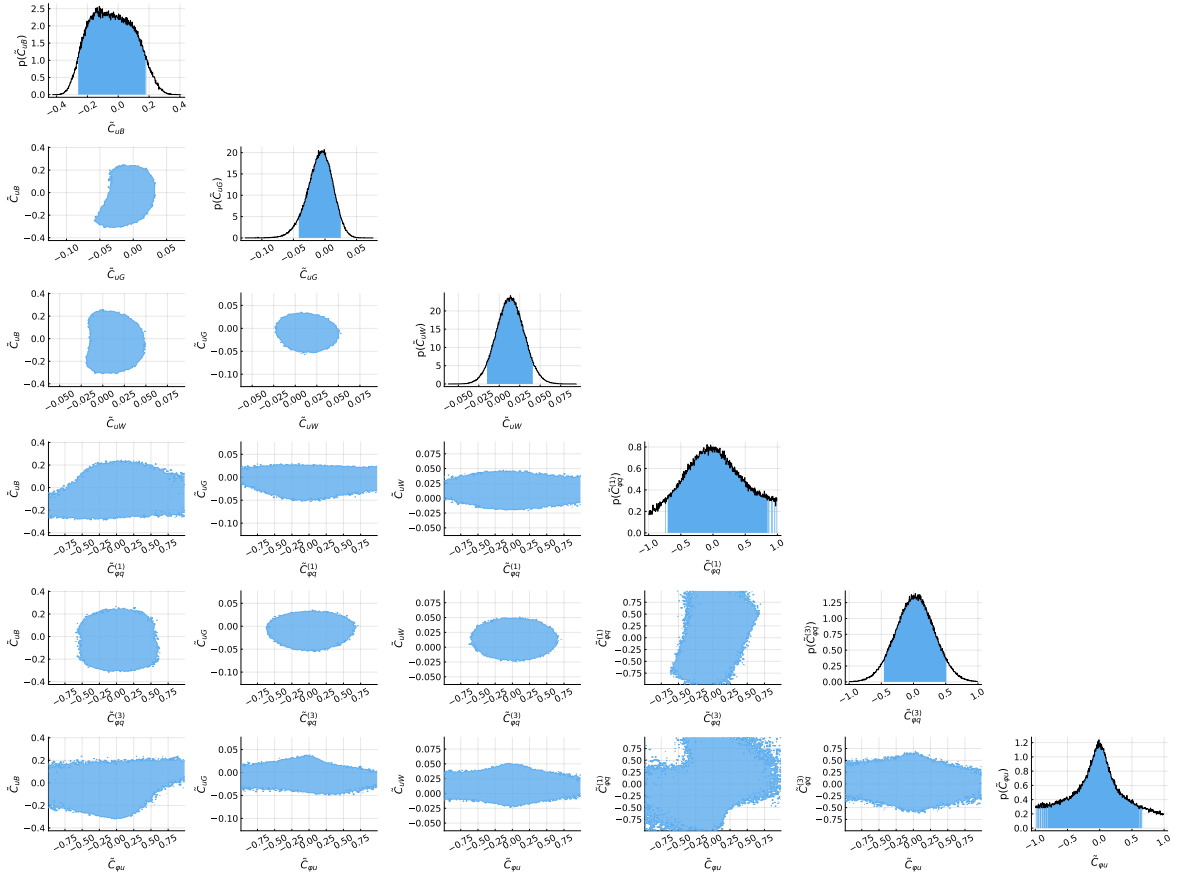


Figure H.1: The posterior distribution for the coefficients \tilde{C}_i obtained in fits of six coefficients to measurements of top-quark observables at the LHC shown in Tab. 6.2. We give the one-dimensional (on-diagonal plots) and two-dimensional projections (off-diagonal plots) of the smallest intervals containing 90% of the posterior probability.

H.3 Fits to present data

In the following, we give additional information on the results of fits to top-quark data in Tab. 6.2, B -physics data in Tab. 6.3 and to the combined dataset.

H.3.1 Fits to top-quark data

In Fig. H.1, we give additional information of the one-dimensional (on-diagonal plots) and two-dimensional (off-diagonal plots) projections of the posterior distribution obtained in a fit of \tilde{C}_{uB} , \tilde{C}_{uG} , \tilde{C}_{uW} , $\tilde{C}_{\varphi q}^{(1)}$, $\tilde{C}_{\varphi q}^{(3)}$, and $\tilde{C}_{\varphi u}$ to top-quark data in Tab. 6.2. As already seen in Fig. 6.3, we observe a strong correlation between $\tilde{C}_{\varphi q}^{(1)}$ and $\tilde{C}_{\varphi u}$ induced by $t\bar{t}Z$ data. Thus, constraints on these coefficients are weaker compared to those of $\tilde{C}_{\varphi q}^{(3)}$ and especially \tilde{C}_{uB} , \tilde{C}_{uG} , and \tilde{C}_{uW} , which are less correlated.

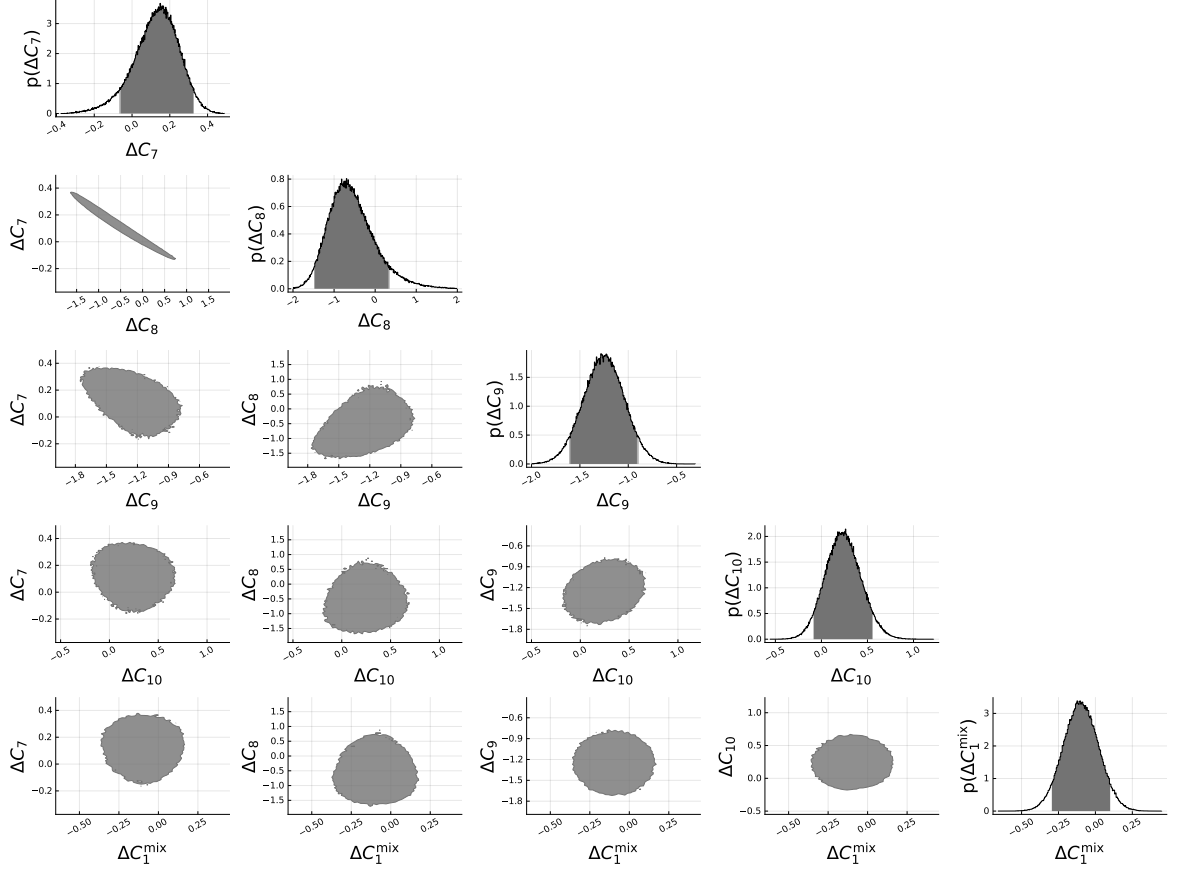


Figure H.2: The posterior distribution for the WET coefficients ΔC_i obtained in fits of five WET coefficients to measurements of B -physics observables in Tab. 6.3. We give the one-dimensional (on-diagonal plots) and the two-dimensional projections (off-diagonal plots) of the smallest intervals containing 90% of the posterior probability. Results are derived with a uniform distribution over the interval $-2 \leq \Delta C_i \leq 2$ as the prior.

H.3.2 Constraints from beauty data

In Fig. H.2, we give additional information on the posterior distribution obtained in fits of WET coefficients to B -physics data in Tab. 6.3. As already indicated in the one-dimensional projections in Fig. 6.5, we find strong correlation between ΔC_7 and ΔC_8 induced by RGE mixing. Correlations of these two coefficients with $\Delta C_{9,10}$ are smaller, because the latter are constrained by a different set of observables: results for $\Delta C_{7,8}$ are dominated by $b \rightarrow s\gamma$ data, while constraints on $\Delta C_{9,10}$ arise only through $b \rightarrow sl^+\ell^-$ observables. In contrast, ΔC_1^{mix} is completely uncorrelated.

H.3.3 Combining top and beauty

In Fig. H.3, we show the results from fits to top-quark data in Tab. 6.2 (blue), Zbb data (light blue), B -physics data in Tab. 6.3 (grey) and the combined set (dark blue). For several coefficients we find that the different sensitivities of the individual datasets strengthen the constraints, as seen in Fig. 6.7. In addition, we find deviations from the SM in the $\tilde{C}_{qe}-\tilde{C}_{lq}^+$ plane, which can also be seen in the one-dimensional projection for \tilde{C}_{qe} . These deviations

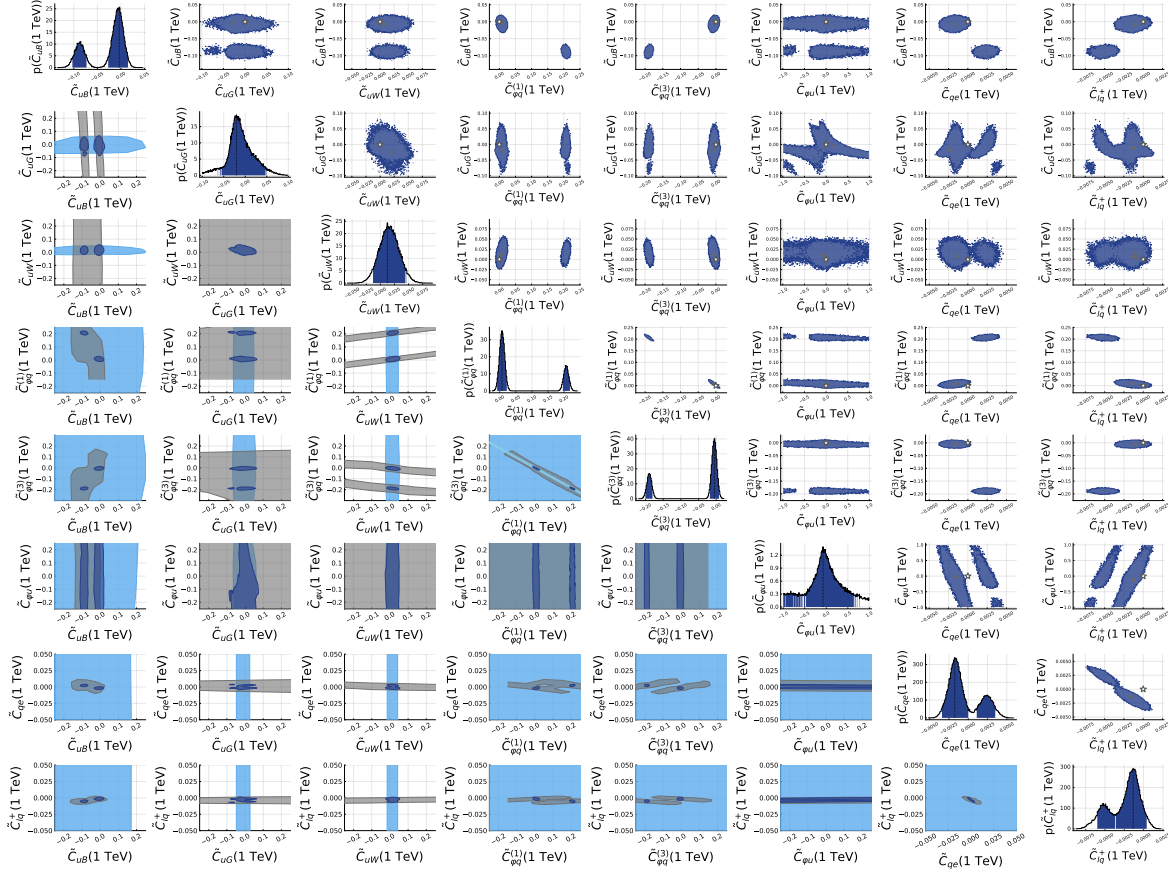


Figure H.3: Constraints on the coefficients in Eq. (6.3.3) obtained in fits of eight coefficients to four datasets: top-quark data (blue), Zbb data (light blue), B data (grey), and the combined set (dark blue). Constraints from Zbb data are only shown in the $\tilde{C}_{\varphi q}^{(1)}-\tilde{C}_{\varphi q}^{(3)}$ plane, as only these two coefficients contribute to $Z \rightarrow b\bar{b}$ transitions. Shown are the one-dimensional (on-diagonal plots) two-dimensional (off-diagonal plots) projections of the smallest intervals containing 90% of the posterior probability. The SM is indicated by the star.

stem from discrepancies found within present data of $b \rightarrow s\mu^+\mu^-$ transitions, in particular in the angular distributions. This is shown in more detail in Fig. 6.8 where we show results from the combined fit. In contrast, $\tilde{C}_{\varphi q}^{(1)}$ and $\tilde{C}_{\varphi q}^{(3)}$, which deviate from the SM in fits to Zbb data only, are found to be in agreement with the SM in the combined fit, see Fig. H.4. We also observe secondary solutions for \tilde{C}_{uB} , $\tilde{C}_{\varphi q}^{(1)}$, $\tilde{C}_{\varphi q}^{(3)}$, \tilde{C}_{qe} , and \tilde{C}_{lq}^+ . As indicated in the two-dimensional projections for these coefficients both the orientation of the ellipses and the position of the solutions indicate sizeable correlations among several coefficients. These correlations are induced by the matching of the SMEFT basis onto the WET one, which can be inferred from the results of the fit to beauty data only.

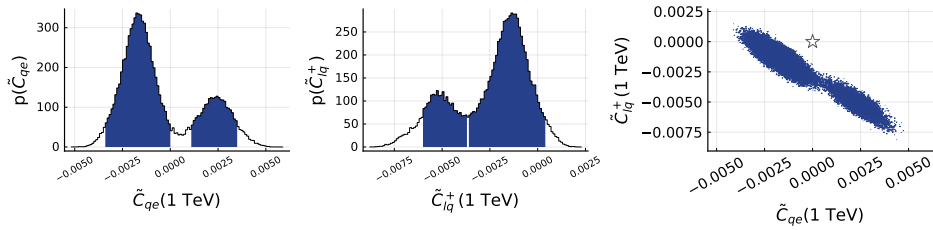


Figure H.4: Same as Fig. 6.8, but for $\tilde{C}_{\varphi q}^{(1)}$ and $\tilde{C}_{\varphi q}^{(3)}$.

H.4 Constraints in future scenarios

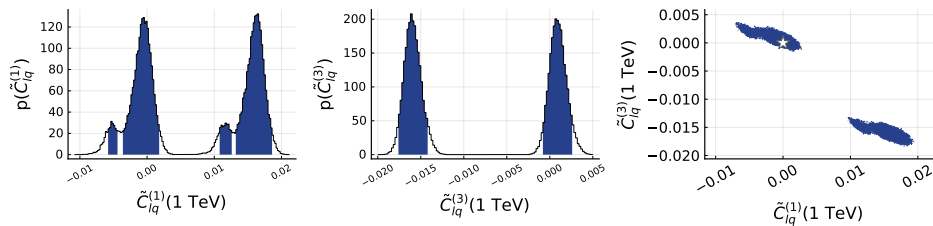


Figure H.5: One-dimensional (left, middle) and two-dimensional (right) projections for the posterior distribution of $\tilde{C}_{lq}^{(1)}$ and $\tilde{C}_{lq}^{(3)}$ obtained in a fit of nine coefficients in the near-future scenario. Colored areas indicate the smallest intervals containing 90% and the star denotes the SM.

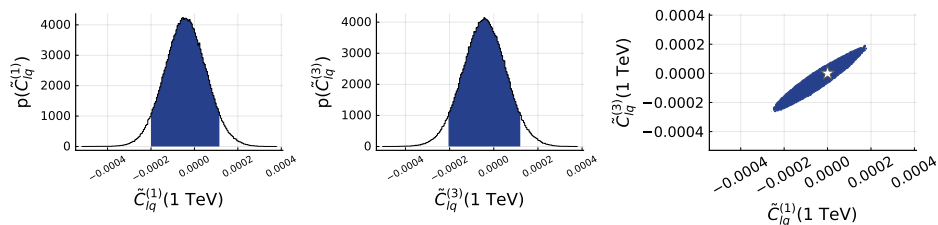


Figure H.6: Same as Fig. 6.12, but assuming SM predictions for projections of Belle II measurements.

In Fig. H.5 show in detail the results for the four-fermion coefficients $\tilde{C}_{lq}^{(1)}$ and $\tilde{C}_{lq}^{(3)}$ obtained in a fit to present data and HL-LHC and Belle II projections. We give the smallest intervals containing 90% in both the one-dimensional projection for both $\tilde{C}_{lq}^{(1)}$ and $\tilde{C}_{lq}^{(3)}$ as well as in the $\tilde{C}_{lq}^{(1)} - \tilde{C}_{lq}^{(3)}$ plane.

In Fig. H.6, we show results from a fit combining present data and projections for HL-LHC, Belle II, and CLIC observables considering SM predictions for central values of future projections. As can be seen, both coefficients show agreement with the SM.

I Vector-like leptons at hadron colliders

In the following, we present additional information on our analysis of signatures of VLLs at the LHC. Properties of production of VLLs at pp colliders are provided in App. I.1. In App. I.2, we summarize the `MadGraph5_aMC@NLO` settings for our event generation and for the showering and detector simulation. Distributions of the scalar momentum sum L_T for several points in the M_F, M_S plane (see Fig. 7.4) are provided in App. I.3. In addition, we provide numerical values of the settings for the event reconstruction and the computation of observables $m_i(\text{diff})$. In App. I.3, we present distributions of the scalar momentum sum L_T for different benchmark scenarios. The $m_i(\text{diff})$ distributions at parton level for Run 2 and HL-LHC are presented in App. I.4. Finally, in App. I.5 we give further information on benchmark scenarios where we consider $\kappa' = 1$ instead of fixing it according to Eq. (7.1.8).

I.1 Production of vector-like leptons

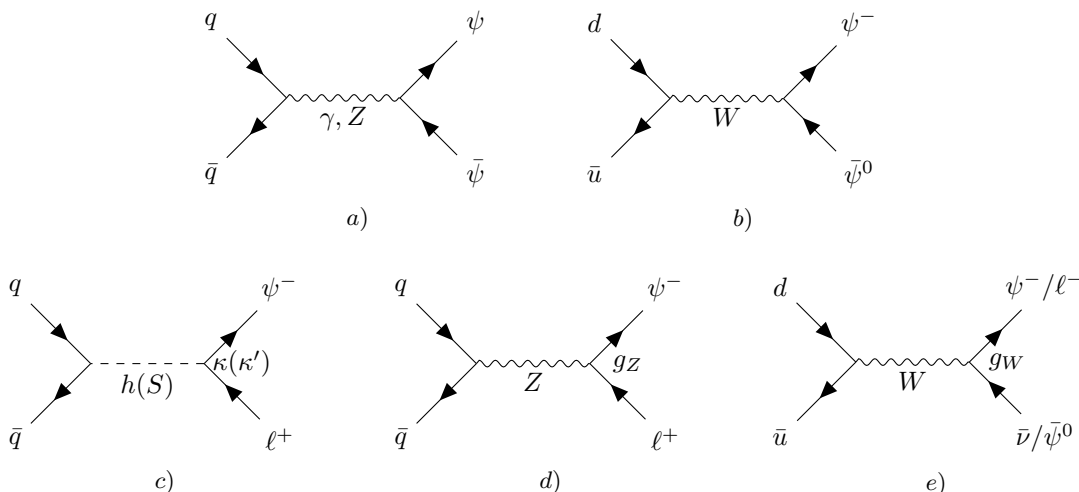


Figure I.1: Examples of Feynman diagrams for pair (upper row) and single (lower production) production of vector-like leptons at pp colliders. Final states $\psi^- \bar{\nu}$ ($\ell^- \bar{\psi}^0$) shown in diagram e) are only possible in the singlet (doublet) model.

In Fig. I.1 we give examples for Feynman diagrams describing single and pair production at the LHC. As shown, pair production is possible via s -channel photon or Z boson diagrams (a), and in the doublet model through a W boson (b), while single production occurs via diagrams with s -channel Higgs and S (c) induced by Higgs-scalar mixing [30], Z (d) or W (e) bosons. Phenomenologically, contributions from Higgs and scalar diagrams to matrix elements are suppressed by at least two orders of magnitude by both small quark Yukawa couplings and PDFs compared to electroweak contributions and are neglected.

Cross sections for single and pair production of VLLs in both the singlet (left) and doublet (right) model are shown in Fig. I.2 for the different final states varying the VLL mass while

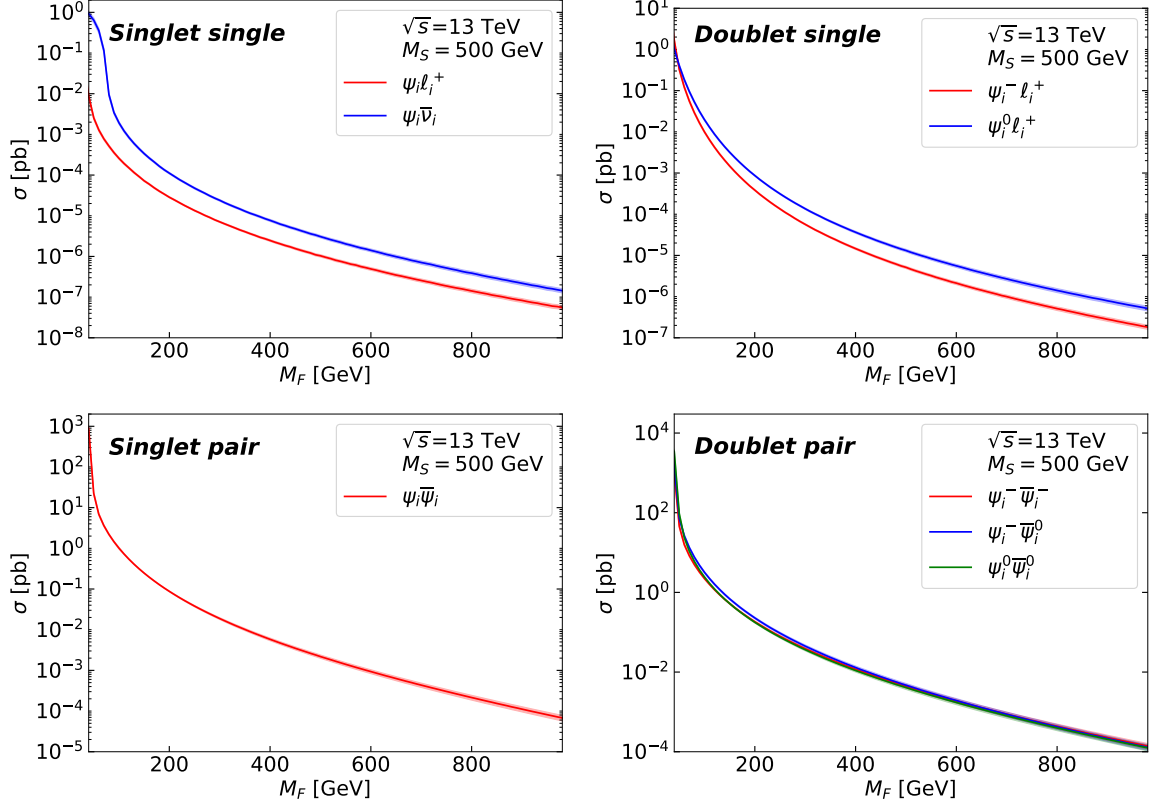


Figure I.2: Cross sections at $\sqrt{s} = 13$ TeV pp collider for ψ_i single production (upper row) and pair production (lower row) for different vector-like lepton masses in the singlet (left) and doublet model (right). For the computation we fix $\epsilon = 10^{-2}$ while κ' is computed for each value of M_F according to Eq. (7.1.8).

setting $M_S = 500$ GeV. For this choice of parameters, pair-production cross sections are about three orders of magnitude larger than the single-production ones, since pair production at hadron colliders is independent of the portal couplings and depends only on the quantum numbers of the VLLs. In contrast, single-production cross sections depend on the values of g_Z and g_W , which are proportional to BSM coupling κ and VLL masses M_F (see Eqs. 7.1.5 and (7.1.7)). Since κ is required to be small to pass constraints from Z -decay data, the cross section is strongly suppressed.

I.2 Madgraph settings

For the event generation we follow the steps outlined in Sec. D.3: Feynman rules at LO are computed employing `FeynRules` and implemented into UFO models. These models are interfaced to `MadGraph5_aMC@NLO`, which is applied to compute cross sections at parton level, while `MadSpin` [439] is employed for decays of on-shell particles. For each process we generate 5×10^4 events using the `MNPDF3.0` PDF set. The corresponding PDF and scale variation uncertainties are computed within `MadGraph5_aMC@NLO`, where scale variation uncertainties are estimated varying factorization and renormalization scales independently between $0.5\mu_0 \leq \mu_{F/R} \leq 2\mu_0$. Here, μ_0 is computed in `MadGraph5_aMC@NLO` with four

Parameters	Cuts	Reconstruction
$\alpha_s(m_Z) = 0.118$	$E_T^{\text{miss}} < 50 \text{ GeV}$	$\Delta m_Z = 15 \text{ GeV}$
$m_Z = 91.188 \text{ GeV}$	$ \eta \leq 2.5$	$\Delta M_S = 5 \text{ GeV}$
$m_h = 125 \text{ GeV}$	$R = 0.5$	$\Delta m_h = 5 \text{ GeV}$
$m_W = 80.379 \text{ GeV}$	$N_U \geq 4$	$\Delta M_F = 100 \text{ GeV}$
$m_t = 172 \text{ GeV}$	$p_T^{\text{jet}} \geq 20 \text{ GeV}$	-
$m_b = 4.7 \text{ GeV}$	$p_T^\ell \geq 20 \text{ GeV}$	-
-	$m_{\ell\ell} \geq 12 \text{ GeV}$	-

Table I.1: Parameters used in the event generation, detector simulation and the reconstruction algorithm.

different schemes, and we consider the maximal difference of the cross section computed in different schemes as the scheme variation uncertainty. The complete theory uncertainty is computed adding PDF uncertainties, scale variation uncertainties, and scheme variation uncertainties in quadrature.

We adapt settings for the event generation similar to those used in the recent CMS study [400]. We focus on 4L final states with a cut on the missing transverse momentum of $p_T^{\text{miss}} < 50 \text{ GeV}$ to resemble the signal region considered by CMS. This allows to suppress contributions from neutrinos stemming from the decay of electroweak bosons. In addition, we require light leptons to have a minimal transverse momentum of $p_T > 20 \text{ GeV}$. Setting $\kappa = 10^{-2}\kappa'$ we consider masses of the new scalars and vector-like leptons in the range $M_S = 300 - 1200 \text{ GeV}$ and $M_F = 100 - 1000 \text{ GeV}$, respectively, and fix κ' according to Eq. (7.1.8). The dominant SM background processes of ZZ , ttZ , and triboson production are computed at LO with `MadGraph5_aMC@NLO`. We include ZZj production at LO and perform a multijet matching with `PYTHIA 8`. In addition, contributions from $gg \rightarrow ZZ$ transitions are computed at one-loop level and are included in the total production cross section. Higher order corrections are considered applying k factors taken from literature [377, 378, 408–413]. Finally, we include contributions from virtual photons to the $pp \rightarrow \ell^+\ell^-\ell^+\ell^-$ process at LO in QCD, and require that (regardless of flavor or sign) invariant masses from any dilepton pair, $m_{\ell\ell}$, are larger than 12 GeV, similar to the CMS analysis.

The parton-level events are hadronized and showered with `PYTHIA 8`. For the fast detector simulation we employ `Delphes 3` and cluster jets with the anti- k_t algorithm using the `FastJet` package. We take into account all criteria from the CMS default card for simplicity. The parameters used in the event generation and the detector simulation are summarized in Tab. I.1.

I.3 Distributions of the scalar transverse momentum sum

In Fig. I.3 we show several distributions for scenarios marked as green and purple dots with a black in Fig. 7.4 with $M_S = 1000 \text{ GeV}$ (upper row) and $M_S = 500 \text{ GeV}$ (lower row) for both the singlet (left) and doublet model (right). The CMS data from Ref. [400] is indicated in all plots together with the upper limit of the 1σ range of the data (grey lines). Given $M_F < M_S$ with $M_S = 1000 \text{ GeV}$ (upper row), we see that in the singlet model masses as low as $M_F \lesssim 600 \text{ GeV}$ are not yet excluded by CMS data. In contrast, in the doublet model VLL masses below 800 GeV are excluded by CMS, as expected. In the case of the inverse mass hierarchy $M_F > M_S$ with $M_S = 500 \text{ GeV}$ (lower row), CMS data is expected to exclude VLL

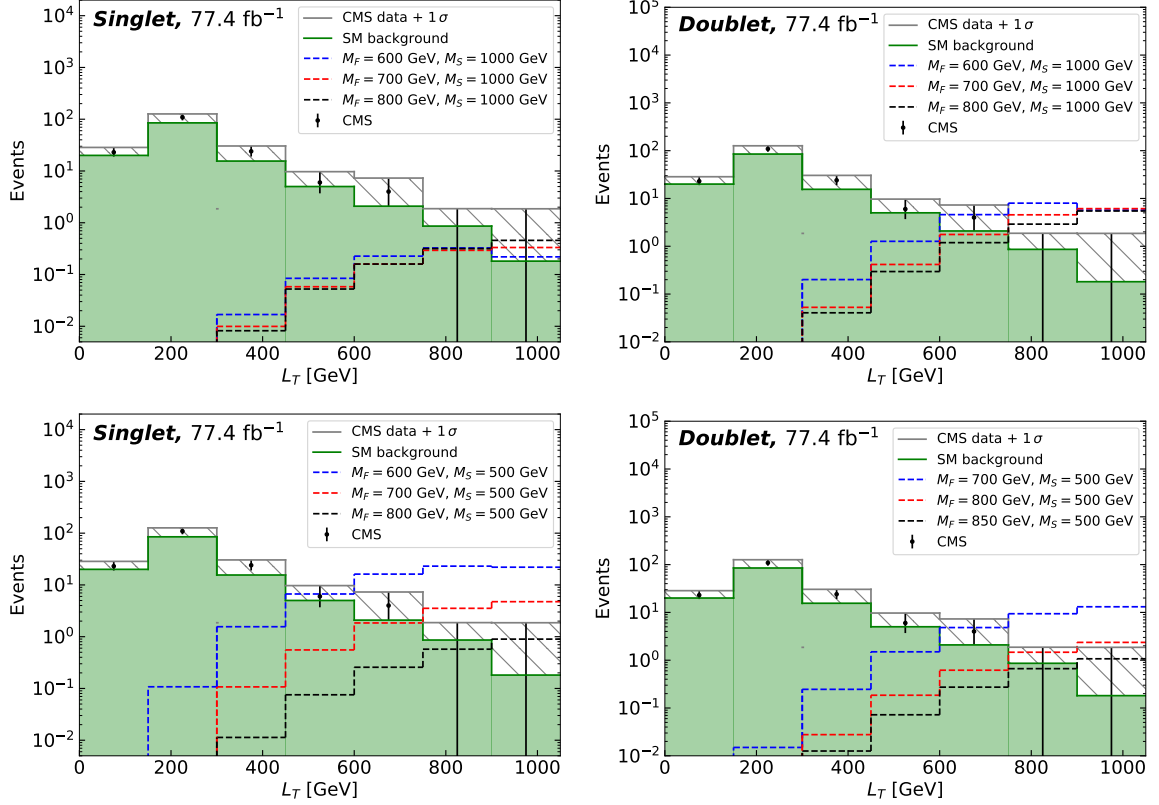


Figure I.3: Scalar sum of transverse momenta L_T in the singlet (left) and the doublet model (right). Shown are distributions for SM background processes and different masses of vector-like fermions with $M_S = 1000$ GeV (upper row) and $M_S = 500$ GeV. The observables are computed for an integrated luminosity of 77.4 fb^{-1} with subsequent detector simulation. CMS data from [400] is indicated (black dots) together with the upper limit of the 1σ interval (grey line).

masses of $M_F < 800$ GeV and $M_F < 850$ GeV in the singlet and doublet model, respectively.

I.4 Novel observables at parton level

The distributions of the m_{i_diff} observables at parton level for benchmark scenarios in the doublet model are shown in Fig. I.4. Similarly to the distributions in the singlet model (Fig. 7.6), the m_{i_diff} observables are significantly cleaner compared to the m_i ones. In the $m_{2\ell}$ distributions we find peaks at the mass of the Z boson (new scalars) for the mass hierarchy $M_F < M_S$ ($M_F > M_S$). In both cases, the number of events in the peak bins is $\mathcal{O}(10^1 - 10^2)$. In contrast, peaks in the SM background and the distribution with $M_F < M_S$ ($M_F = 800$ GeV, red curve) are depleted by two orders of magnitude in $m_{2\ell_diff}$. For scenarios with on-shell S production ($M_F = 850$ GeV, 1000 GeV) we still find peaks with a comparable number of events in the peak bins (blue, black curve). As in the singlet model, in the $m_{3\ell}$ distributions of the doublet model we find peaks (broad resonances) for benchmarks with $M_F < M_S$ ($M_F > M_S$), with $\mathcal{O}(10)$ ($\mathcal{O}(1)$) events in the peak bins. While the peaks are strongly suppressed by two orders of magnitude in the $m_{3\ell_diff}$ distribution ($M_F = 800$ GeV,

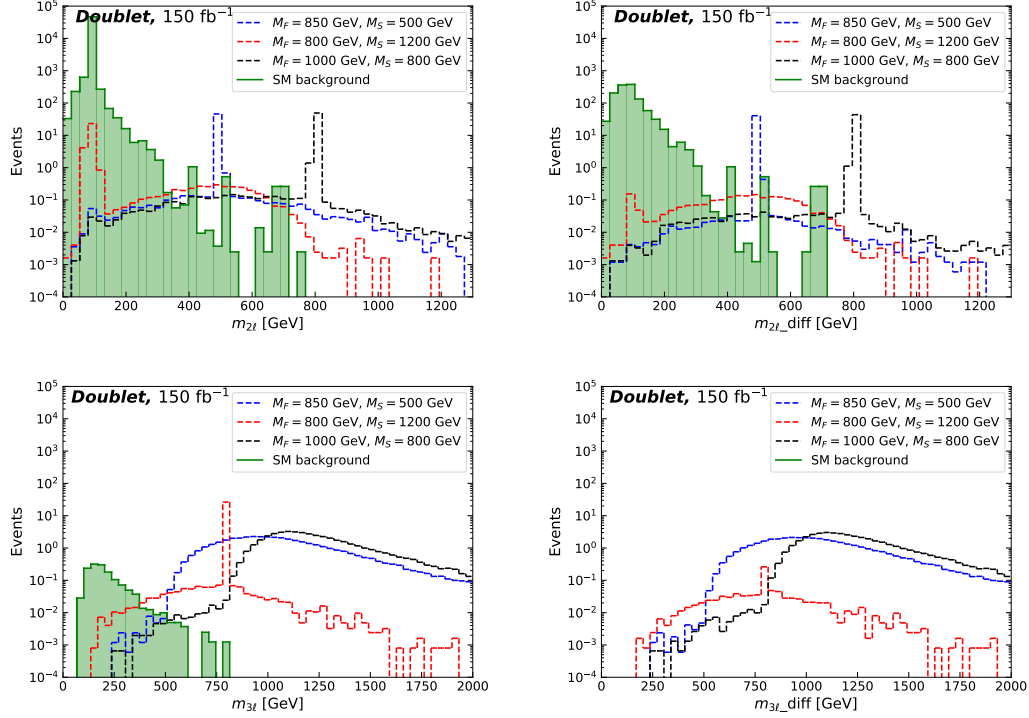


Figure I.4: Parton-level distributions of invariant masses $m_{2\ell}$, $m_{2\ell_diff}$, $m_{3\ell}$, and $m_{3\ell_diff}$ for the singlet model for different benchmark masses of the VLLs and the BSM scalars at a luminosity of 150 fb^{-1} and $\sqrt{s} = 13 \text{ TeV}$. The coupling κ' is fixed according to Eq. (7.1.8).

red curve), the broad resonances are still present with $\mathcal{O}(1)$ events in the peak bins.

Parton-level distributions of the observables for the HL-LHC scenario with $\sqrt{s} = 14 \text{ TeV}$ and 3000 fb^{-1} before detector simulation are shown in Figs. I.5 and I.6. For all benchmark scenarios we find a significant increase in the number of events in all signal distributions as well as in the SM background, according to $\sim 3000/150 = 20$. Considering $m_{2\ell}$ and $m_{2\ell_diff}$, we see that we can separate SM and BSM distributions sufficiently in the region $m_{2\ell}(_diff) \gtrsim 500 \text{ GeV}$. This region allows to test for both off-shell and on-shell production of BSM scalars. In the case of on-shell production, we observe narrow peaks in the mass distribution at M_S while for off-shell production the distributions show a peak around the mass of the SM bosons ($\mathcal{O}(10^2 - 10^3)$ events per bin) which lies significantly below the SM background. The peak bins around the mass of the BSM scalars contain $\mathcal{O}(10^3)$ events in the $m_{2\ell_diff}$ distribution for both singlet and doublet model benchmark scenarios. In contrast, bins around the mass of SM bosons are strongly suppressed both for SM background and signal distributions. The $m_{3\ell}$ and $m_{3\ell_diff}$ distributions allow in both models for a good separation between the signal process and SM background, especially for $m_{3\ell_diff}$ which is completely background free. In the case $M_F < M_S$, we find narrow peaks in the $m_{3\ell}$ distribution. In the singlet model, these peaks have $\mathcal{O}(10^2 - 10^3)$ events for scenarios with $M_F = 600 \text{ GeV}$ and $M_F = 300 \text{ GeV}$ (red and blue curves). Similarly, in the doublet model the narrow peak contains $\mathcal{O}(10^3)$ events ($M_F = 800 \text{ GeV}$, red curve). In the $m_{3\ell_diff}$ distribution, the number of events per is reduced to $\mathcal{O}(1)$ events in the peak bin for all these scenarios. In contrast, for on-shell S -production ($M_F = 850, 1000 \text{ GeV}$) distributions in both $m_{3\ell}$ and $m_{3\ell_diff}$

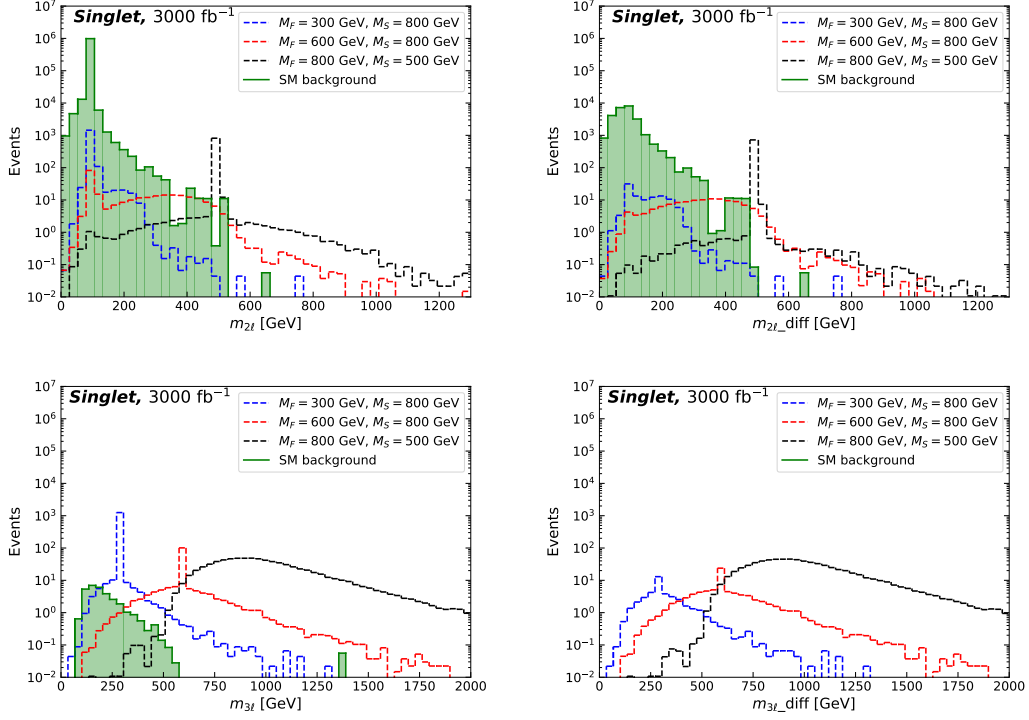


Figure I.5: Distributions of the invariant masses $m_{2\ell}$, $m_{2\ell_diff}$, $m_{3\ell}$, and $m_{3\ell_diff}$ (see Sec. 7.3.1 for details) for the singlet model. We consider different benchmark scenarios for the masses of the VLLs and the BSM scalars at a luminosity of 3000 fb^{-1} and $\sqrt{s} = 14 \text{ TeV}$. The coupling κ' is fixed according to Eq. (7.1.8).

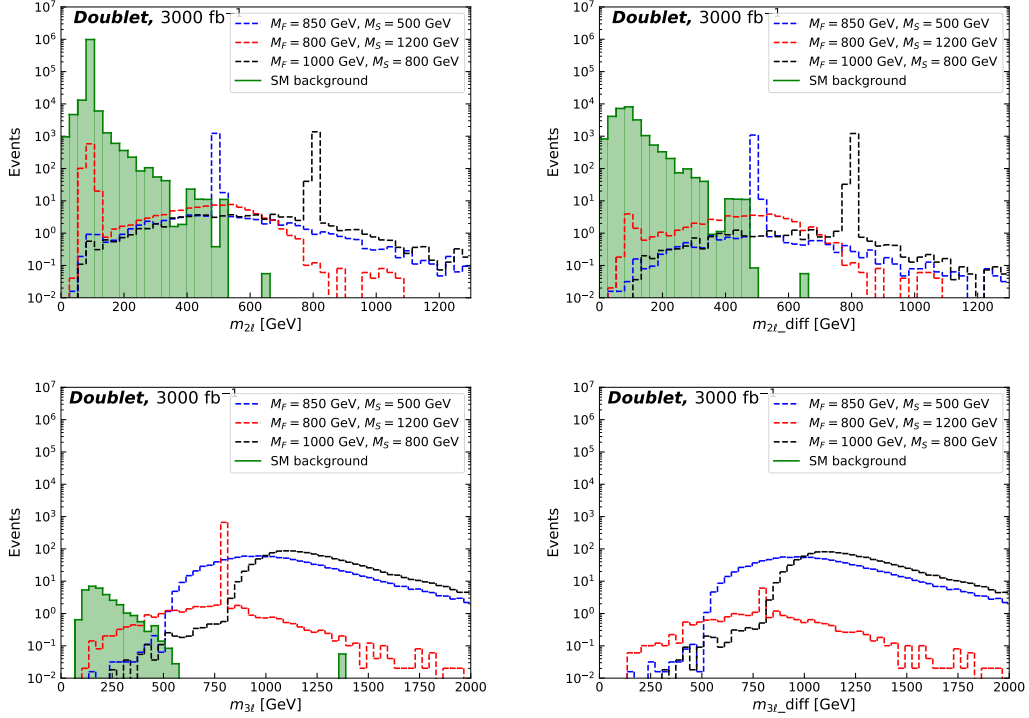


Figure I.6: Same as Fig. I.5 but for the benchmark scenarios in the doublet model.

Model	M_F (GeV)	M_S (GeV)	$m_{2\ell}$	$m_{2\ell_diff}$	$m_{3\ell}$	$m_{3\ell_diff}$
Singlet	300	800	1/7*	1/3*	1/20	1/10
Singlet	600	800	1/5*	1/6*	1/15	1/12
Singlet	800	500	1/10	1/12	1/14**	1/16**
Doublet	850	500	1/10	1/16	1/15**	1/17**
Doublet	800	1200	1/14*	1/4*	1/40	1/15
Doublet	1000	800	1/20	1/26	1/19**	1/22**

Table I.2: Scaling factors $f = N_{\text{peak, det}}/N_{\text{peak}}$ for the different benchmarks of our models. The values correspond to observables computed at $\sqrt{s} = 14$ TeV and a luminosity of 3000 fb^{-1} . Peaks which fall below the SM background (resonances are broad) are marked with * (**).

show very broad resonances for the benchmark scenarios (blue, black curves). The number of events in each of the peak bins reaches $\mathcal{O}(10)$. Scaling factors comparing number of events in the peak bins after and before detector simulation with `Delphes 3` using the HL-LHC default card are shown in Tab. I.2. The results are very similar to those in Tab. 7.2, with slightly larger scaling factors in the HL-LHC scenario due to enhanced detector performance.

I.5 More general benchmark scenarios

In Fig. I.7 we give the L_T distributions for different benchmark scenarios in the singlet model with $\kappa' = 1$. The distributions are computed at 13 TeV at an integrated luminosity of 77.4 fb^{-1} and include effects of the subsequent detector simulation. The benchmark models are the same as in the case where κ' is fixed according to Eq. (7.1.8) with one exception: for $\kappa' = 1$ we find that the scenario with $M_F = 800$ GeV, $M_S = 500$ GeV is in tension with the high- L_T bins of the CMS data. However, a very similar scenario with $M_F = 900$ GeV, $M_S = 500$ GeV is still allowed by present data.

Parton-level distributions of the observables $m_{2\ell}$, $m_{2\ell_diff}$, $m_{3\ell}$ and $m_{3\ell_diff}$ for the different benchmark scenarios are shown in Fig. 7.11. The $m_{2\ell}$ and $m_{2\ell_diff}$ distributions look essentially like the $g - 2$ benchmarks (see Fig. 7.6) and show peaks at the mass of the BSM scalars for on-shell production (black curve). Considering the $m_{3\ell}$ distributions we observe peaks for all benchmark scenarios, which is in contrast to the $g - 2$ distributions in Fig. 7.6. The only difference between on- and off-shell S -production is that in the case $M_F > M_S$ the peak is broader. Scenarios with $M_F = 300$ GeV and $M_F = 900$ GeV show peaks with $\mathcal{O}(10 - 10^2)$ events. In the scenario with $M_F = 600$ GeV the number of events is one order of magnitude smaller due to the smaller cross section. In the $m_{3\ell_diff}$ distributions we find a peak with similar number of events per bin compared to the $m_{3\ell}$ distribution at the mass of the VLLs only for $M_F > M_S$ (black curve). This makes $m_{3\ell_diff}$ the optimal observable for scenarios with this mass hierarchy. Distributions of the other benchmark scenarios are strongly suppressed compared to $m_{3\ell}$ while the SM background is completely absent.

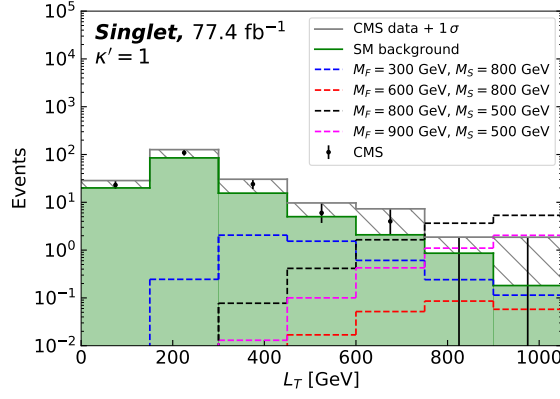


Figure I.7: Scalar sum of transverse momenta L_T in the singlet model for SM background processes and for different masses of vector-like fermions and new scalars with $\kappa' = 1$. The observables are shown for an integrated luminosity of 77.4 fb^{-1} and subsequent detector simulation. We show as well CMS data from [400].

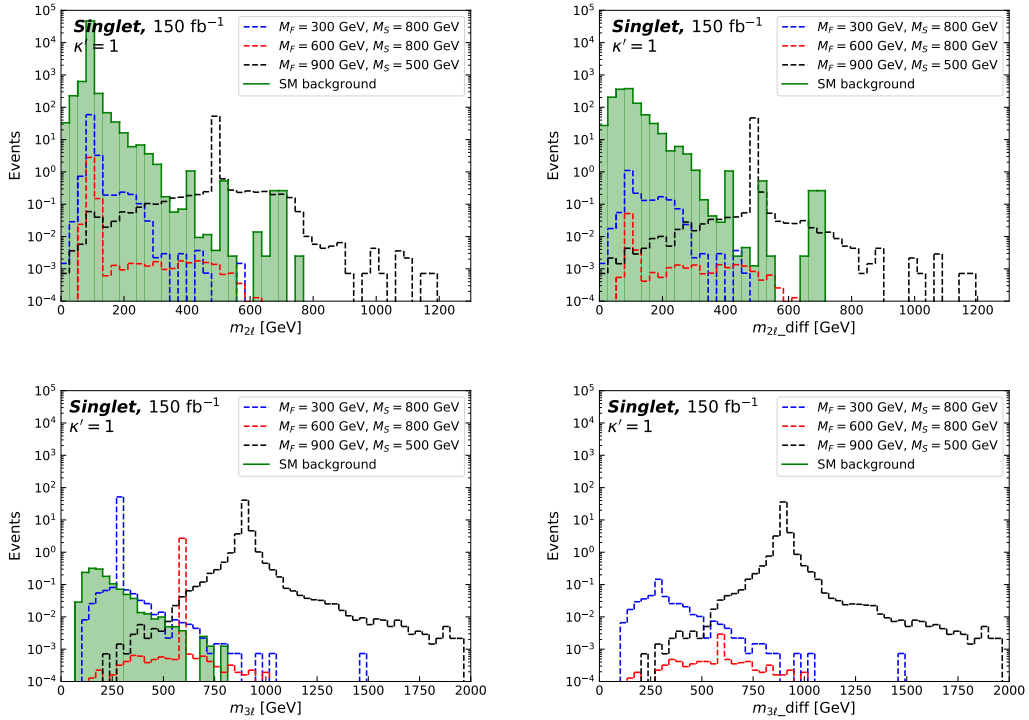


Figure I.8: Distributions of invariant masses m_{2l} , m_{2l_diff} , m_{3l} and m_{3l_diff} for the singlet model with fixed $\kappa' = 1$ at parton level. The observables are computed for the different benchmark scenarios for a luminosity of 150 fb^{-1} and $\sqrt{s} = 13 \text{ TeV}$.

Bibliography

- [1] Georges Aad et al. “Observation of a new particle in the search for the Standard Model Higgs boson with the ATLAS detector at the LHC”. In: *Phys. Lett. B* 716 (2012), pp. 1–29. DOI: 10.1016/j.physletb.2012.08.020. arXiv: 1207.7214 [hep-ex].
- [2] Serguei Chatrchyan et al. “Observation of a New Boson at a Mass of 125 GeV with the CMS Experiment at the LHC”. In: *Phys. Lett. B* 716 (2012), pp. 30–61. DOI: 10.1016/j.physletb.2012.08.021. arXiv: 1207.7235 [hep-ex].
- [3] Peter W. Higgs. “Broken Symmetries and the Masses of Gauge Bosons”. In: *Phys. Rev. Lett.* 13 (1964). Ed. by J.C. Taylor, pp. 508–509. DOI: 10.1103/PhysRevLett.13.508.
- [4] Peter W. Higgs. “Broken symmetries, massless particles and gauge fields”. In: *Phys. Lett.* 12 (1964), pp. 132–133. DOI: 10.1016/0031-9163(64)91136-9.
- [5] F. Englert and R. Brout. “Broken Symmetry and the Mass of Gauge Vector Mesons”. In: *Phys. Rev. Lett.* 13 (1964). Ed. by J.C. Taylor, pp. 321–323. DOI: 10.1103/PhysRevLett.13.321.
- [6] ATLAS and CMS. “Measurements of the Higgs boson production and decay rates and constraints on its couplings from a combined ATLAS and CMS analysis of the LHC pp collision data at $\sqrt{s} = 7$ and 8 TeV”. In: *ATLAS-CONF-2015-044, CMS-PAS-HIG-15-002* (Sept. 2015).
- [7] Rodrigo Alonso, Benjamín Grinstein, and Jorge Martin Camalich. “Lepton universality violation and lepton flavor conservation in B -meson decays”. In: *JHEP* 10 (2015), p. 184. DOI: 10.1007/JHEP10(2015)184. arXiv: 1505.05164 [hep-ph].
- [8] Admir Greljo, Gino Isidori, and David Marzocca. “On the breaking of Lepton Flavor Universality in B decays”. In: *JHEP* 07 (2015), p. 142. DOI: 10.1007/JHEP07(2015)142. arXiv: 1506.01705 [hep-ph].
- [9] Riccardo Barbieri et al. “Anomalies in B -decays and $U(2)$ flavour symmetry”. In: *Eur. Phys. J. C* 76.2 (2016), p. 67. DOI: 10.1140/epjc/s10052-016-3905-3. arXiv: 1512.01560 [hep-ph].
- [10] Lorenzo Calibbi, Andreas Crivellin, and Toshihiko Ota. “Effective Field Theory Approach to $b \rightarrow s\ell\ell^{(\prime)}$, $B \rightarrow K^{(*)}\nu\bar{\nu}$ and $B \rightarrow D^{(*)}\tau\nu$ with Third Generation Couplings”. In: *Phys. Rev. Lett.* 115 (2015), p. 181801. DOI: 10.1103/PhysRevLett.115.181801. arXiv: 1506.02661 [hep-ph].
- [11] Martin Bauer and Matthias Neubert. “Minimal Leptoquark Explanation for the $R_{D^{(*)}}$, R_K , and $(g - 2)_g$ Anomalies”. In: *Phys. Rev. Lett.* 116.14 (2016), p. 141802. DOI: 10.1103/PhysRevLett.116.141802. arXiv: 1511.01900 [hep-ph].
- [12] Svjetlana Fajfer and Nejc Košnik. “Vector leptoquark resolution of R_K and $R_{D^{(*)}}$ puzzles”. In: *Phys. Lett. B* 755 (2016), pp. 270–274. DOI: 10.1016/j.physletb.2016.02.018. arXiv: 1511.06024 [hep-ph].
- [13] M. Tanabashi et al. “Review of Particle Physics”. In: *Phys. Rev. D* 98.3 (2018), p. 030001. DOI: 10.1103/PhysRevD.98.030001.

- [14] D. Hanneke, S. Fogwell, and G. Gabrielse. “New Measurement of the Electron Magnetic Moment and the Fine Structure Constant”. In: *Phys. Rev. Lett.* 100 (2008), p. 120801. DOI: 10.1103/PhysRevLett.100.120801. arXiv: 0801.1134 [physics.atom-ph].
- [15] Richard H. Parker et al. “Measurement of the fine-structure constant as a test of the Standard Model”. In: *Science* 360 (2018), p. 191. DOI: 10.1126/science.aap7706. arXiv: 1812.04130 [physics.atom-ph].
- [16] Léo Morel et al. “Determination of the fine-structure constant with an accuracy of 81 parts per trillion”. In: *Nature* 588.7836 (2020), pp. 61–65. DOI: 10.1038/s41586-020-2964-7.
- [17] John Ellis et al. “Top, Higgs, Diboson and Electroweak Fit to the Standard Model Effective Field Theory”. In: (Dec. 2020). arXiv: 2012.02779 [hep-ph].
- [18] Gauthier Durieux et al. “The electro-weak couplings of the top and bottom quarks – global fit and future prospects”. In: *JHEP* 12 (2019), p. 098. DOI: 10.1007/JHEP12(2019)098. arXiv: 1907.10619 [hep-ph].
- [19] V. Cirigliano et al. “Is there room for CP violation in the top-Higgs sector?” In: *Phys. Rev. D* 94.1 (2016), p. 016002. DOI: 10.1103/PhysRevD.94.016002. arXiv: 1603.03049 [hep-ph].
- [20] V. Cirigliano et al. “Constraining the top-Higgs sector of the Standard Model Effective Field Theory”. In: *Phys. Rev. D* 94.3 (2016), p. 034031. DOI: 10.1103/PhysRevD.94.034031. arXiv: 1605.04311 [hep-ph].
- [21] Rafael Aoude et al. “The impact of flavour data on global fits of the MFV SMEFT”. In: (Mar. 2020). arXiv: 2003.05432 [hep-ph].
- [22] Javier Fuentes-Martin et al. “Charm Physics Confronts High- p_T Lepton Tails”. In: (Mar. 2020). arXiv: 2003.12421 [hep-ph].
- [23] Stefan Bißmann et al. “Constraining top-quark couplings combining top-quark and B decay observables”. In: *Eur. Phys. J. C* 80.2 (2020), p. 136. DOI: 10.1140/epjc/s10052-020-7680-9. arXiv: 1909.13632 [hep-ph].
- [24] Stefan Bißmann et al. “Top and Beauty synergies in SMEFT-fits at present and future colliders”. In: *JHEP* 06 (2021), p. 010. DOI: 10.1007/JHEP06(2021)010. arXiv: 2012.10456 [hep-ph].
- [25] Stefan Bißmann et al. “Correlating uncertainties in global analyses within SMEFT matters”. In: *Phys. Rev. D* 102 (2020), p. 115019. DOI: 10.1103/PhysRevD.102.115019. arXiv: 1912.06090 [hep-ph].
- [26] Stefan Bißmann et al. “Multi-lepton signatures of vector-like leptons with flavor”. In: *Eur. Phys. J. C* 81.2 (2021), p. 101. DOI: 10.1140/epjc/s10052-021-08886-3. arXiv: 2011.12964 [hep-ph].
- [27] Albert M Sirunyan et al. “Search for new physics in top quark production with additional leptons in proton-proton collisions at $\sqrt{s} = 13$ TeV using effective field theory”. In: (Dec. 2020). arXiv: 2012.04120 [hep-ex].
- [28] Gudrun Hiller et al. “Anomalous magnetic moments from asymptotic safety”. In: (Oct. 2019). arXiv: 1910.14062 [hep-ph].
- [29] Gudrun Hiller et al. “Asymptotically safe extensions of the Standard Model with flavour phenomenology”. In: *54th Rencontres de Moriond on Electroweak Interactions and Unified Theories*. 2019, pp. 415–418. arXiv: 1905.11020 [hep-ph].

- [30] Gudrun Hiller et al. “Model Building from Asymptotic Safety with Higgs and Flavor Portals”. In: (Aug. 2020). arXiv: 2008.08606 [hep-ph].
- [31] David J. Gross and Frank Wilczek. “Ultraviolet Behavior of Nonabelian Gauge Theories”. In: *Phys. Rev. Lett.* 30 (1973). Ed. by J.C. Taylor, pp. 1343–1346. DOI: 10.1103/PhysRevLett.30.1343.
- [32] Steven Weinberg. “Nonabelian Gauge Theories of the Strong Interactions”. In: *Phys. Rev. Lett.* 31 (1973), pp. 494–497. DOI: 10.1103/PhysRevLett.31.494.
- [33] H. Fritzsch, Murray Gell-Mann, and H. Leutwyler. “Advantages of the Color Octet Gluon Picture”. In: *Phys. Lett. B* 47 (1973), pp. 365–368. DOI: 10.1016/0370-2693(73)90625-4.
- [34] H.David Politzer. “Reliable Perturbative Results for Strong Interactions?” In: *Phys. Rev. Lett.* 30 (1973). Ed. by J.C. Taylor, pp. 1346–1349. DOI: 10.1103/PhysRevLett.30.1346.
- [35] Steven Weinberg. “A Model of Leptons”. In: *Phys. Rev. Lett.* 19 (1967), pp. 1264–1266. DOI: 10.1103/PhysRevLett.19.1264.
- [36] S.L. Glashow. “Partial Symmetries of Weak Interactions”. In: *Nucl. Phys.* 22 (1961), pp. 579–588. DOI: 10.1016/0029-5582(61)90469-2.
- [37] Abdus Salam. “Weak and Electromagnetic Interactions”. In: *Conf. Proc. C* 680519 (1968), pp. 367–377. DOI: 10.1142/9789812795915_0034.
- [38] J. Goldstone. “Field Theories with Superconductor Solutions”. In: *Nuovo Cim.* 19 (1961), pp. 154–164. DOI: 10.1007/BF02812722.
- [39] Jeffrey Goldstone, Abdus Salam, and Steven Weinberg. “Broken Symmetries”. In: *Phys. Rev.* 127 (1962), pp. 965–970. DOI: 10.1103/PhysRev.127.965.
- [40] S.L. Glashow, J. Iliopoulos, and L. Maiani. “Weak Interactions with Lepton-Hadron Symmetry”. In: *Phys. Rev. D* 2 (1970), pp. 1285–1292. DOI: 10.1103/PhysRevD.2.1285.
- [41] Nicola Cabibbo. “Unitary Symmetry and Leptonic Decays”. In: *Phys. Rev. Lett.* 10 (1963), pp. 531–533. DOI: 10.1103/PhysRevLett.10.531.
- [42] Makoto Kobayashi and Toshihide Maskawa. “CP Violation in the Renormalizable Theory of Weak Interaction”. In: *Prog. Theor. Phys.* 49 (1973), pp. 652–657. DOI: 10.1143/PTP.49.652.
- [43] Ling-Lie Chau and Wai-Yee Keung. “Comments on the Parametrization of the Kobayashi-Maskawa Matrix”. In: *Phys. Rev. Lett.* 53 (1984), p. 1802. DOI: 10.1103/PhysRevLett.53.1802.
- [44] B. Pontecorvo. “Mesonium and anti-mesonium”. In: *Sov. Phys. JETP* 6 (1957), p. 429.
- [45] Q.R. Ahmad et al. “Measurement of the rate of $\nu_e + d \rightarrow p + p + e^-$ interactions produced by 8B solar neutrinos at the Sudbury Neutrino Observatory”. In: *Phys. Rev. Lett.* 87 (2001), p. 071301. DOI: 10.1103/PhysRevLett.87.071301. arXiv: nucl-ex/0106015.
- [46] Y. Fukuda et al. “Evidence for oscillation of atmospheric neutrinos”. In: *Phys. Rev. Lett.* 81 (1998), pp. 1562–1567. DOI: 10.1103/PhysRevLett.81.1562. arXiv: hep-ex/9807003.

- [47] Gerard 't Hooft and M.J.G. Veltman. “Regularization and Renormalization of Gauge Fields”. In: *Nucl. Phys. B* 44 (1972), pp. 189–213. DOI: 10.1016/0550-3213(72)90279-9.
- [48] Steven Weinberg. “New approach to the renormalization group”. In: *Phys. Rev. D* 8 (1973), pp. 3497–3509. DOI: 10.1103/PhysRevD.8.3497.
- [49] Steven Weinberg. “Phenomenological Lagrangians”. In: *Physica A* 96.1-2 (1979). Ed. by S. Deser, pp. 327–340. DOI: 10.1016/0378-4371(79)90223-1.
- [50] Dario Buttazzo et al. “Investigating the near-criticality of the Higgs boson”. In: *JHEP* 12 (2013), p. 089. DOI: 10.1007/JHEP12(2013)089. arXiv: 1307.3536 [hep-ph].
- [51] Tommi Markkanen, Arttu Rajantie, and Stephen Stopyra. “Cosmological Aspects of Higgs Vacuum Metastability”. In: *Front. Astron. Space Sci.* 5 (2018), p. 40. DOI: 10.3389/fspas.2018.00040. arXiv: 1809.06923 [astro-ph.CO].
- [52] Kenneth G. Wilson. “Renormalization group and critical phenomena. 1. Renormalization group and the Kadanoff scaling picture”. In: *Phys. Rev. B* 4 (1971), pp. 3174–3183. DOI: 10.1103/PhysRevB.4.3174.
- [53] Kenneth G. Wilson. “Renormalization group and critical phenomena. 2. Phase space cell analysis of critical behavior”. In: *Phys. Rev. B* 4 (1971), pp. 3184–3205. DOI: 10.1103/PhysRevB.4.3184.
- [54] Steven Weinberg. In: *Ultraviolet divergences in quantum theories of gravitation, in: General Relativity: An Einstein centenary survey, Eds. Hawking, S.W., Israel, W; Cambridge University Press* (1979), pp. 790–831.
- [55] D. Bailin and A. Love. “Asymptotic Near Freedom”. In: *Nucl. Phys. B* 75 (1974), p. 159. DOI: 10.1016/0550-3213(74)90470-2.
- [56] Martin Reuter and Frank Saueressig. “Quantum Einstein Gravity”. In: *New J. Phys.* 14 (2012), p. 055022. DOI: 10.1088/1367-2630/14/5/055022. arXiv: 1202.2274 [hep-th].
- [57] Daniel F. Litim. “Fixed Points of Quantum Gravity and the Renormalisation Group”. In: *PoS QG-Ph* (2007), p. 024. DOI: 10.22323/1.043.0024. arXiv: 0810.3675 [hep-th].
- [58] Roberto Percacci. “Asymptotic Safety”. In: (Sept. 2007), pp. 111–128. arXiv: 0709.3851 [hep-th].
- [59] Max Niedermaier and Martin Reuter. “The Asymptotic Safety Scenario in Quantum Gravity”. In: *Living Rev. Rel.* 9 (2006), pp. 5–173. DOI: 10.12942/lrr-2006-5.
- [60] M. Niedermaier. “The Asymptotic safety scenario in quantum gravity: An Introduction”. In: *Class. Quant. Grav.* 24 (2007), R171–230. DOI: 10.1088/0264-9381/24/18/R01. arXiv: gr-qc/0610018.
- [61] Daniel F. Litim. “Renormalisation group and the Planck scale”. In: *Phil. Trans. Roy. Soc. Lond. A* 369 (2011), pp. 2759–2778. DOI: 10.1098/rsta.2011.0103. arXiv: 1102.4624 [hep-th].
- [62] Daniel F. Litim. “On fixed points of quantum gravity”. In: *AIP Conf. Proc.* 841.1 (2006). Ed. by Lysiane Mornas and Joaquin Diaz Alonso, pp. 322–329. DOI: 10.1063/1.2218188. arXiv: hep-th/0606044.

- [63] Kamila Kowalska et al. “Towards an asymptotically safe completion of the Standard Model”. In: *PoS EPS-HEP2017* (2017). Ed. by Paolo Checchia et al., p. 542. DOI: 10.22323/1.314.0542.
- [64] Andrew D. Bond et al. “Directions for model building from asymptotic safety”. In: *JHEP* 08 (2017), p. 004. DOI: 10.1007/JHEP08(2017)004. arXiv: 1702.01727 [hep-ph].
- [65] Daniel F. Litim and Francesco Sannino. “Asymptotic safety guaranteed”. In: *JHEP* 12 (2014), p. 178. DOI: 10.1007/JHEP12(2014)178. arXiv: 1406.2337 [hep-th].
- [66] Andrew D. Bond and Daniel F. Litim. “Theorems for Asymptotic Safety of Gauge Theories”. In: *Eur. Phys. J. C* 77.6 (2017). [Erratum: *Eur.Phys.J.C* 77, 525 (2017)], p. 429. DOI: 10.1140/epjc/s10052-017-4976-5. arXiv: 1608.00519 [hep-th].
- [67] Andrew D. Bond and Daniel F. Litim. “Price of Asymptotic Safety”. In: *Phys. Rev. Lett.* 122.21 (2019), p. 211601. DOI: 10.1103/PhysRevLett.122.211601. arXiv: 1801.08527 [hep-th].
- [68] Andrew D. Bond et al. “UV conformal window for asymptotic safety”. In: *Phys. Rev. D* 97.3 (2018), p. 036019. DOI: 10.1103/PhysRevD.97.036019. arXiv: 1710.07615 [hep-th].
- [69] Andrew D. Bond and Daniel F. Litim. “More asymptotic safety guaranteed”. In: *Phys. Rev. D* 97.8 (2018), p. 085008. DOI: 10.1103/PhysRevD.97.085008. arXiv: 1707.04217 [hep-th].
- [70] Andrew D. Bond and Daniel F. Litim. “Asymptotic safety guaranteed in supersymmetry”. In: *Phys. Rev. Lett.* 119.21 (2017), p. 211601. DOI: 10.1103/PhysRevLett.119.211601. arXiv: 1709.06953 [hep-th].
- [71] Lincoln Wolfenstein. “Parametrization of the Kobayashi-Maskawa Matrix”. In: *Phys. Rev. Lett.* 51 (1983), p. 1945. DOI: 10.1103/PhysRevLett.51.1945.
- [72] C.D. Froggatt and Holger Bech Nielsen. “Hierarchy of Quark Masses, Cabibbo Angles and CP Violation”. In: *Nucl. Phys. B* 147 (1979), pp. 277–298. DOI: 10.1016/0550-3213(79)90316-X.
- [73] Guido Altarelli and Ferruccio Feruglio. “Discrete Flavor Symmetries and Models of Neutrino Mixing”. In: *Rev. Mod. Phys.* 82 (2010), pp. 2701–2729. DOI: 10.1103/RevModPhys.82.2701. arXiv: 1002.0211 [hep-ph].
- [74] Ivo de Medeiros Varzielas and Gudrun Hiller. “Clues for flavor from rare lepton and quark decays”. In: *JHEP* 06 (2015), p. 072. DOI: 10.1007/JHEP06(2015)072. arXiv: 1503.01084 [hep-ph].
- [75] Stefan de Boer and Gudrun Hiller. “Flavor and new physics opportunities with rare charm decays into leptons”. In: *Phys. Rev. D* 93.7 (2016), p. 074001. DOI: 10.1103/PhysRevD.93.074001. arXiv: 1510.00311 [hep-ph].
- [76] Gudrun Hiller, Dennis Loose, and Kay Schönwald. “Leptoquark Flavor Patterns & B Decay Anomalies”. In: *JHEP* 12 (2016), p. 027. DOI: 10.1007/JHEP12(2016)027. arXiv: 1609.08895 [hep-ph].
- [77] Damir Bečirević et al. “Leptoquark model to explain the B -physics anomalies, R_K and R_D ”. In: *Phys. Rev. D* 94.11 (2016), p. 115021. DOI: 10.1103/PhysRevD.94.115021. arXiv: 1608.08501 [hep-ph].

- [78] Suchismita Sahoo, Rukmani Mohanta, and Anjan K. Giri. “Explaining the R_K and $R_{D^{(*)}}$ anomalies with vector leptoquarks”. In: *Phys. Rev. D* 95.3 (2017), p. 035027. DOI: 10.1103/PhysRevD.95.035027. arXiv: 1609.04367 [hep-ph].
- [79] Heinrich Päs and Erik Schumacher. “Common origin of R_K and neutrino masses”. In: *Phys. Rev. D* 92.11 (2015), p. 114025. DOI: 10.1103/PhysRevD.92.114025. arXiv: 1510.08757 [hep-ph].
- [80] Howard Georgi, Ann E. Nelson, and Aneesh Manohar. “On the Proposition That All Fermions Are Created Equal”. In: *Phys. Lett. B* 126 (1983), pp. 169–174. DOI: 10.1016/0370-2693(83)90584-1.
- [81] Ann E. Nelson and Matthew J. Strassler. “Suppressing flavor anarchy”. In: *JHEP* 09 (2000), p. 030. DOI: 10.1088/1126-6708/2000/09/030. arXiv: hep-ph/0006251.
- [82] Ann E. Nelson and Matthew J. Strassler. “Exact results for supersymmetric renormalization and the supersymmetric flavor problem”. In: *JHEP* 07 (2002), p. 021. DOI: 10.1088/1126-6708/2002/07/021. arXiv: hep-ph/0104051.
- [83] Gudrun Hiller and Clara Hormigos-Feliu. “Flavor from running”. In: (in preparation).
- [84] R. Aaij et al. “Differential branching fractions and isospin asymmetries of $B \rightarrow K^{(*)}\mu^+\mu^-$ decays”. In: *JHEP* 06 (2014), p. 133. DOI: 10.1007/JHEP06(2014)133. arXiv: 1403.8044 [hep-ex].
- [85] Roel Aaij et al. “Angular analysis and differential branching fraction of the decay $B_s^0 \rightarrow \phi\mu^+\mu^-$ ”. In: *JHEP* 09 (2015), p. 179. DOI: 10.1007/JHEP09(2015)179. arXiv: 1506.08777 [hep-ex].
- [86] Aoife Bharucha, David M. Straub, and Roman Zwicky. “ $B \rightarrow V\ell^+\ell^-$ in the Standard Model from light-cone sum rules”. In: *JHEP* 08 (2016), p. 098. DOI: 10.1007/JHEP08(2016)098. arXiv: 1503.05534 [hep-ph].
- [87] R.R. Horgan et al. “Rare B decays using lattice QCD form factors”. In: *PoS LATTICE2014* (2015), p. 372. DOI: 10.22323/1.214.0372. arXiv: 1501.00367 [hep-lat].
- [88] Nico Gubernari, Ahmet Kokulu, and Danny van Dyk. “ $B \rightarrow P$ and $B \rightarrow V$ Form Factors from B -Meson Light-Cone Sum Rules beyond Leading Twist”. In: *JHEP* 01 (2019), p. 150. DOI: 10.1007/JHEP01(2019)150. arXiv: 1811.00983 [hep-ph].
- [89] Roel Aaij et al. “Angular analysis of the $B^0 \rightarrow K^{*0}\mu^+\mu^-$ decay using 3 fb⁻¹ of integrated luminosity”. In: *JHEP* 02 (2016), p. 104. DOI: 10.1007/JHEP02(2016)104. arXiv: 1512.04442 [hep-ex].
- [90] Roel Aaij et al. “Measurement of CP -averaged observables in the $B^0 \rightarrow K^{*0}\mu^+\mu^-$ decay”. In: *Phys. Rev. Lett.* 125.1 (2020), p. 011802. DOI: 10.1103/PhysRevLett.125.011802. arXiv: 2003.04831 [hep-ex].
- [91] ATLAS. “Angular analysis of $B_d^0 \rightarrow K^*\mu^+\mu^-$ decays in pp collisions at $\sqrt{s} = 8$ TeV with the ATLAS detector”. In: *ATLAS-CONF-2017-023* (Apr. 2017).
- [92] CMS. “Measurement of the P_1 and P_5' angular parameters of the decay $B^0 \rightarrow K^{*0}\mu^+\mu^-$ in proton-proton collisions at $\sqrt{s} = 8$ TeV”. In: *CMS-PAS-BPH-15-008* (Mar. 2017).
- [93] Vardan Khachatryan et al. “Angular analysis of the decay $B^0 \rightarrow K^{*0}\mu^+\mu^-$ from pp collisions at $\sqrt{s} = 8$ TeV”. In: *Phys. Lett. B* 753 (2016), pp. 424–448. DOI: 10.1016/j.physletb.2015.12.020. arXiv: 1507.08126 [hep-ex].

- [94] A. Khodjamirian et al. “Charm-loop effect in $B \rightarrow K^{(*)}\ell^+\ell^-$ and $B \rightarrow K^*\gamma$ ”. In: *JHEP* 09 (2010), p. 089. DOI: 10.1007/JHEP09(2010)089. arXiv: 1006.4945 [hep-ph].
- [95] Christoph Bobeth et al. “Long-distance effects in $B \rightarrow K^*\ell\ell$ from analyticity”. In: *Eur. Phys. J. C* 78.6 (2018), p. 451. DOI: 10.1140/epjc/s10052-018-5918-6. arXiv: 1707.07305 [hep-ph].
- [96] Roel Aaij et al. “Test of lepton universality using $B^+ \rightarrow K^+\ell^+\ell^-$ decays”. In: *Phys. Rev. Lett.* 113 (2014), p. 151601. DOI: 10.1103/PhysRevLett.113.151601. arXiv: 1406.6482 [hep-ex].
- [97] R. Aaij et al. “Test of lepton universality with $B^0 \rightarrow K^{*0}\ell^+\ell^-$ decays”. In: *JHEP* 08 (2017), p. 055. DOI: 10.1007/JHEP08(2017)055. arXiv: 1705.05802 [hep-ex].
- [98] Roel Aaij et al. “Search for lepton-universality violation in $B^+ \rightarrow K^+\ell^+\ell^-$ decays”. In: *Phys. Rev. Lett.* 122.19 (2019), p. 191801. DOI: 10.1103/PhysRevLett.122.191801. arXiv: 1903.09252 [hep-ex].
- [99] Marzia Bordone, Gino Isidori, and Andrea Pattori. “On the Standard Model predictions for R_K and R_{K^*} ”. In: *Eur. Phys. J. C* 76.8 (2016), p. 440. DOI: 10.1140/epjc/s10052-016-4274-7. arXiv: 1605.07633 [hep-ph].
- [100] J.P. Lees et al. “Evidence for an excess of $\bar{B} \rightarrow D^{(*)}\tau^-\bar{\nu}_\tau$ decays”. In: *Phys. Rev. Lett.* 109 (2012), p. 101802. DOI: 10.1103/PhysRevLett.109.101802. arXiv: 1205.5442 [hep-ex].
- [101] J.P. Lees et al. “Measurement of an Excess of $\bar{B} \rightarrow D^{(*)}\tau^-\bar{\nu}_\tau$ Decays and Implications for Charged Higgs Bosons”. In: *Phys. Rev. D* 88.7 (2013), p. 072012. DOI: 10.1103/PhysRevD.88.072012. arXiv: 1303.0571 [hep-ex].
- [102] M. Huschle et al. “Measurement of the branching ratio of $\bar{B} \rightarrow D^{(*)}\tau^-\bar{\nu}_\tau$ relative to $\bar{B} \rightarrow D^{(*)}\ell^-\bar{\nu}_\ell$ decays with hadronic tagging at Belle”. In: *Phys. Rev. D* 92.7 (2015), p. 072014. DOI: 10.1103/PhysRevD.92.072014. arXiv: 1507.03233 [hep-ex].
- [103] Y. Sato et al. “Measurement of the branching ratio of $\bar{B}^0 \rightarrow D^{*+}\tau^-\bar{\nu}_\tau$ relative to $\bar{B}^0 \rightarrow D^{*+}\ell^-\bar{\nu}_\ell$ decays with a semileptonic tagging method”. In: *Phys. Rev. D* 94.7 (2016), p. 072007. DOI: 10.1103/PhysRevD.94.072007. arXiv: 1607.07923 [hep-ex].
- [104] S. Hirose et al. “Measurement of the τ lepton polarization and $R(D^*)$ in the decay $\bar{B} \rightarrow D^*\tau^-\bar{\nu}_\tau$ ”. In: *Phys. Rev. Lett.* 118.21 (2017), p. 211801. DOI: 10.1103/PhysRevLett.118.211801. arXiv: 1612.00529 [hep-ex].
- [105] Roel Aaij et al. “Measurement of the ratio of branching fractions $\mathcal{B}(\bar{B}^0 \rightarrow D^{*+}\tau^-\bar{\nu}_\tau)/\mathcal{B}(\bar{B}^0 \rightarrow D^{*+}\mu^-\bar{\nu}_\mu)$ ”. In: *Phys. Rev. Lett.* 115.11 (2015). [Erratum: *Phys. Rev. Lett.* 115, 159901 (2015)], p. 111803. DOI: 10.1103/PhysRevLett.115.111803. arXiv: 1506.08614 [hep-ex].
- [106] R. Aaij et al. “Measurement of the ratio of the $B^0 \rightarrow D^{*-}\tau^+\nu_\tau$ and $B^0 \rightarrow D^{*-}\mu^+\nu_\mu$ branching fractions using three-prong τ -lepton decays”. In: *Phys. Rev. Lett.* 120.17 (2018), p. 171802. DOI: 10.1103/PhysRevLett.120.171802. arXiv: 1708.08856 [hep-ex].
- [107] A. Abdesselam et al. “Precise determination of the CKM matrix element $|V_{cb}|$ with $\bar{B}^0 \rightarrow D^{*+}\ell^-\bar{\nu}_\ell$ decays with hadronic tagging at Belle”. In: (Feb. 2017). arXiv: 1702.01521 [hep-ex].

- [108] E. Waheed et al. “Measurement of the CKM matrix element $|V_{cb}|$ from $B^0 \rightarrow D^{*-} \ell^+ \nu_\ell$ at Belle”. In: *Phys. Rev. D* 100.5 (2019), p. 052007. DOI: 10.1103/PhysRevD.100.052007. arXiv: 1809.03290 [hep-ex].
- [109] Martin Jung and David M. Straub. “Constraining new physics in $b \rightarrow c \ell \nu$ transitions”. In: *JHEP* 01 (2019), p. 009. DOI: 10.1007/JHEP01(2019)009. arXiv: 1801.01112 [hep-ph].
- [110] Jon A. Bailey et al. “ $B \rightarrow D \ell \nu$ form factors at nonzero recoil and $|V_{cb}|$ from 2+1-flavor lattice QCD”. In: *Phys. Rev. D* 92.3 (2015), p. 034506. DOI: 10.1103/PhysRevD.92.034506. arXiv: 1503.07237 [hep-lat].
- [111] Heechang Na et al. “ $B \rightarrow D \ell \nu$ form factors at nonzero recoil and extraction of $|V_{cb}|$ ”. In: *Phys. Rev. D* 92.5 (2015). [Erratum: Phys.Rev.D 93, 119906 (2016)], p. 054510. DOI: 10.1103/PhysRevD.93.119906. arXiv: 1505.03925 [hep-lat].
- [112] Florian U. Bernlochner et al. “Combined analysis of semileptonic B decays to D and D^* : $R(D^{(*)})$, $|V_{cb}|$, and new physics”. In: *Phys. Rev. D* 95.11 (2017). [Erratum: Phys.Rev.D 97, 059902 (2018)], p. 115008. DOI: 10.1103/PhysRevD.95.115008. arXiv: 1703.05330 [hep-ph].
- [113] Dante Bigi, Paolo Gambino, and Stefan Schacht. “ $R(D^*)$, $|V_{cb}|$, and the Heavy Quark Symmetry relations between form factors”. In: *JHEP* 11 (2017), p. 061. DOI: 10.1007/JHEP11(2017)061. arXiv: 1707.09509 [hep-ph].
- [114] R. Aaij et al. “Test of Lepton Flavor Universality by the measurement of the $B^0 \rightarrow D^{*-} \tau^+ \nu_\tau$ branching fraction using three-prong τ decays”. In: *Phys. Rev. D* 97.7 (2018), p. 072013. DOI: 10.1103/PhysRevD.97.072013. arXiv: 1711.02505 [hep-ex].
- [115] A. Abdesselam et al. “Test of lepton flavor universality in $B \rightarrow K^* \ell^+ \ell^-$ decays at Belle”. In: (Apr. 2019). arXiv: 1904.02440 [hep-ex].
- [116] S. Hirose et al. “Measurement of the τ lepton polarization and $R(D^*)$ in the decay $\bar{B} \rightarrow D^* \tau^- \bar{\nu}_\tau$ with one-prong hadronic τ decays at Belle”. In: *Phys. Rev. D* 97.1 (2018), p. 012004. DOI: 10.1103/PhysRevD.97.012004. arXiv: 1709.00129 [hep-ex].
- [117] A. Abdesselam et al. “Measurement of $\mathcal{R}(D)$ and $\mathcal{R}(D^*)$ with a semileptonic tagging method”. In: (Apr. 2019). arXiv: 1904.08794 [hep-ex].
- [118] Dante Bigi and Paolo Gambino. “Revisiting $B \rightarrow D \ell \nu$ ”. In: *Phys. Rev. D* 94.9 (2016), p. 094008. DOI: 10.1103/PhysRevD.94.094008. arXiv: 1606.08030 [hep-ph].
- [119] Sneha Jaiswal, Soumitra Nandi, and Sunando Kumar Patra. “Extraction of $|V_{cb}|$ from $B \rightarrow D^{(*)} \ell \nu_\ell$ and the Standard Model predictions of $R(D^{(*)})$ ”. In: *JHEP* 12 (2017), p. 060. DOI: 10.1007/JHEP12(2017)060. arXiv: 1707.09977 [hep-ph].
- [120] Gudrun Hiller and Frank Kruger. “More model-independent analysis of $b \rightarrow s$ processes”. In: *Phys. Rev. D* 69 (2004), p. 074020. DOI: 10.1103/PhysRevD.69.074020. arXiv: hep-ph/0310219.
- [121] Wolfgang Altmannshofer et al. “Status of the $B \rightarrow K^* \mu^+ \mu^-$ anomaly after Moriond 2017”. In: *Eur. Phys. J. C* 77.6 (2017), p. 377. DOI: 10.1140/epjc/s10052-017-4952-0. arXiv: 1703.09189 [hep-ph].
- [122] Wolfgang Altmannshofer, Peter Stangl, and David M. Straub. “Interpreting Hints for Lepton Flavor Universality Violation”. In: *Phys. Rev. D* 96.5 (2017), p. 055008. DOI: 10.1103/PhysRevD.96.055008. arXiv: 1704.05435 [hep-ph].

- [123] Bernat Capdevila et al. “Patterns of New Physics in $b \rightarrow s\ell^+\ell^-$ transitions in the light of recent data”. In: *JHEP* 01 (2018), p. 093. DOI: 10.1007/JHEP01(2018)093. arXiv: 1704.05340 [hep-ph].
- [124] Li-Sheng Geng et al. “Towards the discovery of new physics with lepton-universality ratios of $b \rightarrow s\ell\ell$ decays”. In: *Phys. Rev. D* 96.9 (2017), p. 093006. DOI: 10.1103/PhysRevD.96.093006. arXiv: 1704.05446 [hep-ph].
- [125] Marco Ciuchini et al. “On Flavourful Easter eggs for New Physics hunger and Lepton Flavour Universality violation”. In: *Eur. Phys. J. C* 77.10 (2017), p. 688. DOI: 10.1140/epjc/s10052-017-5270-2. arXiv: 1704.05447 [hep-ph].
- [126] T. Hurth et al. “Lepton nonuniversality in exclusive $b \rightarrow s\ell\ell$ decays”. In: *Phys. Rev. D* 96.9 (2017), p. 095034. DOI: 10.1103/PhysRevD.96.095034. arXiv: 1705.06274 [hep-ph].
- [127] Jason Aebischer et al. “ B -decay discrepancies after Moriond 2019”. In: *Eur. Phys. J. C* 80.3 (2020), p. 252. DOI: 10.1140/epjc/s10052-020-7817-x. arXiv: 1903.10434 [hep-ph].
- [128] Fred Jegerlehner. “Muon $g - 2$ theory: The hadronic part”. In: *EPJ Web Conf.* 166 (2018). Ed. by A. Di Domenico, p. 00022. DOI: 10.1051/epjconf/201816600022. arXiv: 1705.00263 [hep-ph].
- [129] Michel Davier. “Update of the Hadronic Vacuum Polarisation Contribution to the muon $g-2$ ”. In: *Nucl. Part. Phys. Proc.* 287-288 (2017). Ed. by Changzheng Yuan, Xiaohu Mo, and Liangliang Wang, pp. 70–75. DOI: 10.1016/j.nuclphysbps.2017.03.047. arXiv: 1612.02743 [hep-ph].
- [130] Sz. Borsanyi et al. “Leading-order hadronic vacuum polarization contribution to the muon magnetic moment from lattice QCD”. In: (Feb. 2020). arXiv: 2002.12347 [hep-lat].
- [131] Andreas Crivellin et al. “Hadronic vacuum polarization: $(g - 2)_\mu$ versus global electroweak fits”. In: *Phys. Rev. Lett.* 125.9 (2020), p. 091801. DOI: 10.1103/PhysRevLett.125.091801. arXiv: 2003.04886 [hep-ph].
- [132] Alexander Keshavarzi et al. “Muon $g - 2$ and $\Delta\alpha$ connection”. In: *Phys. Rev. D* 102.3 (2020), p. 033002. DOI: 10.1103/PhysRevD.102.033002. arXiv: 2006.12666 [hep-ph].
- [133] T. Aoyama et al. “The anomalous magnetic moment of the muon in the Standard Model”. In: (June 2020). arXiv: 2006.04822 [hep-ph].
- [134] Hooman Davoudiasl and William J. Marciano. “Tale of two anomalies”. In: *Phys. Rev. D* 98.7 (2018), p. 075011. DOI: 10.1103/PhysRevD.98.075011. arXiv: 1806.10252 [hep-ph].
- [135] Jia Liu, Carlos E.M. Wagner, and Xiao-Ping Wang. “A light complex scalar for the electron and muon anomalous magnetic moments”. In: *JHEP* 03 (2019), p. 008. DOI: 10.1007/JHEP03(2019)008. arXiv: 1810.11028 [hep-ph].
- [136] Susan Gardner and Xinshuai Yan. “Light scalars with lepton number to solve the $(g - 2)_e$ anomaly”. In: (July 2019). arXiv: 1907.12571 [hep-ph].
- [137] Martin Bauer et al. “Axionlike Particles, Lepton-Flavor Violation, and a New Explanation of a_μ and a_e ”. In: *Phys. Rev. Lett.* 124.21 (2020), p. 211803. DOI: 10.1103/PhysRevLett.124.211803. arXiv: 1908.00008 [hep-ph].

- [138] Bhaskar Dutta and Yukihiro Mimura. “Electron $g - 2$ with flavor violation in MSSM”. In: *Phys. Lett. B* 790 (2019), pp. 563–567. DOI: 10.1016/j.physletb.2018.12.070. arXiv: 1811.10209 [hep-ph].
- [139] Motoi Endo and Wen Yin. “Explaining electron and muon $g - 2$ anomaly in SUSY without lepton-flavor mixings”. In: *JHEP* 08 (2019), p. 122. DOI: 10.1007/JHEP08(2019)122. arXiv: 1906.08768 [hep-ph].
- [140] Marcin Badziak and Kazuki Sakurai. “Explanation of electron and muon $g - 2$ anomalies in the MSSM”. In: *JHEP* 10 (2019), p. 024. DOI: 10.1007/JHEP10(2019)024. arXiv: 1908.03607 [hep-ph].
- [141] Thomas Appelquist and J. Carazzone. “Infrared Singularities and Massive Fields”. In: *Phys. Rev. D* 11 (1975), p. 2856. DOI: 10.1103/PhysRevD.11.2856.
- [142] E. Fermi. “An attempt of a theory of beta radiation. 1.” In: *Z. Phys.* 88 (1934), pp. 161–177. DOI: 10.1007/BF01351864.
- [143] A. V. Manohar. “Effective field theories”. In: *Lect. Notes Phys.* 479 (1997). Ed. by H. Latal and W. Schweiger, pp. 311–362. DOI: 10.1007/BFb0104294. arXiv: hep-ph/9606222.
- [144] Matthias Neubert. “Renormalization Theory and Effective Field Theories”. In: *Les Houches Lect. Notes* 108 (2020). Ed. by Sacha Davidson et al. DOI: 10.1093/oso/9780198855743.003.0001. arXiv: 1901.06573 [hep-ph].
- [145] Matthias Neubert. “Effective field theory and heavy quark physics”. In: *Theoretical Advanced Study Institute in Elementary Particle Physics: Physics in $D \geq 4$* . Dec. 2005, pp. 149–194. DOI: 10.1142/9789812773579_0004. arXiv: hep-ph/0512222.
- [146] Antonio Pich. “Effective field theory: Course”. In: *Les Houches Summer School in Theoretical Physics, Session 68: Probing the Standard Model of Particle Interactions*. June 1998, pp. 949–1049. arXiv: hep-ph/9806303.
- [147] Gerhard Buchalla, Andrzej J. Buras, and Markus E. Lautenbacher. “Weak decays beyond leading logarithms”. In: *Rev. Mod. Phys.* 68 (1996), pp. 1125–1144. DOI: 10.1103/RevModPhys.68.1125. arXiv: hep-ph/9512380.
- [148] Andrzej J. Buras. “Weak Hamiltonian, CP violation and rare decays”. In: *Les Houches Summer School in Theoretical Physics, Session 68: Probing the Standard Model of Particle Interactions*. June 1998, pp. 281–539. arXiv: hep-ph/9806471.
- [149] Andrzej J. Buras. “Operator product expansion, renormalization group and weak decays”. In: *Lect. Notes Phys.* 558 (2000). Ed. by P. Breitenlohner and D. Maison, pp. 65–85. arXiv: hep-ph/9901409.
- [150] Elizabeth E. Jenkins, Aneesh V. Manohar, and Peter Stoffer. “Low-Energy Effective Field Theory below the Electroweak Scale: Operators and Matching”. In: *JHEP* 03 (2018), p. 016. DOI: 10.1007/JHEP03(2018)016. arXiv: 1709.04486 [hep-ph].
- [151] Elizabeth E. Jenkins, Aneesh V. Manohar, and Peter Stoffer. “Low-Energy Effective Field Theory below the Electroweak Scale: Anomalous Dimensions”. In: *JHEP* 01 (2018), p. 084. DOI: 10.1007/JHEP01(2018)084. arXiv: 1711.05270 [hep-ph].
- [152] Konstantin G. Chetyrkin, Mikolaj Misiak, and Manfred Munz. “Weak radiative B meson decay beyond leading logarithms”. In: *Phys. Lett. B* 400 (1997). [Erratum: *Phys.Lett.B* 425, 414 (1998)], pp. 206–219. DOI: 10.1016/S0370-2693(97)00324-9. arXiv: hep-ph/9612313.

- [153] Michal Czakon, Ulrich Haisch, and Mikolaj Misiak. “Four-Loop Anomalous Dimensions for Radiative Flavour-Changing Decays”. In: *JHEP* 03 (2007), p. 008. DOI: 10.1088/1126-6708/2007/03/008. arXiv: hep-ph/0612329.
- [154] Mikolaj Misiak and Matthias Steinhauser. “Three loop matching of the dipole operators for $b \rightarrow s\gamma$ and $b \rightarrow sg$ ”. In: *Nucl. Phys. B* 683 (2004), pp. 277–305. DOI: 10.1016/j.nuclphysb.2004.02.006. arXiv: hep-ph/0401041.
- [155] Christoph Bobeth, Mikolaj Misiak, and Jorg Urban. “Photonic penguins at two loops and m_t dependence of $BR[B \rightarrow X_s l^+ l^-]$ ”. In: *Nucl. Phys. B* 574 (2000), pp. 291–330. DOI: 10.1016/S0550-3213(00)00007-9. arXiv: hep-ph/9910220.
- [156] Michał Czakon et al. “The $(Q_7, Q_{1,2})$ contribution to $\bar{B} \rightarrow X_s \gamma$ at $\mathcal{O}(\alpha_s^2)$ ”. In: *JHEP* 04 (2015), p. 168. DOI: 10.1007/JHEP04(2015)168. arXiv: 1503.01791 [hep-ph].
- [157] Simone Alioli et al. “Precision Probes of QCD at High Energies”. In: *JHEP* 07 (2017), p. 097. DOI: 10.1007/JHEP07(2017)097. arXiv: 1706.03068 [hep-ph].
- [158] Christoph Englert et al. “Higgs coupling measurements at the LHC”. In: *Eur. Phys. J. C* 76.7 (2016), p. 393. DOI: 10.1140/epjc/s10052-016-4227-1. arXiv: 1511.05170 [hep-ph].
- [159] John Ellis, Veronica Sanz, and Tevong You. “The Effective Standard Model after LHC Run I”. In: *JHEP* 03 (2015), p. 157. DOI: 10.1007/JHEP03(2015)157. arXiv: 1410.7703 [hep-ph].
- [160] Simone Alioli et al. “Catching a New Force by the Tail”. In: *Phys. Rev. Lett.* 120.10 (2018), p. 101801. DOI: 10.1103/PhysRevLett.120.101801. arXiv: 1712.02347 [hep-ph].
- [161] Simone Alioli et al. “NLO QCD corrections to SM-EFT dilepton and electroweak Higgs boson production, matched to parton shower in POWHEG”. In: *JHEP* 08 (2018), p. 205. DOI: 10.1007/JHEP08(2018)205. arXiv: 1804.07407 [hep-ph].
- [162] Stefan Alte, Matthias König, and William Shepherd. “Consistent Searches for SMEFT Effects in Non-Resonant Dijet Events”. In: *JHEP* 01 (2018), p. 094. DOI: 10.1007/JHEP01(2018)094. arXiv: 1711.07484 [hep-ph].
- [163] D. Barducci et al. “Interpreting top-quark LHC measurements in the standard-model effective field theory”. In: (Feb. 2018). Ed. by Juan Antonio Aguilar-Saavedra et al. arXiv: 1802.07237 [hep-ph].
- [164] Nuno Castro et al. “EFTfitter—A tool for interpreting measurements in the context of effective field theories”. In: *Eur. Phys. J. C* 76.8 (2016), p. 432. DOI: 10.1140/epjc/s10052-016-4280-9. arXiv: 1605.05585 [hep-ex].
- [165] Jorge de Blas et al. “Electroweak precision observables and Higgs-boson signal strengths in the Standard Model and beyond: present and future”. In: *JHEP* 12 (2016), p. 135. DOI: 10.1007/JHEP12(2016)135. arXiv: 1608.01509 [hep-ph].
- [166] John Ellis et al. “Updated Global SMEFT Fit to Higgs, Diboson and Electroweak Data”. In: *JHEP* 06 (2018), p. 146. DOI: 10.1007/JHEP06(2018)146. arXiv: 1803.03252 [hep-ph].
- [167] John Ellis, Veronica Sanz, and Tevong You. “Complete Higgs Sector Constraints on Dimension-6 Operators”. In: *JHEP* 07 (2014), p. 036. DOI: 10.1007/JHEP07(2014)036. arXiv: 1404.3667 [hep-ph].

- [168] Andy Buckley et al. “Results from TopFitter”. In: *PoS CKM2016* (2016), p. 127. DOI: 10.22323/1.291.0127. arXiv: 1612.02294 [hep-ph].
- [169] Anja Butter et al. “The Gauge-Higgs Legacy of the LHC Run I”. In: *JHEP* 07 (2016), p. 152. DOI: 10.1007/JHEP07(2016)152. arXiv: 1604.03105 [hep-ph].
- [170] Aleksandr Azatov et al. “Effective field theory analysis of double Higgs boson production via gluon fusion”. In: *Phys. Rev. D* 92.3 (2015), p. 035001. DOI: 10.1103/PhysRevD.92.035001. arXiv: 1502.00539 [hep-ph].
- [171] Anke Biekötter, Tyler Corbett, and Tilman Plehn. “The Gauge-Higgs Legacy of the LHC Run II”. In: *SciPost Phys.* 6.6 (2019), p. 064. DOI: 10.21468/SciPostPhys.6.6.064. arXiv: 1812.07587 [hep-ph].
- [172] Markus Schulze and Yotam Soreq. “Pinning down electroweak dipole operators of the top quark”. In: *Eur. Phys. J. C* 76.8 (2016), p. 466. DOI: 10.1140/epjc/s10052-016-4263-x. arXiv: 1603.08911 [hep-ph].
- [173] Eduardo da Silva Almeida et al. “Electroweak Sector Under Scrutiny: A Combined Analysis of LHC and Electroweak Precision Data”. In: *Phys. Rev. D* 99.3 (2019), p. 033001. DOI: 10.1103/PhysRevD.99.033001. arXiv: 1812.01009 [hep-ph].
- [174] Sabine Kraml et al. “Constraining new physics from Higgs measurements with Lilith: update to LHC Run 2 results”. In: *SciPost Phys.* 7.4 (2019), p. 052. DOI: 10.21468/SciPostPhys.7.4.052. arXiv: 1908.03952 [hep-ph].
- [175] Celine Degrande et al. “Non-resonant New Physics in Top Pair Production at Hadron Colliders”. In: *JHEP* 03 (2011), p. 125. DOI: 10.1007/JHEP03(2011)125. arXiv: 1010.6304 [hep-ph].
- [176] Steven Weinberg. “Baryon and Lepton Nonconserving Processes”. In: *Phys. Rev. Lett.* 43 (1979), pp. 1566–1570. DOI: 10.1103/PhysRevLett.43.1566.
- [177] Frank Wilczek and A. Zee. “Operator Analysis of Nucleon Decay”. In: *Phys. Rev. Lett.* 43 (1979), pp. 1571–1573. DOI: 10.1103/PhysRevLett.43.1571.
- [178] W. Buchmüller and D. Wyler. “Effective Lagrangian Analysis of New Interactions and Flavor Conservation”. In: *Nucl. Phys. B* 268 (1986), pp. 621–653. DOI: 10.1016/0550-3213(86)90262-2.
- [179] B. Grzadkowski et al. “Dimension-Six Terms in the Standard Model Lagrangian”. In: *JHEP* 10 (2010), p. 085. DOI: 10.1007/JHEP10(2010)085. arXiv: 1008.4884 [hep-ph].
- [180] L.F. Abbott and Mark B. Wise. “The Effective Hamiltonian for Nucleon Decay”. In: *Phys. Rev. D* 22 (1980), p. 2208. DOI: 10.1103/PhysRevD.22.2208.
- [181] Landon Lehman. “Extending the Standard Model Effective Field Theory with the Complete Set of Dimension-7 Operators”. In: *Phys. Rev. D* 90.12 (2014), p. 125023. DOI: 10.1103/PhysRevD.90.125023. arXiv: 1410.4193 [hep-ph].
- [182] Landon Lehman and Adam Martin. “Low-derivative operators of the Standard Model effective field theory via Hilbert series methods”. In: *JHEP* 02 (2016), p. 081. DOI: 10.1007/JHEP02(2016)081. arXiv: 1510.00372 [hep-ph].
- [183] Brian Henning et al. “2, 84, 30, 993, 560, 15456, 11962, 261485, ...: Higher dimension operators in the SM EFT”. In: *JHEP* 08 (2017). [Erratum: *JHEP* 09, 019 (2019)], p. 016. DOI: 10.1007/JHEP08(2017)016. arXiv: 1512.03433 [hep-ph].

- [184] Landon Lehman and Adam Martin. “Hilbert Series for Constructing Lagrangians: expanding the phenomenologist’s toolbox”. In: *Phys. Rev. D* 91 (2015), p. 105014. DOI: 10.1103/PhysRevD.91.105014. arXiv: 1503.07537 [hep-ph].
- [185] Brian Henning et al. “Hilbert series and operator bases with derivatives in effective field theories”. In: *Commun. Math. Phys.* 347.2 (2016), pp. 363–388. DOI: 10.1007/s00220-015-2518-2. arXiv: 1507.07240 [hep-th].
- [186] Andrew Kobach. “Baryon Number, Lepton Number, and Operator Dimension in the Standard Model”. In: *Phys. Lett. B* 758 (2016), pp. 455–457. DOI: 10.1016/j.physletb.2016.05.050. arXiv: 1604.05726 [hep-ph].
- [187] Celine Degrande et al. “Effective Field Theory: A Modern Approach to Anomalous Couplings”. In: *Annals Phys.* 335 (2013), pp. 21–32. DOI: 10.1016/j.aop.2013.04.016. arXiv: 1205.4231 [hep-ph].
- [188] Elizabeth E. Jenkins, Aneesh V. Manohar, and Michael Trott. “Renormalization Group Evolution of the Standard Model Dimension Six Operators I: Formalism and lambda Dependence”. In: *JHEP* 10 (2013), p. 087. DOI: 10.1007/JHEP10(2013)087. arXiv: 1308.2627 [hep-ph].
- [189] Elizabeth E. Jenkins, Aneesh V. Manohar, and Michael Trott. “Renormalization Group Evolution of the Standard Model Dimension Six Operators II: Yukawa Dependence”. In: *JHEP* 01 (2014), p. 035. DOI: 10.1007/JHEP01(2014)035. arXiv: 1310.4838 [hep-ph].
- [190] Rodrigo Alonso et al. “Renormalization Group Evolution of the Standard Model Dimension Six Operators III: Gauge Coupling Dependence and Phenomenology”. In: *JHEP* 04 (2014), p. 159. DOI: 10.1007/JHEP04(2014)159. arXiv: 1312.2014 [hep-ph].
- [191] Christophe Grojean et al. “Renormalization Group Scaling of Higgs Operators and $\Gamma(h \rightarrow \gamma\gamma)$ ”. In: *JHEP* 04 (2013), p. 016. DOI: 10.1007/JHEP04(2013)016. arXiv: 1301.2588 [hep-ph].
- [192] Rodrigo Alonso et al. “Renormalization group evolution of dimension-six baryon number violating operators”. In: *Phys. Lett. B* 734 (2014), pp. 302–307. DOI: 10.1016/j.physletb.2014.05.065. arXiv: 1405.0486 [hep-ph].
- [193] Frederick J. Gilman and Mark B. Wise. “Effective Hamiltonian for $\Delta s = 1$ Weak Nonleptonic Decays in the Six Quark Model”. In: *Phys. Rev. D* 20 (1979), p. 2392. DOI: 10.1103/PhysRevD.20.2392.
- [194] Kaoru Hagiwara et al. “Low-energy effects of new interactions in the electroweak boson sector”. In: *Phys. Rev. D* 48 (1993), pp. 2182–2203. DOI: 10.1103/PhysRevD.48.2182.
- [195] A.Yu. Morozov. “Matrix of mixing of scalar and vector mesons of dimension $D \leq 8$ in QCD. (IN RUSSIAN)”. In: *Sov. J. Nucl. Phys.* 40 (1984), p. 505.
- [196] Eric Braaten, Chong-Sheng Li, and Tzu-Chiang Yuan. “The Evolution of Weinberg’s Gluonic CP Violation Operator”. In: *Phys. Rev. Lett.* 64 (1990), p. 1709. DOI: 10.1103/PhysRevLett.64.1709.
- [197] Kaoru Hagiwara, R. Szalapski, and D. Zeppenfeld. “Anomalous Higgs boson production and decay”. In: *Phys. Lett. B* 318 (1993), pp. 155–162. DOI: 10.1016/0370-2693(93)91799-S. arXiv: hep-ph/9308347.

- [198] Cen Zhang and Fabio Maltoni. “Top-quark decay into Higgs boson and a light quark at next-to-leading order in QCD”. In: *Phys. Rev. D* 88 (2013), p. 054005. DOI: 10.1103/PhysRevD.88.054005. arXiv: 1305.7386 [hep-ph].
- [199] J. Elias-Miro et al. “Higgs windows to new physics through d=6 operators: constraints and one-loop anomalous dimensions”. In: *JHEP* 11 (2013), p. 066. DOI: 10.1007/JHEP11(2013)066. arXiv: 1308.1879 [hep-ph].
- [200] Guido Altarelli and L. Maiani. “Octet Enhancement of Nonleptonic Weak Interactions in Asymptotically Free Gauge Theories”. In: *Phys. Lett. B* 52 (1974), pp. 351–354. DOI: 10.1016/0370-2693(74)90060-4.
- [201] Mikhail A. Shifman, A.I. Vainshtein, and Valentin I. Zakharov. “Nonleptonic Decays of K Mesons and Hyperons”. In: *Sov. Phys. JETP* 45 (1977), p. 670.
- [202] E.G. Floratos, D.A. Ross, and Christopher T. Sachrajda. “Higher Order Effects in Asymptotically Free Gauge Theories. 2. Flavor Singlet Wilson Operators and Coefficient Functions”. In: *Nucl. Phys. B* 152 (1979), pp. 493–520. DOI: 10.1016/0550-3213(79)90094-4.
- [203] Frederick J. Gilman and Mark B. Wise. “ $K \rightarrow \pi e^+ e^-$ in the Six Quark Model”. In: *Phys. Rev. D* 21 (1980), p. 3150. DOI: 10.1103/PhysRevD.21.3150.
- [204] Frederick J. Gilman and Mark B. Wise. “ $K^0 - \bar{K}^0$ mixing in the Six Quark Model”. In: *Phys. Rev. D* 27 (1983), p. 1128. DOI: 10.1103/PhysRevD.27.1128.
- [205] Benjamin Grinstein, Roxanne P. Springer, and Mark B. Wise. “Strong Interaction Effects in Weak Radiative \bar{B} Meson Decay”. In: *Nucl. Phys. B* 339 (1990), pp. 269–309. DOI: 10.1016/0550-3213(90)90350-M.
- [206] William A. Bardeen et al. “Deep Inelastic Scattering Beyond the Leading Order in Asymptotically Free Gauge Theories”. In: *Phys. Rev. D* 18 (1978), p. 3998. DOI: 10.1103/PhysRevD.18.3998.
- [207] Andrzej J. Buras, Matthias Jamin, and Peter H. Weisz. “Leading and Next-to-leading QCD Corrections to ϵ Parameter and $B^0 - \bar{B}^0$ Mixing in the Presence of a Heavy Top Quark”. In: *Nucl. Phys. B* 347 (1990), pp. 491–536. DOI: 10.1016/0550-3213(90)90373-L.
- [208] Gerhard Buchalla, Andrzej J. Buras, and Michaela K. Harlander. “The Anatomy of Epsilon-prime / Epsilon in the Standard Model”. In: *Nucl. Phys. B* 337 (1990), pp. 313–362. DOI: 10.1016/0550-3213(90)90275-I.
- [209] Marco Ciuchini et al. “The $\Delta S = 1$ effective Hamiltonian including next-to-leading order QCD and QED corrections”. In: *Nucl. Phys. B* 415 (1994), pp. 403–462. DOI: 10.1016/0550-3213(94)90118-X. arXiv: hep-ph/9304257.
- [210] C. Arzt, M.B. Einhorn, and J. Wudka. “Effective Lagrangian approach to precision measurements: The Anomalous magnetic moment of the muon”. In: *Phys. Rev. D* 49 (1994), pp. 1370–1377. DOI: 10.1103/PhysRevD.49.1370. arXiv: hep-ph/9304206.
- [211] Giuseppe Degrossi et al. “QCD corrections to the electric dipole moment of the neutron in the MSSM”. In: *JHEP* 11 (2005), p. 044. DOI: 10.1088/1126-6708/2005/11/044. arXiv: hep-ph/0510137.
- [212] Jun Gao, Chong Sheng Li, and C.P. Yuan. “NLO QCD Corrections to dijet Production via Quark Contact Interactions”. In: *JHEP* 07 (2012), p. 037. DOI: 10.1007/JHEP07(2012)037. arXiv: 1204.4773 [hep-ph].

- [213] Harrison Mebane et al. “Effective Field Theory of Precision Electroweak Physics at One Loop”. In: *Phys. Lett. B* 724 (2013), pp. 259–263. DOI: 10.1016/j.physletb.2013.06.021. arXiv: 1304.1789 [hep-ph].
- [214] Harrison Mebane et al. “Constraints on Electroweak Effective Operators at One Loop”. In: *Phys. Rev. D* 88.1 (2013), p. 015028. DOI: 10.1103/PhysRevD.88.015028. arXiv: 1306.3380 [hep-ph].
- [215] Aneesh Manohar and Howard Georgi. “Chiral Quarks and the Nonrelativistic Quark Model”. In: *Nucl. Phys. B* 234 (1984), pp. 189–212. DOI: 10.1016/0550-3213(84)90231-1.
- [216] Elizabeth E. Jenkins, Aneesh V. Manohar, and Michael Trott. “Naive Dimensional Analysis Counting of Gauge Theory Amplitudes and Anomalous Dimensions”. In: *Phys. Lett. B* 726 (2013), pp. 697–702. DOI: 10.1016/j.physletb.2013.09.020. arXiv: 1309.0819 [hep-ph].
- [217] Margherita Ghezzi et al. “NLO Higgs effective field theory and κ -framework”. In: *JHEP* 07 (2015), p. 175. DOI: 10.1007/JHEP07(2015)175. arXiv: 1505.03706 [hep-ph].
- [218] Rhorry Gauld, Benjamin D. Pecjak, and Darren J. Scott. “One-loop corrections to $h \rightarrow b\bar{b}$ and $h \rightarrow \tau\bar{\tau}$ decays in the Standard Model Dimension-6 EFT: four-fermion operators and the large- m_t limit”. In: *JHEP* 05 (2016), p. 080. DOI: 10.1007/JHEP05(2016)080. arXiv: 1512.02508 [hep-ph].
- [219] Rhorry Gauld, Benjamin D. Pecjak, and Darren J. Scott. “QCD radiative corrections for $h \rightarrow b\bar{b}$ in the Standard Model Dimension-6 EFT”. In: *Phys. Rev. D* 94.7 (2016), p. 074045. DOI: 10.1103/PhysRevD.94.074045. arXiv: 1607.06354 [hep-ph].
- [220] Christine Hartmann, William Shepherd, and Michael Trott. “The Z decay width in the SMEFT: y_t and λ corrections at one loop”. In: *JHEP* 03 (2017), p. 060. DOI: 10.1007/JHEP03(2017)060. arXiv: 1611.09879 [hep-ph].
- [221] Jason Aebischer et al. “Matching of gauge invariant dimension-six operators for $b \rightarrow s$ and $b \rightarrow c$ transitions”. In: *JHEP* 05 (2016), p. 037. DOI: 10.1007/JHEP05(2016)037. arXiv: 1512.02830 [hep-ph].
- [222] Patrick J. Fox et al. “Deciphering top flavor violation at the LHC with B factories”. In: *Phys. Rev. D* 78 (2008), p. 054008. DOI: 10.1103/PhysRevD.78.054008. arXiv: 0704.1482 [hep-ph].
- [223] Rigo Bause et al. “Lepton universality and lepton flavor conservation tests with dineutrino modes”. In: (July 2020). arXiv: 2007.05001 [hep-ph].
- [224] Celine Degrande et al. “Single-top associated production with a Z or H boson at the LHC: the SMEFT interpretation”. In: *JHEP* 10 (2018), p. 005. DOI: 10.1007/JHEP10(2018)005. arXiv: 1804.07773 [hep-ph].
- [225] Mikael Chala, Jose Santiago, and Michael Spannowsky. “Constraining four-fermion operators using rare top decays”. In: *JHEP* 04 (2019), p. 014. DOI: 10.1007/JHEP04(2019)014. arXiv: 1809.09624 [hep-ph].
- [226] Gauthier Durieux, Fabio Maltoni, and Cen Zhang. “Global approach to top-quark flavor-changing interactions”. In: *Phys. Rev. D* 91.7 (2015), p. 074017. DOI: 10.1103/PhysRevD.91.074017. arXiv: 1412.7166 [hep-ph].

- [227] J.A. Aguilar-Saavedra. “Effective four-fermion operators in top physics: A Roadmap”. In: *Nucl. Phys. B* 843 (2011). [Erratum: *Nucl.Phys.B* 851, 443–444 (2011)], pp. 638–672. DOI: 10.1016/j.nuclphysb.2011.06.003. arXiv: 1008.3562 [hep-ph].
- [228] Jorgen D’Hondt et al. “Learning to pinpoint effective operators at the LHC: a study of the $t\bar{t}b\bar{b}$ signature”. In: *JHEP* 11 (2018), p. 131. DOI: 10.1007/JHEP11(2018)131. arXiv: 1807.02130 [hep-ph].
- [229] Gauthier Durieux et al. “Probing top-quark couplings indirectly at Higgs factories”. In: *Chin. Phys. C* 42.12 (2018), p. 123107. DOI: 10.1088/1674-1137/42/12/123107. arXiv: 1809.03520 [hep-ph].
- [230] Andy Buckley et al. “Global fit of top quark effective theory to data”. In: *Phys. Rev. D* 92.9 (2015), p. 091501. DOI: 10.1103/PhysRevD.92.091501. arXiv: 1506.08845 [hep-ph].
- [231] Andy Buckley et al. “Constraining top quark effective theory in the LHC Run II era”. In: *JHEP* 04 (2016), p. 015. DOI: 10.1007/JHEP04(2016)015. arXiv: 1512.03360 [hep-ph].
- [232] M. de Beurs et al. “Effective operators in t -channel single top production and decay”. In: *Eur. Phys. J. C* 78.11 (2018), p. 919. DOI: 10.1140/epjc/s10052-018-6399-3. arXiv: 1807.03576 [hep-ph].
- [233] Stephen Brown et al. “TopFitter: Fitting top-quark Wilson Coefficients to Run II data”. In: *PoS ICHEP2018* (2019), p. 293. DOI: 10.22323/1.340.0293. arXiv: 1901.03164 [hep-ph].
- [234] Nathan P. Hartland et al. “A Monte Carlo global analysis of the Standard Model Effective Field Theory: the top quark sector”. In: *JHEP* 04 (2019), p. 100. DOI: 10.1007/JHEP04(2019)100. arXiv: 1901.05965 [hep-ph].
- [235] Fabio Maltoni, Luca Mantani, and Ken Mimasu. “Top-quark electroweak interactions at high energy”. In: *JHEP* 10 (2019), p. 004. DOI: 10.1007/JHEP10(2019)004. arXiv: 1904.05637 [hep-ph].
- [236] Tobias Neumann and Zack Edward Sullivan. “Off-Shell Single-Top-Quark Production in the Standard Model Effective Field Theory”. In: *JHEP* 06 (2019), p. 022. DOI: 10.1007/JHEP06(2019)022. arXiv: 1903.11023 [hep-ph].
- [237] Ilaria Brivio et al. “O new physics, where art thou? A global search in the top sector”. In: *JHEP* 02 (2020), p. 131. DOI: 10.1007/JHEP02(2020)131. arXiv: 1910.03606 [hep-ph].
- [238] Jeff Asaf Dror et al. “Strong tW Scattering at the LHC”. In: *JHEP* 01 (2016), p. 071. DOI: 10.1007/JHEP01(2016)071. arXiv: 1511.03674 [hep-ph].
- [239] Aleksandr Azatov et al. “Helicity selection rules and noninterference for BSM amplitudes”. In: *Phys. Rev. D* 95.6 (2017), p. 065014. DOI: 10.1103/PhysRevD.95.065014. arXiv: 1607.05236 [hep-ph].
- [240] Roberto Contino. “The Higgs as a Composite Nambu-Goldstone Boson”. In: *Theoretical Advanced Study Institute in Elementary Particle Physics: Physics of the Large and the Small*. 2011, pp. 235–306. DOI: 10.1142/9789814327183_0005. arXiv: 1005.4269 [hep-ph].
- [241] Roberto Contino et al. “Strong Double Higgs Production at the LHC”. In: *JHEP* 05 (2010), p. 089. DOI: 10.1007/JHEP05(2010)089. arXiv: 1002.1011 [hep-ph].

- [242] Roberto Contino et al. “Strong Higgs Interactions at a Linear Collider”. In: *JHEP* 02 (2014), p. 006. DOI: 10.1007/JHEP02(2014)006. arXiv: 1309.7038 [hep-ph].
- [243] Sidney R. Coleman, J. Wess, and Bruno Zumino. “Structure of phenomenological Lagrangians. 1.” In: *Phys. Rev.* 177 (1969), pp. 2239–2247. DOI: 10.1103/PhysRev.177.2239.
- [244] Jr. Callan Curtis G. et al. “Structure of phenomenological Lagrangians. 2.” In: *Phys. Rev.* 177 (1969), pp. 2247–2250. DOI: 10.1103/PhysRev.177.2247.
- [245] F. Feruglio. “The Chiral approach to the electroweak interactions”. In: *Int. J. Mod. Phys. A* 8 (1993), pp. 4937–4972. DOI: 10.1142/S0217751X93001946. arXiv: hep-ph/9301281.
- [246] Benjamin Grinstein and Michael Trott. “A Higgs-Higgs bound state due to new physics at a TeV”. In: *Phys. Rev. D* 76 (2007), p. 073002. DOI: 10.1103/PhysRevD.76.073002. arXiv: 0704.1505 [hep-ph].
- [247] C.P. Burgess, J. Matias, and M. Pospelov. “A Higgs or not a Higgs? What to do if you discover a new scalar particle”. In: *Int. J. Mod. Phys. A* 17 (2002), pp. 1841–1918. DOI: 10.1142/S0217751X02009813. arXiv: hep-ph/9912459.
- [248] Riccardo Barbieri et al. “The Higgs boson from an extended symmetry”. In: *Phys. Rev. D* 76 (2007), p. 115008. DOI: 10.1103/PhysRevD.76.115008. arXiv: 0706.0432 [hep-ph].
- [249] P. Hernandez-Leon and L. Merlo. “Distinguishing A Higgs-Like Dilaton Scenario With A Complete Bosonic Effective Field Theory Basis”. In: *Phys. Rev. D* 96.7 (2017), p. 075008. DOI: 10.1103/PhysRevD.96.075008. arXiv: 1703.02064 [hep-ph].
- [250] Luca Merlo, Sara Saa, and Mario Sacristán-Barbero. “Baryon Non-Invariant Couplings in Higgs Effective Field Theory”. In: *Eur. Phys. J. C* 77.3 (2017), p. 185. DOI: 10.1140/epjc/s10052-017-4753-5. arXiv: 1612.04832 [hep-ph].
- [251] M.B. Gavela et al. “The linear–non-linear frontier for the Goldstone Higgs”. In: *Eur. Phys. J. C* 76.12 (2016), p. 690. DOI: 10.1140/epjc/s10052-016-4541-7. arXiv: 1610.08083 [hep-ph].
- [252] I. Brivio et al. “The complete HEFT Lagrangian after the LHC Run I”. In: *Eur. Phys. J. C* 76.7 (2016), p. 416. DOI: 10.1140/epjc/s10052-016-4211-9. arXiv: 1604.06801 [hep-ph].
- [253] G. Buchalla et al. “Fitting Higgs Data with Nonlinear Effective Theory”. In: *Eur. Phys. J. C* 76.5 (2016), p. 233. DOI: 10.1140/epjc/s10052-016-4086-9. arXiv: 1511.00988 [hep-ph].
- [254] I.M. Hierro, L. Merlo, and S. Rigolin. “Sigma Decomposition: The CP-Odd Lagrangian”. In: *JHEP* 04 (2016), p. 016. DOI: 10.1007/JHEP04(2016)016. arXiv: 1510.07899 [hep-ph].
- [255] G. Buchalla et al. “Note on Anomalous Higgs-Boson Couplings in Effective Field Theory”. In: *Phys. Lett. B* 750 (2015), pp. 298–301. DOI: 10.1016/j.physletb.2015.09.027. arXiv: 1504.01707 [hep-ph].
- [256] Rodrigo Alonso et al. “Sigma Decomposition”. In: *JHEP* 12 (2014), p. 034. DOI: 10.1007/JHEP12(2014)034. arXiv: 1409.1589 [hep-ph].

- [257] M.B. Gavela et al. “On the renormalization of the electroweak chiral Lagrangian with a Higgs”. In: *JHEP* 03 (2015), p. 043. DOI: 10.1007/JHEP03(2015)043. arXiv: 1409.1571 [hep-ph].
- [258] M.B. Gavela et al. “CP violation with a dynamical Higgs”. In: *JHEP* 10 (2014), p. 044. DOI: 10.1007/JHEP10(2014)044. arXiv: 1406.6367 [hep-ph].
- [259] I. Brivio et al. “Higgs ultraviolet softening”. In: *JHEP* 12 (2014), p. 004. DOI: 10.1007/JHEP12(2014)004. arXiv: 1405.5412 [hep-ph].
- [260] I. Brivio et al. “Disentangling a dynamical Higgs”. In: *JHEP* 03 (2014), p. 024. DOI: 10.1007/JHEP03(2014)024. arXiv: 1311.1823 [hep-ph].
- [261] Gerhard Buchalla, Oscar Cata, and Giancarlo D’Ambrosio. “Nonstandard Higgs couplings from angular distributions in $h \rightarrow Z\ell^+\ell^-$ ”. In: *Eur. Phys. J. C* 74.3 (2014), p. 2798. DOI: 10.1140/epjc/s10052-014-2798-2. arXiv: 1310.2574 [hep-ph].
- [262] Gerhard Buchalla, Oscar Catà, and Claudius Krause. “Complete Electroweak Chiral Lagrangian with a Light Higgs at NLO”. In: *Nucl. Phys. B* 880 (2014). [Erratum: *Nucl.Phys.B* 913, 475–478 (2016)], pp. 552–573. DOI: 10.1016/j.nuclphysb.2014.01.018. arXiv: 1307.5017 [hep-ph].
- [263] R. Alonso et al. “Flavor with a light dynamical ”Higgs particle””. In: *Phys. Rev. D* 87.5 (2013), p. 055019. DOI: 10.1103/PhysRevD.87.055019. arXiv: 1212.3307 [hep-ph].
- [264] R. Alonso et al. “The Effective Chiral Lagrangian for a Light Dynamical ”Higgs Particle””. In: *Phys. Lett. B* 722 (2013). [Erratum: *Phys.Lett.B* 726, 926 (2013)], pp. 330–335. DOI: 10.1016/j.physletb.2013.04.037. arXiv: 1212.3305 [hep-ph].
- [265] Gerhard Buchalla and Oscar Cata. “Effective Theory of a Dynamically Broken Electroweak Standard Model at NLO”. In: *JHEP* 07 (2012), p. 101. DOI: 10.1007/JHEP07(2012)101. arXiv: 1203.6510 [hep-ph].
- [266] Steven Weinberg. “Implications of Dynamical Symmetry Breaking”. In: *Phys. Rev. D* 13 (1976). [Addendum: *Phys.Rev.D* 19, 1277–1280 (1979)], pp. 974–996. DOI: 10.1103/PhysRevD.19.1277.
- [267] Leonard Susskind. “Dynamics of Spontaneous Symmetry Breaking in the Weinberg-Salam Theory”. In: *Phys. Rev. D* 20 (1979), pp. 2619–2625. DOI: 10.1103/PhysRevD.20.2619.
- [268] Savas Dimopoulos and John Preskill. “Massless Composites With Massive Constituents”. In: *Nucl. Phys. B* 199 (1982), pp. 206–222. DOI: 10.1016/0550-3213(82)90345-5.
- [269] David B. Kaplan and Howard Georgi. “SU(2) x U(1) Breaking by Vacuum Misalignment”. In: *Phys. Lett. B* 136 (1984), pp. 183–186. DOI: 10.1016/0370-2693(84)91177-8.
- [270] David B. Kaplan, Howard Georgi, and Savas Dimopoulos. “Composite Higgs Scalars”. In: *Phys. Lett. B* 136 (1984), pp. 187–190. DOI: 10.1016/0370-2693(84)91178-X.
- [271] Howard Georgi, David B. Kaplan, and Peter Galison. “Calculation of the Composite Higgs Mass”. In: *Phys. Lett. B* 143 (1984), pp. 152–154. DOI: 10.1016/0370-2693(84)90823-2.
- [272] Tom Banks. “CONSTRAINTS ON SU(2) x U(1) BREAKING BY VACUUM MISALIGNMENT”. In: *Nucl. Phys. B* 243 (1984), pp. 125–130. DOI: 10.1016/0550-3213(84)90389-4.

- [273] Howard Georgi and David B. Kaplan. “Composite Higgs and Custodial SU(2)”. In: *Phys. Lett. B* 145 (1984), pp. 216–220. DOI: 10.1016/0370-2693(84)90341-1.
- [274] Michael J. Dugan, Howard Georgi, and David B. Kaplan. “Anatomy of a Composite Higgs Model”. In: *Nucl. Phys. B* 254 (1985), pp. 299–326. DOI: 10.1016/0550-3213(85)90221-4.
- [275] Ilaria Brivio and Michael Trott. “The Standard Model as an Effective Field Theory”. In: *Phys. Rept.* 793 (2019), pp. 1–98. DOI: 10.1016/j.physrep.2018.11.002. arXiv: 1706.08945 [hep-ph].
- [276] Allen Caldwell, Daniel Kollar, and Kevin Kroninger. “BAT: The Bayesian Analysis Toolkit”. In: *Comput. Phys. Commun.* 180 (2009), pp. 2197–2209. DOI: 10.1016/j.cpc.2009.06.026. arXiv: 0808.2552 [physics.data-an].
- [277] Oliver Schulz et al. “BAT.jl – A Julia-based tool for Bayesian inference”. In: (Aug. 2020). arXiv: 2008.03132 [stat.CO].
- [278] Rev. Bayes Thomas. “An essay toward solving a problem in the doctrine of chances”. In: *Phil. Trans. Roy. Soc. Lond.* 53 (1764), pp. 370–418. DOI: 10.1098/rstl.1763.0053.
- [279] Morad Aaboud et al. “Combinations of single-top-quark production cross-section measurements and $|f_{LV}V_{tb}|$ determinations at $\sqrt{s} = 7$ and 8 TeV with the ATLAS and CMS experiments”. In: *JHEP* 05 (2019), p. 088. DOI: 10.1007/JHEP05(2019)088. arXiv: 1902.07158 [hep-ex].
- [280] Georges Aad et al. “Comprehensive measurements of t -channel single top-quark production cross sections at $\sqrt{s} = 7$ TeV with the ATLAS detector”. In: *Phys. Rev. D* 90.11 (2014), p. 112006. DOI: 10.1103/PhysRevD.90.112006. arXiv: 1406.7844 [hep-ex].
- [281] Morad Aaboud et al. “Fiducial, total and differential cross-section measurements of t -channel single top-quark production in pp collisions at 8 TeV using data collected by the ATLAS detector”. In: *Eur. Phys. J. C* 77.8 (2017), p. 531. DOI: 10.1140/epjc/s10052-017-5061-9. arXiv: 1702.02859 [hep-ex].
- [282] Morad Aaboud et al. “Measurement of the inclusive cross-sections of single top-quark and top-antiquark t -channel production in pp collisions at $\sqrt{s} = 13$ TeV with the ATLAS detector”. In: *JHEP* 04 (2017), p. 086. DOI: 10.1007/JHEP04(2017)086. arXiv: 1609.03920 [hep-ex].
- [283] Morad Aaboud et al. “Direct top-quark decay width measurement in the $t\bar{t}$ lepton+jets channel at $\sqrt{s}=8$ TeV with the ATLAS experiment”. In: *Eur. Phys. J. C* 78.2 (2018), p. 129. DOI: 10.1140/epjc/s10052-018-5595-5. arXiv: 1709.04207 [hep-ex].
- [284] Georges Aad et al. “Measurement of the W boson polarization in top quark decays with the ATLAS detector”. In: *JHEP* 06 (2012), p. 088. DOI: 10.1007/JHEP06(2012)088. arXiv: 1205.2484 [hep-ex].
- [285] Morad Aaboud et al. “Measurement of the W boson polarisation in $t\bar{t}$ events from pp collisions at $\sqrt{s} = 8$ TeV in the lepton + jets channel with ATLAS”. In: *Eur. Phys. J. C* 77.4 (2017). [Erratum: Eur.Phys.J.C 79, 19 (2019)], p. 264. DOI: 10.1140/epjc/s10052-017-4819-4. arXiv: 1612.02577 [hep-ex].
- [286] Serguei Chatrchyan et al. “Measurement of the Single-Top-Quark t -Channel Cross Section in pp Collisions at $\sqrt{s} = 7$ TeV”. In: *JHEP* 12 (2012), p. 035. DOI: 10.1007/JHEP12(2012)035. arXiv: 1209.4533 [hep-ex].

- [287] Vardan Khachatryan et al. “Measurement of the t-channel single-top-quark production cross section and of the $|V_{tb}|$ CKM matrix element in pp collisions at $\sqrt{s} = 8$ TeV”. In: *JHEP* 06 (2014), p. 090. DOI: 10.1007/JHEP06(2014)090. arXiv: 1403.7366 [hep-ex].
- [288] Albert M Sirunyan et al. “Cross section measurement of t-channel single top quark production in pp collisions at $\sqrt{s} = 13$ TeV”. In: *Phys. Lett. B* 772 (2017), pp. 752–776. DOI: 10.1016/j.physletb.2017.07.047. arXiv: 1610.00678 [hep-ex].
- [289] CMS. “Single top t-channel differential cross section at 8 TeV”. In: *CMS-PAS-TOP-14-004* (Oct. 2014).
- [290] CMS. “Measurement of the differential cross section for t-channel single-top-quark production at $\sqrt{s} = 13$ TeV”. In: *CMS-PAS-TOP-16-004* (May 2016).
- [291] Serguei Chatrchyan et al. “Measurement of the W-Boson Helicity in Top-Quark decays from $t\bar{t}$ Production in Lepton + Jets Events in pp Collisions at $\sqrt{s} = 7$ TeV”. In: *JHEP* 10 (2013), p. 167. DOI: 10.1007/JHEP10(2013)167. arXiv: 1308.3879 [hep-ex].
- [292] Vardan Khachatryan et al. “Measurement of the W boson helicity in events with a single reconstructed top quark in pp collisions at $\sqrt{s} = 8$ TeV”. In: *JHEP* 01 (2015), p. 053. DOI: 10.1007/JHEP01(2015)053. arXiv: 1410.1154 [hep-ex].
- [293] Vardan Khachatryan et al. “Measurement of the W boson helicity fractions in the decays of top quark pairs to lepton + jets final states produced in pp collisions at $\sqrt{s} = 8$ TeV”. In: *Phys. Lett. B* 762 (2016), pp. 512–534. DOI: 10.1016/j.physletb.2016.10.007. arXiv: 1605.09047 [hep-ex].
- [294] T. Aaltonen et al. “Measurement of W-Boson Polarization in Top-quark Decay in $p\bar{p}$ Collisions at $\sqrt{s} = 1.96$ TeV”. In: *Phys. Rev. Lett.* 105 (2010), p. 042002. DOI: 10.1103/PhysRevLett.105.042002. arXiv: 1003.0224 [hep-ex].
- [295] T. Aaltonen et al. “Measurement of W-Boson Polarization in Top-quark Decay using the Full CDF Run II Data Set”. In: *Phys. Rev. D* 87.3 (2013), p. 031104. DOI: 10.1103/PhysRevD.87.031104. arXiv: 1211.4523 [hep-ex].
- [296] Victor Mukhamedovich Abazov et al. “Measurement of the W Boson Helicity in Top Quark Decays using 5.4 fb⁻¹ of $p\bar{p}$ Collision Data”. In: *Phys. Rev. D* 83 (2011), p. 032009. DOI: 10.1103/PhysRevD.83.032009. arXiv: 1011.6549 [hep-ex].
- [297] Celine Degrande et al. “UFO - The Universal FeynRules Output”. In: *Comput. Phys. Commun.* 183 (2012), pp. 1201–1214. DOI: 10.1016/j.cpc.2012.01.022. arXiv: 1108.2040 [hep-ph].
- [298] J. Alwall et al. “The automated computation of tree-level and next-to-leading order differential cross sections, and their matching to parton shower simulations”. In: *JHEP* 07 (2014), p. 079. DOI: 10.1007/JHEP07(2014)079. arXiv: 1405.0301 [hep-ph].
- [299] A.D. Martin et al. “Parton distributions for the LHC”. In: *Eur. Phys. J. C* 63 (2009), pp. 189–285. DOI: 10.1140/epjc/s10052-009-1072-5. arXiv: 0901.0002 [hep-ph].
- [300] Hung-Liang Lai et al. “New parton distributions for collider physics”. In: *Phys. Rev. D* 82 (2010), p. 074024. DOI: 10.1103/PhysRevD.82.074024. arXiv: 1007.2241 [hep-ph].
- [301] Richard D. Ball et al. “Parton distributions with QED corrections”. In: *Nucl. Phys. B* 877 (2013), pp. 290–320. DOI: 10.1016/j.nuclphysb.2013.10.010. arXiv: 1308.0598 [hep-ph].

- [302] Cen Zhang. “Effective field theory approach to top-quark decay at next-to-leading order in QCD”. In: *Phys. Rev. D* 90.1 (2014), p. 014008. DOI: 10.1103/PhysRevD.90.014008. arXiv: 1404.1264 [hep-ph].
- [303] Andrzej Czarnecki, Jurgen G. Korner, and Jan H. Piclum. “Helicity fractions of W bosons from top quark decays at NNLO in QCD”. In: *Phys. Rev. D* 81 (2010), p. 111503. DOI: 10.1103/PhysRevD.81.111503. arXiv: 1005.2625 [hep-ph].
- [304] Jun Gao, Chong Sheng Li, and Hua Xing Zhu. “Top Quark Decay at Next-to-Next-to-Leading Order in QCD”. In: *Phys. Rev. Lett.* 110.4 (2013), p. 042001. DOI: 10.1103/PhysRevLett.110.042001. arXiv: 1210.2808 [hep-ph].
- [305] Cen Zhang and Scott Willenbrock. “Effective-Field-Theory Approach to Top-Quark Production and Decay”. In: *Phys. Rev. D* 83 (2011), p. 034006. DOI: 10.1103/PhysRevD.83.034006. arXiv: 1008.3869 [hep-ph].
- [306] G. Apollinari et al. “High-Luminosity Large Hadron Collider (HL-LHC): Technical Design Report V. 0.1”. In: *CERN Yellow Report: Monographs 4/2017* (Nov. 2017). DOI: 10.23731/CYRM-2017-004.
- [307] Bohdan Grzadkowski and Mikolaj Misiak. “Anomalous Wtb coupling effects in the weak radiative B-meson decay”. In: *Phys. Rev. D* 78 (2008). [Erratum: Phys.Rev.D 84, 059903 (2011)], p. 077501. DOI: 10.1103/PhysRevD.78.077501. arXiv: 0802.1413 [hep-ph].
- [308] Jure Drobnak, Svjetlana Fajfer, and Jernej F. Kamenik. “Probing anomalous tWb interactions with rare B decays”. In: *Nucl. Phys. B* 855 (2012), pp. 82–99. DOI: 10.1016/j.nuclphysb.2011.10.004. arXiv: 1109.2357 [hep-ph].
- [309] P.A. Zyla et al. “Review of Particle Physics”. In: *PTEP* 2020.8 (2020), p. 083C01. DOI: 10.1093/ptep/ptaa104.
- [310] Gudrun Hiller. “A Challenge to Lepton Universality”. In: *APS Physics* 7 (2014), p. 102. DOI: 10.1103/physics.7.102.
- [311] A.J. Buras et al. “Theoretical uncertainties and phenomenological aspects of $B \rightarrow X(s) \gamma$ decay”. In: *Nucl. Phys. B* 424 (1994), pp. 374–398. DOI: 10.1016/0550-3213(94)90299-2. arXiv: hep-ph/9311345.
- [312] Christoph Greub, Tobias Hurth, and Daniel Wyler. “Virtual corrections to the decay $b \rightarrow s \gamma$ ”. In: *Phys. Lett. B* 380 (1996), pp. 385–392. DOI: 10.1016/0370-2693(96)00496-0. arXiv: hep-ph/9602281.
- [313] Morad Aaboud et al. “Measurements of inclusive and differential fiducial cross-sections of $t\bar{t}\gamma$ production in leptonic final states at $\sqrt{s} = 13$ TeV in ATLAS”. In: *Eur. Phys. J. C* 79.5 (2019), p. 382. DOI: 10.1140/epjc/s10052-019-6849-6. arXiv: 1812.01697 [hep-ex].
- [314] Kirill Melnikov, Markus Schulze, and Andreas Scharf. “QCD corrections to top quark pair production in association with a photon at hadron colliders”. In: *Phys. Rev. D* 83 (2011), p. 074013. DOI: 10.1103/PhysRevD.83.074013. arXiv: 1102.1967 [hep-ph].
- [315] Yasmine Sara Amhis et al. “Averages of b -hadron, c -hadron, and τ -lepton properties as of 2018”. In: (2019). updated results and plots available at <https://hflav.web.cern.ch/>. arXiv: 1909.12524 [hep-ex].

- [316] M. Misiak et al. “Updated NNLO QCD predictions for the weak radiative B-meson decays”. In: *Phys. Rev. Lett.* 114.22 (2015), p. 221801. DOI: 10.1103/PhysRevLett.114.221801. arXiv: 1503.01789 [hep-ph].
- [317] Georges Aad et al. “Observation of top-quark pair production in association with a photon and measurement of the $t\bar{t}\gamma$ production cross section in pp collisions at $\sqrt{s} = 7$ TeV using the ATLAS detector”. In: *Phys. Rev. D* 91.7 (2015), p. 072007. DOI: 10.1103/PhysRevD.91.072007. arXiv: 1502.00586 [hep-ex].
- [318] Morad Aaboud et al. “Measurement of the $t\bar{t}\gamma$ production cross section in proton-proton collisions at $\sqrt{s} = 8$ TeV with the ATLAS detector”. In: *JHEP* 11 (2017), p. 086. DOI: 10.1007/JHEP11(2017)086. arXiv: 1706.03046 [hep-ex].
- [319] Albert M Sirunyan et al. “Measurement of the semileptonic $t\bar{t} + \gamma$ production cross section in pp collisions at $\sqrt{s} = 8$ TeV”. In: *JHEP* 10 (2017), p. 006. DOI: 10.1007/JHEP10(2017)006. arXiv: 1706.08128 [hep-ex].
- [320] A. Limosani et al. “Measurement of Inclusive Radiative B-meson Decays with a Photon Energy Threshold of 1.7-GeV”. In: *Phys. Rev. Lett.* 103 (2009), p. 241801. DOI: 10.1103/PhysRevLett.103.241801. arXiv: 0907.1384 [hep-ex].
- [321] T. Saito et al. “Measurement of the $\bar{B} \rightarrow X_s\gamma$ Branching Fraction with a Sum of Exclusive Decays”. In: *Phys. Rev. D* 91.5 (2015), p. 052004. DOI: 10.1103/PhysRevD.91.052004. arXiv: 1411.7198 [hep-ex].
- [322] A. Abdesselam et al. “Measurement of the inclusive $B \rightarrow X_{s+d}\gamma$ branching fraction, photon energy spectrum and HQE parameters”. In: *38th International Conference on High Energy Physics*. Aug. 2016. arXiv: 1608.02344 [hep-ex].
- [323] Bernard Aubert et al. “Measurement of the $B \rightarrow X_s\gamma$ branching fraction and photon energy spectrum using the recoil method”. In: *Phys. Rev. D* 77 (2008), p. 051103. DOI: 10.1103/PhysRevD.77.051103. arXiv: 0711.4889 [hep-ex].
- [324] J.P. Lees et al. “Precision Measurement of the $B \rightarrow X_s\gamma$ Photon Energy Spectrum, Branching Fraction, and Direct CP Asymmetry $A_{CP}(B \rightarrow X_{s+d}\gamma)$ ”. In: *Phys. Rev. Lett.* 109 (2012), p. 191801. DOI: 10.1103/PhysRevLett.109.191801. arXiv: 1207.2690 [hep-ex].
- [325] J.P. Lees et al. “Exclusive Measurements of $b \rightarrow s\gamma$ Transition Rate and Photon Energy Spectrum”. In: *Phys. Rev. D* 86 (2012), p. 052012. DOI: 10.1103/PhysRevD.86.052012. arXiv: 1207.2520 [hep-ex].
- [326] S. Chen et al. “Branching fraction and photon energy spectrum for $b \rightarrow s\gamma$ ”. In: *Phys. Rev. Lett.* 87 (2001), p. 251807. DOI: 10.1103/PhysRevLett.87.251807. arXiv: hep-ex/0108032.
- [327] Y. Amhis et al. “Averages of b -hadron, c -hadron, and τ -lepton properties as of summer 2016”. In: *Eur. Phys. J. C* 77.12 (2017), p. 895. DOI: 10.1140/epjc/s10052-017-5058-4. arXiv: 1612.07233 [hep-ex].
- [328] Oliver Buchmuller and Henning Flacher. “Fit to moment from $B \rightarrow X_c\ell\bar{\nu}$ and $B \rightarrow X_s\gamma$ decays using heavy quark expansions in the kinetic scheme”. In: *Phys. Rev. D* 73 (2006), p. 073008. DOI: 10.1103/PhysRevD.73.073008. arXiv: hep-ph/0507253.
- [329] Torbjorn Sjostrand, Stephen Mrenna, and Peter Z. Skands. “A Brief Introduction to PYTHIA 8.1”. In: *Comput. Phys. Commun.* 178 (2008), pp. 852–867. DOI: 10.1016/j.cpc.2008.01.036. arXiv: 0710.3820 [hep-ph].

- [330] Eric Conte, Benjamin Fuks, and Guillaume Serret. “MadAnalysis 5, A User-Friendly Framework for Collider Phenomenology”. In: *Comput. Phys. Commun.* 184 (2013), pp. 222–256. DOI: 10.1016/j.cpc.2012.09.009. arXiv: 1206.1599 [hep-ph].
- [331] Eric Conte et al. “Designing and recasting LHC analyses with MadAnalysis 5”. In: *Eur. Phys. J. C* 74.10 (2014), p. 3103. DOI: 10.1140/epjc/s10052-014-3103-0. arXiv: 1405.3982 [hep-ph].
- [332] B. Dumont et al. “Toward a public analysis database for LHC new physics searches using MADANALYSIS 5”. In: *Eur. Phys. J. C* 75.2 (2015), p. 56. DOI: 10.1140/epjc/s10052-014-3242-3. arXiv: 1407.3278 [hep-ph].
- [333] Matteo Cacciari, Gavin P. Salam, and Gregory Soyez. “The anti- k_t jet clustering algorithm”. In: *JHEP* 04 (2008), p. 063. DOI: 10.1088/1126-6708/2008/04/063. arXiv: 0802.1189 [hep-ph].
- [334] Matteo Cacciari, Gavin P. Salam, and Gregory Soyez. “FastJet User Manual”. In: *Eur. Phys. J. C* 72 (2012), p. 1896. DOI: 10.1140/epjc/s10052-012-1896-2. arXiv: 1111.6097 [hep-ph].
- [335] Andrea Alberti et al. “Precision Determination of the Cabibbo-Kobayashi-Maskawa Element V_{cb} ”. In: *Phys. Rev. Lett.* 114.6 (2015), p. 061802. DOI: 10.1103/PhysRevLett.114.061802. arXiv: 1411.6560 [hep-ph].
- [336] Andrzej J. Buras et al. “Completing the NLO QCD calculation of anti-B \rightarrow X(s gamma)”. In: *Nucl. Phys. B* 631 (2002), pp. 219–238. DOI: 10.1016/S0550-3213(02)00261-4. arXiv: hep-ph/0203135.
- [337] H.M. Asatrian et al. “Charm quark mass dependence of the electromagnetic dipole operator contribution to $\bar{B} \rightarrow X_s \gamma$ at $O(\alpha_s^2)$ ”. In: *Phys. Lett. B* 647 (2007), pp. 173–178. DOI: 10.1016/j.physletb.2007.02.027. arXiv: hep-ph/0611123.
- [338] Thorsten Ewerth. “Fermionic corrections to the interference of the electro- and chromomagnetic dipole operators in $\bar{B} \rightarrow X_s \gamma$ at $O(\alpha_s^2)$ ”. In: *Phys. Lett. B* 669 (2008), pp. 167–172. DOI: 10.1016/j.physletb.2008.09.045. arXiv: 0805.3911 [hep-ph].
- [339] R. Boughezal, M. Czakon, and T. Schutzmeier. “NNLO fermionic corrections to the charm quark mass dependent matrix elements in $\bar{B} \rightarrow X_s \gamma$ ”. In: *JHEP* 09 (2007), p. 072. DOI: 10.1088/1126-6708/2007/09/072. arXiv: 0707.3090 [hep-ph].
- [340] H.M. Asatrian et al. “Complete (O_7, O_8) contribution to $B \rightarrow X_s \gamma$ at order α_s^2 ”. In: *Phys. Rev. D* 82 (2010), p. 074006. DOI: 10.1103/PhysRevD.82.074006. arXiv: 1005.5587 [hep-ph].
- [341] Andrea Ferroglia and Ulrich Haisch. “Chromomagnetic Dipole-Operator Corrections in $\bar{B} \rightarrow X_s \gamma$ at $O(\beta_0 \alpha_s^2)$ ”. In: *Phys. Rev. D* 82 (2010), p. 094012. DOI: 10.1103/PhysRevD.82.094012. arXiv: 1009.2144 [hep-ph].
- [342] Mikolaj Misiak and Michal Poradzinski. “Completing the Calculation of BLM corrections to $\bar{B} \rightarrow X_s \gamma$ ”. In: *Phys. Rev. D* 83 (2011), p. 014024. DOI: 10.1103/PhysRevD.83.014024. arXiv: 1009.5685 [hep-ph].
- [343] Stanley J. Brodsky, G.Peter Lepage, and Paul B. Mackenzie. “On the Elimination of Scale Ambiguities in Perturbative Quantum Chromodynamics”. In: *Phys. Rev. D* 28 (1983), p. 228. DOI: 10.1103/PhysRevD.28.228.

- [344] Michael Benzke et al. “Factorization at Subleading Power and Irreducible Uncertainties in $\bar{B} \rightarrow X_s \gamma$ Decay”. In: *JHEP* 08 (2010), p. 099. DOI: 10.1007/JHEP08(2010)099. arXiv: 1003.5012 [hep-ph].
- [345] Thorsten Ewerth, Paolo Gambino, and Soumitra Nandi. “Power suppressed effects in $\bar{B} \rightarrow X_s \gamma$ at $\mathcal{O}(\alpha_s)$ ”. In: *Nucl. Phys. B* 830 (2010), pp. 278–290. DOI: 10.1016/j.nuclphysb.2009.12.035. arXiv: 0911.2175 [hep-ph].
- [346] Andrea Alberti, Paolo Gambino, and Soumitra Nandi. “Perturbative corrections to power suppressed effects in semileptonic B decays”. In: *JHEP* 01 (2014), p. 147. DOI: 10.1007/JHEP01(2014)147. arXiv: 1311.7381 [hep-ph].
- [347] David M. Straub. “flavio: a Python package for flavour and precision phenomenology in the Standard Model and beyond”. In: (Oct. 2018). arXiv: 1810.08132 [hep-ph].
- [348] Jason Aebischer, Jacky Kumar, and David M. Straub. “Wilson: a Python package for the running and matching of Wilson coefficients above and below the electroweak scale”. In: *Eur. Phys. J. C* 78.12 (2018), p. 1026. DOI: 10.1140/epjc/s10052-018-6492-7. arXiv: 1804.05033 [hep-ph].
- [349] Simone Bifani et al. “Review of Lepton Universality tests in B decays”. In: *J. Phys. G* 46.2 (2019), p. 023001. DOI: 10.1088/1361-6471/aaf5de. arXiv: 1809.06229 [hep-ex].
- [350] Gordon L. Kane, G.A. Ladinsky, and C.P. Yuan. “Using the Top Quark for Testing Standard Model Polarization and CP Predictions”. In: *Phys. Rev. D* 45 (1992), pp. 124–141. DOI: 10.1103/PhysRevD.45.124.
- [351] D. Atwood and A. Soni. “Analysis for magnetic moment and electric dipole moment form-factors of the top quark via $e^+e^- \rightarrow t\bar{t}$ ”. In: *Phys. Rev. D* 45 (1992), pp. 2405–2413. DOI: 10.1103/PhysRevD.45.2405.
- [352] Bohdan Grzadkowski, Zenro Hioki, and Michal Szafranski. “Four Fermi effective operators in top quark production and decay”. In: (Dec. 1997). Ed. by Ties Behnke et al., pp. 1113–1135. DOI: 10.1103/PhysRevD.58.035002. arXiv: hep-ph/9712357.
- [353] Longin Brzezinski, Bohdan Grzadkowski, and Zenro Hioki. “Effects of nonstandard interactions for the energy spectrum of secondary leptons in $e^+e^- \rightarrow t \text{ anti-}t$ ”. In: *Int. J. Mod. Phys. A* 14 (1999), pp. 1261–1282. DOI: 10.1142/S0217751X99000646. arXiv: hep-ph/9710358.
- [354] E. Boos et al. “Probe of the Wtb coupling in $t\bar{t}$ pair production at linear colliders”. In: *Eur. Phys. J. C* 16 (2000), pp. 269–278. DOI: 10.1007/s100520050019. arXiv: hep-ph/0001048.
- [355] M. Jezabek, T. Nagano, and Y. Sumino. “Probe of CP violation in $e^+e^- \rightarrow t\bar{t}$ near threshold”. In: *Phys. Rev. D* 62 (2000), p. 014034. DOI: 10.1103/PhysRevD.62.014034. arXiv: hep-ph/0001322.
- [356] Bohdan Grzadkowski and Zenro Hioki. “Optimal observable analysis of the angular and energy distributions for top quark decay products at polarized linear colliders”. In: *Nucl. Phys. B* 585 (2000). [Erratum: *Nucl.Phys.B* 894, 585–587 (2015)], pp. 3–27. DOI: 10.1016/j.nuclphysb.2015.03.020. arXiv: hep-ph/0004223.
- [357] Patrick Janot. “Top-quark electroweak couplings at the FCC-ee”. In: *JHEP* 04 (2015), p. 182. DOI: 10.1007/JHEP04(2015)182. arXiv: 1503.01325 [hep-ph].

- [358] Raoul Röntschi and Markus Schulze. “Probing top- Z dipole moments at the LHC and ILC”. In: *JHEP* 08 (2015), p. 044. DOI: 10.1007/JHEP08(2015)044. arXiv: 1501.05939 [hep-ph].
- [359] P.H. Kiem et al. “Probing New Physics using top quark polarization in the $e^+e^- \rightarrow t\bar{t}$ process at future Linear Colliders”. In: Mar. 2015. arXiv: 1503.04247 [hep-ph].
- [360] Christoph Englert and Michael Russell. “Top quark electroweak couplings at future lepton colliders”. In: *Eur. Phys. J. C* 77.8 (2017), p. 535. DOI: 10.1140/epjc/s10052-017-5095-z. arXiv: 1704.01782 [hep-ph].
- [361] Gauthier Durieux et al. “Global and optimal probes for the top-quark effective field theory at future lepton colliders”. In: *JHEP* 10 (2018), p. 168. DOI: 10.1007/JHEP10(2018)168. arXiv: 1807.02121 [hep-ph].
- [362] M.S. Amjad et al. “A precise characterisation of the top quark electro-weak vertices at the ILC”. In: *Eur. Phys. J. C* 75.10 (2015), p. 512. DOI: 10.1140/epjc/s10052-015-3746-5. arXiv: 1505.06020 [hep-ex].
- [363] M.S. Amjad et al. “A precise determination of top quark electro-weak couplings at the ILC operating at $\sqrt{s} = 500$ GeV”. In: (July 2013). arXiv: 1307.8102 [hep-ex].
- [364] H. Abramowicz et al. “Top-Quark Physics at the CLIC Electron-Positron Linear Collider”. In: *JHEP* 11 (2019), p. 003. DOI: 10.1007/JHEP11(2019)003. arXiv: 1807.02441 [hep-ex].
- [365] A. Abada et al. “FCC-ee: The Lepton Collider: Future Circular Collider Conceptual Design Report Volume 2”. In: *Eur. Phys. J. ST* 228.2 (2019), pp. 261–623. DOI: 10.1140/epjst/e2019-900045-4.
- [366] Tobias Hurth, Sophie Renner, and William Shepherd. “Matching for FCNC effects in the flavour-symmetric SMEFT”. In: *JHEP* 06 (2019), p. 029. DOI: 10.1007/JHEP06(2019)029. arXiv: 1903.00500 [hep-ph].
- [367] Andrzej J. Buras et al. “ $B \rightarrow K^{(*)}\nu\bar{\nu}$ decays in the Standard Model and beyond”. In: *JHEP* 02 (2015), p. 184. DOI: 10.1007/JHEP02(2015)184. arXiv: 1409.4557 [hep-ph].
- [368] Gerhard Buchalla, Gudrun Hiller, and Gino Isidori. “Phenomenology of nonstandard Z couplings in exclusive semileptonic $b \rightarrow s$ transitions”. In: *Phys. Rev. D* 63 (2000), p. 014015. DOI: 10.1103/PhysRevD.63.014015. arXiv: hep-ph/0006136.
- [369] Christoph Bobeth et al. “Yukawa enhancement of Z -mediated new physics in $\Delta S = 2$ and $\Delta B = 2$ processes”. In: *JHEP* 07 (2017), p. 124. DOI: 10.1007/JHEP07(2017)124. arXiv: 1703.04753 [hep-ph].
- [370] Wouter Dekens and Peter Stoffer. “Low-energy effective field theory below the electroweak scale: matching at one loop”. In: *JHEP* 10 (2019), p. 197. DOI: 10.1007/JHEP10(2019)197. arXiv: 1908.05295 [hep-ph].
- [371] Motoi Endo, Satoshi Mishima, and Daiki Ueda. “Revisiting electroweak radiative corrections to $b \rightarrow s\ell\ell$ in SMEFT”. In: (Dec. 2020). arXiv: 2012.06197 [hep-ph].
- [372] Luca Di Luzio et al. “ ΔM_s theory precision confronts flavour anomalies”. In: *JHEP* 12 (2019), p. 009. DOI: 10.1007/JHEP12(2019)009. arXiv: 1909.11087 [hep-ph].

- [373] T. Inami and C.S. Lim. “Effects of Superheavy Quarks and Leptons in Low-Energy Weak Processes $K_L \rightarrow \mu\bar{\mu}$, $K^+ \rightarrow \pi^+\nu\bar{\nu}$ and $K^0 \leftrightarrow \bar{K}^0$ ”. In: *Prog. Theor. Phys.* 65 (1981). [Erratum: *Prog.Theor.Phys.* 65, 1772 (1981)], p. 297. DOI: 10.1143/PTP.65.297.
- [374] Ferruccio Feruglio, Paride Paradisi, and Andrea Pattori. “On the Importance of Electroweak Corrections for B Anomalies”. In: *JHEP* 09 (2017), p. 061. DOI: 10.1007/JHEP09(2017)061. arXiv: 1705.00929 [hep-ph].
- [375] Flavio Archilli. “Rare penguin decays at LHCb”. In: (Mar. 2021). URL: <https://cds.cern.ch/record/2759107>.
- [376] Albert M Sirunyan et al. “Measurement of top quark pair production in association with a Z boson in proton-proton collisions at $\sqrt{s} = 13$ TeV”. In: *JHEP* 03 (2020), p. 056. DOI: 10.1007/JHEP03(2020)056. arXiv: 1907.11270 [hep-ex].
- [377] S. Frixione et al. “Electroweak and QCD corrections to top-pair hadroproduction in association with heavy bosons”. In: *JHEP* 06 (2015), p. 184. DOI: 10.1007/JHEP06(2015)184. arXiv: 1504.03446 [hep-ph].
- [378] D. de Florian et al. “Handbook of LHC Higgs Cross Sections: 4. Deciphering the Nature of the Higgs Sector”. In: 2/2017 (Oct. 2016). DOI: 10.23731/CYRM-2017-002. arXiv: 1610.07922 [hep-ph].
- [379] R. Frederix et al. “The automation of next-to-leading order electroweak calculations”. In: *JHEP* 07 (2018), p. 185. DOI: 10.1007/JHEP07(2018)185. arXiv: 1804.10017 [hep-ph].
- [380] Georges Aad et al. “Measurement of the $t\bar{t}$ production cross-section and lepton differential distributions in $e\mu$ dilepton events from pp collisions at $\sqrt{s} = 13$ TeV with the ATLAS detector”. In: (Oct. 2019). arXiv: 1910.08819 [hep-ex].
- [381] Michal Czakon and Alexander Mitov. “Top++: A Program for the Calculation of the Top-Pair Cross-Section at Hadron Colliders”. In: *Comput. Phys. Commun.* 185 (2014), p. 2930. DOI: 10.1016/j.cpc.2014.06.021. arXiv: 1112.5675 [hep-ph].
- [382] S. Schael et al. “Precision electroweak measurements on the Z resonance”. In: *Phys. Rept.* 427 (2006), pp. 257–454. DOI: 10.1016/j.physrep.2005.12.006. arXiv: hep-ex/0509008.
- [383] O. Lutz et al. “Search for $B \rightarrow h^{(*)}\nu\bar{\nu}$ with the full Belle $\Upsilon(4S)$ data sample”. In: *Phys. Rev. D* 87.11 (2013), p. 111103. DOI: 10.1103/PhysRevD.87.111103. arXiv: 1303.3719 [hep-ex].
- [384] J.P. Lees et al. “Search for $B \rightarrow K^{(*)}\nu\bar{\nu}$ and invisible quarkonium decays”. In: *Phys. Rev. D* 87.11 (2013), p. 112005. DOI: 10.1103/PhysRevD.87.112005. arXiv: 1303.7465 [hep-ex].
- [385] J.P. Lees et al. “Measurement of the $B \rightarrow X_s l^+ l^-$ branching fraction and search for direct CP violation from a sum of exclusive final states”. In: *Phys. Rev. Lett.* 112 (2014), p. 211802. DOI: 10.1103/PhysRevLett.112.211802. arXiv: 1312.5364 [hep-ex].
- [386] Tobias Huber, Tobias Hurth, and Enrico Lunghi. “Inclusive $\bar{B} \rightarrow X_s \ell^+ \ell^-$: complete angular analysis and a thorough study of collinear photons”. In: *JHEP* 06 (2015), p. 176. DOI: 10.1007/JHEP06(2015)176. arXiv: 1503.04849 [hep-ph].

- [387] Y. Sato et al. “Measurement of the lepton forward-backward asymmetry in $B \rightarrow X_s \ell^+ \ell^-$ decays with a sum of exclusive modes”. In: *Phys. Rev. D* 93.3 (2016). [Addendum: *Phys.Rev.D* 93, 059901 (2016)], p. 032008. DOI: 10.1103/PhysRevD.93.059901. arXiv: 1402.7134 [hep-ex].
- [388] Roel Aaij et al. “Differential branching fraction and angular analysis of $\Lambda_b^0 \rightarrow \Lambda \mu^+ \mu^-$ decays”. In: *JHEP* 06 (2015). [Erratum: *JHEP* 09, 145 (2018)], p. 115. DOI: 10.1007/JHEP06(2015)115. arXiv: 1503.07138 [hep-ex].
- [389] Jason Aebischer et al. “A Global Likelihood for Precision Constraints and Flavour Anomalies”. In: *Eur. Phys. J. C* 79.6 (2019), p. 509. DOI: 10.1140/epjc/s10052-019-6977-z. arXiv: 1810.07698 [hep-ph].
- [390] Marco Ciuchini et al. “Lessons from the $B^{0,+} \rightarrow K^{*0,+} \mu^+ \mu^-$ angular analyses”. In: (Nov. 2020). arXiv: 2011.01212 [hep-ph].
- [391] Admir Greljo and David Marzocca. “High- p_T dilepton tails and flavor physics”. In: *Eur. Phys. J. C* 77.8 (2017), p. 548. DOI: 10.1140/epjc/s10052-017-5119-8. arXiv: 1704.09015 [hep-ph].
- [392] ATLAS. “Prospects for the measurement of $t\bar{t}\gamma$ with the upgraded ATLAS detector at the High-Luminosity LHC”. In: *ATL-PHYS-PUB-2018-049* (2018).
- [393] “Addendum to the report on the physics at the HL-LHC, and perspectives for the HE-LHC: Collection of notes from ATLAS and CMS”. In: *CERN Yellow Rep. Monogr.* 7 (2019), Addendum. DOI: 10.23731/CYRM-2019-007.Addendum. arXiv: 1902.10229 [hep-ex].
- [394] CMS. “Anomalous couplings in the $t\bar{t}+Z$ final state at the HL-LHC”. In: *CMS-PAS-FTR-18-036* (Dec. 2018).
- [395] CMS. “Projection of measurements of differential $t\bar{t}$ production cross sections in the e/u +jets channels in pp collisions at the HL-LHC”. In: *CMS-PAS-FTR-18-015* (Dec. 2018).
- [396] W. Altmannshofer et al. “The Belle II Physics Book”. In: *PTEP* 2019.12 (2019). Ed. by E. Kou and P. Urquijo. [Erratum: *PTEP* 2020, 029201 (2020)], p. 123C01. DOI: 10.1093/ptep/ptz106. arXiv: 1808.10567 [hep-ex].
- [397] P. Achard et al. “Search for heavy neutral and charged leptons in e^+e^- annihilation at LEP”. In: *Phys. Lett. B* 517 (2001), pp. 75–85. DOI: 10.1016/S0370-2693(01)01005-X. arXiv: hep-ex/0107015.
- [398] Georges Aad et al. “Search for heavy lepton resonances decaying to a Z boson and a lepton in pp collisions at $\sqrt{s} = 8$ TeV with the ATLAS detector”. In: *JHEP* 09 (2015), p. 108. DOI: 10.1007/JHEP09(2015)108. arXiv: 1506.01291 [hep-ex].
- [399] Nilanjana Kumar and Stephen P. Martin. “Vectorlike Leptons at the Large Hadron Collider”. In: *Phys. Rev. D* 92.11 (2015), p. 115018. DOI: 10.1103/PhysRevD.92.115018. arXiv: 1510.03456 [hep-ph].
- [400] Albert M Sirunyan et al. “Search for vector-like leptons in multilepton final states in proton-proton collisions at $\sqrt{s} = 13$ TeV”. In: *Phys. Rev. D* 100.5 (2019), p. 052003. DOI: 10.1103/PhysRevD.100.052003. arXiv: 1905.10853 [hep-ex].
- [401] Andreas Crivellin et al. “Global Electroweak Fit and Vector-Like Leptons in Light of the Cabibbo Angle Anomaly”. In: (Aug. 2020). arXiv: 2008.01113 [hep-ph].

- [402] Daniel F. Litim, Matin Mojaza, and Francesco Sannino. “Vacuum stability of asymptotically safe gauge-Yukawa theories”. In: *JHEP* 01 (2016), p. 081. DOI: 10.1007/JHEP01(2016)081. arXiv: 1501.03061 [hep-th].
- [403] Andreas Crivellin, Martin Hoferichter, and Philipp Schmidt-Wellenburg. “Combined explanations of $(g - 2)_{\mu,e}$ and implications for a large muon EDM”. In: *Phys. Rev. D* 98.11 (2018), p. 113002. DOI: 10.1103/PhysRevD.98.113002. arXiv: 1807.11484 [hep-ph].
- [404] Arindam Das and Sanjoy Mandal. “Bounds on the triplet fermions in type-III seesaw and implications for collider searches”. In: (June 2020). arXiv: 2006.04123 [hep-ph].
- [405] Danielle Sabatta et al. “Connecting muon anomalous magnetic moment and multi-lepton anomalies at LHC”. In: *Chin. Phys. C* 44.6 (2020), p. 063103. DOI: 10.1088/1674-1137/44/6/063103. arXiv: 1909.03969 [hep-ph].
- [406] Johan Alwall et al. “Comparative study of various algorithms for the merging of parton showers and matrix elements in hadronic collisions”. In: *Eur. Phys. J. C* 53 (2008), pp. 473–500. DOI: 10.1140/epjc/s10052-007-0490-5. arXiv: 0706.2569 [hep-ph].
- [407] Johan Alwall, Simon de Visscher, and Fabio Maltoni. “QCD radiation in the production of heavy colored particles at the LHC”. In: *JHEP* 02 (2009), p. 017. DOI: 10.1088/1126-6708/2009/02/017. arXiv: 0810.5350 [hep-ph].
- [408] F. Campanario et al. “QCD corrections to charged triple vector boson production with leptonic decay”. In: *Phys. Rev. D* 78 (2008), p. 094012. DOI: 10.1103/PhysRevD.78.094012. arXiv: 0809.0790 [hep-ph].
- [409] V. Hankele and D. Zeppenfeld. “QCD corrections to hadronic WWZ production with leptonic decays”. In: *Phys. Lett. B* 661 (2008), pp. 103–108. DOI: 10.1016/j.physletb.2008.02.014. arXiv: 0712.3544 [hep-ph].
- [410] Achilleas Lazopoulos, Kirill Melnikov, and Frank Petriello. “QCD corrections to tri-boson production”. In: *Phys. Rev. D* 76 (2007), p. 014001. DOI: 10.1103/PhysRevD.76.014001. arXiv: hep-ph/0703273.
- [411] T. Binoth et al. “NLO QCD corrections to tri-boson production”. In: *JHEP* 06 (2008), p. 082. DOI: 10.1088/1126-6708/2008/06/082. arXiv: 0804.0350 [hep-ph].
- [412] F. Cascioli et al. “ZZ production at hadron colliders in NNLO QCD”. In: *Phys. Lett. B* 735 (2014), pp. 311–313. DOI: 10.1016/j.physletb.2014.06.056. arXiv: 1405.2219 [hep-ph].
- [413] Fabrizio Caola et al. “QCD corrections to ZZ production in gluon fusion at the LHC”. In: *Phys. Rev. D* 92.9 (2015), p. 094028. DOI: 10.1103/PhysRevD.92.094028. arXiv: 1509.06734 [hep-ph].
- [414] J. de Favereau et al. “DELPHES 3, A modular framework for fast simulation of a generic collider experiment”. In: *JHEP* 02 (2014), p. 057. DOI: 10.1007/JHEP02(2014)057. arXiv: 1307.6346 [hep-ex].
- [415] M. Bona et al. “The Unitarity Triangle Fit in the Standard Model and Hadronic Parameters from Lattice QCD: A Reappraisal after the Measurements of Δm_s and $\text{BR}(B \rightarrow \tau \nu_\tau)$ ”. In: *JHEP* 10 (2006), p. 081. DOI: 10.1088/1126-6708/2006/10/081. arXiv: hep-ph/0606167.
- [416] UTfit. In: (2016). URL: <http://www.utfit.org/UTfit/ResultsSummer2016SM>.

- [417] Bernard Aubert et al. “Determination of the branching fraction for $B \rightarrow X_c \ell \nu$ decays and of $|V_{cb}|$ from hadronic mass and lepton energy moments”. In: *Phys. Rev. Lett.* 93 (2004), p. 011803. DOI: 10.1103/PhysRevLett.93.011803. arXiv: hep-ex/0404017.
- [418] Benjamin Grinstein and Mark B. Wise. “Operator analysis for precision electroweak physics”. In: *Phys. Lett. B* 265 (1991), pp. 326–334. DOI: 10.1016/0370-2693(91)90061-T.
- [419] Ilaria Brivio, Yun Jiang, and Michael Trott. “The SMEFTsim package, theory and tools”. In: *JHEP* 12 (2017), p. 070. DOI: 10.1007/JHEP12(2017)070. arXiv: 1709.06492 [hep-ph].
- [420] M. Beneke, T. Feldmann, and D. Seidel. “Systematic approach to exclusive $B \rightarrow V l^+ l^-, V \gamma$ decays”. In: *Nucl. Phys. B* 612 (2001), pp. 25–58. DOI: 10.1016/S0550-3213(01)00366-2. arXiv: hep-ph/0106067.
- [421] Matthew D. Schwartz. *Quantum Field Theory and the Standard Model*. Cambridge University Press, Mar. 2014. ISBN: 978-1-107-03473-0, 978-1-107-03473-0.
- [422] V.V. Sudakov. “Vertex parts at very high-energies in quantum electrodynamics”. In: *Sov. Phys. JETP* 3 (1956), pp. 65–71.
- [423] T.D. Lee and M. Nauenberg. “Degenerate Systems and Mass Singularities”. In: *Phys. Rev.* 133 (1964). Ed. by G. Feinberg, B1549–B1562. DOI: 10.1103/PhysRev.133.B1549.
- [424] T. Kinoshita. “Mass singularities of Feynman amplitudes”. In: *J. Math. Phys.* 3 (1962), pp. 650–677. DOI: 10.1063/1.1724268.
- [425] George F. Sterman and Steven Weinberg. “Jets from Quantum Chromodynamics”. In: *Phys. Rev. Lett.* 39 (1977), p. 1436. DOI: 10.1103/PhysRevLett.39.1436.
- [426] V.N. Gribov and L.N. Lipatov. “Deep inelastic e p scattering in perturbation theory”. In: *Sov. J. Nucl. Phys.* 15 (1972), pp. 438–450.
- [427] L.N. Lipatov. “The parton model and perturbation theory”. In: *Sov. J. Nucl. Phys.* 20 (1975), pp. 94–102.
- [428] Guido Altarelli and G. Parisi. “Asymptotic Freedom in Parton Language”. In: *Nucl. Phys. B* 126 (1977), pp. 298–318. DOI: 10.1016/0550-3213(77)90384-4.
- [429] Yuri L. Dokshitzer. “Calculation of the Structure Functions for Deep Inelastic Scattering and e+ e- Annihilation by Perturbation Theory in Quantum Chromodynamics”. In: *Sov. Phys. JETP* 46 (1977), pp. 641–653.
- [430] L.A. Harland-Lang et al. “Parton distributions in the LHC era: MMHT 2014 PDFs”. In: *Eur. Phys. J. C* 75.5 (2015), p. 204. DOI: 10.1140/epjc/s10052-015-3397-6. arXiv: 1412.3989 [hep-ph].
- [431] Richard D. Ball et al. “Parton distributions from high-precision collider data”. In: *Eur. Phys. J. C* 77.10 (2017), p. 663. DOI: 10.1140/epjc/s10052-017-5199-5. arXiv: 1706.00428 [hep-ph].
- [432] Sayipjamal Dulat et al. “New parton distribution functions from a global analysis of quantum chromodynamics”. In: *Phys. Rev. D* 93.3 (2016), p. 033006. DOI: 10.1103/PhysRevD.93.033006. arXiv: 1506.07443 [hep-ph].

- [433] S. Alekhin et al. “Parton distribution functions, α_s , and heavy-quark masses for LHC Run II”. In: *Phys. Rev. D* 96.1 (2017), p. 014011. DOI: 10.1103/PhysRevD.96.014011. arXiv: 1701.05838 [hep-ph].
- [434] Pedro Jimenez-Delgado and Ewald Reya. “Delineating parton distributions and the strong coupling”. In: *Phys. Rev. D* 89.7 (2014), p. 074049. DOI: 10.1103/PhysRevD.89.074049. arXiv: 1403.1852 [hep-ph].
- [435] Hamed Abdolmaleki et al. “Impact of low- x resummation on QCD analysis of HERA data”. In: *Eur. Phys. J. C* 78.8 (2018), p. 621. DOI: 10.1140/epjc/s10052-018-6090-8. arXiv: 1802.00064 [hep-ph].
- [436] Adam Alloul et al. “FeynRules 2.0 - A complete toolbox for tree-level phenomenology”. In: *Comput. Phys. Commun.* 185 (2014), pp. 2250–2300. DOI: 10.1016/j.cpc.2014.04.012. arXiv: 1310.1921 [hep-ph].
- [437] John Allison et al. “Geant4 developments and applications”. In: *IEEE Trans. Nucl. Sci.* 53 (2006), p. 270. DOI: 10.1109/TNS.2006.869826.
- [438] LsqFitLsqFit.jl package. In: (2019). URL: <https://github.com/JuliaNLSolvers/LsqFit.jl>.
- [439] Pierre Artoisenet et al. “Automatic spin-entangled decays of heavy resonances in Monte Carlo simulations”. In: *JHEP* 03 (2013), p. 015. DOI: 10.1007/JHEP03(2013)015. arXiv: 1212.3460 [hep-ph].

Glossary

- ADM - Anomalous dimension matrix 27
- AMM - Anomalous magnetic moment 2
- BSM - Beyond the Standard Model 1
- CKM - Cabibbo-Kobayashi-Maskawa 12
- CLIC - Compact Linear Collider 67
- DGLAP - Dokshitzer-Gribov-Lipatov-Altarelli-Parisi 127
- EFT - Effective field theory 2
- EW - Electroweak 5
- EWSB - Electroweak symmetry breaking 11
- FCNC - Flavor changing neutral current 21
- FCC - Future Circular Collider 67
- HEFT - Higgs Effective Field Theorie 36
- HFLAV - Heavy Flavor Averaging Group 59
- HL-LHC - High-Luminosity Large Hadron Collider 52
- IR - Infrared 20
- ILC - International Linear Collider 67
- LEFT - Low-energy effective theory 29
- LEP - Large Electron-Positron Collider 67
- LHC - Large Hadron Collider 1
- LO - Leading order 20
- MCMC - Markow chain Monte Carlo 37
- MS - Minimal subtraction 14
- $\overline{\text{MS}}$ - Modified minimal subtraction 14
- MC - Monte Carlo 43
- NDA - Naive dimensional analysis 31

- NLO - Next-to leading order 15
- NNLO - Next-to-next-to leading order 35
- PDF - Parton distribution function 41
- OCDF - Opposite charge and different flavor 99
- OCSF - Opposite charge and same flavor 99
- QCD - Quantum chromodynamics 5
- QED - Quantum electrodynamics 9
- RGE - Renormalization group equation 16
- SSB - Spontaneous symmetry breaking 10
- SM - Standard Model 1
- SMEFT - Standard Model Effective Field Theory 2
- UV - Ultraviolet 13
- UFO - Universal Feynrules Output 41
- VEV - Vacuum expectation value 10
- VLL - Vector-like leptons 89
- WET - Weak Effective Theory 26

Eidesstattliche Versicherung

Ich versichere hiermit an Eides statt, dass ich die vorliegende Dissertation mit dem Titel *Synergies of flavor anomalies with top-quark physics in the Standard Model Effective Field Theory and direct searches* selbstständig und ohne unzulässige fremde Hilfe erbracht habe. Ich habe keine anderen als die angegebenen Quellen und Hilfsmittel benutzt, sowie wörtliche und sinngemäße Zitate kenntlich gemacht. Die Arbeit hat in gleicher oder ähnlicher Form noch keiner Prüfungsbehörde vorgelegen.

Ort, Datum

Unterschrift

Belehrung

Wer vorsätzlich gegen eine die Täuschung über Prüfungsleistungen betreffende Regelung einer Hochschulprüfungsordnung verstößt, handelt ordnungswidrig. Die Ordnungswidrigkeit kann mit einer Geldbuße von bis zu 50 000 € geahndet werden. Zuständige Verwaltungsbehörde für die Verfolgung und Ahndung von Ordnungswidrigkeiten ist der Kanzler/die Kanzlerin der Technischen Universität Dortmund. Im Falle eines mehrfachen oder sonstigen schwerwiegenden Täuschungsversuches kann der Prüfling zudem exmatrikuliert werden (§ 63 Abs. 5 Hochschulgesetz –HG–).

Die Abgabe einer falschen Versicherung an Eides statt wird mit Freiheitsstrafe bis zu 3 Jahren oder mit Geldstrafe bestraft.

Die Technische Universität Dortmund wird ggf. elektronische Vergleichswerkzeuge (wie z. B. die Software “turnitin”) zur Überprüfung von Ordnungswidrigkeiten in Prüfungsverfahren nutzen.

Die oben stehende Belehrung habe ich zur Kenntnis genommen.

Ort, Datum

Unterschrift